Étude de Techniques de Réception des Modulations de Fréquence pour la Télémesure Aéronautique

Rami Othman

UNIVERSITE BRETAGNE LOIRE / MATHSTIC

CentraleSupélec

THESE DE DOCTORAT DE

CENTRALESUPELEC
COMUE UNIVERSITE BRETAGNE LOIRE

ECOLE DOCTORALE N° 601
Mathématiques et Sciences et Technologies de l'Information et de la Communication
Spécialité : *Télécommunications*

Par

« Rami OTHMAN »

« Étude de Techniques de Réception des Modulations de Fréquence pour la Télémesure Aéronautique »

Thèse présentée et soutenue à Rennes, le 17 janvier 2019
Unité de recherche : UMR 6164 – IETR (Équipe SCEE)
Thèse N° :

Rapporteurs avant soutenance :

Charly POULLIAT	Professeur de l'INP Toulouse
Giulio COLAVOLPE	Professeur de l'université de Parme

Composition du Jury :

Attention, en cas d'absence d'un des membres du Jury le jour de la soutenance, la composition ne comprend que les membres présents

Karine AMIS	Maître de conférences de l'IMT Atlantique
Guillaume FERRÉ	Maître de conférences de l'IMS Bordeaux

Président *(à préciser après la soutenance)*

Prénom Nom	Fonction et établissement d'exercice

Directeur de thèse	
Yves LOUËT	Professeur de CentraleSupélec
Encadrant	
Alexandre SKRZYPCZAK	Ingénieur de recherche de Zodiac Data Systems

À la mémoire de ma mère.

Remerciements

And I would like to acknowledge ...

Résumé

Résumé ici...

Abstract

Abstract goes here...

Contents

Nomenclature

Acronyms and Abbreviations

BT	*Bandwidth Time product*
AM	*Amplitude Modulation*
APSK	*Amplitude Phase-Shift Keying*
ARTM	*Advanced Range Telemetry Group*
ASM	*Asynchronous Marker*
AWGN	*Additive White Gaussian Noise*
BCJR	*Bahl, Cocke, Jelinek and Raviv*
BER	*Bit Error Rate*
BPSK	*Binary Phase-Shift Keying*
CA-MLSD	*Conventional Adaptive Maximum Likelihood Sequence Detection*
CFO	*Carrier Frequency Offset*
CM	*Constant Modulus*
CMA	*Constant Modulus Algorithm*
COFDM	*Coded Orthogonal Frequency Division Multiplexing*
CPFSK	*Continuous Phase Frequency Shift Keying*
CPM	*Continuous Phase Modulation*
dB	*Decibel*
DBD	*DuoBinary Decomposition*
DF	*Decision Feedback*
DVB-RCS2	*Digital Video Broadcasting - Return Channel via Satellite - Second Generation*
FEC	*Forward Error Correction*

FIR	*Finite Impulse Response*
FM	*Frequency Modulation*
FQPSK	*Feher-patented Quadrature Phase-Shift Keying*
GFSK	*Gaussian Frequency Shift Keying*
GHz	*Gigahertz*
GMSK	*Gaussian Minimum Shift Keying*
GSM	*Global System for Mobile communication*
Hz	*Hertz*
I&D	*Integrate and Dump*
I.I.D	*Independent and Identically Distributed*
INET	*Integrated Network Enhanced Telemetry*
IRIG	*Inter-Range Instrumentation Group*
ISI	*Inter-Symbol Interference*
LDPC	*Low Parity Density Check*
LLR	*Log-Likelihood Ratio*
LMS	*Least Mean Square*
LOS	*Line Of Sight*
LS	*Least Square*
M-PSK	*M-ary Phase-Shift Keying*
M-QAM	*M-ary Quadrature Amplitude Modulation*
MAP	*Maximum A Posteriori*
Max-Log-MAP	*Maximum Logarithm Maximum A Posteriori*
Mbps	*Megabits per second*
MHz	*Megahertz*
MIL-STD SOQPSK	*Military Standard Shaped Offset Quadrature Phase-Shift Keying*
MIMO	*Multiple Input Multiple Output*
MISO	*Multiple Input Single Output*
ML	*Maximum Likelihood*

ML-ASM	*Maximum Likelihood - Approximate Signal Model*
MLSD	*Maximum Likelihood Sequence Detection*
MLSE	*Maximum Likelihood Sequence Estimation*
MMSE	*Minimum Mean Square Error*
MSE	*Mean Square Error*
MSK	*Minimum Shift Keying*
NA-MLSD	*Non-Adaptive Maximum Likelihood Sequence Detection*
NASA's JPL	*National Aeronautics and Space Administration's Jet Propulsion Lab*
NLOS	*Non-Line Of Sight*
NRZ	*Non-Return to Zero*
OD	*Offset Decode*
OQPSK	*Offset Quadrature Phase-Shift Keying*
PAM	*Pulse Amplitude Modulation*
PCM/FM	*Pulse Code Modulation/Frequency Modulation*
PRD	*Perrins-Rice Decomposition*
PSK	*Phase-Shift Keying*
PSP	*PerSurvivor Processing*
RC	*Raised Cosine*
RCC	*Range Commanders Council*
REC	*Rectangular*
RF	*Radio Frequency*
RLS	*Recursive Least Square*
SBPSK	*Shaped Binary Phase-Shift Keying*
SER	*Symbol Error Rate*
SISO	*Single Input Single Output*
SMA	*Saint Martin Airport*
SNR	*Signal-to-Noise Ratio*
SOQPSK	*Shaped Offset Quadrature Phase-Shift Keying*

SOQPSK-MIL	*Shaped Offset Quadrature Phase-Shift Keying Military*
SOQPSK-TG	*Shaped Offset Quadrature Phase-Shift Keying Telemetry Group*
SOVA	*Soft Output Viterbi Algorithm*
STBC	*Space-Time Block Coding*
STBD	*Space-Time Block Decoder*
STC	*Space-Time Coding*
SxS	*Sample by Sample*
TBA	*Toulouse-Blagnac Airport*
US	*United States*
V2V	*Vehicle To Vehicle*
XTCQM	*Cross-correlated Trellis Coded Modulation*

Introduction

General context

The work presented in this PhD thesis applies in aeronautical telemetry, which is the process of remotely collecting measurements done by electronic equipment on board the aircraft and transmitting these data to a distant location for monitoring, display, and recording [1].

An aeronautical telemetry system is used during the flight testing phase to monitor the behavior of the plane by transmitting the aircraft dynamics settings (such as velocities, vibrations, temperatures, stress and strain parameters,...) from the aircraft to the ground station over a radio-frequency (RF) link. Aeronautical telemetry is a one-way link from the plane to the ground (i.e., there is no uplink mode) that requires real-time data transmission and analysis to ensure the pilot's safety. This makes the use of the aeronautical telemetry a critical task that demands highly reliable systems. The transmitter side of an aeronautical telemetry system (on board the aircraft) is generally composed of transducers that convert a physical stimulus into an electrical signal, multiplexers that combine the measurements into one signal, a transmitting equipment that modulates the data and one (or sometimes two) omnidirectional "blade" antenna(s). When the flight test range is going to be beyond 100 km or when higher link reliability is required, a power amplifier can also be added at the transmitter side [2]. As for the receiver side (ground station), it is generally composed of a high gain parabolic dish antenna that allows tracking the aircraft, a low-noise amplifier that amplifies the signal without significantly decreasing the signal-to-noise ratio (SNR), a receiver demodulator that converts the modulated signal back to data, a recorder, and a demultiplexor.

The design and the performance of the transmitting/ receiving equipment are mainly defined by the adopted modulation that conveys the data. The first telemetry systems were analog and used frequency modulation (FM) of analog waveforms instead of amplitude modulation (AM) [3]. This choice favored the use of power amplifiers at their saturation mode without distorting the FM constant envelope signal and provided better bandwidth occupancy/performance trade-off than AM-based systems. Then, analog FM has been progressively upgraded to digital FM by feeding the transmitter with filtered digital data instead of analog waveforms. This change

only required slight modifications of the infrastructure and it did not impact the bandwidth occupancy [3]. The digital FM version is known as the non-return to zero (NRZ) pulse code modulation/frequency modulation (PCM/FM), and it can be considered as continuous phase frequency shift keying (CPFSK) modulation or more generally as continuous phase modulation (CPM) [4].

PCM/FM has been the reference modulation for decades [5] because it has proven its robustness as well as its reliability for such high-risk use and because the required data rates were low compared to the available bandwidth before the 1990's. In the telemetry literature, this modulation is sometimes called the "legacy modualtion" and is still used nowadays in several telemetry setups all over the world. However, over the past few years, two major factors have impacted the telemetering community. The first one is the exponential expansion of wireless communication systems and especially of the commercial mobile services. As an illustration, the number of mobile-broadband subscriptions has grown more than 20% annually in the last five years and has reached 4.3 billion globally by the end of 2017 [6]. This huge increase has urged telecommunication service providers to seek more bandwidth and has consequently made RF spectrum more and more costly (for instance, the United States (US) government auctioned 25 MHz of the L-band at a record of 44.89 billion dollars in 2015 [7]). As a result, the spectrum of aeronautical telemetry has been shortened by almost 35% and reallocated for the commercial applications [8].
The second factor is the data deluge of aeronautical telemetry, which is due to the use of multiple sensors on board the aircraft to acquire more and more information during the flight. This data increase comes also as a consequence of reducing the flight testing duration for cost-effectiveness. In fact, significant resources are devoted during the flight testing phase and cost around 50 thousand dollars in labor per hour [9, 10]. Therefore, reducing the test duration without decreasing the amount of transferred data is a major demand for aerospace companies. On the one hand, this significant increase in data transfer requires the adoption of more spectrally efficient modulations than PCM/FM. On the other hand, it broadens the signal bandwidth, which makes the aeronautical telemetry channel frequency selective [11] and therefore impacts the availability of the aeronautical telemetry link. The latter issue is a real burden for aerospace companies since one delayed or canceled test mission due to the unavailability of telemetry link could cost more than 1 million dollars [10].

Both economical and technical challenges have stimulated the flight test telemetry community to adopt more power and bandwidth efficient modulations than PCM/FM. This has been done via the advanced range telemetry (ARTM) program [12], which resulted in 2 spectrally efficient CPM modulations: the shaped offset quadrature phase shift keying telemetry group (SOQPSK-TG) modulation and ARTM CPM. These modulations figure in the inter-range instrumentation group (IRIG) 106 standard for aeronautical telemetry, which ensures the interoperability of telemetry systems at the range commanders council (RCC) member ranges

[5]. Both modulations are transmitter friendly since they have a constant complex envelope and require minimal infrastructure change. Moreover, they allow increasing the spectral efficiency by at least a factor of 2 compared to PCM/FM while keeping excellent power efficiency. These attractive benefits have been achieved by carefully choosing the parameters that define a CPM. However, they come at the expense of increasing the receiver complexity, especially when considering complicated scenarios such as the presence of multipath or the use of multiple-antenna transmitters [13]. This complexity is mainly due to two factors. The first one is the presence of an inherent memory that ensures the continuity of the phase of the modulation, and the second one is the nonlinear nature of CPM since the aforementioned modulation is not a linear function of the transmitted symbols. Therefore, unlike linear modulations (such as M-PSK, M-quadrature amplitude modulation (M-QAM), amplitude and phase-shift keying (APSK),...), it is not straightforward to take advantage of the properties of linear algebra to develop reduced complexity receivers.

Even if PCM/FM is still widely used in aeronautical telemetry, we observe that more and more actors, especially in the US military ranges, migrated or started the migration to the SOQPSK solution. In such a context, the telemetry industry should develop new solutions and algorithms in order to guarantee the best possible telemetry link for these highly demanding customers. This work, supervised by Zodiac Data Systems which is one of the leading companies in aeronautical telemetry for civil and military applications, enrolls in this prospective. In this thesis, we mainly focus on SOQPSK-TG whose use is getting more and more popular in aeronautical telemetry. This modulation belongs to a particular CPM family since it transmits ternary symbols instead of binary ones. Simultaneously, it can also be interpreted as an offset modulation, i.e., it can be seen as a modulation whose quadrature component contains a timing offset compared to the in-phase component. The goal of this work is to develop reception algorithms for SOQPSK-TG under different scenarios to ensure the availability of aeronautical telemetry link. These solutions should maintain a good power efficiency without prohibitive complexity for real-time implementation.

Previous work on SOQPSK-TG

SOQPSK-TG signal representations and approximations

SOQPSK-TG is a ternary CPM whose ternary symbols are linked to the binary bits using a specific precoder given in [5] and whose modulation index $h = 1/2$. The role of the precoder is to make the phase of SOQPSK-TG behaves like the phase of an OQPSK signal when both are driven by the same bit sequence [14]. As for the pulse shape that modulates the ternary symbols in the instantaneous frequency, it spans several symbol periods. The choice of these parameters increases the spectral efficiency at the expense of creating long memory and inter-symbol

interference (ISI). Thus, if we take this CPM definition, the resulting reception algorithms would be highly complex. Moreover, they would be restricted to simple scenarios due to the nonlinear nature of CPM. As a consequence, it is necessary to view this modulation differently to make it more versatile.

The first pioneering work in this direction has been done by E. Perrins in [14] where he showed that SOQPSK-TG could be written as a finite sum of pulse-amplitude modulated (PAM) components. The pulses of this decomposition, namely PRD, modulate pseudo-symbols. These pseudo-symbols contain memory and are nonlinear functions of the ternary symbols. This work is the extension of the Laurent decomposition [15], initially developed for binary CPM. The advantage of this approach is that it approximates the signal as a sum of only two PAM waveforms. However, this does not completely "linearize" the signal because of mapping between the ternary symbols and the pseudo-symbols, which keeps the long memory effect in the approximation.

The second work has been carried by T. Nelson in [16] where he took advantage of the offset nature of SOQPSK-TG and created a direct mapping between the binary bits (i.e., the bits that are used to generate the ternary symbols) and the different waveforms that constitute the eye-diagram of the signal. The representation that makes this connection (which is not evident unlike linear modulations) is known as the cross-correlated trellis coded quadrature modulation (XTCQM) representation. After some mathematical manipulations, this representation can accurately approximate SOQPSK-TG using a bank of 8 XTCQM waveforms, each one of them being defined by only 3 binary bits. The advantage of this approach is that it offers an approximation of SOQPSK-TG with a short inherent memory. However, it generates data dependent waveforms, which means that we cannot separate the contribution of the bits and the pulse shape in a clear way.

Each representation of SOQPSK-TG has its own benefits and drawbacks. Therefore, the choice between one of them depends on the desired application.

Reduced complexity detection algorithms

Several reduced detection algorithms have been proposed in the literature for SOQPSK-TG. The first ones are linear integrate and dump (I&D) detectors. They can be used to detect the binary symbols thanks to the presence of the SOQPSK-TG precoder (to the best of our knowledge, the reason why is not analytically explained in the literature). Several I&D detector implementations are given in [17], but they are sub-optimal. The best one of them suffers from a performance loss of 0.72 dB for a probability of error of 10^{-5} compared to the optimal case. Then, very near-optimal performance detectors have been developed, and they rely on the presented above approximations. The first one is presented in [18] and uses the PAM approximation of PRD and operates using a dynamic trellis of 4 states. The different transitions

and the order of the path states in the this trellis depend on the parity of bit index. The second very near-optimal reduced complexity detector uses a trellis composed of 16 states and relies on the XTCQM representation of SOQPSK-TG. The performance loss of these detectors is within 0.2 dB compared to the optimal case.

Multipath mitigation techniques

Due to the bandwidth expansion of SOQPSK-TG signal as highlighted above, the aeronautical telemetry channel becomes frequency selective. As a consequence, the receiver may capture several delayed copies of the transmitted signal with different attenuations. The transmission is thus made over a multipath channel, which can result in significant performance loss if we use the described above detectors without introducing multipath mitigation techniques, i.e., equalizers. Channel estimation and equalization is very sparsely addressed in the literature in the SOQPSK case, contrary to other modulations. To the best of our knowledge, very few works [19, 20, 21] have focused on multipath mitigation techniques for SOQPSK-TG, and they mainly rely on the constant modulus algorithm (CMA) due to the constant envelope nature of this modulation. The performance of CMA can sometimes be unsatisfactory for some channel configurations.

The two-antenna problem on aeronautical telemetry

The previous architectures mentioned above are built regardless of the number of transmitting antennas. However, this parameter has an important impact on both transmitter and receiver architectures. The first aeronautical telemetry systems used one transmitting antenna fixed underneath the aircraft fuselage and one receiving antenna on a fixed ground station. However, this scheme does not guarantee an optimal telemetry link because the receiver cannot always capture the line of sight (LOS) path when the aircraft performs certain maneuvers. To overcome this situation, two antennas are then placed on the aircraft in a way that an omnidirectional transmission is guaranteed no matter how the plane is oriented. Nevertheless, if the same signal is transmitted over both antennas using the same carrier frequency, the receiver may capture both copies in a destructive way, which causes the loss of the aeronautical telemetry link. This problem is known as the two-antenna problem in aeronautical telemetry [22]. A solution has been proposed in [13], which consists of creating transmit diversity using Alamouti space-time block coding (STBC) [23]. This solution significantly reduces the mutual interference of the SOQPSK-TG signals and has been recently standardized in IRIG-106 [5]. However, it makes recovering the data bits a hard task because of the used modulation as well as the presence of an unusual channel impairment, which is the differential delay. This perceptible delay represents a non-negligible portion of the symbol peiod as explained in details in Chapter 5. It appears since both signals arrive with different delays. Several decoding architectures relying on the

XTCQM representation have been proposed in [16, 24] but only one of them offers satisfying performance at the expense of relatively high implementation complexity. Moreover, the best decoder only provides hard outputs and does not contain any mechanism that allows mitigating multipath in the space-time coding (STC) scenario.

Contributions

This dissertation addresses all the aforementioned points and proposes different solutions for each scenario. The important contributions are summarized as follows:

- A new PAM decomposition has been developed for SOQPSK-TG. It allows approximating the signal as a simple linear modulation and providing a straightforward mapping between the binary bits and the pseudo-symbols of this decomposition. This decomposition, namely DBD in this manuscript, is the root of all the proposed solutions of this work.
- A mathematical link has been developed between this proposed PAM decomposition and the XTCQM representation for SOQPSK.
- Several reduced complexity detectors have been proposed for SOQPSK-TG based on DBD. Each class of detectors relies on a certain approach (Kaleh approach [25], Ungerboeck approach [26] and Forney approach [27]).
- To combat multipath interference, a joint channel estimation and detection algorithm has been developed for SOQPSK-TG. It relies on the proposed decomposition and the per-survivor processing (PSP) principle [28] and offers very attractive bit error rate (BER) performance for different channel configurations.
- Two different decoding structures have been proposed for the STC scenario without changing the encoder structure. The first one offers a complexity 8 times less than the state of the art decoder with very acceptable BER performance in the presence of the differential delay. The second one outperforms the state of the art decoder while keeping a lower complexity. Both proposed solutions can provide soft outputs (i.e., log-likelihood ratios).
- A new multipath channel estimator has been developed for the STC scenario and can be used along with the second proposed decoder.
- A new STC scheme has been developed that offers a better transmission rate for SOQPSK-TG than the IRIG standardized one. Moreover, the resulting decoding structure can process the even bits separately from the odd ones in the presence of non-zero differential delay and offers very attractive BER performance (within 1.1 dB of the single input single

output (SISO) bound). The complexity of the proposed decoder is at least 8 times less than the state of the art decoder associated with the standardized encoding.

Dissertation outline

This dissertation is organized as follows.

We remind in **Chapter 1** the CPM model and we define its main parameters. We then describe the different aeronautical telemetry modulations and we highlight how the spectral efficiency is achieved for each modulation. We then focus on SOQPSK and we present the state of the art representations and approximations of this signal (i.e, the PAM decomposition and the XTCQM representation as well as their respective approximations).

In **Chapter 2**, we first introduce a new vision of the precoder structure by decomposing it into two different stages: the first stage is a recursive encoder and the second one is a duobinary encoder. We then exploit this new vision to develop a new PAM decomposition of duobinary encoded CPM and we apply the obtained results to SOQPSK. We also establish in this chapter a link between the proposed PAM decomposition (DBD) of SOQPSK and its XTCQM representation as well its OQPSK interpretation. Furthermore, we detail the exact role of each stage that constitutes the SOQPSK precoder.

In **Chapter 3**, we build several detection architectures as a direct consequence of proposing a new PAM decomposition. We take advantage of several approaches of the literature. Some rely on the CPM definition of SOQPSK and then exploit the PAM decomposition (Kaleh approach [25] and others use the proposed "linearized" model of SOQPSK (Ungerboeck approach [26] and Forney approach [27]). A complexity study of all the proposed detectors is also carried in this chapter.

In **Chapter 4**, we consider the presence of multipath in the SISO scenario. We first make a classification of the existing aeronautical telemetry channels of the literature. We then present the CMA solution and its different variants. We later propose a new joint channel estimation and detection algorithm for SOQPSK-TG. This solution is an adapted version of the PSP principle and relies on the proposed PAM decomposition given in Chapter 2.

In **Chapter 5**, we focus on the IRIG standardized transmit diversity scheme that allows resolving the two-antenna problem. After introducing the IRIG standardized encoder structure and the state of the art decoders, we develop two decoding structures and we present their different variants. We then consider the presence of multipath in the STC scenario in the second part of this chapter, and we detail the derivation of the new multipath estimator.

The results given in **Chapter 5** show that the performance of proposed decoders are angle dependent due to employing the standardized scheme. For this reason, we propose in **Chapter**

6 a new encoding scheme that almost eliminates this angle dependency. Moreover, the scheme ameliorates the transmission rate and allows further complexity reduction of the decoding algorithm. In the second part of this chapter, we highlight that space-time coding is not the only way to overcome the two-antenna problem. We show that sending a SOQPSK-TG signal over one antenna and its artificially delayed copy over the other can also greatly reduce their mutual interference. After determining the necessary delay that should be applied, we show that the proposed interference mitigation technique given in Chapter 4 can also be used in this scenario. Thus, the same receiver architecture can be employed whether one or two antennas are mounted on the aircraft using this approach.

Chapter 1

Continuous Phase Modulation for Aeronautical Telemetry

Contents

1.1 CPM signal model

The complex envelope of a CPM containing the information symbols $\underline{\alpha} = \{\alpha_i\}_{i\in\mathbb{Z}}$ is expressed as [4]

$$s(t;\underline{\alpha}) = \sqrt{\frac{E}{T}} \exp\left\{j\varphi(t;\underline{\alpha})\right\}, \tag{1.1}$$

where E is the energy per information symbol, T the symbol time duration and $\varphi(.)$ is the phase of the signal. Denoting M the constellation order, the symbol alphabet is $\{\pm1, \pm3, ..., \pm(M-1)\}$ when M is even and $\{\pm0, \pm2, ..., \pm(M-1)\}$ when M is odd. Equation (1.1) clearly shows that CPM is not a linear function of the transmitted symbols and that it has a constant complex envelope. The information is carried by the phase of the signal, which is defined as

$$\varphi(t;\underline{\alpha}) = 2\pi \sum_i h_{\underline{\underline{i}}} \alpha_i q(t - iT), \tag{1.2}$$

where $\{h_{\underline{\underline{i}}}\}$ is a set of N_h modulation indexes and the double underlined subscript notation is

$$\underline{\underline{i}} = i \bmod N_h. \tag{1.3}$$

The function $q(t)$ is called the phase pulse and represents the time integral of the frequency pulse $g(t)$ whose time support equals LT and whose area is $\frac{1}{2}$. If $L = 1$, the signal has a full response frequency pulse. Otherwise, the signal has a partial response one. The phase pulse $q(t)$ is defined as

$$q(t) = \begin{cases} 0, & t \leq 0, \\ \int_0^t g(\tau)d\tau, & 0 < t < LT, \\ \frac{1}{2}, & t \geq LT. \end{cases} \tag{1.4}$$

Due to the definition of $q(t)$ and for $t \in [nT, (n+1)T[$, the phase of the signal can be decomposed into a cumulative phase θ_{n-L} that represents the memory of CPM and a time dependent phase $\theta(t)$. To do so, we first simplify (1.2) as follows

$$\varphi(t;\underline{\alpha}) = 2\pi \sum_{i=-\infty}^{n} h_{\underline{\underline{i}}} \alpha_i q(t - iT), \qquad nT \leq t < (n+1)T, \tag{1.5}$$

since we know that $q(t-iT)=0$ when $i>n$. Then, using the fact that the phase pulse becomes constant when $i\in]-\infty,n-L]$, we get

$$\varphi(t;\underline{\alpha})=\underbrace{2\pi\sum_{i=n-L+1}^{n}\underline{\underline{h}}_i\alpha_i q(t-iT)}_{\theta(t)}+\underbrace{\pi\sum_{i=-\infty}^{n-L}\underline{h}_i\alpha_i}_{\theta_{n-L}},\qquad nT\leq t<(n+1)T. \tag{1.6}$$

The inherent memory is particular to CPM since it ensures the continuity of the phase, however its presence makes handling this modulation less tractable at the receiver side. The straightforward solution to overcome this problem is to develop differential phase based receivers [4] since the differential phase (or the instantaneous frequency) is expressed as

$$\Omega_s(t)=\frac{\partial\varphi(t;\underline{\alpha})}{\partial t}=\frac{\partial\theta(t)}{\partial t}=2\pi\sum_{i=n-L+1}^{n}\underline{\underline{h}}_i\alpha_i g(t-iT),\qquad nT\leq t<(n+1)T. \tag{1.7}$$

In this case, the cumulative phase is invisible due to the derivation operation.

1.2 Classical CPM signals

In the majority of practical CPM schemes, the modulation index is constant (i.e., $N_h=1$) and rational. These CPMs are referred to as single-h CPMs, and they are used in applications such as:

- The GSM mobile communications [29]. The used modulation is a single-h binary CPM with a modulation index $h=1/2$ and a partial response Gaussian frequency pulse of length $L=2$. The latter is also characterized by a parameter called the bandwidth-symbol time product BT and equals 0.5. This modulation is known as the Gaussian minimum shift keying (GMSK).
- The Bluetooth data transmissions [30]. For this standard, the used modulation is called Gaussian frequency shift keying (GFSK). The corresponding CPM scheme has the same parameters as the one used for GSM except for the modulation index value. The latter can instead vary between 0.28 and 0.35.
- Tactical communications [31, 32]. Several single-h binary CPM schemes are defined in the standard according to the used mode. If we take as an example the mode $C7$, which offers high throughput for short coverage. The corresponding modulation index h equals $1/8$ and the frequency pulse is rectangular and spans 3 symbol periods.

- Digital video broadcasting standard DVB-RCS2 [33, 34]. This standard relies on some linear modulations as well as CPMs. The CPM schemes use a quaternary alphabet $M \in \{\pm 3, \pm 1\}$ and a rational modulation index. The frequency pulse is of length $L = 2$ and its shape is a weighted average of a raised cosine (RC) pulse and a rectangular one.

- Deep space communications [35]. The modulation used for this application is the military standard shaped offset quadrature phase-shift keying (SOQPSK-MIL). It was developed as a variant of shaped binary phase-shift keying (SBPSK) [36][1] and it was first adopted as a part of a military standard [37]. This version was referred to as MIL-STD SOQPSK or SOQPSK-MIL. The alphabet of this modulation is ternary $M \in \{-1, 0, +1\}$ and its modulation index $h = 1/2$. The frequency pulse has a rectangular shape and is of length $L = 1$.

The least popular cases are when the modulation index is integer (see [38] for example) or $N_h > 1$. In the latter case, the value of the modulation index changes cyclically as described in (1.3) and this CPM scheme is referred to as multi-h CPM [39].

1.3 Aeronautical telemetry modulations

Aeronautical telemetry has witnessed some drastic changes in the late 1990's because of the data deluge and because its spectrum has been shortened and reallocated for other commercial applications. To cope with this situation, a program, known as the advanced range telemetry (ARTM) program, has been initiated to adopt, on the one hand, more bandwidth efficient modulations than the traditional aeronautical telemetry modulation, which is the pulse code modulation/ frequency modulation (PCM/FM). On the other hand, the detection efficiency of these modulations should remain comparable to PCM/FM. Aeronautical telemtery modulations are now classified in the inter range instrumentation group (IRIG) recommendations [5] according to their spectral efficiencies as follows

- Tier 0: PCM/FM

- ARTM Tier 1 ($\approx 2\times$ more spectrally efficient than PCM/FM): Feher-patented FQPSK, SOQPSK-TG

- ARTM Tier 2 ($\approx 2.5\times$ more spectrally efficient than PCM/FM): ARTM CPM

Except for FQPSK, all the aforementioned modulations are CPMs. We describe in the following these modulations and we explain in Section 1.4 how the spectral efficiency improvement is achieved compared to PCM/FM.

[1] This modulation was introduced in the 1980's to take advantage of the constant envelope nature of CPM and the good spectral containment while keeping the designed equipment for the linear modulation BPSK compatible.

1.3.1 PCM/FM

The non return zero (NRZ) PCM/FM has been the legacy modulation for aeronautical telemetry. It has been used since the 1970's as the necessary data rates were relatively low at that time. Moreover, using this modulation does not require complex equipment on both transmitting and receiving sides. PCM/FM is by definition a single-h binary CPM with a modulation index $h = 0.7$. Its frequency pulse is the normalized impulse response of a 6^{th} order Bessel filter [40]. To illustrate this modulation, we rather use the following raised cosine (RC) pulse shape of length $L = 2$, which is very close to the exact Bessel filter

$$g(t) = \begin{cases} \dfrac{1}{2LT}\left[1 - \cos\left(\dfrac{2\pi t}{LT}\right)\right], & 0 \leq t \leq LT, \\ 0, & \text{otherwise.} \end{cases} \tag{1.8}$$

We plot in Figure 1.1 $g(t)$ and $q(t)$ and we illustrate the phase tree of PCM/FM in Figure 1.2. The latter depicts all the phase trajectories $\varphi(t;\underline{\alpha})$ having a common start phase at time $t = 0$ [41].

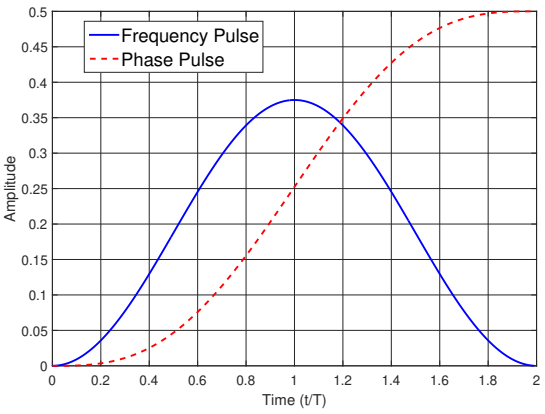

Figure 1.1 – Frequency Pulse & Phase Pulse of PCM/FM

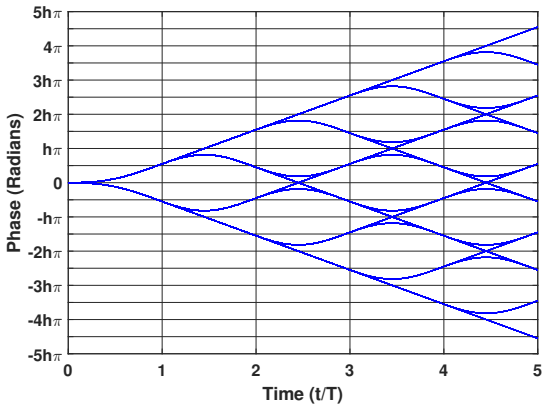

Figure 1.2 – Phase Tree of PCM/FM

Due to the reallocation of the telemetry frequency bands in 1997 [42] and to the increasing high data rates, PCM/FM is now giving its place to more bandwidth efficient modulations such as SOQPSK-TG.

1.3.2 SOQPSK-TG

Along with SOQPSK-MIL described in Section 1.2, more bandwidth efficient variants of SOQPSK were introduced by Hill [43] and were referred to as SOQPSK-A and SOQPSK-B. The good spectral efficiency of these versions compared to SOQPSK-MIL is achieved thanks to the partial response nature of the frequency pulse. This modulation is non-proprietary,

and its partial response versions can lead to similar bit error rate (BER) performance to the proprietary FQPSK [44]. These attractive characteristics led to adopting a SOQPSK variant, namely SOQPSK-TG (less known as SOQPSK-A*) in the IRIG recommendations as a Tier 1 telemetry modulation along with FQPSK.
SOQPSK is defined as a single-h ternary CPM signal having a modulation index $h = h_{\underline{i}} = 1/2$ and whose ternary symbols $\underline{\alpha}$ are generated using the following mapping [35]

$$\alpha_n = (-1)^{n+1} \frac{b_{n-1}(b_n - b_{n-2})}{2}, \tag{1.9}$$

where $b_n \in \{-1, +1\}$ is a random binary symbol. The aim of using this precoder is to make the phase of the SOQPSK behaves like the phase of an OQPSK driven by the bit sequence $\underline{b} = \{b_n\}_{n\in\mathbb{Z}}$. This feature allows the use of simple integrate and dump (I&D) detectors to recover the binary data at the receiver side [17]. A more detailed explanation of the role of this precoder will be given in Chapter 2. This precoder generates symbols belonging to the alphabet $\{-1, 0, +1\}$. Thus, in order to be consistent with the CPM definition given in Section 1.1, SOQPSK can also be seen as a CPM with $h = 1/4$ and $\alpha_n \in \{-2, 0, +2\}$ [45].
The frequency pulse of SOQPSK is of length $L = 8$ and is expressed as

$$g(t) = m(t) \times v(t), \tag{1.10}$$

where

$$m(t) = \frac{A\cos\left(\frac{\pi\mu Bt}{2T}\right)}{1 - 4\left(\frac{\mu Bt}{2T}\right)^2} \times \frac{\sin\left(\frac{\pi Bt}{2T}\right)}{\frac{\pi Bt}{2T}}, \tag{1.11}$$

and

$$v(t) = \begin{cases} 1, & |\frac{t}{2T}| < T_1 \\ \frac{1}{2} + \frac{\cos\left(\frac{\pi}{T_2}(|\frac{t}{2T}| - T_1)\right)}{2}, & T_1 < \left|\frac{t}{2T}\right| < T_1 + T_2, \\ 0, & |\frac{t}{2T}| > T_1 + T_2. \end{cases} \tag{1.12}$$

Each variant of the partial response SOQPSK has its own set of parameters μ, B, T_1, T_2 as illustrated in Table 1.1. The parameter A is a constant so that $\int g(t)\, dt = 1/2$. We plot in Figure 1.3 $g(t)$ and $q(t)$ and in Figure 1.4 the phase tree of SOQPSK-TG.

Table 1.1 – SOQPSK frequency pulse parameters

Modulation \ Parameters	μ	B	T_1	T_2
SOQPSK-A	1	1.35	1.4	0.6
SOQPSK-B	0.5	1.45	2.8	1.2
SOQPSK-TG	0.7	1.25	1.5	0.5

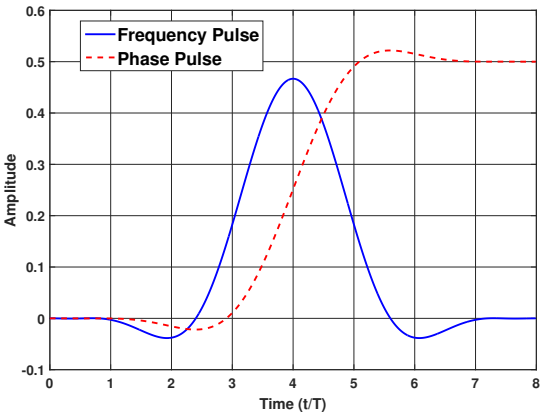

Figure 1.3 – Frequency Pulse & Phase Pulse of SOQPSK-TG

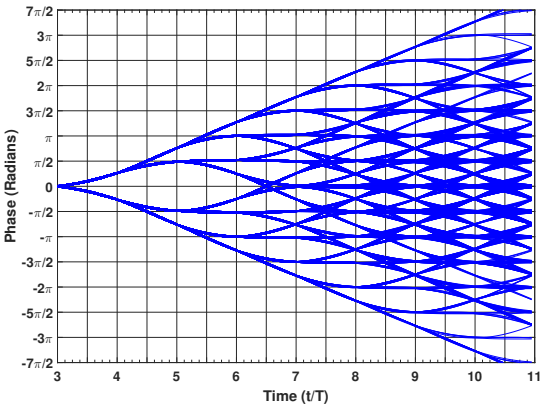

Figure 1.4 – Phase Tree of SOQPSK-TG

1.3.3 ARTM CPM

ARTM CPM is the most bandwidth efficient modulation among all the standardized telemetry modulations. It is approximately $2,5$ times more bandwidth efficient than PCM/FM [5]. This modulation is a dual-h quaternary CPM whose frequency pulse is a raised cosine filter of length $L = 3$ [46]. The modulation indexes are $h_{\underline{i}} = \{\frac{4}{16}, \frac{5}{16}\}$ and the quaternary symbols α_n belong to the alphabet $\{\pm 1, \pm 3\}$ and can be generated as follows

$$\alpha_n = 2\gamma_{1,n} + \gamma_{2,n} \tag{1.13}$$

where $(\gamma_{1,n}, \gamma_{2,n}) \in \{-1, +1\}^2$. We illustrate in Figure 1.5 both frequency and phase pulses of this modulation and its phase tree in Figure 1.6.

The advantage of using two modulation indexes instead of one is that it increments the minimum distances and reduces the symbol error probability. However this comes at the expense of increasing the detection complexity. We summarize in Table 1.2 the parameters that define all the aforementioned modulations.

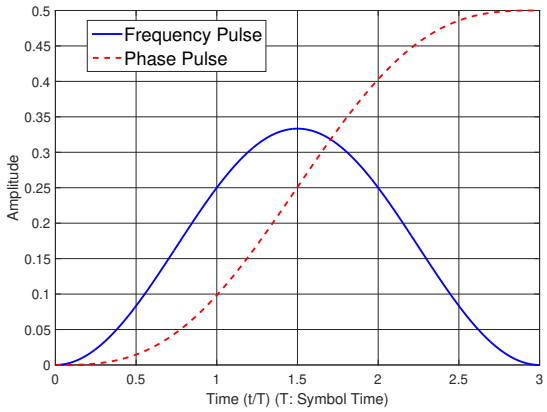

Figure 1.5 – Frequency Pulse & Phase Pulse of ARTM CPM

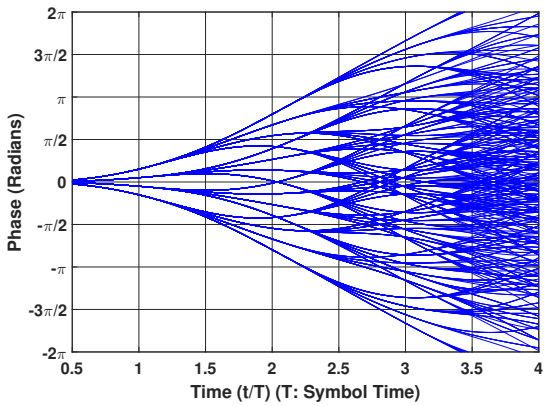

Figure 1.6 – Phase Tree of ARTM CPM

Table 1.2 – Summary of the aeronautical telemetry modulations

CPM / Parameters	PCM/FM	SOQPSK-TG	ARTM CPM
Alphabet	$\{-1,+1\}$	$\{-1,0,+1\}$	$\{-3,-1,+1,+3\}$
Modulation index	0.7	$\frac{1}{2}$	$\underline{h}_i = \{\frac{4}{16}, \frac{5}{16}\},\ N_h = 2$
Symbol time duration	Bit time duration	Bit time duration	2×Bit time duration
Frequency pulse	(1.8)	(1.10)	(1.8)
L: Length of the frequency pulse	2	8	3

1.4 Spectral efficiency and power efficiency trade-off of the aeronautical telemetry modulations

In this section, we briefly explain how the spectral and power efficiencies of SOQPSK-TG and ARTM CPM are improved compared to PCM/FM. The spectral efficiency is numerically evaluated by calculating the ratio of the bit rate and the bandwidth occupied by 99.9% of the overall signal power. The power efficiency is determined by how much signal to noise ratio (SNR) is needed to achieve a bit error rate (BER) or a symbol error rate (SER) of 10^{-5}. The aforementioned value is the adopted threshold in aeronautical telemetry [5]. This criterion is sufficient to evaluate the power efficiency since PCM/FM, SOQPSK-TG and ARTM CPM belong to the CPM family. Therefore, we can assume that the impact of power amplifiers on the power efficiency is the same for these CPM variants. The required SNR value can be determined as a function of the used detector. In this section, we rather give the values that can be achieved theoretically for each modulation. These values are extracted from [47, 18, 48] and they are determined based on the concept of error events and minimum distances [4]. This concept will be detailed in Chapter 3.

We first plot in Figure 1.7 the power spectrum density (PSD) of the different modulations and we give in Table 1.3 their spectral efficiency values as well as the required SNR values to get a BER performance of 10^{-5}. To explain the trade-off between the spectral and the power efficiency, we compare the parameters of these modulations given in Table 1.2 and we discuss the impact of each one of them.

Table 1.3 – Spectral efficiency and detection efficiency of the aeronautical telemetry modulations

CPM / Criterion	PCM/FM	SOQPSK-TG	ARTM CPM
Spectral efficiency (bits/s/Hz)	0.51	0.99	1.34
Required SNR at BER= 10^{-5}	8.32	10.22	10.63

1.4.1 Comparison between PCM/FM and SOQPSK-TG

The spectral efficiency improvement of SOQPSK-TG compared to PCM/FM is achieved due to the following changes: the first one consists of decreasing the modulation index from 0.7 to 0.5. The second improvement is made to the frequency pulse. We can notice that the length of SOQPSK-TG frequency pulse is much higher than 2, which explains the absence of the secondary lobes in the PSD of SOQPSK-TG. Moreover, the ternary precoder of SOQPSK-TG further improves the spectral efficiency. This observation will be confirmed in Chapter 2 since to the best our knowledge, the impact of this precoder on the spectral efficiency has not been studied in the literature. All these improvements come at the expense of the power efficiency as highlighted in Table 1.3. We can see that achieving a bit error probability of 10^{-5} requires a 1.9 dB SNR enhancement compared to PCM/FM. This is due to decreasing h and increasing L, which beget lower minimum distance values.

1.4.2 Comparison between SOQPSK-TG and ARTM CPM

The set of parameters of ARTM CPM were chosen based on the results given in [4, 49] where it was highlighted that choosing $M = 4$ (i.e., a quaternary scheme) provides a very good trade-off between bandwidth utilization, detection performance, and implementation [46]. Furthermore, smoothing the frequency pulse and increasing its length result in more spectral efficiency improvement like the SOQPSK-TG case. The crucial change is the use of two low modulation indexes in a cyclic way. This feature allows improving more the spectral efficiency while reducing the symbol error probability. This trade-off cannot be achieved if only one modulation index is used.

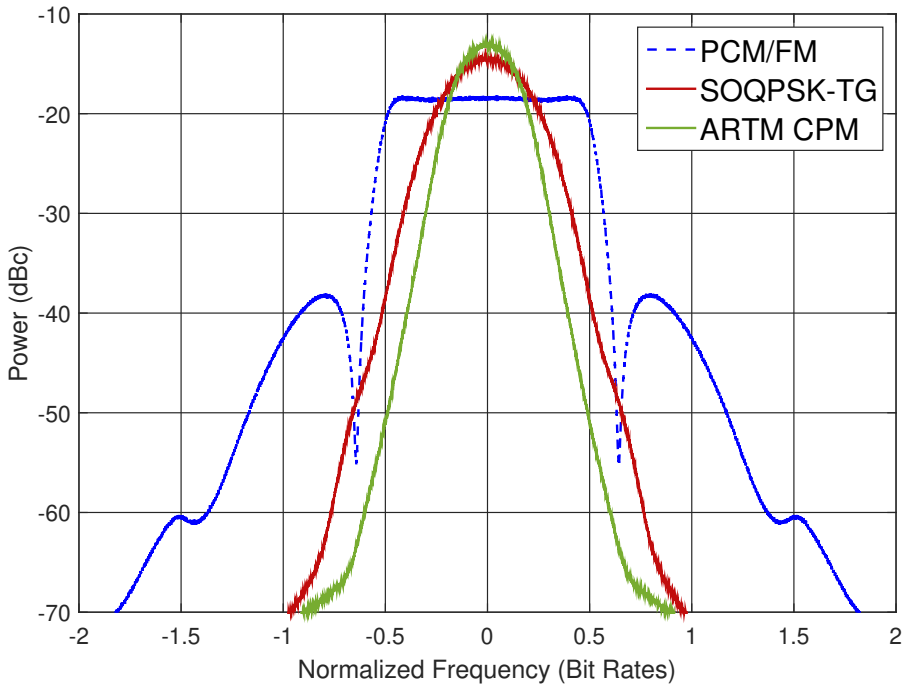

Figure 1.7 – PSD Comparison of the Telemetry Waveforms

1.5 CPM signal decompositions and approximations - Application to SOQPSK

1.5.1 Introduction

After presenting the aeronautical telemetry modulations, we mainly focus on SOQPSK-TG in the rest of this work. This modulation belongs to a particular CPM family as highlighted in Section 1.3.2. The CPM nature of the SOQPSK-TG, its ternary alphabet, and its high lengthed frequency pulse make the use of its original definition sometimes impractical since it begets highly complex receivers as well as considering very limited transmission scheme scenarios. If we take for instance the Gaussian channel case, using SOQPSK-TG requires a detector operating with 512 states [50]. Hence, it is necessary to adopt alternative representations (or decompositions) for this modulation and to find flexible approximations. Therefore, we first present in the following the most popular decomposition for binary CPM, which is the pulse amplitude modulation (PAM) decomposition. We then focus on the state of the art decompositons for SOQPSK.

1.5.2 PAM decomposition of binary CPM: the Laurent decomposition

Several approaches are proposed in the literature to get a more tractable representation of CPM than its original definition such as the Rimoldi decomposition [51], the orthogonal decomposition [52], the non-symmetric non-orthogonal exponential expansion method [53], etc. Nevertheless, the most popular CPM signal representation among all of them is the Laurent decomposition. It was initially developed for single-h binary CPM having non-integer modulation index, and it tackled the problem of CPM non-linearity by showing in [15] that any binary CPM signal can be decomposed into a sum of $Q = 2^{L-1}$ pulse-amplitude modulated (PAM) components, i.e.,

$$s(t;\underline{\gamma}) = \sum_{k=0}^{Q-1} \sum_{i} \beta_{k,i} c_k(t - iT), \tag{1.14}$$

where $\underline{\gamma} = \{\gamma_i\}_{i\in\mathbb{Z}}$, $\gamma_i \in \{\pm 1\}$, $\beta_{k,i}$ are the pseudo-symbols associated with the waveform $c_k(t)$ and are linked to the transmitted data $\underline{\gamma}$. We give the expressions of $c_k(t)$ and $\beta_{k,i}$

$$c_k(t) = \prod_{v=0}^{L-1} u(t + vT + LT\eta_{k,v}, q, h), \tag{1.15}$$

$$\beta_{k,i} = \exp\left\{ jh\pi \left[\sum_{m=-\infty}^{i} \gamma_m - \sum_{v=0}^{L-1} \gamma_{i-v}\eta_{k,v} \right] \right\}, \tag{1.16}$$

where $\eta_{k,v} \in \{0, 1\}$ is the vth bit in the radix-2 representation of the integer k, i.e.,

$$k = \sum_{v=1}^{L-1} 2^{v-1}\eta_{k,q}. \tag{1.17}$$

The variable $\eta_{k,0} = 0$ for all k. The pseudo-symbols $\beta_{k,i}$ are only decorrelated when $h = 1/2$. The function $u(t, q, h)$ depends on the phase pulse $q(t)$ and the modulation index h, and it is expressed as

$$u(t,q,h) = \begin{cases} \sin(2\pi hq(t)) \ / \ \sin(h\pi), & 0 \le t < LT, \\ \sin(h\pi - 2\pi hq(t - LT)) \ / \ \sin(h\pi), & LT \le t < 2LT, \\ 0, & \text{otherwise.} \end{cases} \tag{1.18}$$

The pulses $c_k(t)$ have decreasing time durations as highlighted in Table 1.4.

Table 1.4 – Pulse durations of the Laurent decomposition

Pulse	Duration
$c_0(t)$	$(L+1)T$
$c_1(t)$	$(L-1)T$
$c_2(t), c_3(t)$	$(L-2)T$
$c_4(t), c_5(t), c_6(t), c_7(t)$	$(L-3)T$
...	...
$c_{Q/2}(t), ..., w_{Q-1}(t)$	T

If we take PCM/FM as an example, it can be shown from (1.14) that the modulation can exactly be decomposed into a sum of two linear modulations and can be written as

$$s(t;\underline{\gamma}) = \sum_{k=0}^{1} \sum_{i} \beta_{k,i} c_k(t - iT), \tag{1.19}$$

where the pulses $c_0(t)$ and $c_1(t)$ are illustrated in Figure 1.8.

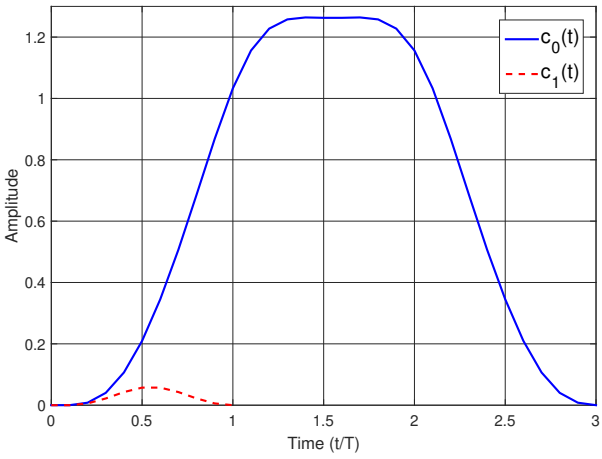

Figure 1.8 – PAM waveforms of PCM/FM

One of the most important properties of the Laurent decomposition is that the pulses have decreasing signal energies according to their ranks [15]. The direct consequence is that the signal can be exactly represented (for the full response case) or approximated with a very good accuracy (for the partial response case) by a "main pulse" that contains a significant part of the overall signal energy. If we go back to the PCM/FM example, it can be noticed that this signal can be approximated as a linear modulation whose pulse shape is the main pulse $c_0(t)$, i.e.,

$$s(t;\underline{\gamma}) \approx \sum_{i} \exp\left\{ jh\pi \sum_{m=-\infty}^{i} \gamma_m \right\} c_0(t - iT). \tag{1.20}$$

We can notice from (1.20) that the inherent memory of the CPM modulation is now perceivable in the pseudo-symbols. This observation further highlights the difference between CPM and linear modulations. We plot in Figure 1.9 the real part of PCM/FM using the original definition of (1.1) and its PAM approximation of (1.20). We also illustrate in Figure 1.10 their corresponding phase trajectories. Both figures confirm the accuracy of the PAM approximation.

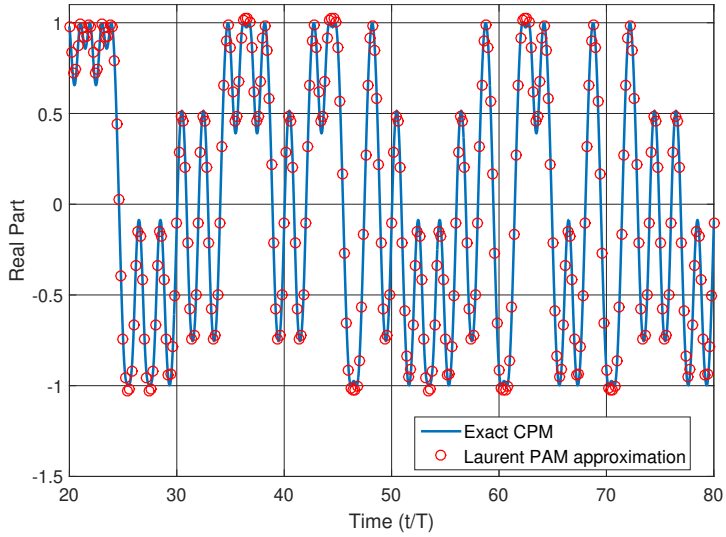

Figure 1.9 – The real part of the exact PCM/FM signal and its PAM approximation

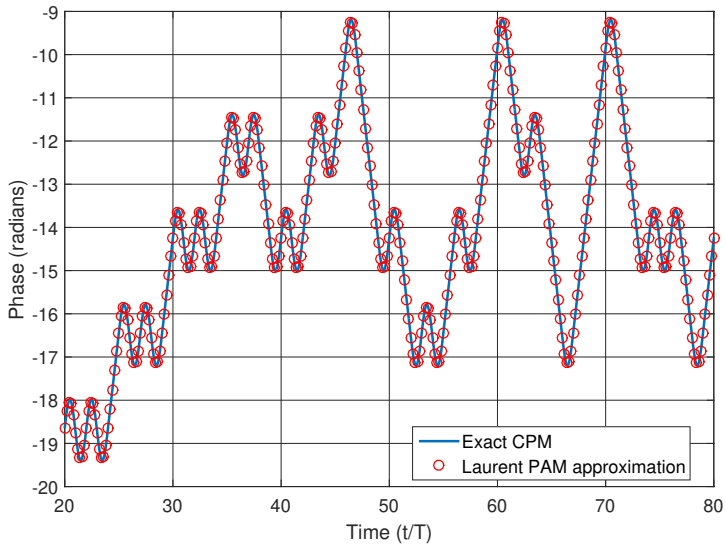

Figure 1.10 – The phase trajectory of the exact PCM/FM signal and its PAM approximation

Due to the attractive properties of the PAM decomposition, the concept has been extended to most of CPM families such as binary CPM with integer modulation index [54], M-ary CPMs where M is an even integer [55] as well as multi-h CPMs [56, 57]. Since this work is focused on the ternary CPM SOQPSK, we present in the following section the PAM decomposition of this family.

1.5.3 PAM decomposition of ternary CPM: The Perrins-Rice decomposition (PRD)

Perrins and Rice extended in [45] the PAM decomposition of single-h binary CPM signals to the single-h ternary CPM case. To do so, they considered that the ternary symbol α_i can be written as a half sum of two random binary antipodal symbols $(\gamma_{1,i},\gamma_{2,i}) \in \{-1,+1\}^2$, i.e.,

$$\alpha_i = \frac{1}{2}(\gamma_{1,i} + \gamma_{2,i}). \tag{1.21}$$

Thus, the ternary CPM signal $s(t;\underline{\alpha})$ can be written as a product of two binary CPM signals $s(t;\underline{\gamma_1})$ and $s(t;\underline{\gamma_2})$. Therefore, it is possible to apply the Laurent PAM decomposition for each binary CPM signal and to write $s(t;\underline{\alpha})$ as follows:

$$s(t;\underline{\alpha}) = \underbrace{\left(\sum_{k=0}^{Q-1}\sum_{i}\beta_{k,i}^{1}c_k(t-iT)\right)}_{s(t;\underline{\gamma_1})} \times \underbrace{\left(\sum_{k=0}^{Q-1}\sum_{i}\beta_{k,i}^{2}c_k(t-iT)\right)}_{s(t;\underline{\gamma_2})}, \tag{1.22}$$

where $\beta_{k,i}^{1}$, $\beta_{k,i}^{2}$ are the pseudo-symbols defined in (1.16) and associated with $\gamma_{1,i}$ and $\gamma_{2,i}$ respectively. Note also that both signals $s(t;\underline{\gamma_1})$ and $s(t;\underline{\gamma_2})$ have a modulation index equal to $\frac{h}{2}$. The simplification of (1.22) requires expanding the product of the two representations to a sum. This problem is similar to the one tackled by Mengali & Morelli in [58] for M-ary CPM with the exception that they considered the product of binary sub-signals with different modulation indexes. Perrins and Rice have first applied the results in [58] for $M = 4$ and then have exploited the fact the modulation indexes are identical for both signals $s(t;\underline{\gamma_1})$ and $s(t;\underline{\gamma_2})$. The mathematical development has led to an expression of the ternary CPM signal as a sum of $R = 2 \times 3^{L-1}$ PAM waveforms weighted by the pseudo-symbols $\nu_{k,i}$, i.e.,

$$s(t;\underline{\alpha}) = \sum_{k=0}^{R-1}\sum_{i}\nu_{k,i}p_k(t-iT). \tag{1.23}$$

The derivation of the different PAM waveforms and the pseudo-symbols are detailed in [45] and unlike the binary case, it generally leads to two main pulses with significant energies. The expressions of the two main pulses $p_0(t)$ and $p_1(t)$ as well as the pseudo-symbols $\nu_{0,i}$ and $\nu_{1,i}$ are given by

$$\begin{cases} p_0(t) = \left(\prod_{v=0}^{L-1} u(t+vT,q,\frac{h}{2})\right)^2, \\ p_1(t) = 2\left(\prod_{v=0}^{L-1} u(t+vT,q,\frac{h}{2})\right)\left(\prod_{v=0}^{L-1} u(t+vT+T,q,\frac{h}{2})\right), \end{cases} \tag{1.24}$$

and

$$\begin{cases} \nu_{0,i} = \exp\left\{jh\pi \sum_{n=0}^{i} \alpha_n\right\}, \\ \nu_{1,i} = \frac{1}{2}\exp\left\{jh\pi \sum_{n=0}^{i-1} \alpha_n\right\}\left(e^{j\frac{h\pi}{2}\gamma_{1,i}} + e^{j\frac{h\pi}{2}\gamma_{2,i}}\right). \end{cases} \tag{1.25}$$

The presence of the inherent memory is also perceivable in the expressions of the pseudo-symbols like the binary case. We call the described decomposition the Perrins Rice decomposition (PRD) and we apply in the following section this decomposition to SOQPSK. We consider the telemetry version of SOQPSK (SOQPSK-TG) as well as the military version, namely SOQPSK-MIL.

Application to SOQPSK-MIL

Even though SOQPSK-MIL does not appear in IRIG (it is used in the military standard [37]), it is of particular interest since its frequency pulse has a rectangular shape of duration T. Thus, it can be seen as a full response system of ternary CPM. Using PRD, SOQPSK-MIL can exactly be decomposed into a sum of two linear modulations, i.e., $R = 2$. The PAM waveforms are expressed as

$$p_0(t) = \left(u(t, q, \frac{h}{2})\right)^2, \qquad p_1(t) = 2\left(u(t, q, \frac{h}{2})\right)\left(u(t+T, q, \frac{h}{2})\right), \tag{1.26}$$

and are plotted in Figure 1.11. The pseudo-symbols are given in (1.25) and we remind that the modulation index $h = 1/2$. The energetic significance of each pulse can roughly be determined based on the pulse amplitude and it can clearly be seen from Figure 1.11 that $p_0(t)$ and $p_1(t)$ are main pulses, which means that we cannot discard one or the other if we want to approximate SOQPSK-MIL as a linear modulation.

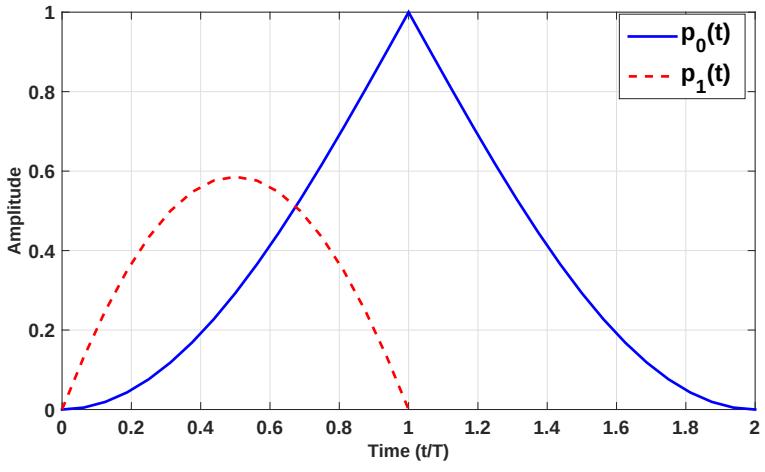

Figure 1.11 – PAM Waveforms of SOQPSK-MIL using PRD

Application to SOQPSK-TG

We now focus on the bandwidth efficient partial response version, SOQPSK-TG. The length of the frequency pulse L is equal to 8 as mentioned in Section 1.3.2. Therefore, using PRD, the PAM decomposition of this version requires $R = 4374$ PAM components, which is very important. However, this is not troublesome since Perrins showed in [14] that a very good approximation can be found by only keeping the first two pulses p_0 and p_1 given in (1.24) and plotted in Figure 1.12. Thus SOQPSK-TG can be approximated as

$$s(t;\underline{\alpha}) \approx \sum_{k=0}^{1} \sum_{i} \nu_{k,i} p_k(t - iT), \tag{1.27}$$

where the pseudo-symbols are the ones given in (1.25).

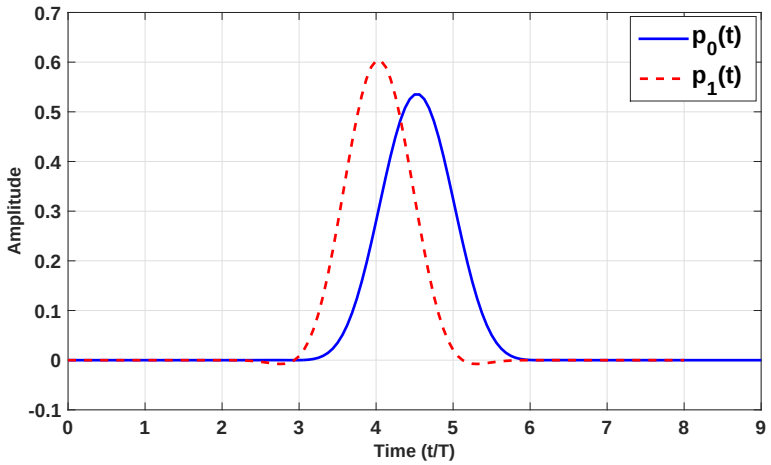

Figure 1.12 – PAM waveforms of SOQPSK-TG using PRD

In order to verify this approximation, we calculate the normalized mean squared error (NMSE) of the approximation as follows

$$\epsilon(\tilde{s}) = \frac{\int_{-\infty}^{+\infty} |s(t) - \tilde{s}(t)|^2 dt}{\int_{-\infty}^{+\infty} |s(t)|^2 dt}, \tag{1.28}$$

where $\tilde{s}$ is the PAM approximation of the signal s. The NMSE of the approximation given in (1.27) is equal to $\epsilon(\tilde{s}) = -23.7$ dB, which is very low. Moreover, the time domain plot of SOQPSK-TG and its approximation illustrated in Figure 1.13 also confirms the accuracy of this approximation.

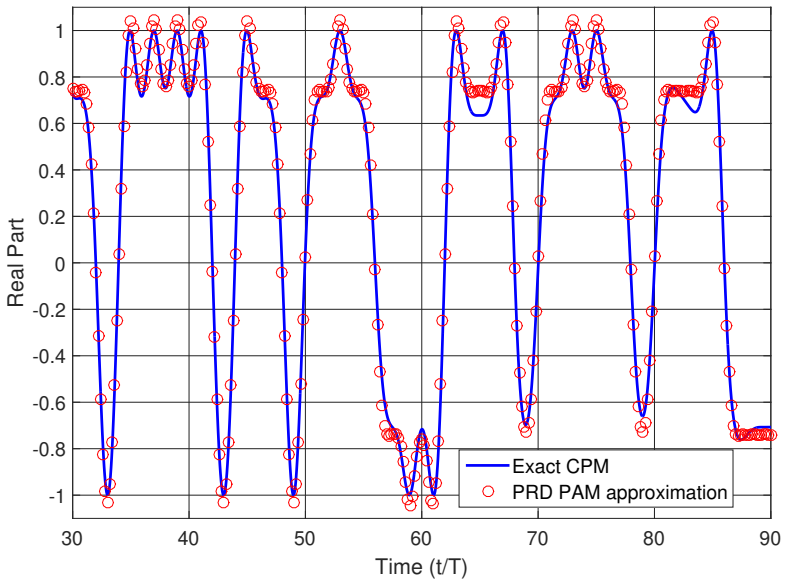

(a) Real Part

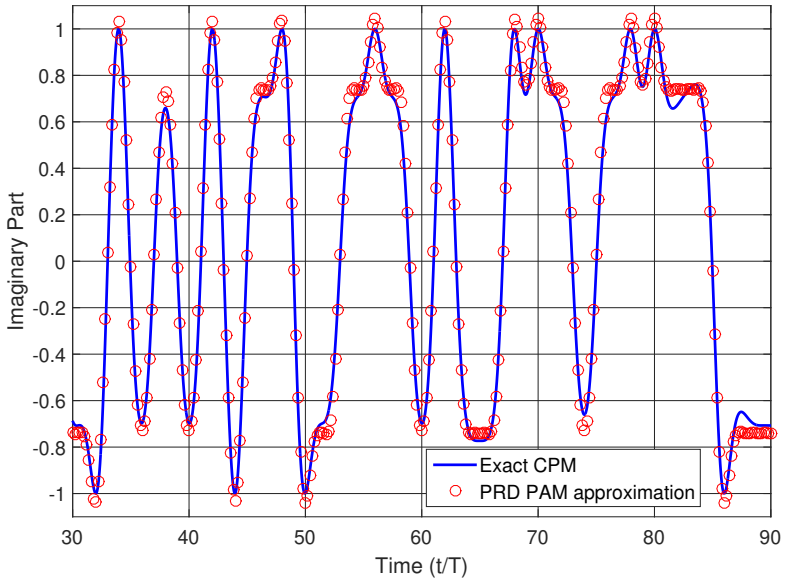

(b) Imaginary Part

Figure 1.13 – Comparison between the exact SOQPSK-TG signal and its PAM approximation of (1.27)

Discussion

Despite the aforementioned attractive properties of PRD, which were used to develop reduced complexity detectors [18, 59], several questions regarding SOQPSK remain unanswered and are listed below:

- Besides the good spectral efficiency of SOQPSK, one of the main reasons for adopting this modulation in the IRIG recommendations is the simplicity of the detection scheme as highlighted in Section 1.3.2. In fact, simple I&D detectors [17] are capable of detecting the

transmitted data. This advantage is not analytically explained, and the only justification relies on the use of the precoder of (1.9). However, if we look at the aforementioned PAM approximation, the presence of the inherent memory in the pseudo-symbols expressions of (1.25) suggests otherwise.

- The reason why it is necessary to generate ternary symbols: The fact that the precoder of (1.9) generates zeros and prevents a direct transition from $+1$ to -1 and vice versa does not necessarily make the phase of the signal behaves like the phase of an OQPSK and does not necessarily undo the inherent memory.

- The link between SOQPSK an OQPSK using the PAM decomposition: we mentioned in Section 1.3.2 that the ternary symbols are generated using the precoder of (1.9) to make the phase of SOQPSK behaves like the phase of OQPSK when the same data sequence $\underline{b}$ drives both modulations. However, this observation is not reflected in the PAM decomposition of SOQPSK, which is surprising since the link between CPM (more precisely, minimum shift keying (MSK) modulations, i.e., CPM with a modulation index $h = 1/2$) and OQPSK was found in [15] thanks to the Laurent decomposition.

The presence of the two main pulses, as well as the large inherent memory of the pseudo-symbols $\{\nu_{k,i}\}_{k\in\{0,1\}}$, promoted the appearance of an alternative representation for SOQPSK, which is the cross-correlated trellis-coded quadrature modulation representation.

1.5.4 XTCQM representation of SOQPSK

Along with the PAM decomposition, another representation of SOQPSK has been proposed in the literature to link it to OQPSK and Feher-patented quadrature phase-shift keying (FQPSK) [44]. This representation allows to interpret SOQPSK as a cross-correlated trellis-coded quadrature modulation (XTCQM), i.e., it enables to visualize the modulation as a scheme that contains both memory and cross-correlation between the in-phase and the quadrature-phase paths [60]. Moreover, The XTCQM representation of SOQPSK allows creating a direct link between the transmitted bits and the different transitions of the signal eye-diagram. It gives a direct mapping between a given number of consecutive bits and the various waveforms of length $2T$ that constitute the eye-diagram of the signal. This link is not straightforward due to the ternary mapping and because the modulation is not a linear function of the transmitted symbols. We give in the following the XTCQM representation of both full and partial response versions of SOQPSK.

SOQPSK-MIL

The XTCQM representation has been first investigated for SOQPSK-MIL in [60]. It has been shown that this signal is composed of 16 possible data dependent complex-valued waveforms of length $2T$ and can be expressed as follows

$$s(t;\underline{\alpha}) = \sum_n X_{16}(t-2nT; b_{2n-2},...,b_{2n+1}), \tag{1.29}$$

$$= \sum_n S_{I,16}(t-2nT; b_{2n-2},...,b_{2n+1}) + jS_{Q,16}(t-2nT; b_{2n-2},...,b_{2n+1}), \tag{1.30}$$

where

$$S_{I,16}(t-2nT; b_{2n-2},...,b_{2n+1}) = Re\left\{s(t-2nT;\alpha_{2n},\alpha_{2n+1})\right\}, \tag{1.31}$$

$$= \cos\left(\varphi(t-2nT;\alpha_{2n},\alpha_{2n+1}) + \frac{\pi}{4}\right), \tag{1.32}$$

$$S_{Q,16}(t-2nT; b_{2n-2},...,b_{2n+1}) = Im\left\{s(t-2nT;\alpha_{2n},\alpha_{2n+1})\right\}, \tag{1.33}$$

$$= \sin\left(\varphi(t-2nT;\alpha_{2n},\alpha_{2n+1}) + \frac{\pi}{4}\right), \tag{1.34}$$

and

$$\varphi(t-2nT;\alpha_{2n},\alpha_{2n+1}) = \begin{cases} \frac{\pi\alpha_{2n}}{2T}(t-2nT), & 2nT \le t \le (2n+1)T \\ \frac{\pi\alpha_{2n}}{2} + \frac{\pi\alpha_{2n+1}}{2T}(t-(2n+1)T), & (2n+1)T \le t \le (2n+2)T. \end{cases} \tag{1.35}$$

Equations (1.32) and (1.34) show that the signal depends on 4 bits $\{b_{2n-2}, b_{2n-1}, b_{2n}, b_{2n+1}\}$ when $2nT \le t < 2(n+1)T$, i.e., the different waveforms are a function of 2 ternary symbols $\{\alpha_{2n}, \alpha_{2n+1}\}$. The waveforms of the I channel $S_{I,16}$ are plotted in Figure 1.14 as an illustration.

We can notice that we have 8 distinct waveforms as highlighted in [60]. Note that the waveforms of the Q channel are the same but with a different mapping with the 4 bits. Simon and Li showed in [61] that OQPSK has a similar XTCQM representation with only 2 possible waveforms for the I channel since its phase can be expressed as

$$\varphi_{OQPSK}(t-2nT;\alpha_{2n},\alpha_{2n+1}) = \begin{cases} \frac{\pi}{2}\alpha_{2n}, & 2nT \le t \le (2n+1)T, \\ \frac{\pi}{2}(\alpha_{2n}+\alpha_{2n+1}), & (2n+1)T \le t \le (2n+2)T. \end{cases} \tag{1.36}$$

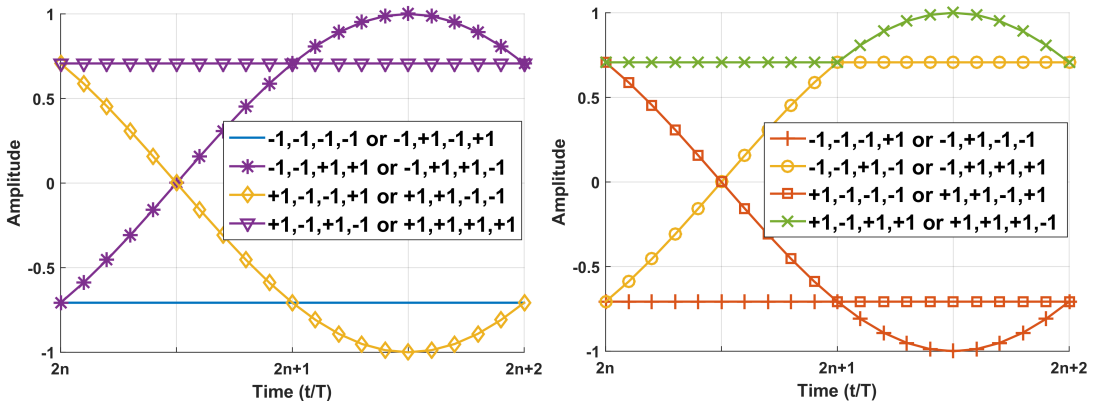

(a) I Channel (1/2) (b) I Channel (2/2)

Figure 1.14 – XTCQM waveforms of the I channel for SOQPSK-MIL

Therefore, a first link has been established between SOQPSK-MIL and OQPSK via the XTCQM representation and as a consequence, optimum and reduced complexity detectors have been proposed in [60] for SOQPSK-MIL based on this approach.

SOQPSK-TG

The XTCQM representation has been extended for SOQPSK-TG in [62] where it has been shown that the signal can be written as in (1.30) but with a different expression of φ. When $2nT \leq t \leq 2(n+1)T$, the phase pulse φ depends on 11 consecutive bits and therefore, the signal is composed of 2048 complex waveforms of length $2T$ and can be written as

$$s(t;\underline{\alpha}) = \sum_n \underbrace{S_{I,2048}(t-2nT;b_{2n-9},...,b_{2n+1}) + jS_{Q,2048}(t-2nT;b_{2n-9},...,b_{2n+1})}_{X_{2048}(t-2nT;b_{2n-9},...,b_{2n+1})}, \quad (1.37)$$

where

$$S_{I,2048}(t-2nT;b_{2n-9},...,b_{2n+1}) = \cos[\varphi(t-2nT;\alpha_{2n-7},\alpha_{2n+1}) + \frac{\pi}{4}], \quad (1.38)$$

$$S_{Q,2048}(t-2nT;b_{2n-9},...,b_{2n+1}) = \sin[\varphi(t-2nT;\alpha_{2n-7},\alpha_{2n+1}) + \frac{\pi}{4}], \quad (1.39)$$

We plot in Figure 1.15 $S_{I,2048}$ and $S_{Q,2048}$.

Since the number of the XTCQM waveforms is huge, Nelson proposed in [16] a way to reduce the number of these waveforms by applying an averaging technique inspired from [35]. It consists of removing the dependence of the XTCQM waveforms from the first and the last bits by doing the following operation

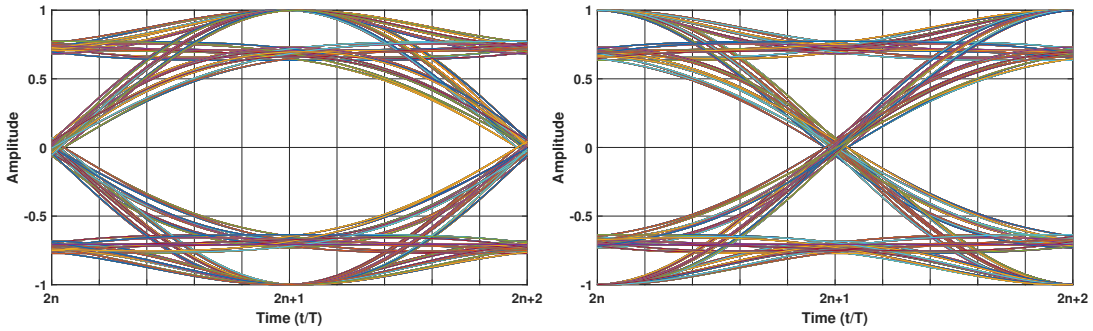

(a) $S_{I,2048}$ (b) $S_{Q,2048}$

Figure 1.15 – 2048-XTCQM complex waveforms for SOQPSK-TG

$$\begin{aligned} X_{512}(t-2nT;b_{2n-8},...,b_{2n}) =& \frac{1}{4}(X_{2048}(t-2nT;-1,b_{2n-8},...,b_{2n},-1) \\ & \frac{1}{4}(X_{2048}(t-2nT;-1,b_{2n-8},...,b_{2n},+1) \\ & \frac{1}{4}(X_{2048}(t-2nT;+1,b_{2n-8},...,b_{2n},-1) \\ & \frac{1}{4}(X_{2048}(t-2nT;+1,b_{2n-8},...,b_{2n},+1). \end{aligned} \tag{1.40}$$

We then get from (1.40) 512 complex XTCQM waveforms. If we continue averaging the same way as above, we obtain X_{128} from X_{512}, then X_{32} from X_{128}, then X_8 from X_{32} and X_2 from X_8. From the last operation, we get 2 complex XTCQM waveforms that are illustrated in Figure 1.16, which echoes back to the OQPSK case since the latter is composed of 2 complex XTCQM waveforms as mentioned in Section 1.5.4.

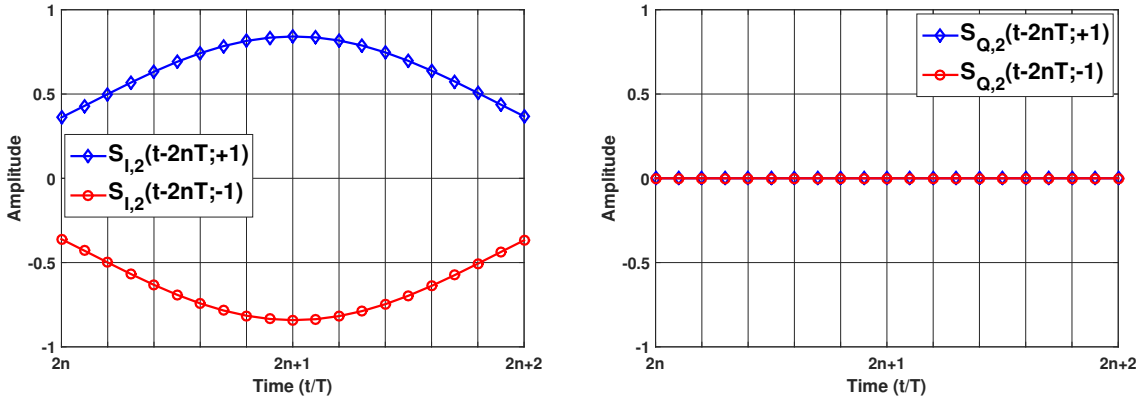

(a) $S_{I,2}(t-2nT;b_{2n-4})$ (b) $S_{Q,2}(t-2nT;b_{2n-4})$

Figure 1.16 – 2-XTCQM complex waveforms for SOQPSK-TG

By limiting the number of bits that define the XTCQM waveforms, several reduced complexity detectors have been proposed in [16, 63] with near optimal BER performance.

1.5.5 Limitations of the state of the art representations of SOQPSK

Both PAM and XTCQM decompositions have their own benefits and drawbacks when applied to SOQPSK. The PAM decomposition allows approximating SOQPSK-TG (and exactly representing SOQPSK-MIL) as a sum of 2 linear modulations. However, this does not completely "linearize" the signal because of the found mapping between the ternary symbols and the pseudo-symbols. We can see for instance from (1.25) that the pseudo-symbol $\mu_{0,n}$ is a function of all the ternary sequence $\alpha_0, ..., \alpha_n$, which is undesirable. This result suggests that the SOQPSK precoder is not fully exploited since its role is to eliminate the infinite memory of the modulation as stated in [18]. If we now focus on the XTCQM representation, we can see that the averaging process allows shrinking the inherent memory. If we take for example the $X_8(.;.)$, the described process shows that SOQPSK-TG can be reconstructed using a bank of 8 XTCQM waveforms, which are a function of only 3 bits. However, the main drawback of this representation is that the XTCQM waveforms are data dependent, which means that we cannot separate the contribution of the bits and the pulse shape in a clear way like in the PAM decomposition. Moreover, the number of XTCQM waveforms increases exponentially with the inherent memory, and that is not suitable in the presence of frequency-selective channels for example since the latter would induce additional memory [64]. Therefore, the applications that are derived based on the XTCQM representation are generally limited to the Gaussian channel case.

1.6 Conclusion

We introduced in this chapter the CPM signal model and presented the standardized aeronautical telemetry modulations. Since our work focuses on SOQPSK, we presented two representations of the signal along with the CPM definition: the PAM representation of PRD and the XTCQM representation. We summarize in Figure 1.17 the connections between these representations. In the next chapter, we present a revamped PAM decomposition for SOQPSK, and we show that it gathers the desired advantages of both PRD and XTCQM representations.

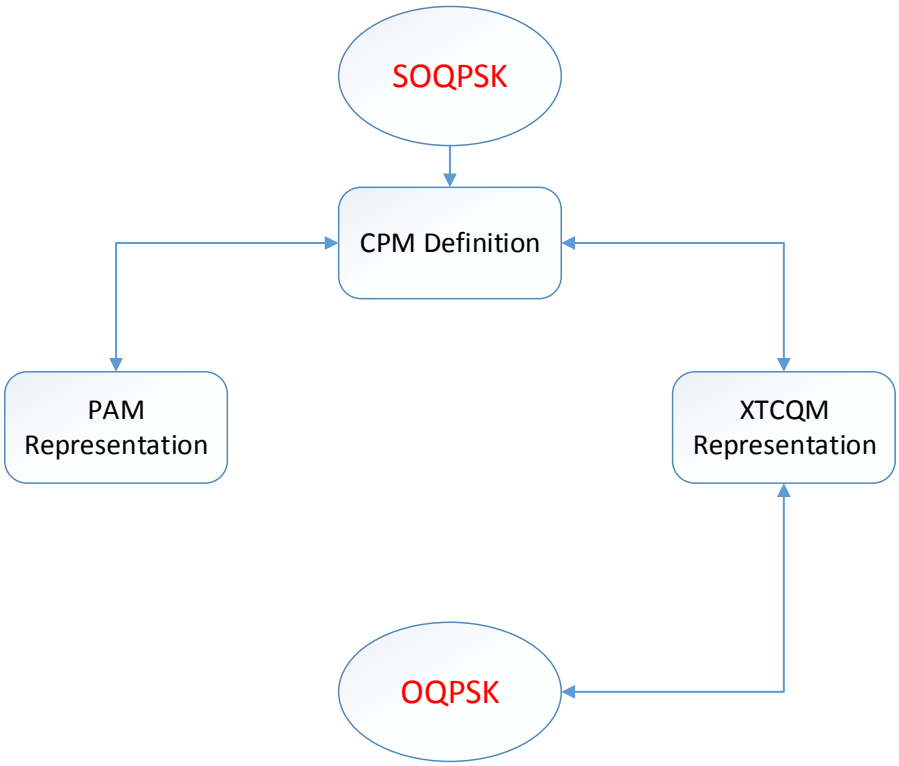

Figure 1.17 – The connections between the state of the art representations of SOQPSK

Chapter 2

The Revamped (or Novel) Decompositions of SOQPSK

Contents

2.1 Introduction

The PAM decomposition introduced by Perrins and Rice for SOQPSK has been a pioneering work [45] since it allowed to make a first connection between this signal and linear modulations. However, this decomposition has several cons such as the presence of two main pulses instead of one and the relatively large inherent memory of the pseudo-symbols that are associated with the main pulses. These drawbacks are mainly due to the first assumption that has been taken to perform the decomposition, which is that the ternary symbols of SOQPSK are generated randomly instead of considering the precoder of (1.9). If we instead expand the expression of this precoder, (1.9) can be rewritten as

$$\alpha_n = \frac{1}{2}(\gamma_n + \gamma_{n-1}), \tag{2.1}$$

where

$$\gamma_n = (-1)^{n+1} b_n b_{n-1}, \qquad \gamma_n \in \{-1, +1\}. \tag{2.2}$$

Hence, the precoder used for SOQPSK modulation is nothing else than a duobinary encoder [65] applied on $\bar{\gamma}$ as shown in Figure 2.1.

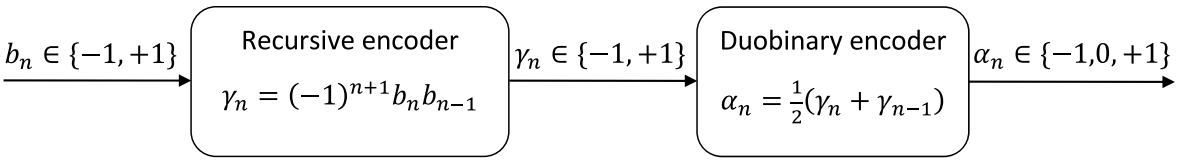

Figure 2.1 – New Vision of the SOQPSK Precoder

Consequently, SOQPSK can be seen not only as a simple ternary CPM but also as a duobinary CPM [66], i.e., a CPM whose ternary symbols are generated with a duobinary encoder. We investigate in the next section the PAM decomposition of the duobinary CPM family, and we apply the obtained results to SOQPSK.

2.2 PAM decomposition of ternary CPM with duobinary encoding

In this section, we consider the general case where random binary data are encoded using only the duobinary encoder and then passed through a single-h CPM modulator as shown in Figure 2.2

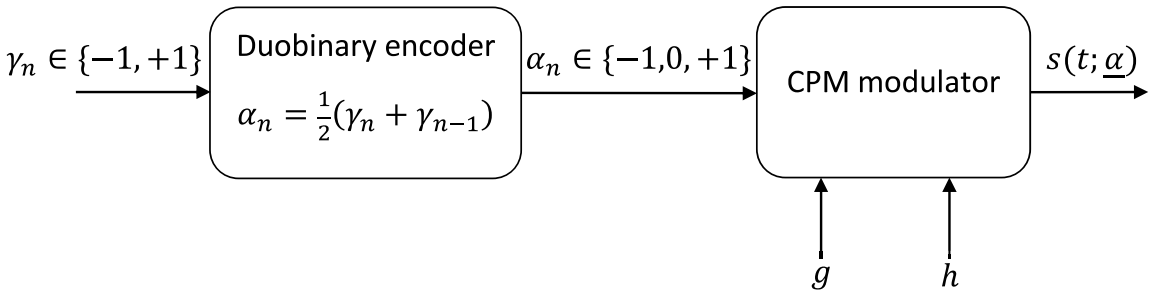

Figure 2.2 – Duobinary CPM modulator scheme

2.2.1 Perrins Rice PAM Decomposition

Since duobinary CPM is a particular case of ternary CPM, we can use PRD to decompose the duobinary CPM signal as a sum of R waveforms. The expressions of the PAM waveforms would be unchanged from what has been presented in Section 1.5.3. Thus, the number of main pulses would remain the same. There will be only a slight modification in the expressions of the pseudo-symbols since $\gamma_{1,i}$ and $\gamma_{2,i}$ given in (1.21) are now linked. In the duobinary CPM case, we have $\gamma_{1,i} = \gamma_i$ and $\gamma_{2,i} = \gamma_{i-1}$. Therefore, the expressions of the pseudo-symbols $\nu_{0,i}$ and $\nu_{1,i}$ become

$$\begin{aligned}\nu_{0,i} &= \exp\left\{jh\pi \sum_{n=0}^{i} \alpha_n\right\}, \\ &= \exp\left\{jh\pi \sum_{n=0}^{i-1} \gamma_n\right\} \times \exp\left\{j\frac{h\pi}{2}\left(\gamma_i + \gamma_{-1}\right)\right\},\end{aligned} \tag{2.3}$$

$$\begin{aligned}\nu_{1,i} &= \frac{1}{2}\exp\left\{jh\pi \sum_{n=0}^{i-1} \alpha_n\right\} \times \left(e^{j\frac{h\pi}{2}\gamma_i} + e^{j\frac{h\pi}{2}\gamma_{i-1}}\right), \\ &= \frac{1}{2}\exp\left\{jh\pi \sum_{n=0}^{i-2} \gamma_n\right\} \times \left(e^{j\frac{h\pi}{2}(\gamma_{i-1}+\gamma_i)} + e^{jh\pi\gamma_{i-1}}\right) e^{j\frac{h\pi}{2}\gamma_{-1}}.\end{aligned} \tag{2.4}$$

The consequence of the mapping between the pseudo-symbols and the binary symbols γ_i will be exploited in Section 2.3 for SOQPSK. By using PRD, the PAM decomposition of duobinary CPM inherits the same properties of the PAM decomposition of random ternary such as the number of main pulses and the correlation of pseudo-symbols whatever the value of h (see Appendix A for the calculation details of the correlation of the pseudo-symbols). In the next section, we go back to the starting point of Laurent development, and then we take advantage of the duobinary encoding to get an alternative PAM decomposition. We consider the case where the modulation index is non-integer as well as the case where h integer for the sake of completeness.

2.2.2 The proposed duobinary decomposition (DBD) for non-integer h

We base our developments on [15]. We first use (1.6) to rewrite $s(t;\underline{\alpha})$ as follows

$$s(t;\underline{\alpha}) = \exp\left\{jh\pi \sum_{i=-\infty}^{N-L} \alpha_i\right\} \times \prod_{i=N-L+1}^{N} \exp\left\{j2h\pi\alpha_i q(t-iT)\right\}, \tag{2.5}$$

where $NT \leq t < (N+1)T$. We then replace in (2.5) the expression of the ternary symbol α_i obtained by duobinary encoding described in (2.1), we then get

$$s(t;\underline{\alpha}) = A \times B, \qquad NT \leq t < (N+1)T, \tag{2.6}$$

where

$$A = \exp\left\{j2h\pi\frac{h\pi}{2}\left[\sum_{i=-\infty}^{N-L}\gamma_i + \sum_{i=-\infty}^{N-L}\gamma_{i-1}\right]\right\}, \tag{2.7}$$

and

$$B = \exp\left\{j\sum_{i=N-L+1}^{N}\frac{(\gamma_i+\gamma_{i-1})}{2}q(t-iT)\right\}. \tag{2.8}$$

After some rearrangements in (2.7) and (2.8), we obtain

$$A = \exp\left\{jh\pi\sum_{i=-\infty}^{N-(L+1)}\gamma_i\right\}.\exp\left\{j\frac{h\pi}{2}\gamma_{N-L}\right\}, \tag{2.9}$$

and

$$B = \exp\left\{j2h\pi\sum_{i=N-L+1}^{N}\frac{\gamma_i}{2}q(t-iT) + j2h\pi\sum_{i=N-L}^{N-1}\frac{\gamma_i}{2}q(t-(i+1)T)\right\}. \tag{2.10}$$

Since $NT \leq t < (N+1)T$, we derive that $t-(N+1)T < 0$ and $t-(N-L)T \geq LT$. Then, from (1.4)

$$\begin{cases} \frac{\gamma_N}{2}q(t-(N+1)T) = 0, \\ \frac{\gamma_{N-L}}{2}q(t-(N-L)T) = \frac{\gamma_{N-L}}{4}. \end{cases} \tag{2.11}$$

By adding these terms in (2.10), we obtain

$$B = \exp\left\{j2h\pi\sum_{i=N-L}^{N}\gamma_i\frac{1}{2}\left[q(t-iT)+q(t-(i+1)T)\right]\right\} \times \exp\left\{-j\frac{h\pi}{2}\gamma_{N-L}\right\}. \tag{2.12}$$

Let us denote

$$\tilde{q}(t) = \frac{1}{2}(q(t)+q(t-T)). \tag{2.13}$$

and

$$\tilde{g}(t) = \frac{1}{2}(g(t) + g(t-T)). \tag{2.14}$$

The function $\tilde{q}(t)$ has the same properties of a phase pulse associated with a frequency pulse $\tilde{g}(t)$ as defined in (1.4). Its time varying portion spans ($L_d = L + 1$) bit periods. From (2.9) and (2.12), we then get

$$s(t;\underline{\alpha}) = \exp\left\{jh\pi \sum_{i=-\infty}^{N-L_d} \gamma_i\right\} \times \prod_{i=N-L_d+1}^{N} \exp\left\{j2h\pi\gamma_i\tilde{q}(t-iT)\right\}. \tag{2.15}$$

Therefore, it can be easily shown that

$$\exp(j2h\pi\gamma_i\tilde{q}(t-iT)) = \frac{\sin(h\pi - 2h\pi\tilde{q}(t-iT))}{\sin(h\pi)} + e^{jh\pi\gamma_i} \times \frac{\sin(2h\pi\tilde{q}(t-iT))}{\sin(h\pi)}. \tag{2.16}$$

This result is strictly equivalent to the one found by Laurent in [15]. Therefore, $s(t;\underline{\alpha})$ can be decomposed into a sum of M_d pulses and can be written as

$$s(t;\underline{\alpha}) = \sum_{k=0}^{M_d-1} \sum_{i} \rho_{k,i} w_k(t-iT), \tag{2.17}$$

where

$$\begin{cases} M_d = 2^{L_d-1} = 2 \times 2^{L-1}, & (2.18) \\ w_k(t) = \prod_{v=0}^{L_d-1} u(t + vT + L_d T\eta_{k,v}^d, \tilde{q}, h), & (2.19) \\ \rho_{k,i} = \exp\left\{jh\pi\left[\sum_{m=-\infty}^{i} \gamma_m - \sum_{q=0}^{L_d-1} \gamma_{i-q}\eta_{k,q}^d\right]\right\}. & (2.20) \end{cases}$$

Function $u(.)$ is defined in (1.18) and $\eta_{k,q}^d \in \{0,1\}$ such that $k = \sum_{q=1}^{L_d-1} 2^{q-1}\eta_{k,q}^d$. The variable $\eta_{k,0}^d$ is defined zero for all k. Like in [15], the pulses $w_k(t)$ have distinct time durations which are listed in table 2.1.

Table 2.1 – Pulse durations of the proposed decomposition for non-integer modulation index

Pulse	Duration
$w_0(t)$	$(L+2)T$
$w_1(t)$	LT
$w_2(t), w_3(t)$	$(L-1)T$
$w_4(t), w_5(t), w_6(t), w_7(t)$	$(L-2)T$
...	...
$w_{M/2}(t), ..., w_{M-1}(t)$	T

The aforementioned results show that the proposed decomposition follows a Laurent decomposition of a binary CPM signal with an equivalent frequency pulse $\tilde{g}(t)$ as illustrated in Figure 2.3. This observation is of great importance since this alternative decomposition keeps the key features of the Laurent decomposition such as the number of pulses needed to exactly represent a duobinary CPM and the decreasing energy of the pulses according to their ranks. This claim is discussed in detail in Section 2.3. Furthermore, the pseudo-symbols are now uncorrelated for $h = 1/2$ like the binary case as shown in Appendix A. In the following section, we propose a PAM decomposition of duobinary CPM for integer modulation index values.

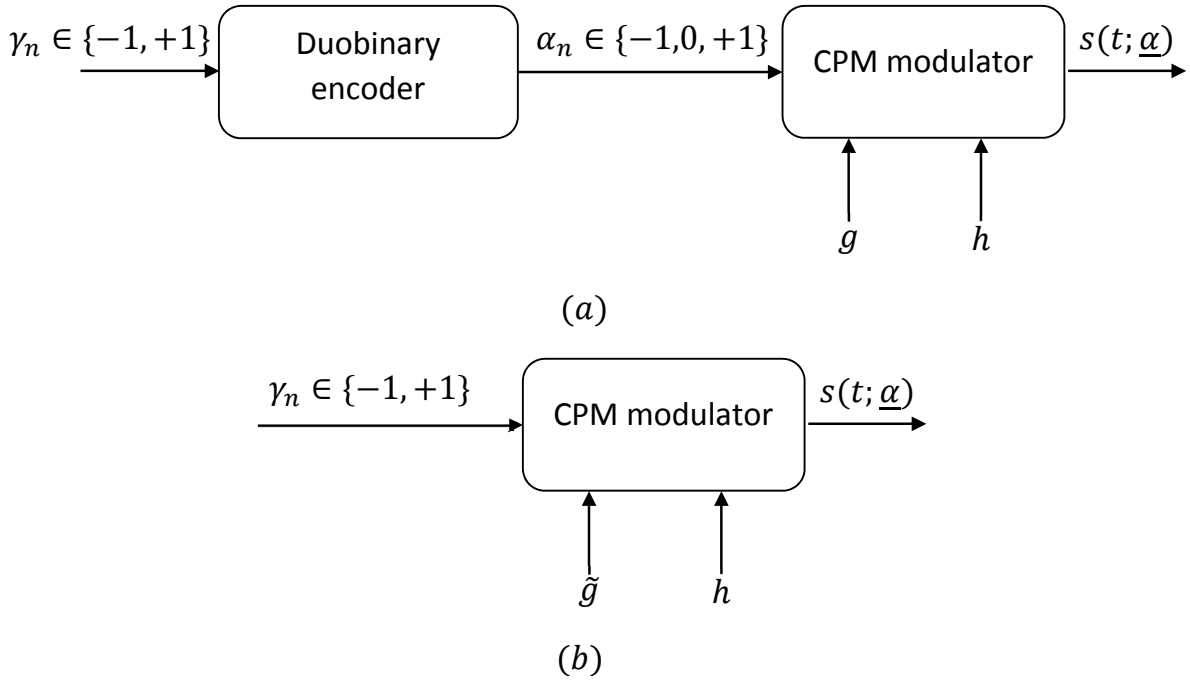

Figure 2.3 – (a) Duobinary CPM (b) Equivalent binary CPM

2.2.3 The proposed duobinary decomposition (DBD) for integer h

We base our development on [54] and we follow the same steps as presented in Section 2.2.2. Using (2.15), it can be shown that for $NT \leq t \leq (N+1)T$,

$$s(t;\underline{\alpha}) = \exp\left\{jh\pi \sum_{i=-\infty}^{-L_d} \gamma_i\right\} \times \cos^N(h\pi) \times \prod_{i=N-L_d+1}^{N} \left[\cos(2h\pi\tilde{q}(t-iT)) + j\gamma_i \sin(2h\pi\tilde{q}(t-iT))\right]. \quad (2.21)$$

This result is also strictly equivalent to the one shown in [54]. Therefore, $s(t;\underline{\alpha})$ can be expressed as

$$s(t;\underline{\alpha}) = \sum_{n=-\infty}^{+\infty} J^n h_0(t-nT) + \sum_{n=-\infty}^{+\infty} J^n \sum_{k=1}^{M_d} a_{k,n} h_k(t-nT), \tag{2.22}$$

where

$$\begin{cases} J = \cos(h\pi), & (2.23) \\ h_0(t) = \prod_{i=-L_d+1}^{0} \cos(2h\pi\tilde{q}(t-iT)), & (2.24) \\ h_k(t) = \left(\prod_{v=1}^{L_d-1} \cos(2h\pi\tilde{q}(t-vT)) \right) \\ \qquad \times \left(\prod_{v=0}^{L_d-1} \left[(1-\eta_{k,v}) \cos(2h\pi\tilde{q}(t+vT)) + \eta_{k,v} \sin(2h\pi\tilde{q}(t+vT)) \right] \right), & (2.25) \\ a_{k,n} = \prod_{i=0}^{L_d-1} \left(1 - \eta_{k,i} + j\eta_{k,i}\gamma_{n-i}\right). & (2.26) \end{cases}$$

The parameter $\eta_{k,i}$ is in $\{0,1\}$ such that $2k-1 = \sum_{i=0}^{L_d-1} 2^i \eta_{k,i}$. The duration of each pulse $h_k(t)$ is given in Table 2.2.

Equation (2.22) also shows that the proposed decomposition is nothing else than a PAM decomposition of a binary CPM with an equivalent phase pulse. Therefore, it keeps the same properties presented in [54]. We summarize in Table 2.3 the characteristics of the different PAM decompositions presented in this manuscript.

Table 2.2 – Pulse durations of the proposed decomposition for integer modulation index

Pulse	Duration
$h_0(t)$	T
$h_1(t)$	L_dT
$h_2(t)$	$(L_d-1)T$
$h_3(t), h_4(t)$	$(L_d-2)T$
$h_5(t), h_6(t), h_7(t), h_8(t)$	$(L_d-3)T$
...	...
$h_{M/2+1}(t), ..., h_M(t)$	T

Table 2.3 – Comparison between the PAM decompositions of duobinary CPM

PAM Decomposition	PRD	proposed (DBD)	
modulation index	non integer	non integer	integer
Number of pulses	$2 \times 3^{L-1}$	$2 \times 2^{L-1}$	$2 \times 2^{L-1}+1$
Number of main pulses	2	1	1
Correlation of the pseudo-symbols	Yes	No for $h = 1/2$	No

2.3 Application to SOQPSK

2.3.1 SOQPSK-MIL

We start by applying the obtained results to SOQPSK-MIL. Using PRD, the exact decomposition requires 2 pulses whose expressions remain unchanged from (1.26). However, by taking advantage of (2.2) and (2.3), we can express the pseudo-symbols $\nu_{0,i}$ and $\nu_{1,i}$ as a function of the binary data b_i (see appendix B for the calculation details) as follows

$$\nu_{0,i} = \frac{1}{2}\left[(b_{i-1} + b_i) + j(-1)^i(b_{i-1} - b_i)\right], \tag{2.27}$$

$$\nu_{1,i} = \frac{\sqrt{2}}{8}\left[3b_{i-1} - b_{i-2}b_{i-1}b_i + b_{i-2} + b_i \;\; + j(-1)^i(3b_{i-1} - b_{i-2}b_{i-1}b_i - b_{i-2} - b_i)\right]. \tag{2.28}$$

Both Equations (2.27) and (2.28) show the importance of the new vision of the SOQPSK precoder given in Figure 2.1 since it allows to get a mapping between the pseudo-symbols of the main pulses and the transmitted data. Moreover, we can see that $\nu_{0,i}$ and $\nu_{1,i}$ have limited inherent memories since they only depend on $\{b_{i-1}, b_i\}$ and $\{b_{i-2}, b_{i-1}, b_i\}$, respectively.
We now apply the decomposition described in Section 2.2.2 (DBD). An exact representation of the signal requires $M_d = 2$ pulses as well. Using (2.19), we obtain

$$w_0(t) = \begin{cases} \frac{\sqrt{2}}{4}\left(1 - \cos\left(\frac{\pi t}{2T}\right) + \sin\left(\frac{\pi t}{2T}\right)\right), & 0 \le t \le 3T \\ 0, & \text{otherwise,} \end{cases} \tag{2.29}$$

$$w_1(t) = \begin{cases} \frac{\sqrt{2}}{4}\left(\cos\left(\frac{\pi t}{2T}\right) - 1 + \sin\left(\frac{\pi t}{2T}\right)\right), & 0 \le t \le T \\ 0, & \text{otherwise.} \end{cases} \tag{2.30}$$

The pseudo-symbols expressions associated with these PAM waveforms can be simplified using the properties of $\underline{\gamma}$ (see Appendix C for more details). Therefore, given (2.20) we get

$$\begin{cases} \rho_{0,i} = b_i, & \rho_{1,i} = -jb_{i-2}b_{i-1}b_i, & i \text{ even}, \\ \rho_{0,i} = jb_i, & \rho_{1,i} = -b_{i-2}b_{i-1}b_i, & i \text{ odd}. \end{cases} \tag{2.31}$$

The different PAM waveforms for SOQPSK-MIL are plotted in Figure 1.11 (PRD) and Figure 2.4 (proposed). We can notice from Figure 2.4 that we have one significant pulse $w_0(t)$ of duration $(L_d + 1)T$ and a less significant one $w_1(t)$ of duration $(L_d - 1)T$.

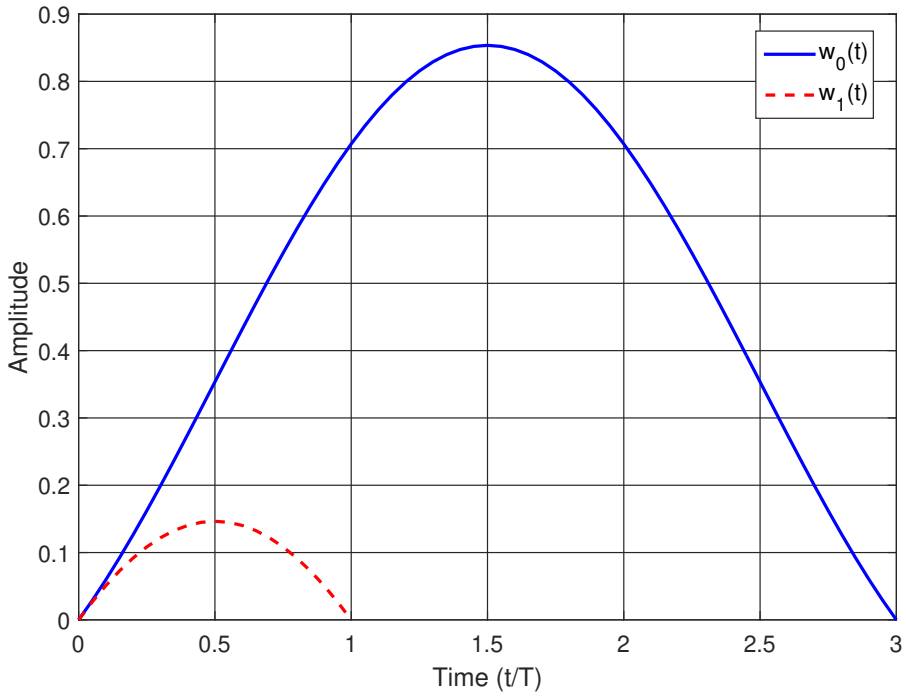

Figure 2.4 – PAM waveforms of SOQPSK-MIL using DBD

Given this decomposition, we can assume that SOQPSK-MIL can be approximated by a single PAM like the binary case as follows

$$s(t;\underline{\alpha}) \approx \sum_{i} \rho_{0,i} w_0(t - iT). \tag{2.32}$$

The accuracy of this approximation can be seen in Figure 2.5 and quantitatively confirmed in Table 2.4.

We now discuss the final expressions of the pseudo-symbols in (2.27) and (2.28) for PRD and (2.31) for DBD. We can see that the mapping found between the binary symbols $\underline{b} = \{b_i\}_{i\in\mathbb{Z}}$ and the pseudo-symbols of PRD is quite complex especially for the pseudo-symbol $\nu_{1,i}$. Conversely, the pseudo-symbols introduced in the proposed DBD are simply generated (see (2.31)). Additionally, they are uncorrelated.

Another important observation is that the final expressions in (2.31) are similar to the ones found in [25, 67] for the Gaussian Minimum Shift Keying (GMSK) signal. Therefore, these results ensure that the different classes of reduced complexity demodulation schemes described in [25, 68] can now be applied to the SOQPSK case.

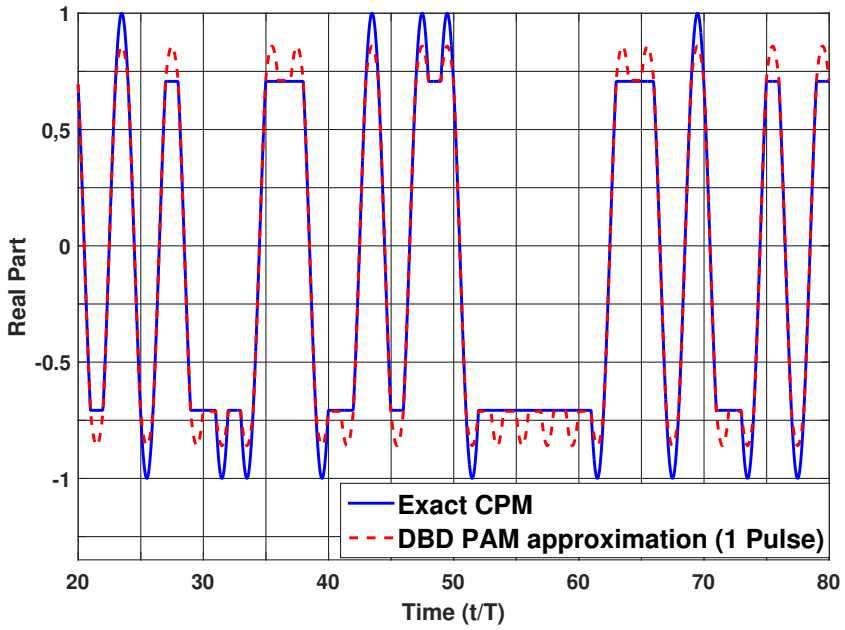

Figure 2.5 – Comparison between the exact SOQPSK-MIL signal and its DBD PAM approximation of (2.32)

2.3.2 SOQPSK-TG

We now consider SOQPSK-TG. Using PRD, the obtained pseudo-symbols in (2.27) and (2.28) associated with the main pulses given in (1.24) remain unchanged. If we apply DBD, SOQPSK-TG can be exactly decomposed using a sum of $M_d = 256$ pulses ($M_d << R$). The different pulses can be computed using (2.19) and the first four ones are plotted in Figure 2.6. We observe that the longest pulse $w_0(t)$ represents the main pulse of the signal. The second pulse $w_1(t)$ contains significantly less energy than the main one unlike what has been observed in Figure 1.12 (PRD). The other pulses are negligible. The first two pulses are expressed as

$$\begin{cases} w_0(t) = \prod_{v=0}^{L} u\left(t + vT, \tilde{q}, h\right), & (2.33) \\ w_1(t) = u\left(t, \tilde{q}, h\right) u\left(t + (L+2)T, \tilde{q}, h\right) \prod_{v=2}^{L} u\left(t + vT, \tilde{q}, h\right). & (2.34) \end{cases}$$

The pseudo-symbols related to $w_0(t)$ and $w_1(t)$ are unchanged from (2.31). Therefore, the different observations mentioned earlier for SOQPSK-MIL remain valid for SOQPSK-TG and for any other version of SOQPSK. Unlike PRD, we can consider two PAM approximations for SOQPSK-TG: the first one only keeps a single PAM waveform, i.e.,

$$s(t; \underline{\alpha}) \approx \sum_i \rho_{0,i} w_0(t - iT), \tag{2.35}$$

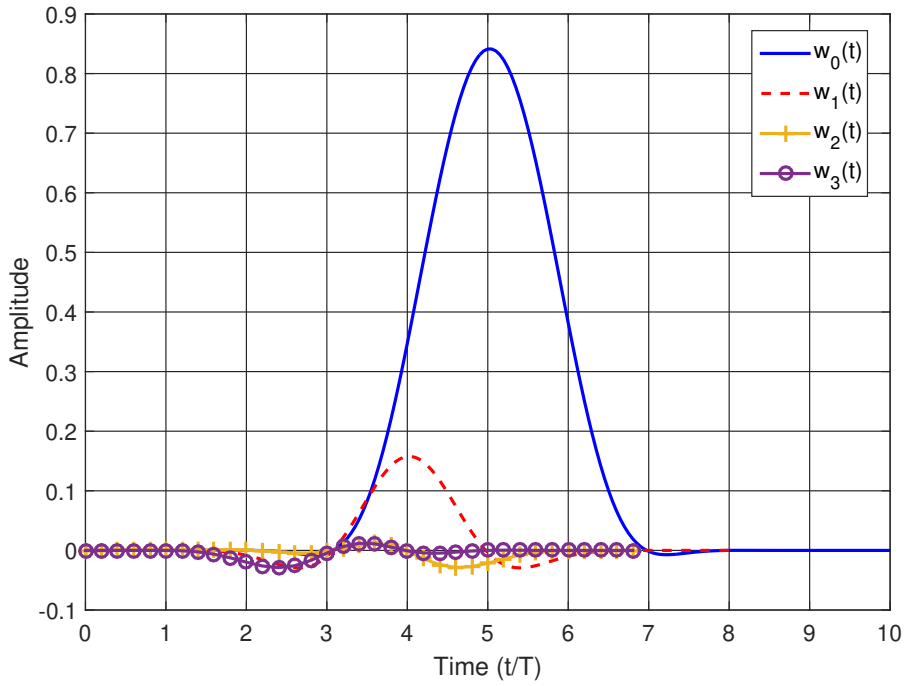

Figure 2.6 – PAM waveforms of SOQPSK-TG using DBD

and the second one is to keep the first 2 PAM waveforms:

$$s(t;\underline{\alpha}) \approx \sum_{k=0}^{1} \sum_{i} \rho_{k,i} w_k(t - iT). \tag{2.36}$$

A time domain plot is given in Figure 2.7 to compare these approximations with the exact SOQPSK-TG signal, and the NMSE values of the aforementioned assumptions are summarized in Table 2.4. We also give the NMSE value of the PAM approximation of GMSK modulation. The relevance of the PAM approximation of this signal has been studied in depth by several authors in the case where only the main pulse or 2 pulses are considered [68, 69, 70, 71, 72]. We can see that if SOQPSK-MIL is approximated by just keeping $w_0(t)$, the degradation is very close to the GMSK case. Also, 98.8% of the signal energy is contained in $w_0(t)$. Therefore, we can assume that SOQPSK-MIL can be seen as a pulse amplitude modulation whose pulse shape is the main pulse $w_0(t)$ like observed in Figure 2.5. As for SOQPSK-TG, the DBD approximation is better than the one using PRD if we take into account the two pulses $w_0(t)$ and $w_1(t)$. The main pulse $w_0(t)$ contains 97.6% of the signal energy.

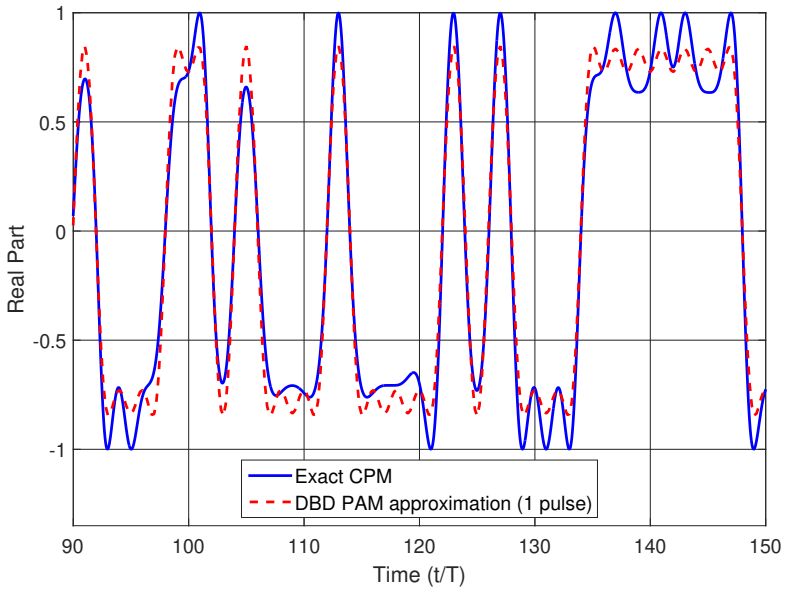

(a) DBD PAM Approximation of (2.35)

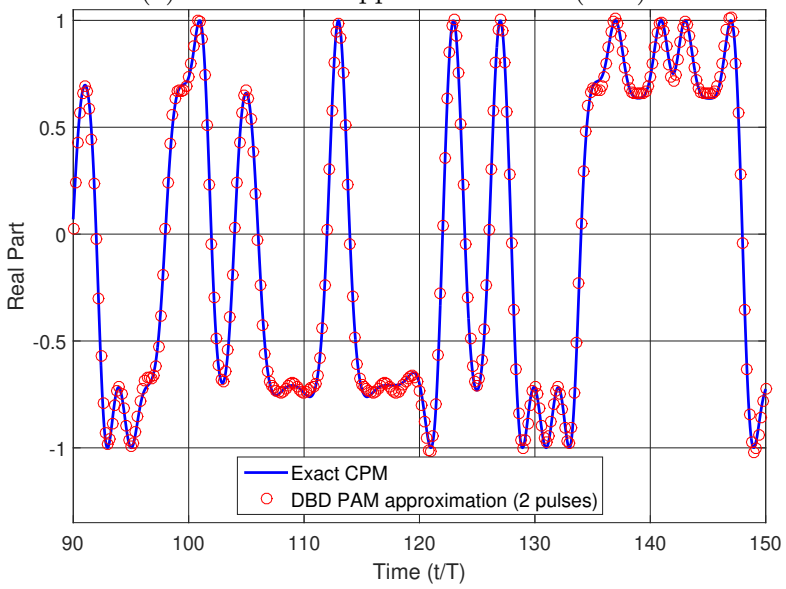

(b) DBD PAM Approximation of (2.36)

Figure 2.7 – Comparison between the exact SOQPSK-TG signal and its DBD PAM approximations

Table 2.4 – Normalized mean squared error of the PAM approximations (dB)

Selected Pulses / Modulation	Laurent (binary)	PRD		Proposed (DBD)	
	Main pulse	p_0&p_1	p_0	w_0&w_1	w_0
SOQPSK-MIL	-	$-\infty$	-8.72	$-\infty$	-19.48
SOQPSK-TG	-	-23.7	-	-28.15	-16.3
Binary GMSK ($BT = 0.25$)	-20.98	-	-	-	-

2.4 The link between the XTCQM interpretation and the revamped PAM decomposition

The revamped PAM decomposition of SOQPSK has allowed us to overcome one of the main limitations of PRD given in Section 1.5.3, which is the absence of a direct mapping between the binary data and the pseudo-symbols. The establishment of this mapping can thus give us a link between the eyediagram traces of the signal and the binary symbols like the XTCQM representation. Since both representations describe the same signal, we show in this section that there is a mathematical relationship between the XTCQM waveforms and the PAM decomposition. To do so, we express the XTCQM waveforms described in Section 1.5.4 as a function of the PAM waveforms of DBD and the antipodal transmitted symbols for both SOQPSK versions.

2.4.1 SOQPSK-MIL

We start with the military version by determining the list of the shifted versions of $w_0(t)$ that contribute to eye-diagram when $2nT \leq t \leq 2(n+1)T$. Since the time support of $w_0(t)$ is $3T$, the list of the waveforms and their associated time shifted versions is

$$\begin{aligned} &w_0(t-2nT+2T): && (2n-2)T \leq t \leq (2n+1)T, \\ &w_0(t-2nT+T): && (2n-1)T \leq t \leq (2n+2)T, \\ &w_0(t-2nT): && 2nT \leq t \leq (2n+3)T, \\ &w_0(t-2nT-T): && (2n+1)T \leq t \leq (2n+4)T. \end{aligned} \tag{2.37}$$

Equation (2.37) shows that an XTCQM waveform involves 4 shifted versions of $w_0(t)$. We do the same thing for $w_1(t)$ whose time support is T:

$$\begin{aligned} &w_1(t-2nT): && 2nT \leq t \leq (2n+1)T, \\ &w_1(t-2nT-T): && (2n+1)T \leq t \leq (2n+2)T. \end{aligned} \tag{2.38}$$

Using (2.31), (2.37) and (2.38), SOQPSK-MIL can now be written as

$$\begin{aligned} s(t;\underline{\alpha}) = \sum_n \Bigg[&\left(\sum_{i=n-1}^{n} b_{2i} w_0(t-2iT) - b_{2n-1}b_{2n}b_{2n+1} w_1'(t-2nT) \right) \\ &+ j \left(\sum_{i=n-1}^{n} b_{2i+1} w_0(t-2iT-T) - b_{2n-2}b_{2n-1}b_{2n} w_1'(t-2nT+T) \right) \Bigg], \end{aligned} \tag{2.39}$$

where

$$w_1'(t) = \begin{cases} w_1(t-T), & \text{if } T \leq t < L_d T \\ 0, & \text{otherwise.} \end{cases} \tag{2.40}$$

Equation (2.39) shows that the signal depends on 4 bits $\{b_{2n-2}, b_{2n-1}, b_{2n}, b_{2n+1}\}$ when $2nT \leq t < 2(n+1)T$, i.e., the different waveforms are a function of 2 ternary symbols $\{\alpha_{2n}, \alpha_{2n+1}\}$. Therefore, we have 16 complex waveforms. If we process the real part and the imaginary independently, it can be seen that we only have 8 different waveforms of length $2T$ on both I and Q channels. These observations are in accordance with what has been presented in Section 1.5.4. Therefore using (1.30) and (2.39), we show that

$$S_{I,16}(t-2nT; b_{2n-2}, ..., b_{2n+1}) = \sum_{i=n-1}^{n} b_{2i} w_0(t-2iT) - b_{2n-1} b_{2n} b_{2n+1} w_1'(t-2nT), \tag{2.41}$$

$$S_{Q,16}(t-2nT; b_{2n-2}, ..., b_{2n+1}) = \sum_{i=n-1}^{n} b_{2i+1} w_0(t-2iT-T) - b_{2n-2} b_{2n-1} b_{2n} w_1'(t-2nT+T). \tag{2.42}$$

The generated waveforms using the PAM decomposition are identical to the ones illustrated in Figure 1.14. Therefore, the link between the PAM decomposition and the XTCQM representation has been analytically established for SOQPSK-MIL.

2.4.2 SOQPSK-TG

In order to link the XTCQM representation given in Section 1.5.4 to the PAM decomposition of SOQPSK-TG, it is necessary to take the exact PAM decomposition by considering the 256 PAM waveforms. This approach is hardly tractable due to the expression of the pseudo-symbols. Therefore, we rather choose to take the PAM approximation of SOQPSK-TG by considering 2 PAM waveforms instead of 256. This approximation is justified since $99,8\%$ of the signal energy is contained in the first two pulses. To link the PAM approximation to the XTCQM representation, we first determine the list of shifted versions of $w_0(t)$ and $w_1(t)$ that contribute to the XTCQM waveforms when $2nT \leq t \leq 2(n+1)T$. We begin with $w_0(t)$ whose time

support is $10T$:

$$\begin{aligned}
&w_0(t-2nT+9T): && (2n-9)T \le t \le (2n+1)T,\\
&w_0(t-2nT+8T): && (2n-8)T \le t \le (2n+2)T,\\
&w_0(t-2nT+7T): && (2n-7)T \le t \le (2n+3)T,\\
&w_0(t-2nT+6T): && (2n-6)T \le t \le (2n+4)T,\\
&w_0(t-2nT+5T): && (2n-5)T \le t \le (2n+5)T,\\
&w_0(t-2nT+4T): && (2n-4)T \le t \le (2n+6)T,\\
&w_0(t-2nT+3T): && (2n-3)T \le t \le (2n+7)T,\\
&w_0(t-2nT+2T): && (2n-2)T \le t \le (2n+8)T,\\
&w_0(t-2nT+1T): && (2n-1)T \le t \le (2n+9)T,\\
&w_0(t-2nT): && 2nT \le t \le (2n+10)T,\\
&w_0(t-2nT-T): && (2n+1)T \le t \le (2n+11)T.
\end{aligned} \tag{2.43}$$

Thus, there are 11 shifted versions of $w_0(t)$ that contribute to the XTCQM waveforms $2nT \le t \le 2(n+1)T$. We keep the same line of reasoning for $w_1'(t)$ whose time support is $8T$:

$$\begin{aligned}
&w_1'(t-2nT+8T): && (2n-7)T \le t \le (2n+1)T,\\
&w_1'(t-2nT+7T): && (2n-6)T \le t \le (2n+2)T,\\
&w_1'(t-2nT+6T): && (2n-5)T \le t \le (2n+3)T,\\
&w_1'(t-2nT+5T): && (2n-4)T \le t \le (2n+4)T,\\
&w_1'(t-2nT+4T): && (2n-3)T \le t \le (2n+5)T,\\
&w_1'(t-2nT+3T): && (2n-2)T \le t \le (2n+6)T,\\
&w_1'(t-2nT+2T): && (2n-1)T \le t \le (2n+7)T,\\
&w_1'(t-2nT+1T): && 2nT \le t \le (2n+8)T,\\
&w_1'(t-2nT): && (2n+1)T \le t \le (2n+9)T.
\end{aligned} \tag{2.44}$$

Using (2.43) and (2.44), the signal $s(t,\underline{\alpha})$ can therefore be approximated as

$$\begin{aligned}
s(t;\underline{\alpha}) \approx \sum_n \Bigg[&\left(\sum_{i=n-4}^{n} b_{2i} w_0(t-2iT) - b_{2i-1} b_{2i} b_{2i+1} w_1'(t-2iT) \right) \\
&+ j \left(\sum_{i=n-5}^{n} b_{2i+1} w_0(t-2iT-T) - \sum_{i=n-4}^{n-1} b_{2i} b_{2i+1} b_{2i+2} w_1'(t-2iT-T) \right) \Bigg].
\end{aligned} \tag{2.45}$$

Equation (2.45) shows that the signal depends on 11 consecutive bits. Thus, this PAM approximation is composed of a set of 2048 complex waveforms that are illustrated in Figure 2.8 and are denoted $X_{2048}(t; b_{2n-9}, ..., b_{2n+1})$.

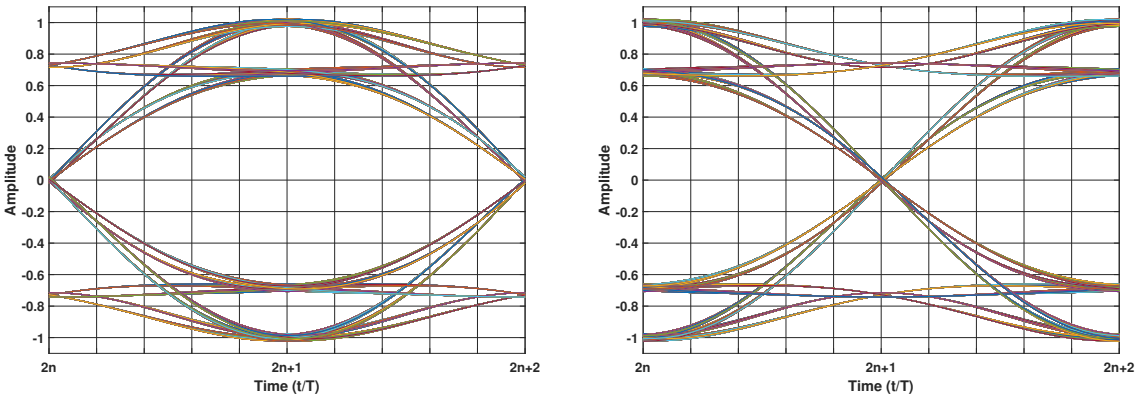

(a) I channel (b) Q channel

Figure 2.8 – XTCQM-PAM pulses of the I & Q channels for SOQPSK-TG

Even though we get the same number of XTCQM waveforms as the ones introduced in [62], it is important to mention that this PAM based XTCQM representation is different from the XTCQM representation of Section 1.5.4 due to the PAM approximation that has been used to generate the waveforms. Therefore, we call the obtained XTCQM representation XTCQM-PAM. The averaging technique can also be applied on (2.45): we first average the waveforms that differ in the first bit to get 1024 complex ones, i.e.,

$$X_{1024}(t-2nT; b_{2n-8}, ..., b_{2n+1}) = \frac{1}{2}(X_{2048}(t-2nT; -1, b_{2n-8}, ..., b_{2n+1}) + X_{2048}(t-2nT; +1, b_{2n-8}, ..., b_{2n+1})). \quad (2.46)$$

Then, we average the waveforms that differ in the last bit this time to get 512 complex waveforms. We carry on the same process until reaching the stage where the signal can be approximated by only considering the dependence of 3 consecutive bits. This approximation is similar to the 8-Waveform XTCQM [24] and may be expressed as a function of the PAM approximation of SOQPSK-TG as follows

$$\begin{aligned} s(t;\underline{\alpha}) &\approx \sum_n X_8(t-2nT; b_{2n-1}, b_{2n}, b_{2n+1}), \\ &\approx \sum_n \Big(S_{I,8}(t-2nT; b_{2n-1}, b_{2n}, b_{2n+1}) + jS_{Q,8}(t-2nT; b_{2n-1}, b_{2n}, b_{2n+1})\Big), \end{aligned} \quad (2.47)$$

where

$$S_{I,8}(t-2nT;b_{2n-1},b_{2n},b_{2n+1}) = b_{2n}w_0(t-2nT) - b_{2n-1}b_{2n}b_{2n+1}w_1'(t-2nT), \tag{2.48}$$

$$S_{Q,8}(t-2nT;b_{2n-1},b_{2n},b_{2n+1}) = b_{2n-1}w_0(t-2nT+T) + b_{2n+1}w_0(t-2nT-T). \tag{2.49}$$

The different waveforms are plotted in Figure 2.9 and compared to the exact 8-waveform XTCQM representation of Section 1.5.4 (this XTCQM representation is referred to as XTCQM-CPM here since it is derived from the exact CPM expression). We can notice that the two representations are identical even though the XTCQM-PAM waveforms are generated using the PAM approximation, and this can be explained as follows: since the pseudo-symbols associated with the pulses $\{w_k\}_{k>1}$ contain lengthy memories, their contributions are erased due to averaging.

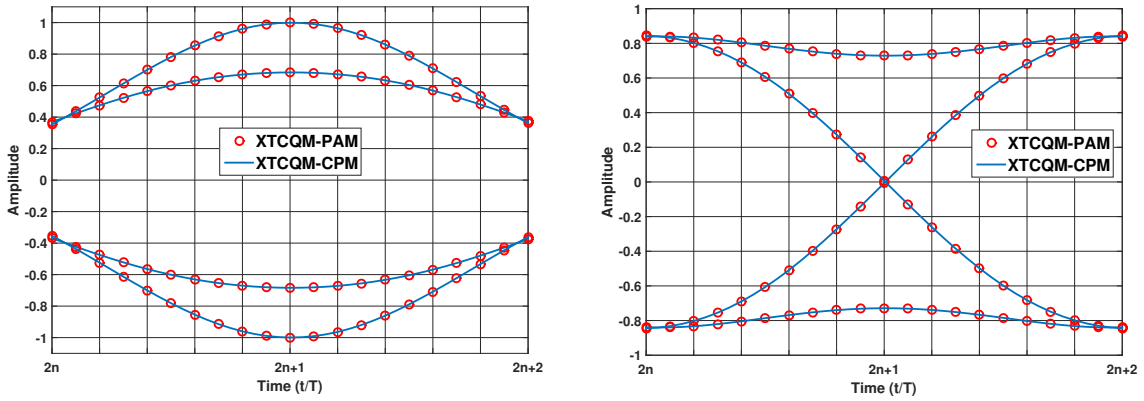

(a) $S_{I,8}(t-2nT;b_{2n-1},b_{2n},b_{2n+1})$ (b) $S_{Q,8}(t-2nT;b_{2n-1},b_{2n},b_{2n+1})$

Figure 2.9 – Comparison between the 8-Waveform XTCQM-PAM and the 8-Waveform XTCQM-CPM representations for SOQPSK-TG

In this section, we established a mathematical link between the DBD PAM decomposition of SOQPSK and its XTCQM representation. We showed this link could be found via the exact DBD PAM decomposition if we focus on SOQPSK-MIL or the DBD PAM approximation for SOQPSK-TG. In both cases, both waveforms $w_0(t)$ and $w_1(t)$ and their corresponding pseudo-symbols constitute the XTCQM waveforms. The above derivation can further highlights why SOQPSK can be visualized as a scheme that contains both memory and cross-correlation between the I and Q paths using the PAM components. The memory is present especially due to the presence of $w_1(t)$. As for the cross-correlation between I and Q channels, it is due to the fact that $w_0(t) \neq 0$ when $t \geq 2T$.

2.5 The link between the OQPSK interpretation and SOQPSK

In this section, we focus on the link between SOQPSK and OQPSK. This connection is essential since SOQPSK inherits its name from OQPSK even though, to the best of our knowledge, the signal has never been expressed as an OQPSK-type signal using the PAM decomposition.

Thanks to the DBD decomposition, the link between SOQPSK and OQPSK can be identified merely by considering the first PAM approximation of Section 2.3.2, i.e.,

$$s(t;\underline{b}) \approx \sum_i b_{2i} w_0(t-2iT) + j \sum_i b_{2i+1} w_0(t-2iT-T). \tag{2.50}$$

Equation (2.50) shows that the odd bit sequence is time shifted by one bit period. Therefore, if we consider a symbol composed of one even bit and one odd bit, we go back to the definition of the classical OQPSK with $w_0(t)$ as a shaping pulse of length $3T$ for SOQPSK-MIL and $10T$ for SOQPSK-TG.

The different connections presented in this work between SOQPSK and its all the aforementioned representations have been mainly achieved thanks to the new vision of the SOQPSK precoder introduced at beginning of this chapter. For this reason, we detail in the following section the role of each element that composes this precoder.

2.6 The role of SOQPSK precoder

2.6.1 The duobinary encoder

Duobinary encoding is a technique that has been normalized in optical fiber communications for efficient use of channel bandwidth in the late 1990's [73]. It is known as a simple technique that significantly increases the spectral efficiency of the signal [65]. However, to our knowledge, this was only studied for linear modulations. Since duobinary encoding is present in the SOQPSK precoder, one can assume that it has an impact on the spectral efficiency of this modulation and CPM in general. Thus, we propose in this section to study the spectral efficiency of duobinary CPM in order to confirm this hypothesis.

The duobinary encoder shares one property with the encoder described in [74]: it generates ternary symbols such that a direct transition from -1 to $+1$ and vice versa never occur, i.e., a zero state is necessary. This observation implies that the duobinary encoder might have an impact on the spectral efficiency of the signal like the one described in [74]. One interesting way to characterize the added value of the duobinary encoder is to evaluate its spectral efficiency as defined in [75]:

$$SE = \frac{I}{BT}, \qquad [\text{bit/s/Hz}], \tag{2.51}$$

where I is the information rate (IR), and B is the bandwidth occupied by the transmitted signal. This definition considers the amount of the transmitted information per channel use while taking into account the bandwidth occupancy of the modulation format. The computation of IR between the input process (transmitted symbols) and the channel output process (received signal) can be performed using the simulation-based technique described in [76], which requires an optimal maximum a posteriori (MAP) symbol detector for an additive white Gaussian noise channel (AWGN). This can be performed using a BCJR [1] algorithm as described in [77, 78] for CPM. Since the power spectrum density of a CPM has rigorously infinite support, we define the bandwidth B as the band of frequency containing 99% of the overall signal power. The computation of B is done numerically [4].

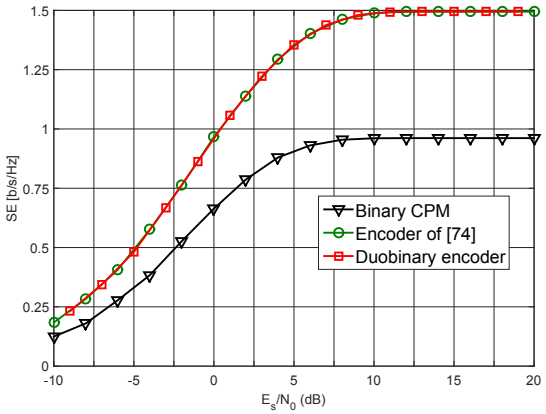

Figure 2.10 – SE for 1-REC modulation with $h = 1/3$

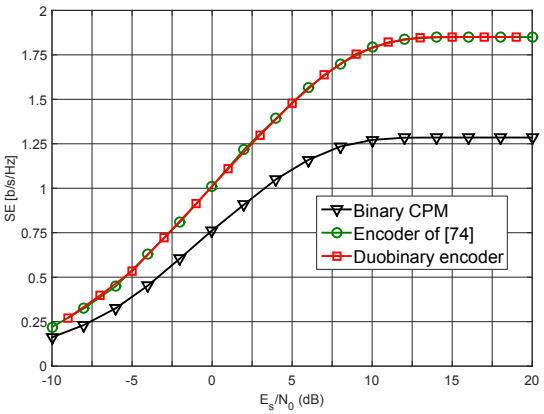

Figure 2.11 – SE for 2-RC modulation with $h = 1/4$

We plot the SE for a full response system with a rectangular frequency pulse (1-REC) and a modulation index equal to 1/3 (Figure 2.10) as well as the SE for a partial response one with a raised cosine frequency pulse of length $L = 2$ (2-RC) and $h = 1/4$ (Figure 2.11). It can be seen that the SE of the duobinary encoder is identical to the SE of the best encoder in [74] and is always better than binary CPM one for the different modulation formats and modulation indices.

We now consider the whole structure of the SOQPSK precoder (see Figure 2.1). Figure 2.12 and Figure 2.13 show the SE of CPM with a half-integer modulation index. We choose $h = 1/2$ since the simplifications that are introduced by the recursive encoder in (2.31) are only valid for this particular case. We consider 1-REC and 2-RC modulation formats. We can notice that the recursive encoder introduced in Figure 2.1 does not influence the SE of binary CPM. This result was expected since the output of this recursive encoder does not impose any special rules on the phase trajectory of the signal. We can, however, see a performance improvement

[1] Bahl, Cocke, Jelinek and Raviv

compared to the binary case when we consider the SOQPSK precoder. The SE is identical to the one proposed in [74] thanks to the presence of the duobinary encoder in the precoder structure.

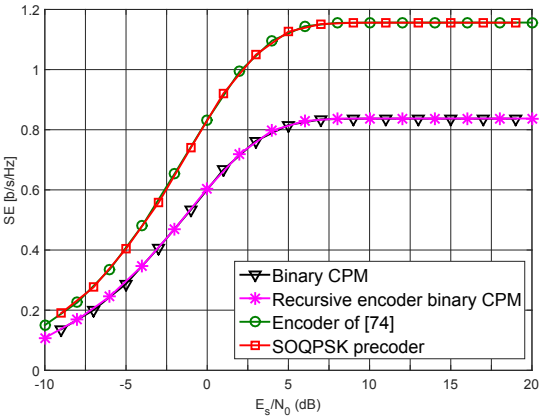

Figure 2.12 – SE for 1-REC modulation with $h = 1/2$

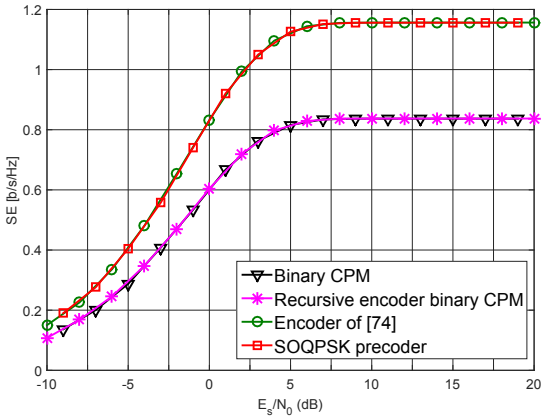

Figure 2.13 – SE for 2-RC modulation with $h = 1/2$

The aforementioned results confirm the attractive properties of the duobinary encoder regarding the spectral efficiency for CPM. However, it does not allow to attain the spectral efficiency gains of linear modulations because of the following reasons:

- Applying duobinary encoding on the symbols that are encapsulated in the instantaneous frequency does not beget duobinary encoded pseudo-symbols of the PAM decomposition. Similarly, if we look at the expression of the main pulse of DBD, we can see that it is not a half sum of the of the main pulse of the binary Laurent Decomposition and its time-shifted version, i.e.,

$$w_0(t) \neq \frac{1}{2}\left(c_0(t) + c_0(t-T)\right), \tag{2.52}$$

$$\neq c_0^d(t). \tag{2.53}$$

  To illustrate this, we can take as a straightforward example the PAM decomposition of 1-REC binary CPM with a modulation index $h = 1/2$. From (1.15), its main pulse is expressed as

$$c_0(t) = \begin{cases} \sin(\dfrac{\pi t}{2T}), & 0 \leq t < 2T, \\ 0, & \text{otherwise.} \end{cases} \tag{2.54}$$

The pulse $c_0^d(t)$ is then expressed as

$$c_0^d(t) = \begin{cases} \frac{1}{2}\sin(\frac{\pi t}{2T}), & 0 \le t < T, \\ \frac{1}{2}\left(\sin(\frac{\pi t}{2T}) - \cos(\frac{\pi t}{2T})\right), & T \le t < 2T, \\ -\frac{1}{2}\cos(\frac{\pi t}{2T}), & 2T \le t < 3T, \\ 0, & \text{otherwise.} \end{cases} \tag{2.55}$$

It is clear that the obtained pulse shape is different from the main pulse of duobinary encoded 1-REC CPM given in (2.29).

- The fact that the frequency pulse is expanded by a one-bit period due to duobinary encoding would generate additional PAM waveforms to keep the complex envelope of the signal constant. Therefore, the presence of these waveforms may result in less SE than the SE of the OQPSK-type signal whose pulse shape is w_0. This is because CPMs generally have worse spectral properties than linear modulations [79].

2.6.2 The recursive encoder

Since SOQPSK is by definition a CPM, its information is carried in the change of phase rather than the phase itself. Therefore, it is inherently a differential encoded modulation. To overcome this inherent property and to make the information carried in the phase, the recursive encoder described in (2.2) is used. The proof of this claim is depicted in both Appendixes B and C thanks to the PAM decomposition. Therefore, any binary (or duobinary) MSK-type signal that takes advantage of the recursive encoder can be exactly decomposed or accurately approximated as

$$s(t;\underline{b}) \approx \sum_i b_{2i} c_0(t-2iT) + j\sum_i b_{2i+1} c_0(t-2iT-T), \tag{2.56}$$

or

$$\begin{aligned} s(t;\underline{b}) \approx \sum_i &\left[b_{2i} c_0(t-2iT) - j b_{2i-1} b_{2i} b_{2i+1} c_1(t-2iT)\right] \\ &+ \sum_i \left[j b_{2i+1} c_0(t-2iT-T) - b_{2i} b_{2i+1} b_{2i+2} c_1(t-2iT-T)\right] \end{aligned} \tag{2.57}$$

and can be interpreted as an OQPSK-type modulation or a XTCQM-type one.

2.7 Conclusion

In this chapter, we showed that the Perrins Rice decomposition described in Chapter 1 is not the only PAM decomposition for all ternary CPMs. If we consider the particular case where the ternary symbols are generated using a duobinary encoder, we proved that the PAM decomposition of this duobinary CPM follows an alternative PAM decomposition, namely DBD, that retains the key features of the binary Laurent decomposition. Figure 2.14 summarizes the link between the different PAM representations of single-h CPM.

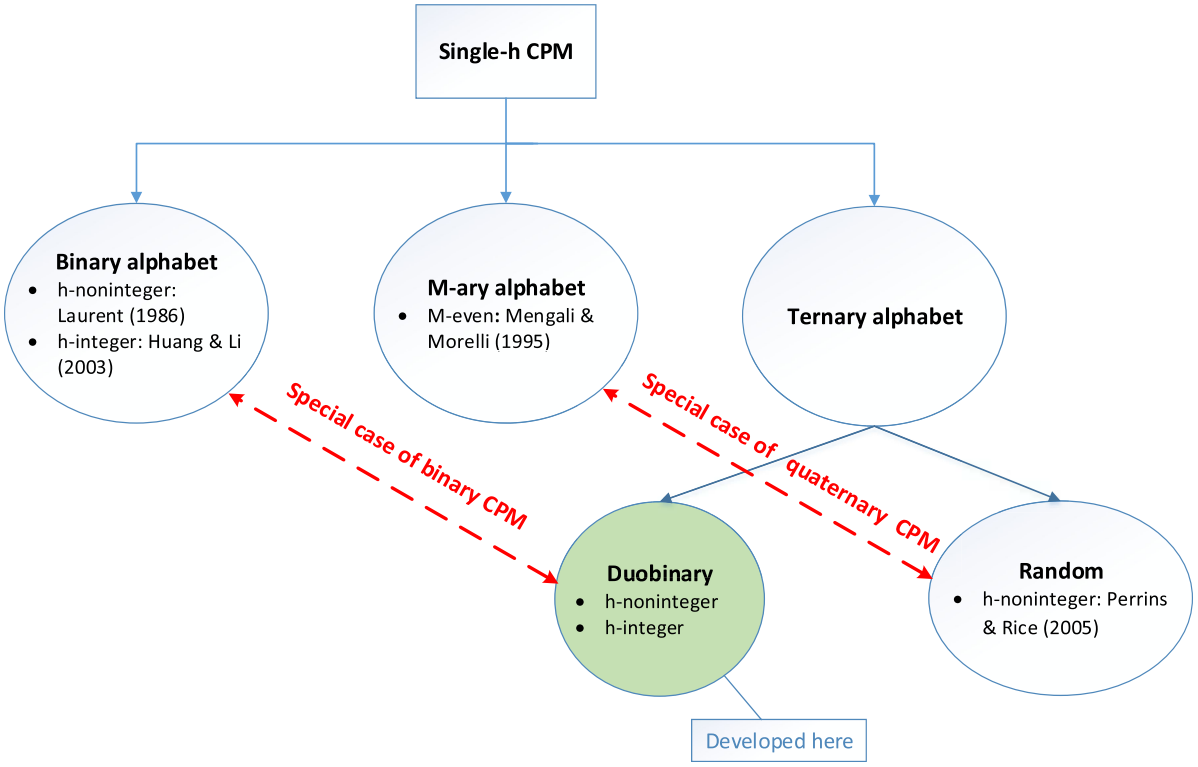

Figure 2.14 – Summary of the PAM decompositions of single-h CPM

We then showed that SOQPSK belongs to the duobinary CPM family thanks to its precoder and we derived a new PAM decomposition for this signal via DBD. This revamped representation is characterized by the presence of a single main pulse unlike PRD and by uncorrelated pseudo-symbols thanks to the half-integer modulation index. Moreover, we took advantage of the recursive encoder given in (2.2) to simplify the expressions of the pseudo-symbols.

Applying DBD to SOQPSK allowed us to link together the different interpretations of this signal as illustrated in Figure 2.15 and to better understand the role of its ternary precoder: the presence of the duobinary encoder in the precoder structure allows increasing the spectral efficiency of the signal whereas the presence of the recursive encoder removes the inherent

memory of the modulation and realizes the connection between SOQPSK and OQPSK as well as between SOQPSK and the XTCQM representation.

The results obtained in this chapter are of great importance since they demonstrate that dealing with SOQPSK modulation does no longer require additional assumptions compared to partial response binary CPM systems. In fact, SOQPSK can be seen as a binary MSK-type signal with a partial response equivalent frequency pulse. This result ensures that the works initially developed for MSK-type CPM can now be fully applied to SOQPSK.

In the following chapters, we will investigate the consequences of using the revamped decomposition on the detection architectures (Chapter 3), the channel estimation and equalization (Chapter 4) as well as on the scenario where the aircraft is equipped with two transmitting antennas whereas the ground station only contains one receiving antenna (Chapter 5 and Chapter 6).

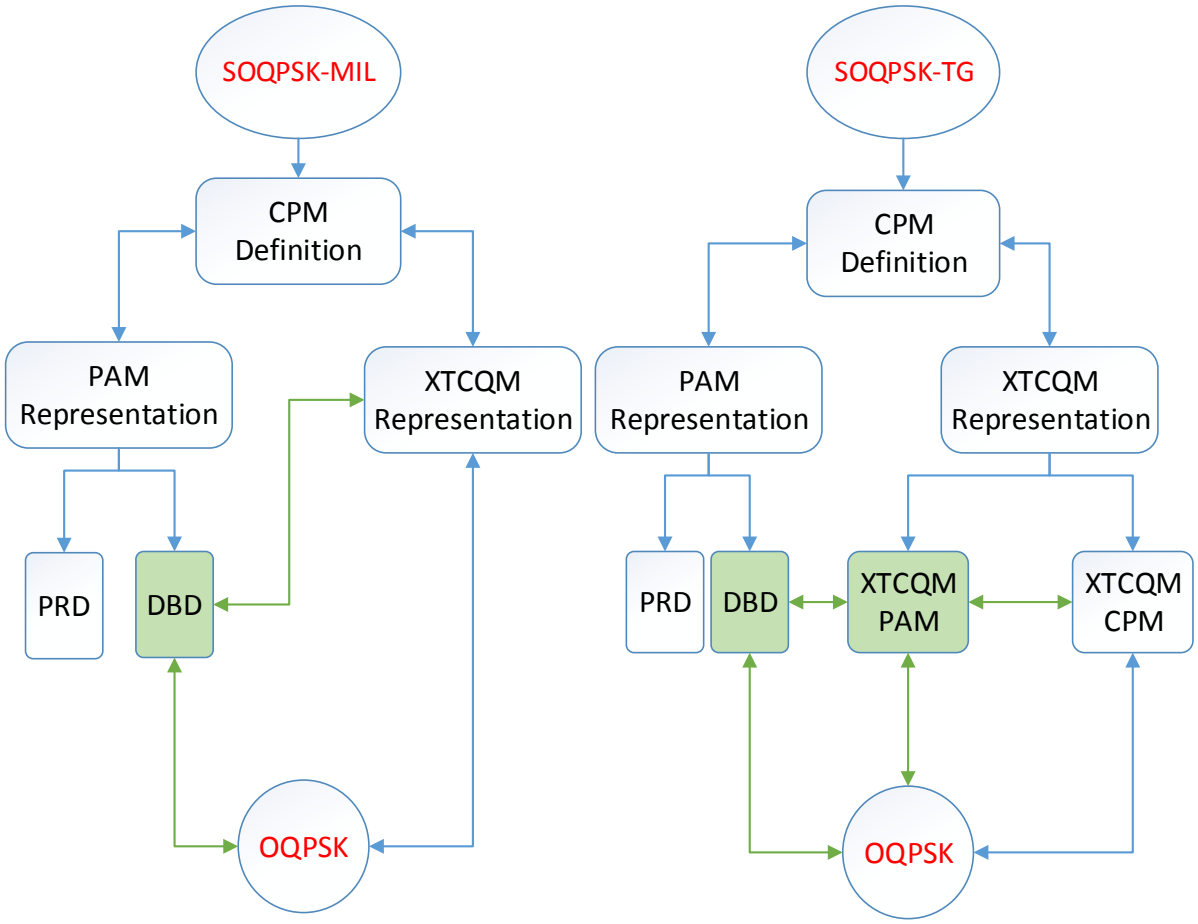

Remark: The boxes and arrows highlighted in green depict our contribution

Figure 2.15 – Connection Between the Different Representations of SOQPSK

Chapter 3

Reduced Complexity Detection Architectures Based on the Duobinary PAM Decomposition

Contents

3.1 Introduction

Besides from the attractive spectral containment of SOQPSK-TG, one of the major advantages that boosted the adoption of this modulation in the IRIG recommendations is the simplicity of detecting its data symbols with acceptable BER performance; in fact, simple linear integrate and dump detectors, initially designed for OQPSK-type modulations, can be used for the different versions of SOQPSK [17, 80]. This can be achieved thanks to the SOQPSK precoder that makes the phase transitions of SOQPSK similar to OQPSK [36]. However, this was not proved analytically, and moreover, the BER performances of these detectors are not optimal.

The first detector, capable of reaching optimal BER performance, was first introduced by Li and Simon in [61] for SOQPSK-MIL by taking advantage of its XTCQM interpretation given in Chapter 1. This interpretation highlighted the need for a memory type of receiver instead of a linear one to achieve optimal BER performance. Similarly, the XTCQM interpretation was introduced for SOQPSK-TG to develop trellis based detectors as well as common detectors between SOQPSK-TG and FQPSK since both are inter-operable standards in aeronautical telemetry. These detectors are described in [16, 63], and the one that possesses the best BER performance & complexity trade-off is composed of 16 states.

Perrins took another approach in [14, 18] where he instead considered the ternary CPM definition of SOQPSK instead of its XTCQM or OQPSK interpretations and took advantage of its PAM decomposition (PRD) to develop a reduced complexity 4-states Viterbi detector with optimal BER performance for SOQPSK-MIL and near-optimal one for SOQPSK-TG. This solution is described in Appendix D. However, due to the chosen ternary PAM decomposition, the resulting trellis is dynamic, i.e., the different transitions and the order of the path states in the trellis diagram depend on the parity of the bit index. Moreover, the fact that this decomposition generates two pulses of similar weights makes deriving linear detectors using this approach unfeasible.

In this chapter, we derive new detection architectures for both versions of SOQPSK (i.e., SOQPSK-MIL and SOQPSK-TG) based the on the revamped PAM decomposition (DBD) as well as the XTCQM-PAM representation given in Chapter 2. We first consider Kaleh approach [81] who developed different detection structures for binary CPM and we show that three possible architectures can be obtained for SOQPSK: an optimum detector, a reduced complexity one with very near-optimal performance and a near-optimal linear one. We then assume that SOQPSK is a linear modulation thanks to the obtained results in Section 2.3 and we apply the Ungerboeck approach [26] to derive a novel OQPSK-type detector for SOQPSK. Finally, we further exploit the simple mapping between the data symbols and the pseud-symbols to derive a least squares detector that has a better performance & complexity trade-off than the 16 states XTCQM-CPM based detector given in [63].

3.2 Kaleh approach

We assume that the SOQPSK signal $s(t;\underline{\alpha})$ transmits N ternary symbols $\underline{\alpha} = \{\alpha_i\}_{0\leq i<N}$ using (1.9) and is corrupted by a AWGN $n(t)$ of double-sided power spectral density $N_0/2$. The received signal is then expressed as follows

$$r(t) = s(t;\underline{\alpha}) + n(t). \tag{3.1}$$

The log-likelihood function of the binary sequence $\underline{b}$ that is used to generate $\underline{\alpha}$ is then [64]

$$\Lambda(\underline{b}) = -\frac{1}{N_0}\int_0^{NT} |r(t) - s(t;\underline{\alpha})|^2\, dt. \tag{3.2}$$

If we develop (3.2),

$$\Lambda(\underline{b}) = -\frac{1}{N_0}\left(\int_0^{NT} |r(t)|^2\, dt + \int_0^{NT} |s(t;\underline{\alpha})|^2\, dt - 2\int_0^{NT} Re\left\{r(t)s^*(t;\underline{\alpha})\right\} dt\right), \tag{3.3}$$

we can simplify $\Lambda(\underline{b})$ to the following expression

$$\Lambda(\underline{b}) = \frac{2}{N_0} Re\left\{\int_0^{NT} r(t)s^*(t;\underline{\alpha})dt\right\}. \tag{3.4}$$

This result is true because the term $|r(t)|^2$ does not depend on $\underline{b}$ and is common for all paths of a given trellis and because $|s(t;\underline{\alpha})|^2$ is constant due to the CPM nature of SOQPSK.

3.2.1 Optimum detector

The key idea of Kaleh [81] is to replace $s(t;\underline{\alpha})$ in (3.4) by its PAM decomposition. Using (2.17), we get

$$\Lambda(\underline{b}) = \frac{2}{N_0}\sum_{n=0}^{N-1} Re\left\{\int_0^{NT} r(t)\left(\sum_{k=0}^{M_d-1} \rho_{k,i}^* w_k(t-nT)\right) dt\right\}. \tag{3.5}$$

By permuting the integral and the second sum and by discarding the constant term $\frac{2}{N_0}$ in (3.5), the optimal detector maximizes the following branch metric

$$\Lambda(\underline{b}) = \sum_{n=0}^{N-1} \lambda(n), \tag{3.6}$$

where

$$\begin{cases} \lambda(n) = Re\left(\sum_{k=0}^{M_d-1} y_k(n)\rho_{k,n}^*\right), & (3.7) \\ y_k(n) = \int_{nT}^{(n+D_k)T} r(t)w_k(t-nT)dt. & (3.8) \end{cases}$$

The parameter D_k is the length of the pulse $w_k(t)$ as described in Table 2.1.

Discussion:
We can notice from (3.8) that the correlation involves the observation of the received noisy signal during a time span of D_kT. However, as shown in Table 2.1, the time support of the pulses $\{w_k\}_{k<M_d/2}$ is greater than T. One can then assume that the contribution of the pseudo-symbols $\{\rho_{k,m}\}_{m<n}$ is discarded in (3.8) and therefore, the described detector is not really optimal. Even though the pseudo-symbol interference caused by the correlation of pulses $\{w_k\}_{k<M_d/2}$ is taken into account in the metrics of the previous L_d sections, this assumption is correct if we want to consider a maximum a posteriori probability (MAP) symbol decoder based on these correlations as highlighted in [82, 83]. However in our case, since we deal with a sequence decision based estimator (and not a symbol decision based one), the described receiver is optimal.

We begin by introducing the optimal detector for SOQPSK-MIL: since the exact DBD representation of this modulation requires 2 PAM waveforms as shown in Section 2.3.1, the metric $\lambda(n)$ of the optimal detector is expressed as follows

$$\lambda(n) = \begin{cases} b_n Re\{y_0(n)\} - b_n b_{n-1} b_{n-2} Im\{y_1(n)\}, & n \text{ even}, \\ b_n Im\{y_0(n)\} - b_n b_{n-1} b_{n-2} Re\{y_1(n)\}, & n \text{ odd}. \end{cases} \quad (3.9)$$

Equation (3.9) shows that the detection process can be performed using a 4-states Viterbi algorithm with 2 branches. Each branch is defined by the triplet

$$\sigma_n = (b_{n-2}, b_{n-1}, b_n). \quad (3.10)$$

We illustrate in Figure 3.1 the trellis of this detector. We can notice that the proposed trellis is static, i.e., the branch directions do not depend on the parity of the symbol index n, contrary to the trellis proposed in [18] and described in Appendix D. Only the branch metrics values depend on the parity of n as shown in (3.9). We now move on to the telemetry modulation SOQPSK-TG: an optimal detector requires 256 matched filters since the exact duobinary PAM decomposition (DBD) requires that same number of pulses. In order to determine the number of states for the Viterbi algorithm, we only need to compute the pseudo-symbol of the $M_d{}^{\text{th}}$ pulse because it encapsulates the biggest memory amount among all the other pseudo-symbols.

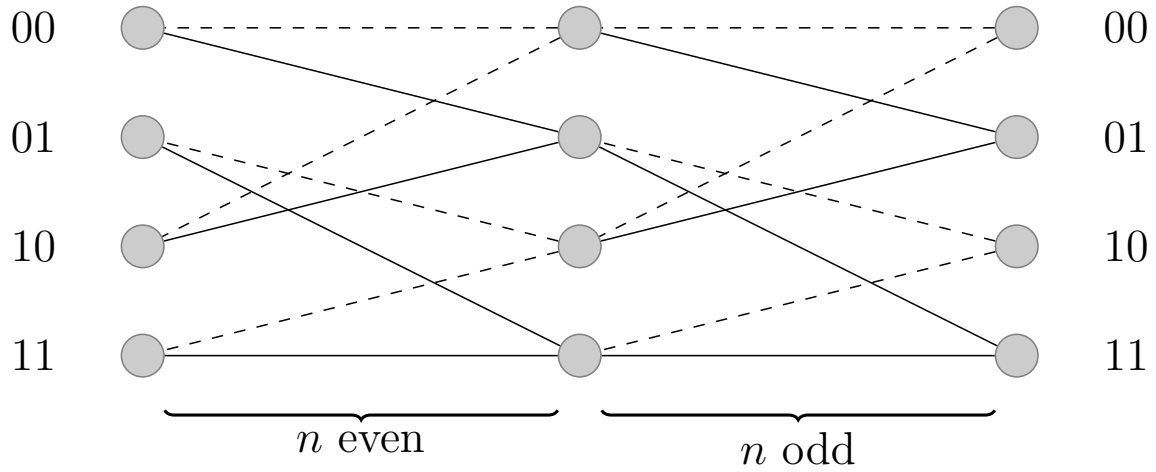

legend: dashed line: $\sigma_n = (b_{n-2}, b_{n-1}, -1)$, solid line: $\sigma_n = (b_{n-2}, b_{n-1}, +1)$

Figure 3.1 – 4 states trellis for SOQPSK

This can be proved by rewriting $\rho_{k,n}$ given in (2.20) as follows:

$$\rho_{k,n} = \exp\left\{ jh\pi \left[\sum_{m=-\infty}^{n} \gamma_m - \sum_{q=0}^{L_d-1} \gamma_{n-q}\eta_{k,q}^{d} \right] \right\}, \tag{3.11}$$

$$= \underbrace{\exp\left\{ jh\pi \sum_{m=-\infty}^{n-L_d} \gamma_m \right\}}_{\rho_{0,n-L_d}} \times \exp\left\{ jh\pi \sum_{q=0}^{L_d-1} \gamma_{n-q}\left(1-\eta_{k,q}^{d}\right) \right\}. \tag{3.12}$$

By noticing that $1-\eta_{k,q}^{d} = \eta_{M_d-1-k,q}^{d}$ [82] where $M_d = 256$ for SOQPSK-TG, we get

$$\rho_{k,n} = \rho_{0,n-L_d} \times \exp\left\{ jh\pi \sum_{q=0}^{L_d-1} \gamma_{n-q}\eta_{M_d-1-k,q}^{d} \right\}. \tag{3.13}$$

From (3.13), we can see that inherent memory associated with the pseudo-symbol $\rho_{k,n}$ proportionally increases with k. The best case (i.e. no inherent memory) is when $k = 0$ since $\eta_{M_d-1,q}^{d} = 1$ for $0 \leq q \leq L_d - 1$ and the worst case is when $k = M_d - 1$ because $\eta_{M_d-1,q}^{d} = 0$ for $0 \leq q \leq L_d - 1$. In the latter situation, we have

$$\rho_{255,n}(n) = \rho_{0,n-9}(n) = \begin{cases} jb_{n-9}, & n \text{ even}, \\ b_{n-9}, & n \text{ odd}. \end{cases} \tag{3.14}$$

Consequently, the optimal detector of SOQPSK-TG requires a 512-state Viterbi algorithm with 2 branches. Each branch is defined by the 10-tuple

$$\sigma_n = (b_{n-9}, b_{n-8}, ..., b_{n-1}, b_n). \tag{3.15}$$

The number of states is high and coincides with the number of states of the optimal detector presented in [50] for SOQPSK-TG. It is then necessary to reduce the complexity of this receiver for a real-time implementation.

3.2.2 Reduced complexity Viterbi detector

In order to reduce the complexity of the optimal detector of SOQPSK-TG, we exploit the observation given in Section 2.3.2 regarding the energy distribution of the signal among the PAM waveforms. Since 99.75% of the signal energy is contained in the first two PAM waveforms, the number of matched filters can be reduced from 256 to 2. The metric of the reduced complexity detector becomes

$$\lambda(n) = \begin{cases} b_n Re\left\{y_0(n)\right\} - b_n b_{n-1} b_{n-2} Im\left\{y_1(n)\right\}, & n \text{ even}, \\ b_n Im\left\{y_0(n)\right\} - b_n b_{n-1} b_{n-2} Re\left\{y_1(n)\right\}, & n \text{ odd}. \end{cases} \tag{3.16}$$

The obtained metric is identical to the optimal metric of SOQPSK-MIL detector. Therefore, the resulting trellis is the same as the one depicted in Figure 3.1 and the number of necessary states is reduced to 4 since the branch of the trellis is now defined by the 3-tuple given in (3.10). We give in Figure 3.2 the architecture of the reduced complexity detector.

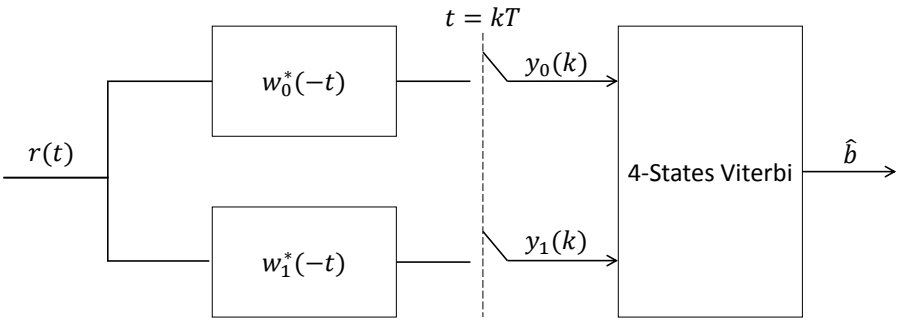

Figure 3.2 – Architecture of the Kaleh based reduced complexity detector for SOQPSK

Another way to reduce the complexity of the detector is to truncate the used matched filters for SOQPSK-TG. We can see from Figure 2.6 that the pulses equal zero below D_kT. Therefore,

the matched filters outputs $\{y_k\}_{k\in\{0,1\}}$ can be obtained as follows

$$y_k(n) = \int_{nT}^{(n+\tilde{D}_k)T} r(t)\tilde{w}_k(t-nT)dt, \qquad k \in \{0,1\}, \tag{3.17}$$

where

$$\tilde{w}_k(t) = \begin{cases} w_k\left(t + \dfrac{D_k - \tilde{D}_k}{2}\right), & 0 \le t \le \tilde{D}_k, \\ 0, & \text{otherwise.} \end{cases} \tag{3.18}$$

and $1 \le \tilde{D}_k \le D_k$.

3.2.3 Linear detector

We can further exploit the properties of DBD by reducing the number of matched filters from 2 to 1. This can be justified since DBD generates one main pulse $w_0(t)$. The metric $\lambda(n)$ becomes

$$\lambda(n) = \begin{cases} b_n Re\left\{y_0(n)\right\}, & n \text{ even}, \\ b_n Im\left\{y_0(n)\right\}, & n \text{ odd}. \end{cases} \tag{3.19}$$

Since we deal with a maximization problem, the above metric expression leads to the following symbol-by-symbol detector

$$\hat{b}(n) = \begin{cases} sign\left(Re\left\{y_0(n)\right\}\right), & n \text{ even}, \\ sign\left(Im\left\{y_0(n)\right\}\right), & n \text{ odd}. \end{cases} \tag{3.20}$$

As discussed in Section 3.2.1, due to the length of the matched filter, the sampled matched filter output $y_0(n)$ at epoch n does not only involve the pseudo-symbol $\rho_{0,n}$, but also the pseudo-symbols $\{\rho_{0,m}\}_{m<n}$. Moreover, even though the energy contained in the pulse w_1 is low, $y_0(n)$ can also be perturbed by the pseudo-symbols $\{\rho_{1,m}\}_{m\le n}$ associated with w_1. To illustrate this, we first express the received signal $r(t)$ as follows

$$r(t) = \sum_{k=0}^{1}\sum_{i}\rho_{k,i}w_k(t-iT) + n(t) + \epsilon(t), \tag{3.21}$$

where $\epsilon(t) = 0$ for SOQPSK-MIL and

$$\epsilon(t) = \sum_{k=2}^{255}\sum_{i}\rho_{k,i}w_k(t-iT), \tag{3.22}$$

for SOQPSK-TG. The function $\epsilon(t)$ can be neglected since it contains less than 0.25% of the signal energy. The sampled matched filter output y_0 can thus be written as

$$y_0(n) = \sum_m \rho_{0,n-m} R_{00}(m) + \sum_m \rho_{1,n-m} R_{01}(m) + \mu(n), \tag{3.23}$$

where

$$R_{0k}(m) = \int w_k(t) w_0(t - mT) dt, \qquad k \in \{0, 1\}, \tag{3.24}$$

and

$$\mu(n) = \int n(t) w_0(t - nT) dt. \tag{3.25}$$

We now focus on the the samples that are involved in (3.19), which are $Re\{y_0(2n)\}$ and $Im\{y_0(2n+1)\}$:

$$Re\{y_0(2n)\} = \sum_m b_{2(n-m)} R_{00}(2m) - \sum_m b_{2(n-m)+1} b_{2(n-m)} b_{2(n-m)-1} R_{01}(2m+1) + Re\{\mu(2n)\}, \tag{3.26}$$

$$Im\{y_0(2n+1)\} = \sum_m b_{2(n-m)+1} R_{00}(2m) - \sum_m b_{2(n-m)+2} b_{2(n-m)+1} b_{2(n-m)} R_{01}(2m+1) + Im\{\mu(2n+1)\}. \tag{3.27}$$

Equations (3.26), (3.27) and figures 3.3, 3.4 show that the sample $y_0(n)$ that is used to detect the symbol b_n does not only contain the statistics of b_n, but also those of other data symbols $\{b_m\}_{m \neq n}$.

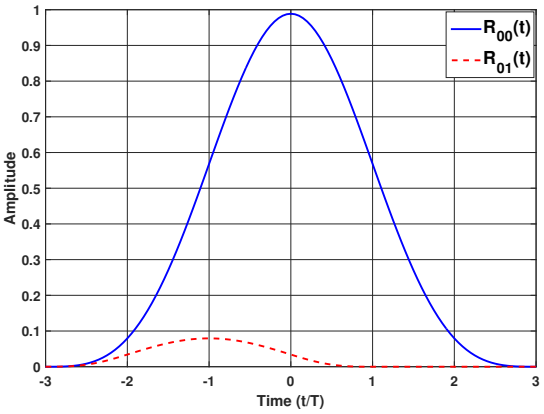

Figure 3.3 – Illustration of $R_{00}(t)$ and $R_{01}(t)$ for SOQPSK-MIL

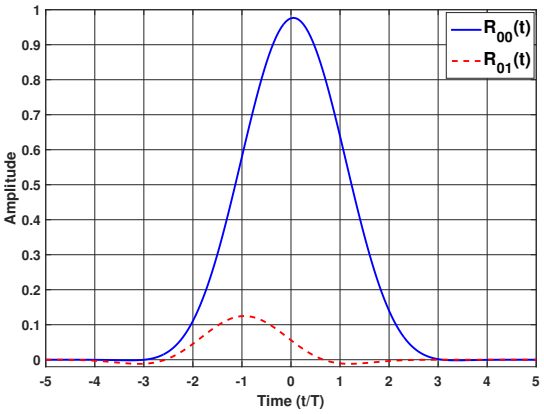

Figure 3.4 – Illustration of $R_{00}(t)$ and $R_{01}(t)$ for SOQPSK-TG

Therefore, it is necessary to mitigate the interference caused by $\{b_m\}_{m\neq n}$. To do so, Kaleh has proposed in [25] the use of a Wiener filter in addition to the filter matched to w_0 in order to reduce this intersymbol interference and thus to deliver an optimum estimate of y_0. This filter is built based on the minimum mean square error (MMSE) criterion [64], and its coefficients are computed using the described method in [25]. We plot in Figure 3.5 and Figure 3.6 the combined matched filter $\tilde{w}_0(t)$ for both versions of SOQPSK, i.e., the filter that is formed by combining the main pulse w_0 and the Wiener filter coefficients C_k^{WF} as follows

$$\tilde{w}_0(t) = \sum_{k=-\infty}^{+\infty} C_k^{WF} w_0(-t + 2kT). \tag{3.28}$$

It can be seen that this filter $\tilde{w}_0$ of Figure 3.6 looks very much like the optimal filter described in [17] and drawn in [84]. Therefore, we can assume that the optimal filter that has been found by simulation in [17] is now obtained analytically.

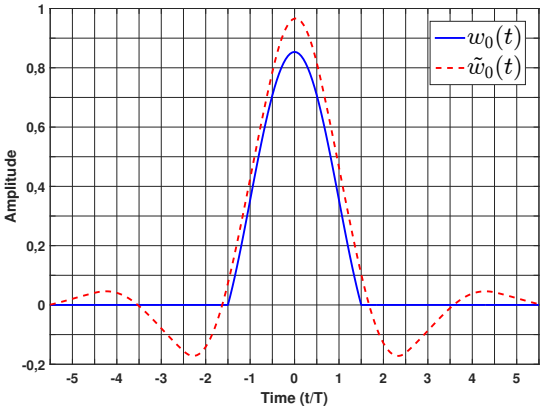

Figure 3.5 – Illustration of $w_0(t)$ and $\tilde{w}_0(t)$ for SOQPSK-MIL

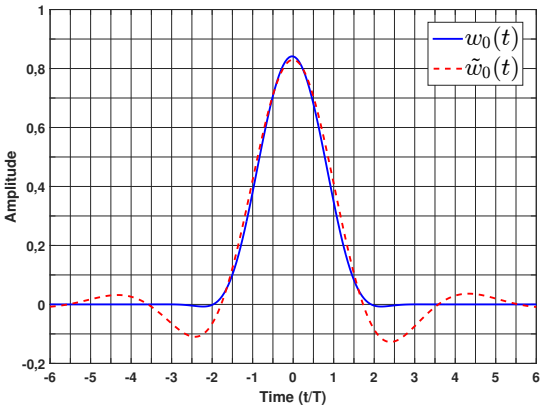

Figure 3.6 – Illustration of $w_0(t)$ and $\tilde{w}_0(t)$ for SOQPSK-TG

3.2.4 Performance analysis

The bit error probability P_b of the optimal receiver can be determined by using the concept of error events and minimum distances. Given two ternary error sequences $\underline{\alpha}_I$ and $\underline{\alpha}_J$, the normalized Euclidean distance of CPM is defined as [4]

$$d^2 = \frac{log_2(M)}{2T} \int |s(t, \underline{\alpha}_I) - s(t, \underline{\alpha}_J)|^2 dt, \tag{3.29}$$

where $log_2(M)$ is the number of information bits per symbol, which is equal to 1 for duobinary CPM. Since the latter can be seen as a binary CPM signal with an equivalent phase pulse as illustrated in Figure 2.3, the error sequences may be determined based on the antipodal binary

sequence $\underline{\gamma}$ that generates the ternary sequence[1]. For a modulation index equal to 1/2, we consider the bit error sequences

$$\underline{\gamma}_I = \ldots\ldots\ldots\ldots, \quad \gamma_{k-1}, \quad \gamma_k, \ldots\ldots\ldots\ldots$$
$$\underline{\gamma}_J = \ldots\ldots\ldots\ldots, -\gamma_{k-1}, -\gamma_k, \ldots\ldots\ldots\ldots$$

where k is an arbitrarily chosen index. The computation of (3.29) for the four different cases results in two distinct distances: the minimum distance d_0^2 is obtained when $\gamma_{k-1} = -\gamma_k$ whereas the largest distance d_1^2 is found when $\gamma_{k-1} = \gamma_k$. Hence, as shown in [18], the bit error probability P_b of the optimal receiver is bounded by

$$P_b \leq \frac{1}{2} Q\left(\sqrt{d_0^2 \frac{E_b}{N_0}}\right) + \frac{1}{2} Q\left(\sqrt{d_1^2 \frac{E_b}{N_0}}\right), \tag{3.30}$$

where

$$Q(t) = \frac{1}{\sqrt{2\pi}} \int_t^{+\infty} e^{-u^2/2} du, \tag{3.31}$$

and E_b is the bit energy. The numerical results are given in Table 3.1 for the different versions of SOQPSK.

Table 3.1 – Euclidean Distances for SOQPSK

	d_0^2	d_1^2
SOQPSK-MIL	1.73	2.36
SOQPSK-TG	1.60	2.59

3.2.5 Simulation results

Figure 3.7 and Figure 3.8 show the BER curves of the detectors using the proposed decomposition. For SOQPSK-MIL, it has to be noticed that the 4-states Viterbi detector is optimal since the decomposition of the signal is not an approximation. The linear filter using a Wiener filter gives a very near optimal performance as the loss is equal to 0.2 dB at $P_b = 10^{-5}$. If we do not use the Wiener filter, the degradation is equal to 1 dB. For SOQPSK-TG, the 4-state detector is very near-optimal, and its performance is identical to the detector introduced in [18]. The degradation does not exceed 0.1 dB at $BER = 10^{-5}$ compared to the optimal detector. In this figure, we have also plotted the performance bound of this detector. This bound is determined based on the analysis made in [48], which derives the exact expression of the pairwise error probability for PAM-based CPM detectors in AWGN. Since the detectors presented in this chapter are mismatched ones, i.e., they are not matched to the transmitted signal, the Euclidian distances corresponding to the error events described in Section 3.2.4 are different in our case.

[1]Here we take the general case where $\underline{b} = \underline{\gamma}$. In the presence of the intermediate encoder, the error sequences of $\underline{b}$ are identical to the ones described in [18].

The Euclidean distances of this detector range from 1.39 to 1.81 for the lower distance and from 2.31 to 2.865 for the higher distance.

If we now compare the linear detectors, it can be seen that adding a Wiener filter improves the detection performance by 1.6 dB compared to the linear detector based on $w_0(t)$ only. It also gives similar performance to the optimal linear detector described in [17]. These results emphasize the usefulness of the proposed decomposition and additionally offer reduced complexity detection architectures for SOQPSK modulation. The complexity reduction of the Viterbi detector is with respect to the optimal detector of SOQPSK-TG and not to the one described in [18].

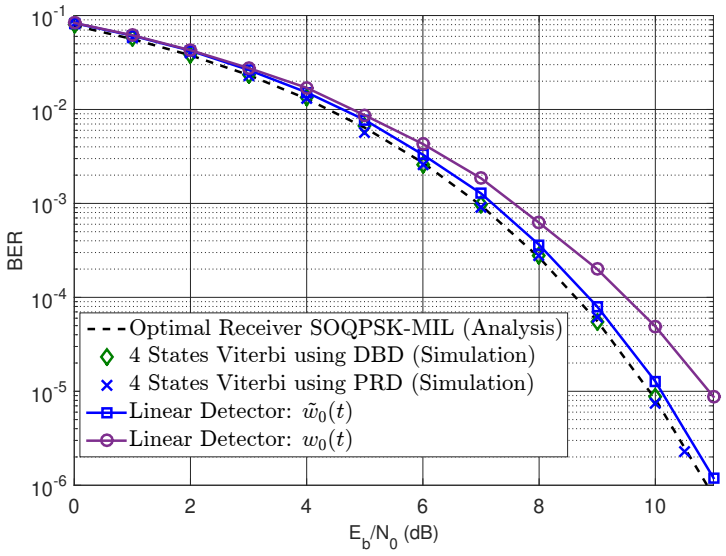

Figure 3.7 – BER performance for SOQPSK-MIL - Kaleh based detectors

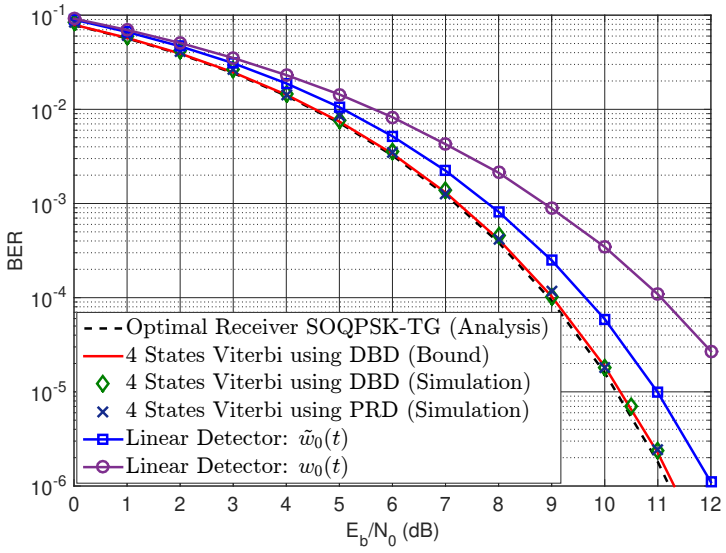

Figure 3.8 – BER performance for SOQPSK-TG - Kaleh based detectors

3.3 OQPSK-type detectors using Ungerboeck approach

3.3.1 Theory

In this section, we take advantage of the knowledge of the main waveform $w_0(t)$ that links SOQPSK to OQPSK (see Section 2.5) to develop another OQPSK type detector close to the one introduced in [61, 85]. To do so, we use the signal model of (2.50), and we consider that N bits are transmitted. The received signal is then expressed as

$$r(t) \approx \underbrace{\sum_{m=0}^{N-1} \rho_{0,m} w_0(t - mT)}_{s(t;\underline{\alpha})} + n(t), \tag{3.32}$$

The log-likelihood function for $\underline{b}$ that generates the ternary sequence $\underline{\alpha}$ is given in (3.2). After developing (3.2) we get (3.3). However the transition from (3.3) to (3.4) is no longer valid in this case because we consider that SOQPSK is a PAM and not a CPM. Therefore, we cannot assume that $|s(t;\underline{\alpha})|^2$ is constant. We then replace $s(t;\underline{\alpha})$ by its PAM approximation as follows

$$\Lambda(\underline{b}) = -\frac{1}{N_0}\left(\int_0^{NT} |r(t)|^2\, dt + \int_0^{NT} \left|\sum_{m=0}^{N-1} \rho_{0,m} w_0(t - mT)\right|^2 dt \right. \\ \left. -2\int_0^{NT} Re\left\{\sum_{m=0}^{N-1} \rho_{0,m}^* r(t) w_0(t - mT)\right\} dt\right). \tag{3.33}$$

After discarding the constant term $1/N_0$, the mathematical development of (3.33) leads to the following expression

$$\Lambda(\underline{b}) = 2Re\left[\sum_{m=0}^{N-1} \rho_{0,m}^* y_0(m)\right] - \sum_{m=0}^{N-1}\sum_{n=0}^{N-1} \rho_{0,m}^* R_{00}(m-n)\rho_{0,n}, \tag{3.34}$$

where y_0 and R_{00} are defined in (3.8) and (3.24), respectively. Ungerboeck showed in [26] that (3.34) can be simplified as

$$\Lambda(\underline{b}) = \sum_{m=0}^{N-1} 2Re\left[\rho_{0,m}^* \left(y_0(m) - \rho_{0,m}\frac{R_{00}(0)}{2} - \sum_{n\leq m-1} \rho_{0,n} R_{00}(n-m)\right)\right], \tag{3.35}$$

$$= \sum_{m=0}^{N-1} \lambda(m). \tag{3.36}$$

Given that the autocorrelation R_{00} has a one-side length of $L+2$, the maximum likelihood sequence estimator (MLSE) is built on the following branch metric

$$\lambda(m) = 2Re\left\{\rho_{0,m}^{*}\left(y_0(m) - \rho_{0,m}\frac{R_{00}(0)}{2} - \sum_{l=1}^{L+2}\rho_{0,m-l}R_{00}(l)\right)\right\}. \tag{3.37}$$

A Viterbi algorithm can be used to evaluate (3.35) whose branch metrics are defined according to $\lambda(m)$ of (3.37). A basic application of (3.37) requires a Viterbi algorithm operating with $2^{L+2} = 1024$ states since the branch is defined with the following 11-tuple

$$\sigma_m = (b_{m-10}, b_{m-9}, ..., b_{m-1}, b_m). \tag{3.38}$$

However, if we plot R_{00} for both SOQPSK versions as shown in Figure 3.9, we can notice that it can approximately be zero after several bit periods lower than $(L+2)T$. Thus, it can be possible to truncate the length of R_{00} from $L+2$ to L_R, and we can express (3.37) as

$$\lambda(m) = 2Re\left\{\rho_{0,m}^{*}\left(y_0(m) - \rho_{0,m}\frac{R_{00}(0)}{2} - \sum_{l=1}^{L_R}\rho_{0,m-l}R_{00}(l)\right)\right\}. \tag{3.39}$$

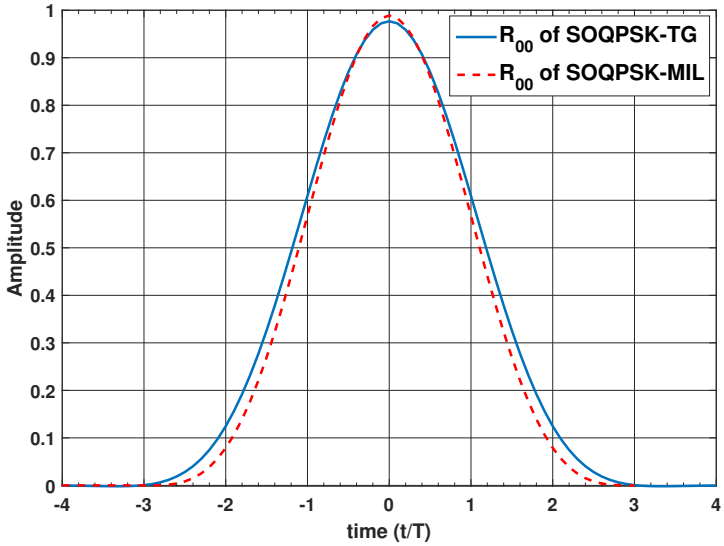

Figure 3.9 – Auto-correlation R_{00}

From Figure 3.9, a first approximation to simplify (3.39) is to take $L_R = 2$. However, it is also possible to consider a stronger hypothesis, i.e., $L_R = 1$. In the following, we analyze the consequence of these approximations on the detection algorithm.

Case 1: $L_R = 2$

For this first assumption, $\lambda(m)$ is expressed as follows

$$\lambda(m) = 2Re\left\{\rho^*_{0,m}\left(y_0(m) - \rho_{0,m}\frac{R_{00}(0)}{2} - \rho_{0,m-1}R_{00}(1) - \rho_{0,m-2}R_{00}(2)\right)\right\}. \tag{3.40}$$

Given that the signal is transmitted through an AWGN channel and $w_0(t)$ is a real-valued function, the imaginary part of R_{00} is always zero. Using (3.13) and after discarding the factor 2, we get

$$\lambda(m) = \begin{cases} b_m\left[Re\{y_0(m)\} - b_{m-2}R_{00}(2)\right] & m \text{ even}, \\ b_m\left[Im\{y_0(m)\} - b_{m-2}R_{00}(2)\right] & m \text{ odd}. \end{cases} \tag{3.41}$$

Equation (3.41) shows that the detection process can be performed via a Viterbi algorithm. We can also notice that even and odd indexed bits can be processed independently like any other OQPSK type signal [85]. In fact, if we consider for instance the case where m is even, i.e., $m = 2p$, the branch metric is a function of b_{2p} and $b_{2(p-1)}$ and is defined by the following 2-tuple

$$\sigma_{2p} = (b_{2(p-1)}, b_{2p}), \tag{3.42}$$

$$\sigma^e_p = (b^e_{p-1}, b^e_p), \tag{3.43}$$

where $\{b^e_p = b_{2p}\}_{p\in\mathbb{N}}$. The same observation applies for the odd case. Therefore, this detector is composed of two 2-states trellises as shown in Figure 3.10.

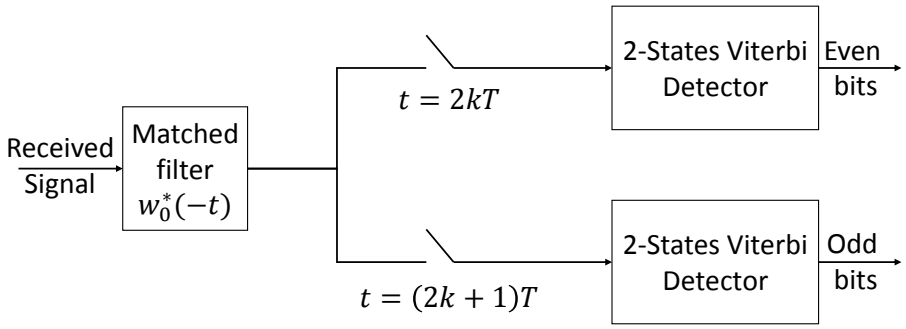

Figure 3.10 – 2x2 states detector for SOQPSK

The complexity reduction can further be performed by taking advantage of the reduced state sequence detection technique, which was first introduced in [86] for PAM and then expanded for CPM in [87]. Since the Viterbi algorithm determines the survivor paths at each merging node of the trellis, the first element of the 2-tuple that defines the branch metric can be replaced by

its decision as follows

$$\sigma_m = (\hat{b}_{m-2}, b_m), \tag{3.44}$$

where $\hat{b}_{m-2}$ is the decision of b_{m-2}. The branch metric becomes

$$\lambda(m) = \begin{cases} b_m \left[Re\{y_0(m)\} - \hat{b}_{m-2} R_{00}(2) \right] & m \text{ even}, \\ b_m \left[Im\{y_0(m)\} - \hat{b}_{m-2} R_{00}(2) \right] & m \text{ odd}. \end{cases} \tag{3.45}$$

Since we deal with a maximization problem, (3.45) leads to the following decision feedback (DF) linear detector

$$\hat{b}_m = \begin{cases} sign\left(Re\{y_0(m)\} - \hat{b}_{m-2} R_{00}(2) \right) & m \text{ even}, \\ sign\left(Im\{y_0(m)\} - \hat{b}_{m-2} R_{00}(2) \right) & m \text{ odd}. \end{cases} \tag{3.46}$$

The even bit sequence and the odd one are estimated separately as explained above and as depicted in Figure 3.11

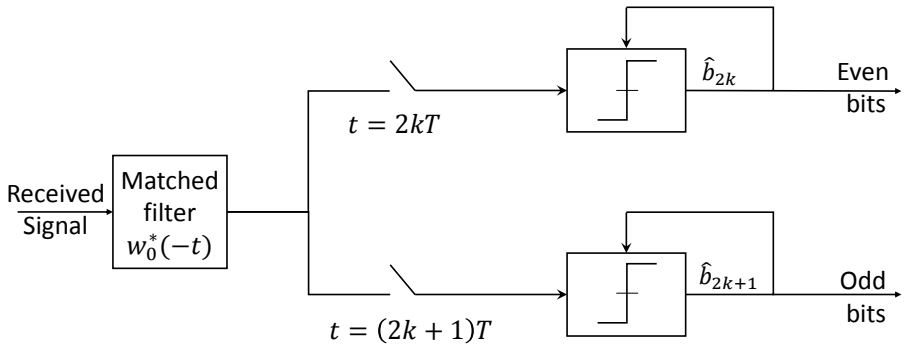

Figure 3.11 – Decision feedback (DF) linear detector for SOQPSK

Case 2: $L_R = 1$

Based on this assumption and following the same steps as in Section 3.3.1, $\lambda(m)$ becomes

$$\lambda(m) = \begin{cases} b_m Re\{y_0(m)\} & m \text{ even}, \\ b_m Im\{y_0(m)\} & m \text{ odd}. \end{cases} \tag{3.47}$$

Given the fact that we deal with a maximization problem, (3.47) leads to the following symbol by symbol detector identical to the one described in Section 3.2.3

$$\hat{b}_m = \begin{cases} sign\left(Re\{y_0(m)\} \right) & m \text{ even}, \\ sign\left(Im\{y_0(m)\} \right) & m \text{ odd}. \end{cases} \tag{3.48}$$

Hence, the fulfillment of the second case proves that the symbol by symbol detector described above is optimal in the MLSE sense. This result is also similar to the one described in [81] for GMSK.

3.3.2 Simulation results

Preliminary results

We begin our simulations with the scenario where the transmitted signal is the first PAM approximation of SOQPSK given in (2.50). Figure 3.12 shows the BER performance of the described detectors in the case where the main pulse of SOQPSK-MIL is used whereas Figure 3.13 illustrates the example where the main pulse of SOQPSK-TG is employed.

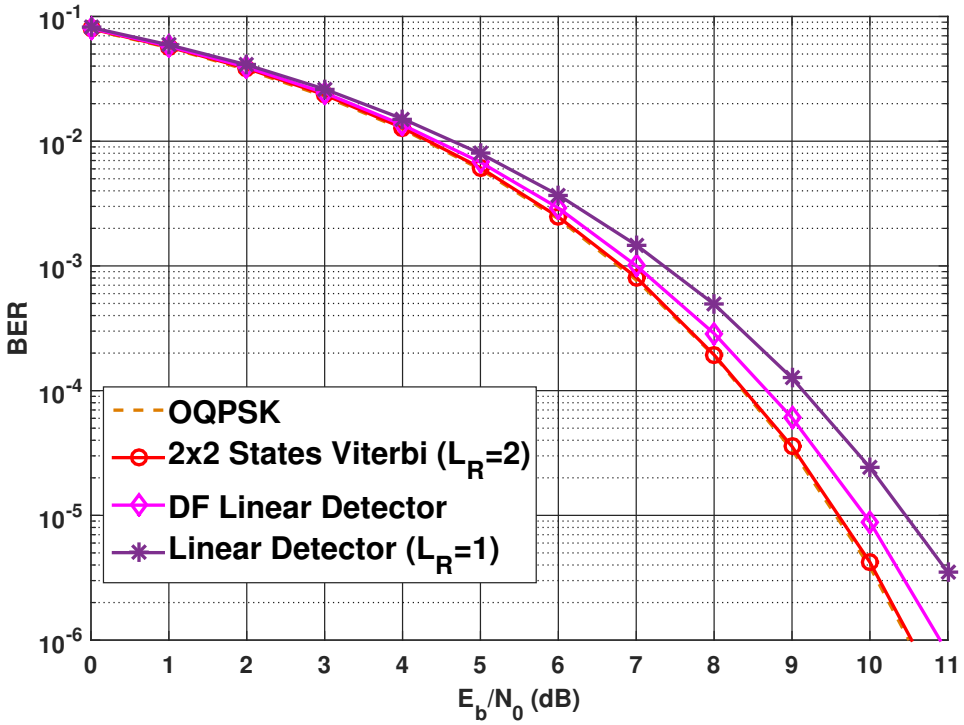

Figure 3.12 – BER performance of the OQPSK-type detectors - transmitted signal: the PAM approximation of SOQPSK-MIL

We can remark from these figures that the 2x2 states detector is optimal since its BER curve coincides with the theoretical bound of OQPSK. Therefore, if there is a BER loss when the transmitted signal is SOQPSK, it would only be due to the presence of the secondary PAM waveforms. We can also see that adding a decision feedback loop to the linear detector improves its performance by 0.5 dB for the case shown in Figure 3.12 and by 1.18 dB for the case of Figure 3.13 at $BER = 10^{-5}$. The performance loss of these linear detectors with respect to the OQPSK curve confirms that they are not optimal in the MLSE sense.

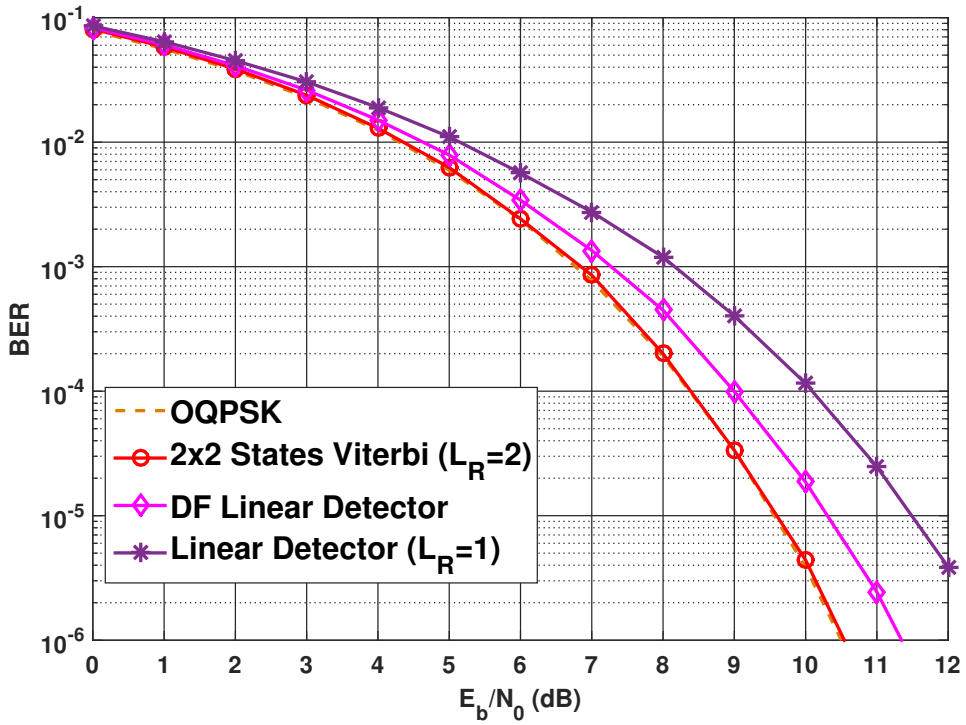

Figure 3.13 – BER performance of the OQPSK-type detectors - transmitted signal: the PAM approximation of SOQPSK-TG

Results for CPM transmission

We now consider the exact CPM definition, and we plot in Figure 3.14 and Figure 3.15 the BER performance of the different detection architectures covered in this section for both SOQPSK versions. We also depict the performance bound of the 2x2 states detector. The latter is determined based on the analysis made in [48], which derives the exact expression of the pairwise error probability for PAM-based CPM detectors in AWGN. Since the detectors presented in this chapter are mismatched ones, i.e., they are not matched to the transmitted signal, the Euclidian distances corresponding to the error events described in Section 3.2.4 are different in our case. For SOQPSK-MIL, the minimum distance becomes 1.676 whereas the highest distance is equal to 2.304. For SOQPSK-TG, the squared distances of the performance bound are clustered around the values given in Table 3.1 and range from 1.254 to 1.785 for the lower distances and from 2.258 to 2.635 for the higher distances. We can notice that the BER curves of the 2x2 states detector are slightly shifted from their optimal receiver curves unlike the first scenario (where we considered the transmitted signal is the PAM approximation). Therefore we can conclude the BER performance loss of this detector is only due to the presence of the remaining PAM waveforms. However, if we only consider the symbol by symbol detector described in Section 3.3.1, we notice that the performance loss is greater than the one introduced by the other detection architectures and it is to due to two factors:

- The PAM approximation since we only keep the main pulse w_0.
- The auto-correlation function of the main pulse w_0 since it does not meet the condition $R_{00}(k) = 0$ for $k \geq 2$.

Thus, it is necessary to mitigate the inter-symbol interference (ISI) introduced by either the pulse $w_1(t)$ (we use a Wiener filter as shown in Section 3.2.1) or by the main pulse $w_0(t)$ itself to reach very near optimal BER performance.

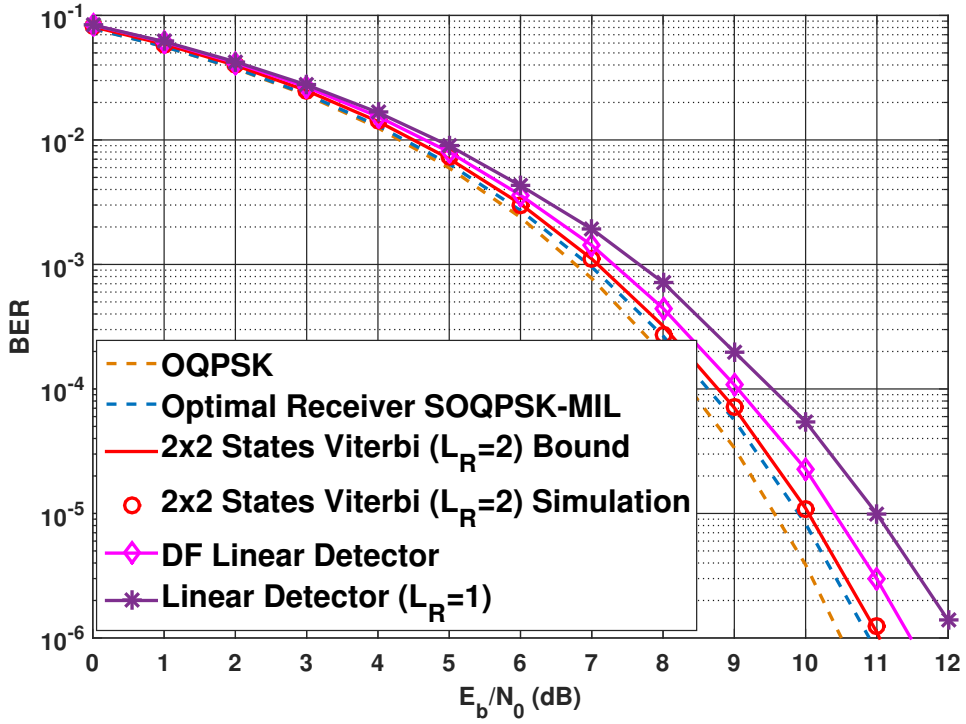

Figure 3.14 – BER performance for SOQPSK-MIL - OQPSK-type detectors

3.4 Least Squares (LS) Approach

3.4.1 Theory

The XTCQM interpretation of Simon [60] and Nelson [62] has been exploited to develop an optimal and a simplified Viterbi detector for SOQPSK-MIL [61]. As for SOQPSK-TG, a near optimal 16 states Viterbi detector has been proposed in [63] by considering the 8-waveform XTCQM approximation. This detector consists of filtering the received signal with a bank of filters matched to the 16 possible in-phase waveforms and the 16 possible quadrature-phase waveforms, then using the sampled matched filters outputs to estimate the bit sequence as

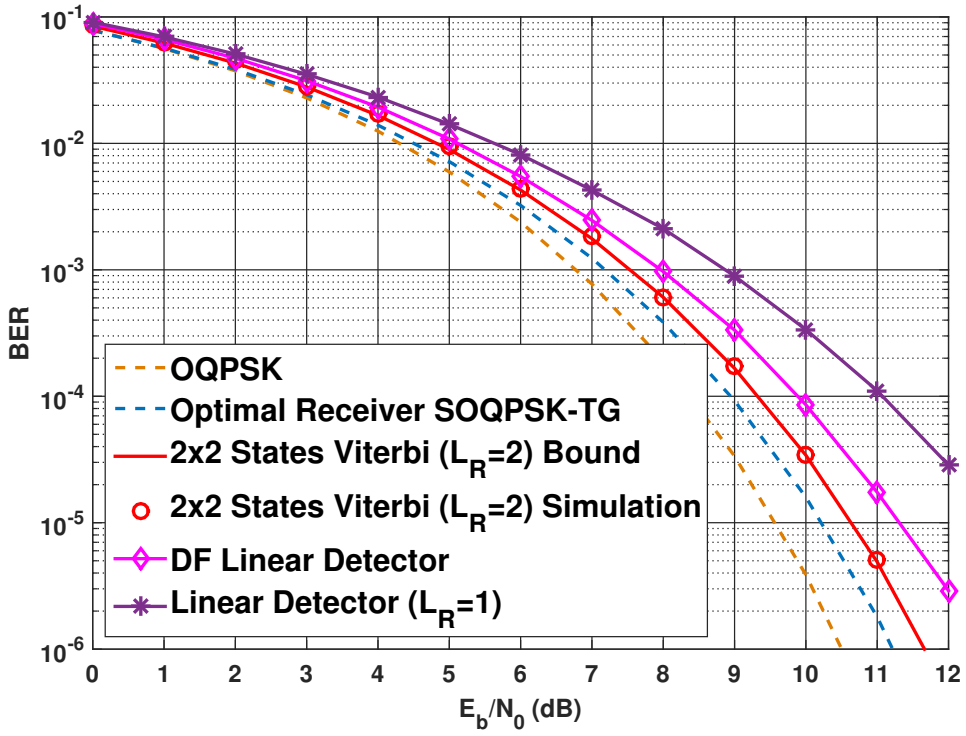

Figure 3.15 – BER performance for SOQPSK-TG - OQPSK-type detectors

highlighted in [63]. In this section, we take advantage of the mapping between the bits and the XTCQM-PAM representation to develop a reduced complexity detector based on the least squares approach [27]. The received signal is first filtered with a detection filter f and sampled at the bit rate T. We then get

$$y_f(m) = \int r(t) f(t - mT) dt. \tag{3.49}$$

The sampled filtered signal $y_f(m)$ can also written as

$$y_f(m) = s_f(m) + n_f(m), \tag{3.50}$$

where

$$s_f(m) = \int s(t; \underline{\alpha}) f(t - mT) dt, \tag{3.51}$$

and

$$n_f(m) = \int n(t) f(t - mT) dt. \tag{3.52}$$

In both Sections 3.2 and 3.3, the log-likelihood function was built on the continuous time domain and under the assumption that the noise $n(t)$ is complex AWGN. However, in this section, we build the log-likelihood function on the discrete time domain and according to the

distribution of $n_f(m)$. Even though $n(t)$ is white, its filtered and T-sampled version $n_f(m)$ is not necessarily a white random process. The "whiteness" of $n_f(m)$ depends on the used detection filter. If we assume that $n_f(m)$ is white, the log-likelihood function can be expressed as

$$\Lambda_f(\underline{b}) = \sum_{m=0}^{N-1} |y_f(m) - s_f(m)|^2. \tag{3.53}$$

In this section, we choose to use the XTCQM-PAM representation of $s(t;\underline{\alpha})$ instead of its CPM definition to model $s_f(m)$. Therefore (3.53) becomes

$$\Lambda_f(\underline{b}) = \sum_{m=0}^{N-1} |y_f(m) - \hat{s}_f(m)|^2, \tag{3.54}$$

$$= \sum_{m=0}^{N-1} \lambda_f(m), \tag{3.55}$$

where $\hat{s}_f(m)$ is a reconstructed version of $s_f(m)$, which represents the convolution of the XTCQM-PAM representation of $s(t;\underline{\alpha})$ and the detection filter. Equation (3.54) defines a least-square detector and is valid if the noise remains white after filtering. The quality of the approximation used to generate $\hat{s}_f(m)$ depends on the XTCQM-PAM approximation of the filtered signal, which is now a function of the filtered versions of the PAM pulses, denoted $\{w_i^f\}_{i\in\{0,1\}}$, instead of the pulses $\{w_i\}_{i\in\{0,1\}}$. If we use the 2048-XTCQM-PAM approximation for instance for the filtered SOQPSK-TG, the branch metric $\lambda_f(m)$ would be defined by the following 11-tuple

$$\sigma_m = (b_{m-9}, b_{m-8}, ..., b_m, b_{m+1})\,. \tag{3.56}$$

The Viterbi algorithm would then be operating with 1024 states. However, if we use the 8-XTCQM-PAM approximation, only 4 states are necessary since the branch metric would be expressed as

$$\lambda_f(m) = \begin{cases} \left| y_f(m) - \left(b_m w_0^f(0) - b_{m-1}b_m b_{m+1} w_1^f(0) + j(b_{m-1} + b_{m+1}) w_0^f(T) \right) \right|^2, & m \text{ even}, \\ \left| y_f(m) - \left(j b_m w_0^f(0) - j b_{m-1}b_m b_{m+1} w_1^f(0) + (b_{m-1} + b_{m+1}) w_0^f(T) \right) \right|^2, & m \text{ odd}. \end{cases} \tag{3.57}$$

We call this detector the 8-XTCQM-PAM detector. If we want to consider that SOQPSK is a linear PAM, we can simply assume that $w_1(0) = 0$. If we generate $\hat{s}_f(m)$ by considering the

2-XTCQM-PAM approximation, we get the following branch metric expression

$$\lambda_f(m) = \begin{cases} \left| y_f(m) - b_m w_0^f(0) \right|^2, & m \text{ even}, \\ \\ \left| y_f(m) - j b_m w_0^f(0) \right|^2, & m \text{ odd}. \end{cases} \tag{3.58}$$

We can notice from (3.58) that the branch metrics do not depend on the second pulse w_1 and therefore, this detector can no longer mitigate the presence of w_1. After converting the log-likelihood function to a maximization problem, developing the quadratic distance and discarding the terms that do not depend on $\underline{b}$, we get the following symbol-by-symbol detector

$$\hat{b}_m = \begin{cases} sign(Re\{y_f(m)\}), & m \text{ even}, \\ sign(Im\{y_f(m)\}), & m \text{ odd}. \end{cases} \tag{3.59}$$

We can notice that this detector is similar to the one introduced in (3.41); the only difference is that the filter f is not matched to the main pulse $w_0(t)$. That explains why it is possible to use different detection filters (see [17] for some examples of detection filters) other than $w_0(t)$ to detect the bit sequence. This detector is labeled the 2-XTCQM-PAM detector in this manuscript.

3.4.2 Simulation results

Preliminary results: Choice of the detection filter

The choice of a suitable detection filter is a challenging task for SOQPSK because the straightforward solution, which is the main pulse $w_0(t)$, generates colored noise. Therefore, it is necessary to find an alternative solution, either by introducing a whitening filter or a Wiener filter like it has been done in Section 3.2.1 or by investigating other detection filters like in [17] for the I&D detectors. A suitable detection filter in our case should satisfy the following constraints:

- It has to be at least of length $2T$ so that it does not corrupt the useful bandwidth of the signal.
- It does not correlate the noise too much unlike the matched filter based on the main pulse $w_0(t)$.
- It does not greatly expand the XTCQM-PAM representation described in Section 2.4: if the 8-XTCQM-PAM is accurate enough for the unfiltered signal, it does not necessarily remain accurate for the filtered signal. Thus we need to employ the 32-XTCQM-PAM representation (or more) instead. This is due to the convolution effect.

- It is not very lengthy so that the complexity remains low.

To evaluate the satisfaction of these criteria for a given detection filter, we consider that SOQPSK-TG is a PAM whose pulse shape is $w_0(t)$ and we plot the BER performance of the 4-states 8-XTCQM-PAM detector. The branch metric of this detector is given in (3.57), however, we consider that $w_1(0) = 0$. Ideally, if the first three constraints are met for a given detection filter, the BER performance of the detector associated with it would coincide with the optimal OQPSK BER curve. We perform this test on three detection filters given in Figure 3.16: the first one is the main pulse of SOQPSK-TG; the second one is a combined filter $\tilde{w}_0$ composed of the main pulse followed by a Wiener filter as described in (3.28) (however this filter is slightly different from the one shown in Figure 3.6 because we considered here that $w_1(t) = 0$ when computing the Wiener coefficients C_k^{WF}) and the third one is a truncated Equiripple FIR of length $4T$.

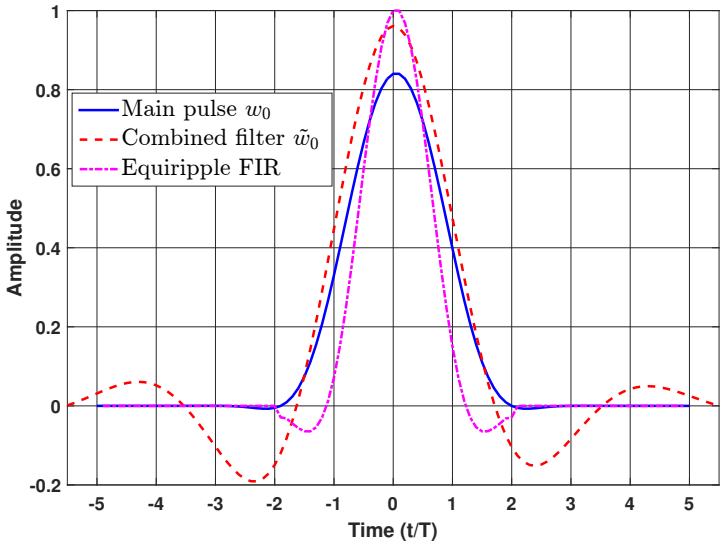

Figure 3.16 – Detection filter

The BER curve depicted in Figure 3.17 shows that the Equiripple FIR filter seems to be an excellent candidate since its BER performance curve is very close to the optimal one while using the 8-XTCQM-PAM detector. This shows that the filtered and T-sampled noise nearly remains white and that the 8-XTCQM-PAM representation of the filtered signal is very accurate. The combined filter $\tilde{w}_0$ is also an excellent candidate compared to the main pulse based detector. The degraded performance of the latter is due to:

- The inaccuracy of the 8-XTCQM-PAM representation of the filtered signal. Thus it is necessary to use the 32-XTCQM-PAM representation as shown in Figure 3.18. As a consequence, that increases the number of states of the Viterbi algorithm from 4 to 16.

- The noise correlation that shifts the BER curve by almost 0.5 dB.

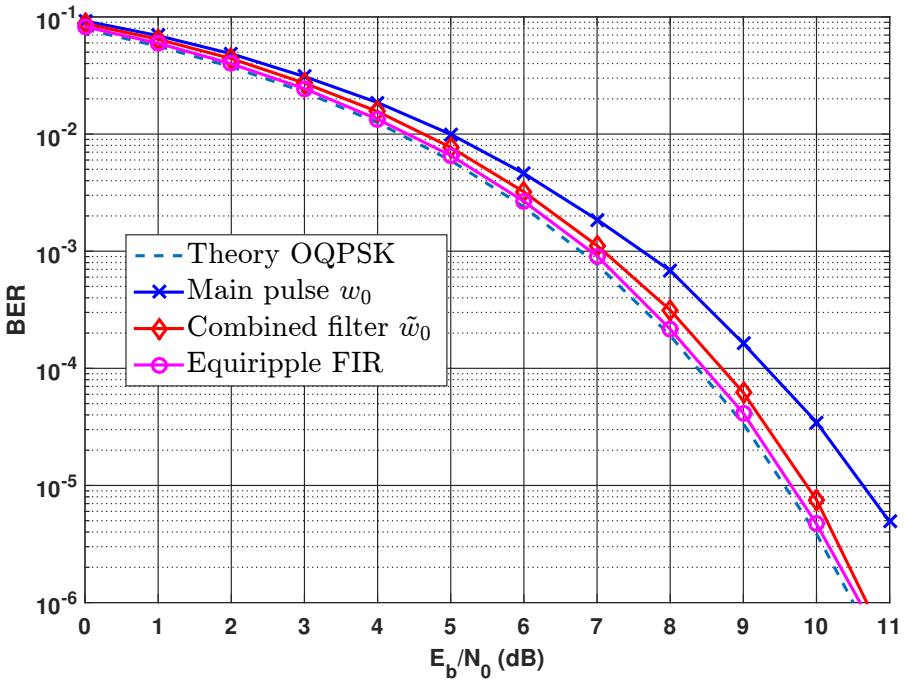

Figure 3.17 – BER performance of the 8-XTCQM-PAM detector using different detection filters - transmitted signal: SOQPSK-TG PAM approximation using 1 main pulse

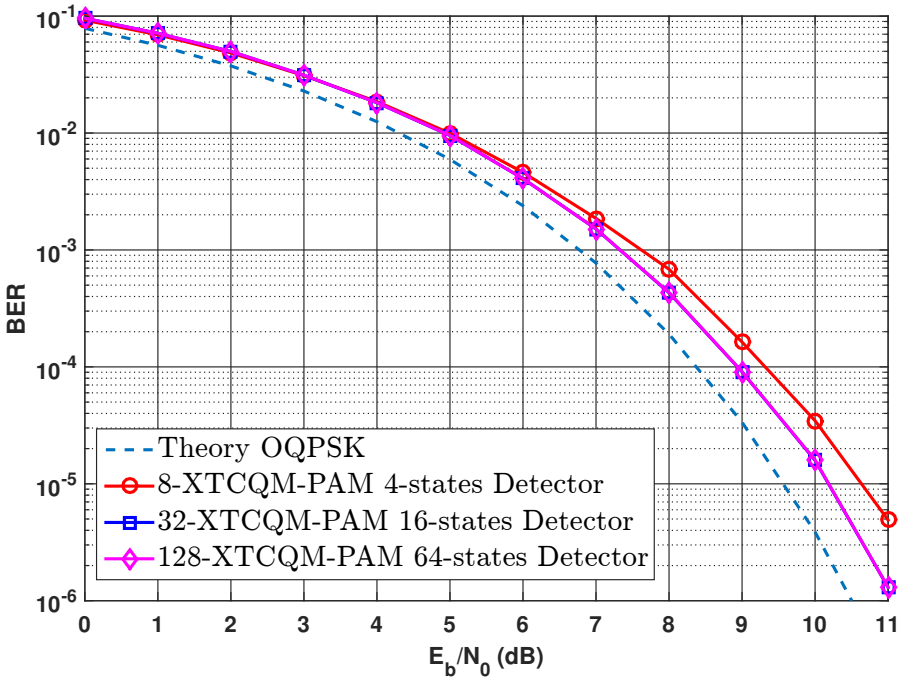

Figure 3.18 – BER performance of the XTCQM-PAM detectors using the main pulse as detection filter - transmitted signal: SOQPSK-TG PAM approximation using 1 main pulse

Results for CPM transmission

We now consider the exact CPM definition of SOQPSK, and we plot in Figure 3.19 and Figure 3.20 the BER performance of the different detection architectures covered in this section for both SOQPSK versions. We use the Equiripple FIR as a detection a filter. Distinguishing the cases where $w_1^f(0) = 0$ or not is essential because in the first case the receiver assumes that SOQPSK-TG is a simple pulse amplitude modulation whereas in the second case the receiver considers that SOQPSK-TG is a sum of two linear modulations. It can be seen that the performance loss between the two assumptions is impalpable for SOQPSK-MIL and very low for SOQPSK-TG.

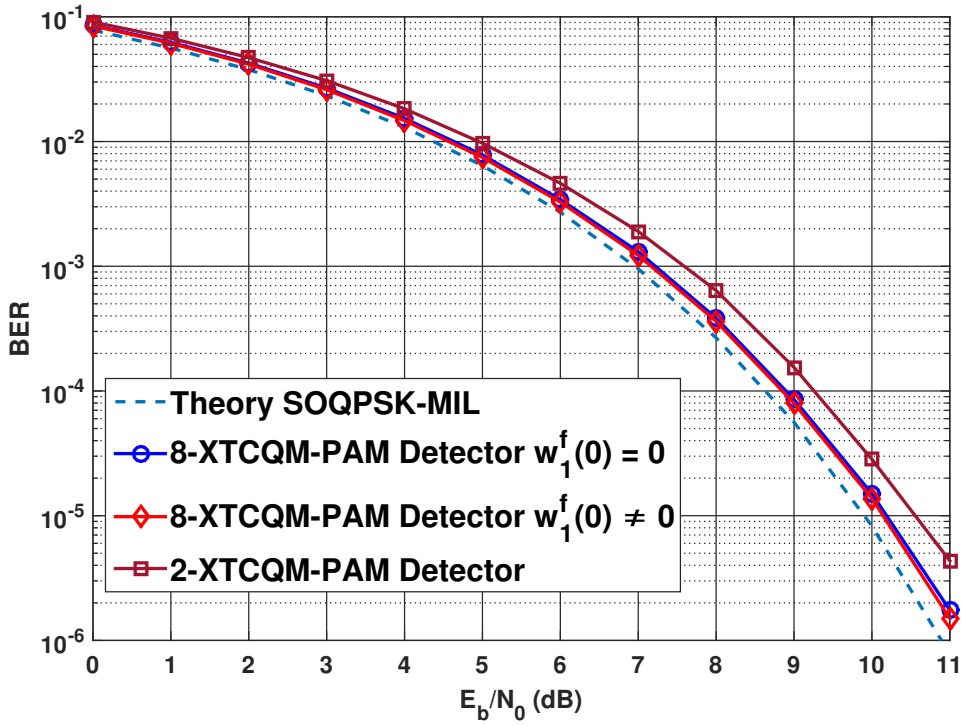

Figure 3.19 – BER performance for SOQPSK-MIL - XTCQM-PAM detector

3.5 Complexity comparison

In this section, we compare the complexity of all the aforementioned detectors. The complexity can be evaluated by giving the number of the real-valued detection filters of length T and the number of states of each detector. This method is inspired from [63] and can be seen as equivalent as computing the number of operations because the latter increase linearly with the number of matched filters of length T and exponentially with the number of states. The complexity/performance comparison of the Viterbi detectors is summarized in both Tables 3.2 and 3.4 for SOQPSK-MIL and SOQPSK-TG, respectively. The complexity/performance

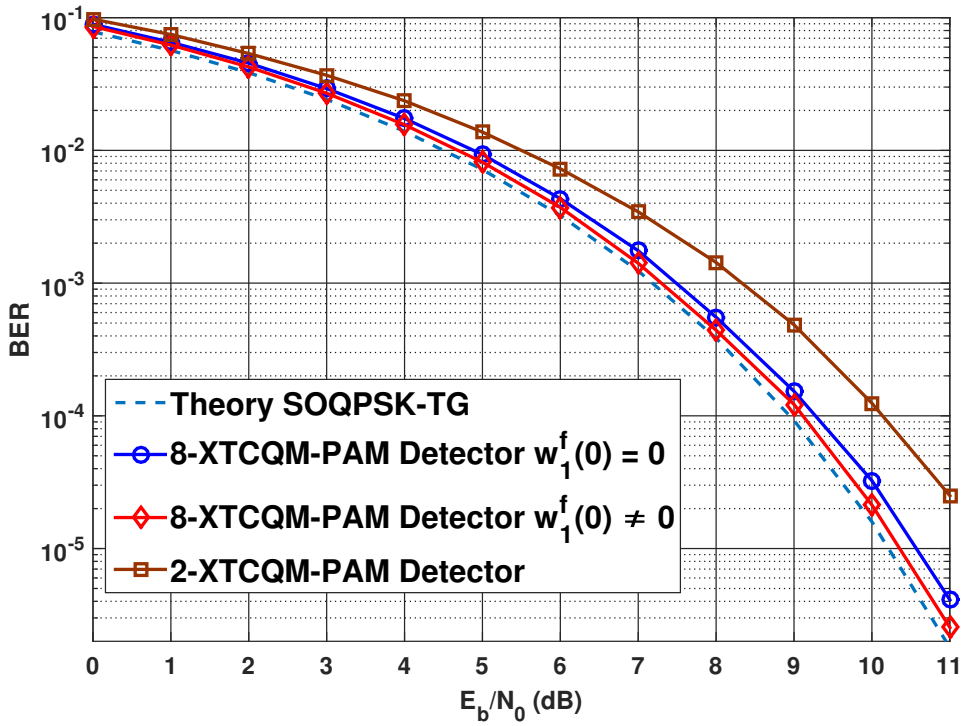

Figure 3.20 – BER performance for SOQPSK-TG PAM approximation - XTCQM-PAM detector

comparison of the linear detectors is given in Table 3.3 and Table 3.5. The length of the detection filters has been optimized as explained in Section 3.2.2. We begin our evaluation with SOQPSK-MIL: it can be seen that the BER performance and complexity of the proposed Viterbi detectors are close to each other. Moreover, considering that SOQPSK-MIL as a linear modulation (i.e., $w_1(t) = 0$) does not significantly affect the BER performance. As for linear filters, the best linear filters in respect of performance/complexity trade-off are the $\tilde{w}_0$ filter and the linear decision feedback detector. These comments are also valid for SOQPSK-TG. The only difference is that BER performance loss is more perceptible due to the approximations that are used to build each detector.

Table 3.2 – Performance/Complexity evaluation of the Viterbi detectors - SOQPSK-MIL

	Kaleh Based Detector	2x2 States Detector	8-XTCQM-PAM Detector $w_1(0) \neq 0$	8-XTCQM-PAM Detector $w_1(0) = 0$
Length-T detection filters	4	3	4	4
Number of states	4	4	4	4
$\frac{E_b}{N_0}$ Performance loss w.r.t optimal (dB)	0	0.14	0.15	0.16

Table 3.3 – Performance/Complexity evaluation of the linear detectors - SOQPSK-MIL

	Detection filter: w_0	Detection filter: $\tilde{w}_0$	Decision feedback: detector	Detection filter: Equiripple FIR
Length-T detection filters	3	10	3	4
$\frac{E_b}{N_0}$ Performance loss w.r.t optimal (dB)	1.1	0.2	0.5	0.65

Table 3.4 – Performance/Complexity evaluation of the Viterbi detectors - SOQPSK-TG

	Kaleh Based Detector	2x2 States Detector	8-XTCQM-PAM Detector $w_1(0) \neq 0$	8-XTCQM-PAM Detector $w_1(0) = 0$
Length-T detection filters	6	4	4	4
Number of states	4	4	4	4
$\frac{E_b}{N_0}$ Performance loss w.r.t optimal (dB)	0.1	0.42	0.12	0.42

Table 3.5 – Performance/Complexity evaluation of the linear detectors - SOQPSK-TG

	Detection filter: w_0	Detection filter: $\tilde{w}_0$	Decision feedback: detector	Detection filter: Equiripple FIR
Length-T detection filters	4	10	4	4
$\frac{E_b}{N_0}$ Performance loss w.r.t optimal (dB)	2.32	0.72	1.08	1.23

3.6 Conclusion

In this chapter, we proposed a wide range of reduced complexity detectors based on the revamped PAM decomposition of SOQPSK. We first adopted Kaleh approach; then we showed that other detection algorithms could be obtained using the Ungerboeck approach (OQPSK-type detectors) and Forney approach (XTCQM-PAM LS detectors). What is interesting with the OQPSK-type and XTCQM-PAM based detectors is that they can be built on the assumption that SOQPSK is a linear PAM at the receiver side. This result proves that the developed architectures in the literature for PAM can also be applied for SOQPSK and therefore we can generally "forget about" the particular CPM nature of this modulation thanks to the revamped PAM decomposition. In all the aforementioned simulations, we assumed that the receiver only captures one line of sight signal and that the channel does not vary in time. In the next chapter, we consider the presence of multipath channel, and we develop channel estimation techniques for SOQPSK.

Chapter 4

Interference Mitigation in Frequency Selective Time Varying Aeronautical Telemetry Channels

Contents

4.1 Introduction

In the previous chapter, we focused on demodulating SOQPSK-TG in the presence of AWGN without considering fading effects, introduced by the aeronautical multipath channel during the different phases of the flight. Nevertheless, if we have a look at the different channel soundings given in [88, 89, 11], we can notice that the receiving antenna can capture several copies of the transmitted signal when the aircraft is at the apron (the area where the aircraft is parked) due to multipath propagation at the airport buildings. Also, since the speed of the aircraft is increasing on the runway during take-off (or decreasing during landing) while remaining in a multipath environment, it results in an important Doppler spread. These phenomena, if not mitigated, can cause severe performance loss.

The literature regarding channel estimation and equalization is extensive for linear modulations, and it can mainly be classified according to (i) which domain the formalism is done (time domain or frequency domain) (ii) how much knowledge of the transmission link the receiver is given. However, when it comes to CPM, these techniques cannot directly be applied because of the non-linear nature of such modulation. The non-linear property prevents us from writing the received signal as a convolution of the transmitted symbols and a transversal filter that models the channel. Thus it makes handling multipath mitigation less mathematically tractable. Nevertheless, the constant complex envelope nature of the CPM has promoted the use of the constant modulus algorithm (CMA) as a solution to equalize the channel [90]. However, despite its low complexity, this solution is not robust enough in the presence of time-variant fading channels.

In this chapter, we first make a classification of the existing aeronautical telemetry channels based on what approach was taken to model multipath and Doppler spread. We then present the CMA solution and its main variants for SOQPSK, and we tackle the channel estimation problem by taking advantage of the PAM decomposition of SOQPSK. We focus on time domain channel estimation due to the absence of cyclic prefixes (CP) or unique words (UW) in the IRIG recommendations [5], which makes the frequency domain equalization techniques introduced in [91, 92, 93, 94] unsuitable since the channel matrix is not always circular. We exploit one of the essential properties of the PAM decomposition of SOQPSK-TG presented Chapter 2, that is the signal can be approximated as a simple linear modulation since $97,6\%$ of the signal energy is contained in one pulse. We then adapt the per-survivor processing (PSP) technique initially developed in [28] to jointly estimate the channel and the symbols of the received signal. We then evaluate the performance of the proposed solution over different air-to-ground telemetry channels.

4.2 Aeronautical Telemetry Channel Models

Different channel sounding experiments have been conducted to model the aeronautical telemetry channel in several environments, and for different scenarios. These experiments use different techniques and different modulations (BPSK [11, 95, 96], chirp modulation [89], COFDM [88]...). We summarize in the following the main models of the literature for aeronautical telemetry, and we give the channel parameters that are used in this work to evaluate the performance of the interference mitigation techniques.

4.2.1 Time-invariant wide-band channel model

In most works [11, 95, 19, 96], the aeronautical telemetry channel is modeled as a time-invariant wide-band channel since it is considered that the signal bandwidth is in the order or larger than the coherence bandwidth of the channel. If we take as an example the channel soundings given in [11], the signal bandwidth ($\approx$ 20 MHz) is higher than the coherence bandwidth ($\approx$ 13.5 Mhz). In this case, the channel is frequency selective and can be modeled as a linear, time-invariant system whose baseband impulse response is [11]

$$l(t) = \sum_{k=0}^{L_p-1} A_k \exp\{-j2\pi f_c \tau_k\} \delta(t-\tau_k), \tag{4.1}$$

where A_k and τ_k are the complex gain and the propagation delay of the kth path, respectively and $\delta(t)$ is the Dirac function. The parameter f_c is the carrier frequency. It has been shown in [11, 95] that an accurate model for multipath in different en-route scenarios is composed of three paths (i.e., $L_p = 3$). The gains and delays of these paths depend on the flight phase, its environment (over water or terrestrial), its altitude (high or low), etc. In this work, we use a three-ray propagation model introduced in [97] which summarizes those scenarios. We take $f_c = 2,2$ GHz as a carrier frequency in the lower S-band for this model, and we give in Table 4.1 the path gains and delays. The bandwidth coherence of this channel equals 8.6 MHz. Therefore, to keep the wide-band assumption valid, we can use bit rates approximately starting from 10 Megabits per second (Mbps) for SOQPSK-TG.

Table 4.1 – Time-invariant wide-band channel parameters of the three-ray propagation model

Path number	0	1	2
Path delay (μs)	0	0.1	0.8
Path gain (dB)	0	-3	-15

4.2.2 Time-variant wide-band channel model

The time-variant wide-band channel model has been introduced in [89] and takes into account the Doppler spread effect, which appears as a result of the presence of the Doppler shifts of the multipath components and represents the spread of the Doppler spectrum. The channel sounding experiments were performed at the Airbus Saint-Martin airport (SMA) and were done in the C-band. Under the assumption that the channel is wide sense stationary uncorrelated scattering (WSSUS) [98], the channel model thus becomes

$$l(t) = \sum_{k=0}^{L_p-1} A_k \exp\{-j2\pi f_c \tau_k\} \exp\left\{j2\pi f_k^d t\right\} \delta(t-\tau_k), \tag{4.2}$$

where f_k^d is the Doppler shift associated with the kth path. Three typical channel characteristics are described in [89] that depict the take-off/landing situation, the en-route situation and the apron/taxiing one. In this work, we choose to take the taxiing profile to illustrate the time-variant wide-band channel model. The channel parameters are given in Table 4.2 and they show high delay spread (20 μs) due to the important multipath propagation at the Saint-Martin airport (SMA) buildings. However, the Doppler spread is low due to the low aircraft velocity. The line of sight component is highlighted in bold in Table 4.2. For this channel the measured delay spread is 20 μs, thus we take a symbol time of 1 μs for SOQPSK-TG.

Table 4.2 – Time-variant wide-band channel parameters of the taxiing scenario - SMA

Path number	0	1	2	3	4	**5**	6	7	8	9	10	11	12	13	14	15
Path delay (μs)	0	0.14	0.34	0.50	0.56	**0.64**	0.76	0.82	0.90	1.02	1.12	1.42	1.56	2.92	9.16	10.40
Path gain (dB)	−5.07	−9.55	−8.83	−4.42	−16.99	**0**	−0.94	−1.87	−2.51	−2.46	−7.75	−9.24	−10.76	−9.17	−8.63	−10.27
Doppler shift (Hz)	0	0	0	0	0	**0**	0	47.68	47.68	47.68	47.68	47.68	47.68	0	47.68	47.68

4.2.3 Narrow-band channel model

Few works consider the aeronautical telemetry as a narrow-band one [88, 99], which reflects the situation where the signal bandwidth is much smaller than the coherence bandwidth of multipath channel [64]. In this case, the multipath components are represented with probabilistic models since they are not resolvable. The most common used distributions for modeling the narro-wband fadings are the Rayleigh distribution and the Rice distribution. In the first case, the channel $l(t)$ can be seen as a sum of L_p independent complex random multipath components (each one of them has a certain mean and a certain variance). Hence, as a consequence of the central limit theorem, $l(t)$ is a complex Gaussian process whose magnitude $|l(t)|$ is driven by the following Rayleigh distribution [100]:

$$p(r) = \frac{r}{\sigma_l^2} \exp\left\{-\frac{r^2}{2\sigma_l^2}\right\}, \tag{4.3}$$

where r is a positive real value and σ_l^2 is the variance of the channel. This model describes a non-line of sight (NLOS) situation, which means that the signal that is originally sent from the transmitting antenna can partially be obstructed by a physical object like shown in Figure 4.1. This situation can occur when we deal with cellular networks and thus the fading follows a Rayleigh distribution [101]. If we consider the presence of a line of sight (LOS) component, namely $l_0(t)$, then the magnitude of the overall channel $|l_0(t) + l(t)|$ follows a Rice distribution [100, 102] of probability density function $p_{\text{Rice}}(r)$:

$$p_{\text{Rice}}(r) = \frac{r}{\sigma_l^2} \exp\left\{-\frac{r^2 + (\sigma_l^0)^2}{2\sigma_l^2}\right\} I_0\left(\frac{r\sigma_l^0}{\sigma_l^2}\right), \qquad r \geq 0, \tag{4.4}$$

where $I_0(.)$ is the modified Bessel function of the first kind with order zero and $(\sigma_l^0)^2$ is the variance of the LOS component. The Rice distribution is especially characterized with the K-factor, which reflects the ratio between the power of the LOS path and the remaining NLOS ones, i.e.,

$$K = \frac{(\sigma_l^0)^2}{\sigma_l^2}. \tag{4.5}$$

When $K \to 0$, we go back to the Rayleigh case given in (4.3) and when $K \to \infty$, the channel becomes close to the AWGN case with specular interference. The Rice fading model is commonly used to model land mobile satellite channel fadings [103], as well as vehicle to vehicle (V2V) channels [104]. Furthermore, this model can reflect an aeronautical telemetry channel as emphasized in [88, 99]. In this work, we choose to take two channel configurations that have been measured by Zodiac Data Systems at Toulouse-Blagnac airport (TBA) in the C-band (5.135 GHz) [88]. During the sounding experiments, two antennas are installed to ensure a permanent data link availability: one at the nose of the aircraft and one at the tail.

The first setting is given in Table 4.3, and it describes the apron/taxiing scenario, i.e., when the aircraft is moving from the apron to the taxiway, and the second one depicts the case where the aircraft is on the runway (Table 4.4). In the apron/taxiing situation, the aircraft has low velocity and hence low Doppler spread. However, it is surrounded by buildings and other vehicles, which explains the presence of short-time and relatively high magnitude reflections. The K-factor is estimated around 13.02 dB, which is higher than the K-factor assumed in [105] for Tokyo airport. When the aircraft is on the runway, we notice the presence of one short echo with -3 dB attenuation because both nose and tail antennas are visible by the ground antenna. Moreover, due to the airport's configuration, long echoes with very low magnitudes have also been observed. In addition to this, the measured maximum Doppler spread for this scenario is around 400 Hz.

For these two channels mentioned above, we use a bit rate of 1 Mbps because the bit rate range for Tier 1 modulations shall be between 1 Mbps and 20 Mbps as claimed in the IRIG

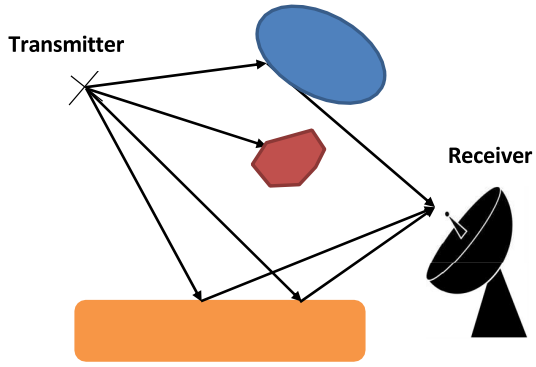

Figure 4.1 – NLOS Situation

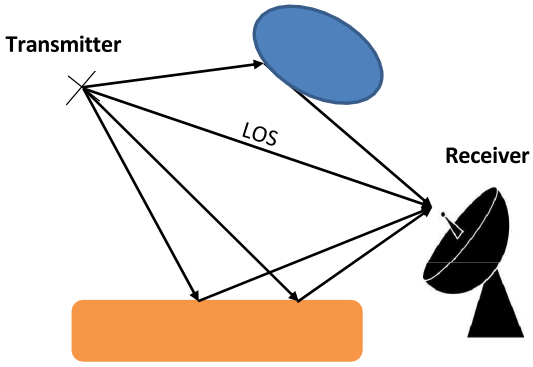

Figure 4.2 – LOS Situation

recommendations [5]. Moreover, if we choose a higher bit rate (for example 10 Mbps or 15), we do no longer respect the narrow-band channel assumption since the coherence bandwidth of both apron/taxiway and the runway channels are in the order of few MHz. This also explains why the wide-band channel models are the most used ones.

Table 4.3 – Narrow-band channel parameters of the apron/taxiing scenario - TBA

Path number	0	1	2	3
Path delay (μs)	0	0.7	1.7	4
Average path gain (dB)	0	-3	-10	-15
K-factor (Linear)	20	0	0	0
Maximum Doppler spread (Hz)	50			

Table 4.4 – Narrow-band channel parameters of the runway scenario - TBA

Path number	0	1	2	3	4
Path delay (μs)	0	0.8	4	8	12
Average path gain (dB)	0	-3	-10	-25	-35
K-factor (Linear)	50	0	0	0	0
Maximum Doppler spread (Hz)	400				

All the aforementioned channel models and configurations show that the receiving antenna captures multiple echoes with different delays and attenuations during the phases of a flight. Therefore, it is necessary to introduce multipath mitigation algorithms at the receiver to get an acceptable BER performance. We present in the following the "legacy" multipath mitigation technique that is used for SOQPSK, which is the constant modulus algorithm (CMA), and its variants. We then propose a joint channel estimation and symbol detection scheme based on the persurvivor processing (PSP) principle and the PAM decomposition.

4.3 The Constant Modulus (CM) Algorithm

4.3.1 Principle

The CM algorithm (CMA) is the classic time domain equalizer that is used for SOQPSK [20]. It is a blind equalizer, i.e., it works without introducing a training sequence, and it has been initially developed for linear modulations of independent and identically distributed (i.i.d) symbol sequences. Its use for SOQPSK is justified because of the constant modulus nature of this modulation. If we assume that the transmitted signal is corrupted by a multipath channel $l(t)$ and by an AWGN $n(t)$, then the received signal is expressed as

$$r(t) = s(t;\underline{\alpha}) * l(t) + n(t), \tag{4.6}$$

where the operator $*$ stands for the convolution. We consider that the received signal is sampled at the sampling period T_s and then passed through an equalizer $(g_k)_{k\in\mathbb{Z}}$. The equalized signal is expressed as

$$z(n) = \sum_i g_i r(n-i), \tag{4.7}$$

where $r(n) = r(t = nT_s)$. The coefficients of the equalizer $\underline{g} = (g_k)_{k\in\mathbb{Z}}$ are chosen to minimize the constant modulus cost function

$$J_{T_s}(\underline{g}) = E\left\{(|z(n)|^2 - 1)^2\right\}. \tag{4.8}$$

Even though using the CMA seems to be a natural choice for CPM in general and for SOQPSK in particular, it is important to mention that the behavior of this equalizer is different from the case where linear modulations are employed. In fact, it has been shown in [106, 107, 108] that when the symbol sequence is i.i.d and under some technical assumptions, the CMA allows to successfully cancel the inter-symbol interference for linear modulations since the minimization of the CM criterion converges towards a delayed and a rotated version of the transmitted symbol sequence. However, it is not always the case for binary CPM as highlighted in [109, 110]. Bianchi's work shows that the minimization of the CM criterion can lead to undesirable solutions in addition to desirable ones in the case where $T_s = T$ and where $\frac{T_s}{T}$ is rational or irrational. The desirable solution here is a delayed and a rotated version of the transmitted signal. The full characterization of theses solutions is found in [110] for full response binary CPM and in [109] for partial response binary CPM with a modulation index $h \neq \frac{1}{2}$. However, the set of solutions for the case where $h = \frac{1}{2}$ and $L > 1$ has not been identified. Since SOQPSK can be seen as a partial response binary CPM with a modulation index $h = 1/2$ as highlighted in Chapter 2, the behavior of the CMA is not analytically identified when paired

with this modulation. Therefore, we make the assumption that the CM criterion may converge towards a rotated and a delayed version of SOQPSK.

4.3.2 Description of the algorithm

The implementation of CMA has been thoroughly studied in the literature [90, 111, 112, 113, 114, 115], and can be distinguished by the way the defined cost function of (4.8) is approximated and by the way the equalizer coefficients are updated. The first version of CMA is known as the stochastic gradient CMA [90], and it operates by dropping the expectation operator in (4.8). It works in a recursive or a "sample-by-sample" way, and at each epoch, the equalizer coefficients are updated using the steepest descent gradient method. However, this technique converges slowly and it is very sensitive to the choice of the step size. Other sample-by-sample versions of CMA are proposed in [113, 114] that rely on the recursive least squares (RLS) principle to update $(g_k)_{k\in\mathbb{Z}}$ under the assumption of slowly varying environments. In this work, we describe the block version of CMA, which consists of approximating the expectation given in (4.8) with a mean of N_w elements as follows [112]

$$J_{T/2}(\underline{g}) = \frac{1}{N_w}\sum_{n=0}^{N_w-1}\Big(|z(n)|^2-1\Big)^2, \tag{4.9}$$

where z is the equalized signal sampled at twice the bit rate (i.e. $T_s = \frac{T}{2}$). If we suppose that the filter $\underline{g} = [g_0, ..., g_{N_g-1}]$ is composed of N_g taps, the equalized signal can be written as

$$z(n) = \underline{g}^{\mathcal{T}}\underline{r}_n, \tag{4.10}$$

where $(.)^{\mathcal{T}}$ is the transpose operator and $\underline{r}_n = [r(n-N_g+1), ..., r(n)]$. The algorithm can be iterative: at each iteration i, the received signal $r(n)$ is filtered with $\underline{g}^i$, then the equalizer coefficients are updated as follows

$$\underline{g}^{i+1} = \underline{g}^i - \frac{\mu}{\left\|\nabla J_T(\underline{g}^i)\right\|}\nabla J_T(\underline{g}^i) \tag{4.11}$$

where μ is the step size, $\|.\|$ the Euclidean norm and $\nabla J_T(\underline{g}^i) = \left[\nabla J_T(g_0^i), ..., \nabla J_T(g_{N_g-1}^i)\right]$ such that

$$\nabla J_T(g_k^i) = \frac{4}{N_w}\sum_{n=0}^{N_w-1}\Big(|z(n)|^2-1\Big)z(n)\Big)\, r(n-k)^*, \qquad k\in\{0,...,N_g-1\}. \tag{4.12}$$

In (4.11), we considered a search direction of $\nabla J_T(\underline{g}^i)/\left\|\nabla J_T(\underline{g}^i)\right\|$ instead of the non normalized one to increase the convergence speed. This update rule is not the only one, others can be found in [111, 116]. As for the step size μ, it can be fixed beforehand or it can be optimally

computed at each iteration as as shown in [115]. Once N_{it} are reached for a given block, the filter $\underline{g}^{N_{it}}$ is used to initialize the filter $\underline{g}^{1}$ of the upcoming block.

4.3.3 Preliminary simulation results for CMA

In this section, we evaluate the performance of some of the aforementioned CMA schemes. We choose three version: the initial sample-by-sample (SxS) CMA [90], the RLS CMA [113] and the iterative block CMA described in Section 4.3.2. All the algorithms work with a sampling time $T_s = \frac{T}{2}$ and with $N_g = 64$ taps. We take a window size $N_w = 400$ and $N_{it} = 50$ for the block CMA. The step size $\mu = 5.10^{-3}$ and the filters are initialized with double center taps. As for RLS CMA, the forgetting factor is chosen either 0.99 or 0.9999 and the inverse covariance matrix is initialized at the identity. The received signal is corrupted by AWGN with 30-dB signal to noise ratio (SNR).

We take as a performance metric the mean square error (MSE) between the instantaneous frequency Ω_z of the equalized signal and the instantaneous frequency Ω_s of the transmitted signal. We remind that the definition of the instantaneous frequency is given in (1.7). We choose to take this metric because of the following reasons: in Section 4.3.1, we assumed that the equalizer can converge towards a delayed and a rotated version of the transmitted signal. Thus, under this assumption, the equalized signal is also a CPM whose data symbols are encapsulated in Ω_z. Since we are interested in recovering the transmitted symbols contained in Ω_s, evaluating the error at the instantaneous frequency level gives us pertinent information regarding the quality of the equalizer. Moreover, the equalized signal $z(n)$ has a constant unknown phase ambiguity. Therefore, by taking the proposed performance metric, the presence of this phase ambiguity does not affect the values of the computed MSE since Ω_z is the differential phase of $z(n)$.

We plot in Figure 4.3, Figure 4.4 and Figure 4.5 the MSE values in the presence of the channels described in Table 4.1, Table 4.2 and Table 4.3, respectively. Each marker in the figures represents the average MSE value of 2000 samples and over 100 channel, source and noise realizations. It can be seen from the figures that the behavior of the different versions of CMA depends on the chosen channel model. If we take for instance Figure 4.3, we can see that the performance of the three variants is almost similar and that the RLS CMA has the lowest MSE values. However, this observation is no longer valid in Figure 4.5: the block CMA outperforms the other CMA versions and the MSE curves are more tangible. Figure 4.4 shows that the three CMA versions suffer from MSE fluctuations due to the change of statistics of the channel in the taxiing scenario.

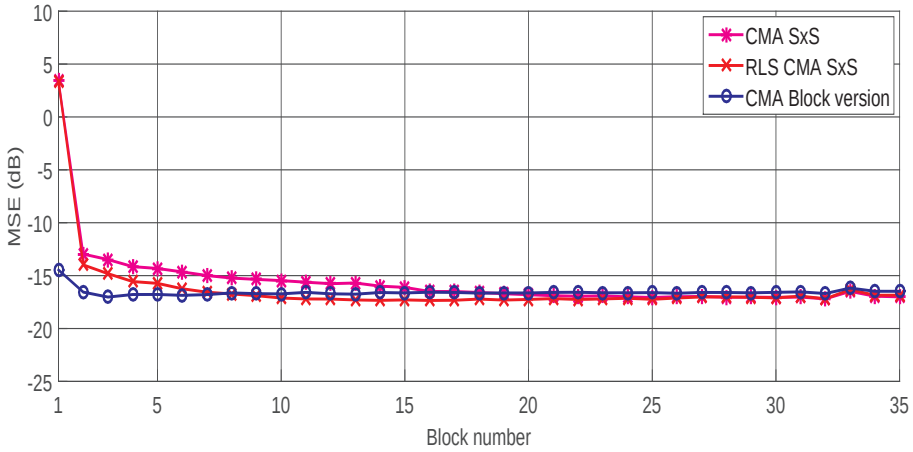

Figure 4.3 – MSE values of different CMA variants - Three-ray wide-band channel

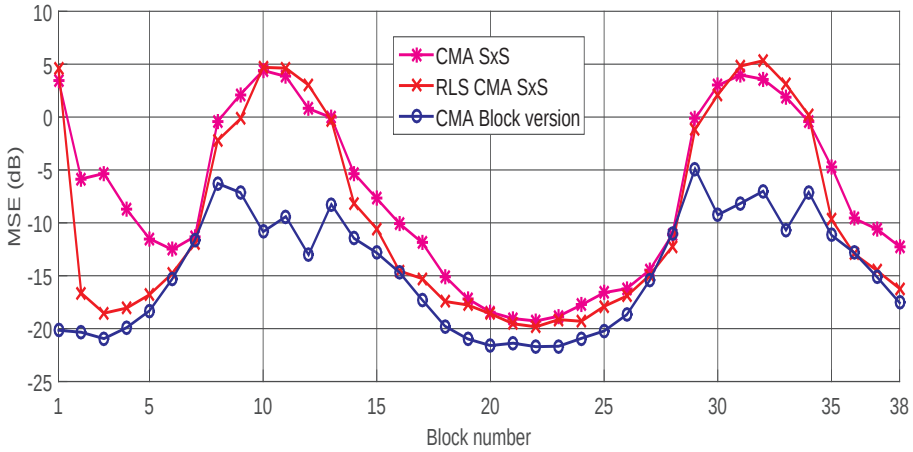

Figure 4.4 – MSE values of different CMA variants - wide-band taxiing channel SMA

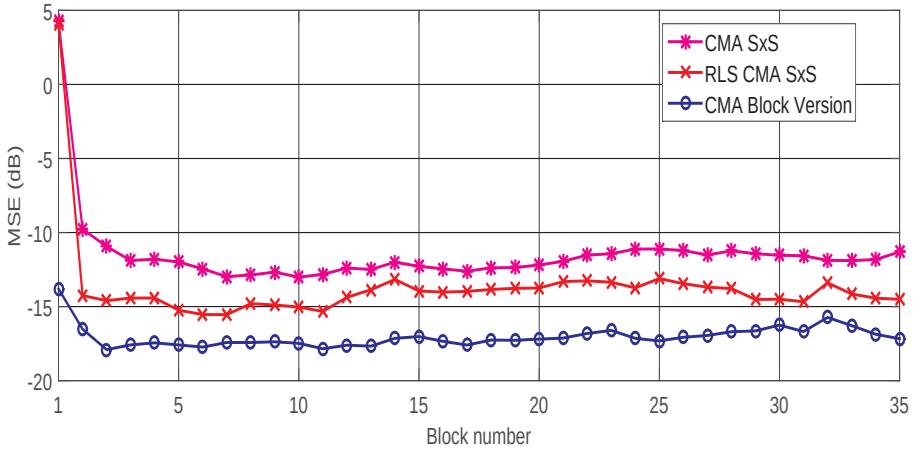

Figure 4.5 – MSE values of different CMA variants - narrow-band apron/taxiing channel TBA

All the aforementioned preliminary results show that the block CMA version is more robust than the other studied CMA versions whether we consider wide-band channel models or narrow-band ones. This is because the algorithm works in an iterative and recursive way. Moreover, the block version takes advantage of N_w samples instead of one when computing the cost function and updating the filter taps, which makes this algorithm more robust than the other sample-by-sample versions in the presence of time-varying channels.

In this section, we have presented a well-known equalizer based on the CPM definition of SOQPSK. In the following section, we propose a joint channel estimation and symbol detection technique that is based on the proposed PAM decomposition given in Chapter 2.

4.4 The Per-survivor Processing algorithm (PSP)

4.4.1 Received signal model approximation

We remind that the transmitted signal is corrupted by a multipath channel $l(t)$, and by an AWGN $n(t)$. In this section, we use the signal approximations given in (2.35) and (2.36). The complex envelope of the received signal is then approximated as

$$r(t) \approx \sum_{i=-\infty}^{+\infty} \rho_{0,i} \tilde{f}_0(t - iT) + n(t), \tag{4.13}$$

or as

$$r(t) \approx \sum_{k=0}^{1} \sum_{i=-\infty}^{+\infty} \rho_{k,i} \tilde{f}_k(t - iT) + n(t), \tag{4.14}$$

where

$$\tilde{f}_k(t) = \int_{-\infty}^{+\infty} w_k(t - \tau) l(\tau) d\tau, \qquad k \in \{0, 1\}. \tag{4.15}$$

We remind that $w_k(t)$ is the kth pulse of proposed PAM decomposition given in Chapter 2 (DBD). In this section, we propose a third approximation, which can be seen as a trade-off between the first approximation given in (4.13) and the second on given in (4.14). To do so, we replace w_1 by w_1' defined in (2.40) and we assume that

$$\begin{cases} w_1'(t) \approx \psi w_0(t), \\ \psi = \dfrac{w_1'(5T)}{w_0(5T)}. \end{cases} \tag{4.16}$$

Using (4.14) and (4.16), $r(t)$ can be approximated as follows

$$r(t) \approx \sum_{i=-\infty}^{+\infty} [\rho_{0,i} + \psi\rho_{1,i}]\, \tilde{f}_0(t - iT) + n(t). \tag{4.17}$$

To validate this model, we plot in figure 4.6 the real parts of $r(t)$ and its different approximations, and we give in Table 4.5 the NMSE values of the approximations. We use as channel the three rays model given in Table 4.1. We use the following convention for the rest of the chapter: Approx. 1, Approx. 2, Approx. 3 refer to the approximations given in (4.13), (4.14), (4.17), respectively. It can be seen that through the NMSE values that Approx. 3 offers a better approximation than Approx. 1 while assuming that $r(t)$ is seen as a single linear modulation. Therefore, the receiver only requires the perfect knowledge of $f_0(t)$ instead of $f_0(t)$ and $f_1(t)$ to detect the data symbols. Since the goal is to conceive a receiver that can work in any channel configuration, it is then necessary to estimate $f_0(t)$ either in the frequency domain or the time domain. Choosing the first option generally requires a cyclic prefix (CP) or a unique word (UW) in order to *circularize* the channel. On the other hand, estimating the channel in the time domain can be performed blindly or semi-blindly using joint channel/data estimation algorithms. Due to the absence of CP and UW in the IRIG recommendations, we choose to apply the second option techniques for our case, i.e., time domain equalization.

Table 4.5 – NMSE values of the different approximations - Three ray channel model - bit rate: 10 Mbps

Approximation	Approx. 1	Approx. 2	Approx. 3
NMSE (dB)	−18.00	−30.26	−20.55

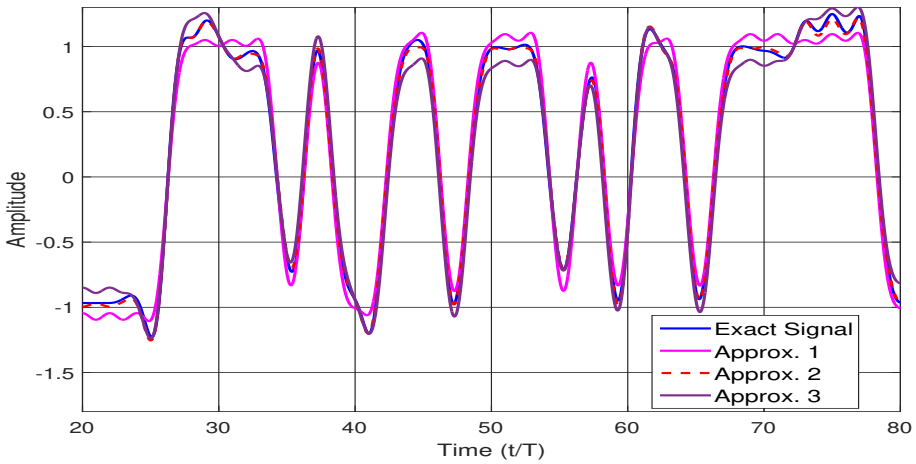

Figure 4.6 – Real part of $r(t)$ and its approximations - Three-ray channel - bit rate: 10 Mbps

4.4.2 Joint data and channel estimation using PSP: Description of the proposed algorithm

The received signal $r(t)$ is filtered using the detection filter $\tilde{w}_f$ given in Section 3.4.2 (the Equiripple FIR), and then sampled at the bit rate. If we suppose that the channel is sparse, then the filtered signal $r * \tilde{w}_f$ becomes null after N_t samples, i.e.,

$$y(m) = \sum_{k=0}^{N_t-1} f_0(k)[\rho_{0,m-k} + \psi\rho_{1,m-k}] + n_f(m), \tag{4.18}$$

where

$$f_0(m) = \int \tilde{f}_0(\tau)\tilde{w}_f(\tau - mT)d\tau, \tag{4.19}$$

and

$$n_f(m) = \int n(\tau)\tilde{w}_f(\tau - mT)d\tau. \tag{4.20}$$

We verified in Section 3.4.2 that the filtered noise can be assumed as a white Gaussian one. Hence, if we consider that N symbols are transmitted, the associated log-likelihood function can be expressed as

$$\Lambda(\underline{b}, \underline{f_0}) = \sum_{m=0}^{N-1} \left| y(m) - \sum_{k=0}^{N_t-1} f_0(k)[\rho_{0,m-k} + \psi\rho_{1,m-k}] \right|^2, \tag{4.21}$$

where $\underline{f_0} = [f_0(0), ..., f_0(N_t - 1)]$ and we remind that $[\rho_{0,m} + \psi\rho_{1,m}]$ can be expressed as a function of the binary symbol b_m as

$$\rho_{0,m} + \psi\rho_{1,m} = \begin{cases} b_m \left(1 - \psi b_{m-1} b_{m+1}\right), & m \text{ even}, \\ j b_m \left(1 - \psi b_{m-1} b_{m+1}\right), & m \text{ odd}, \end{cases} \tag{4.22}$$

In the conventional (or traditional) methods, the channel $\underline{f_0}$ can first be estimated using a pilot sequence and then fed to the Viterbi algorithm whose branch metric is defined by the $N_t + 2$-tuple

$$\sigma_n = (b_{n-N_t}, ..., b_{n+1}). \tag{4.23}$$

The Viterbi algorithm is thus operating with 2^{N_t+1} states. The estimation of the channel can be done via LMS, RLS, Kalman filtering, etc. This method can be efficient if the channel remains unchanged between two pilot sequences, which is not the case for the time-varying models given Section 4.2. This scheme is called in this manuscript the non-adaptive maximum likelihood sequence detection (NA-MLSD), and it is depicted in Figure 4.7.

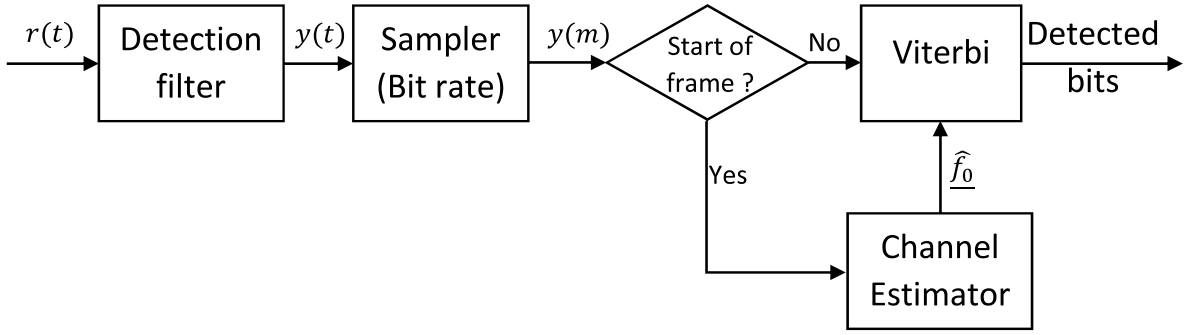

Figure 4.7 – NA-MLSD architecture

In order to make this scheme adaptive, a decision feedback mechanism can be introduced by taking advantage of the tentative decisions given by the Viterbi algorithm [117, 118]. The architecture of this scheme is shown in Figure 4.8, and its main drawback is that the channel estimation heavily relies on the quality of the data estimation. If the symbols are poorly estimated (for example at low SNR), the channel estimation would be deteriorated, which results in error propagation [119]. This architecture is called the conventional adaptive-MLSD (CA-MLSD).

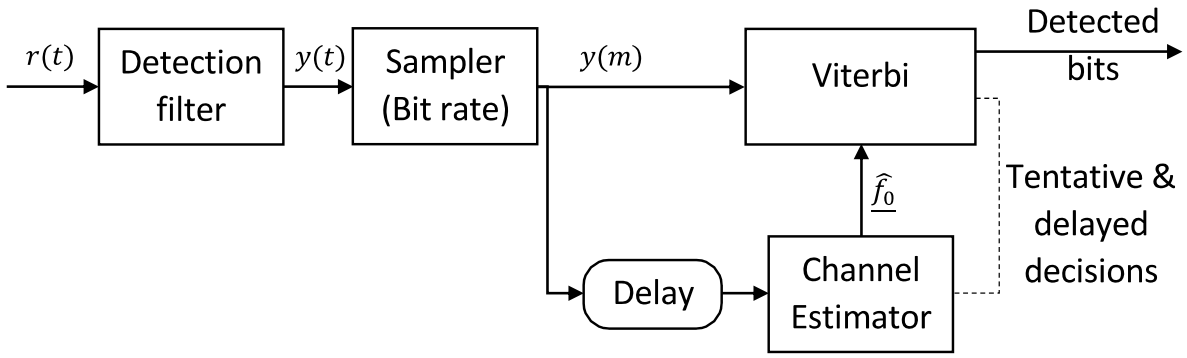

Figure 4.8 – CA-MLSD architecture

In this work, we choose to employ another architecture that allows estimating the channel and the data symbols in the Viterbi algorithm. This solution is known as the per-survivor processing (PSP) [28]. In this solution, we associate to each hypothetical path of the trellis a channel estimation, which means that the number of channel candidates is equal to the number of the states of the trellis. We then update the channel estimations at each epoch. In order to explain how this algorithm works in our case, we first define the state of the trellis μ_{m-1} at epoch $m-1$

$$\mu_{m-1} = (b_{m-N_t+1}, ..., b_{m-1}), \tag{4.24}$$

and $\mu_{m-1} \to \mu_m$ as the transition from the state μ_{m-1} to the state μ_m. Using this definition, the Viterbi algorithm operates with 2^{N_t-1} instead of 2^{N_t+1} states as highlighted above. We then define 3 binary vectors of length N_t associated with the transition $\mu_{m-1} \to \mu_m$

$$\begin{cases} \underline{b_p}(\mu_{m-1} \to \mu_m) = [0, b_{m-N_t+1}, ..., b_{m-1}], \\ \underline{b}(\mu_{m-1} \to \mu_m) = [b_{m-N_t+1}, ..., b_m], \\ \underline{b_a}(\mu_{m-1} \to \mu_m) = [b_{m-N_t+2}, ..., b_m, 0]. \end{cases} \tag{4.25}$$

Using (4.21), the branch metric at epoch m associated with the transition $\mu_{m-1} \to \mu_m$ is expressed as

$$\lambda(\mu_{m-1} \to \mu_m) = |e(\mu_{m-1} \to \mu_m)|^2, \tag{4.26}$$

where

$$e(\mu_{m-1} \to \mu_m) = y(m) - x(\mu_{m-1} \to \mu_m), \tag{4.27}$$

and

$$x(\mu_{m-1} \to \mu_m) = \begin{cases} \left[\underline{\hat{f}_0}(\mu_{m-1}) \odot \underline{1i^e}\right] \left[\underline{b}(\mu_{m-1} \to \mu_m) \odot \Big(\underline{1} \right. \\ \qquad \left. -\psi \underline{b_p}(\mu_{m-1} \to \mu_m) \odot \underline{b_a}(\mu_{m-1} \to \mu_m)\Big)\right]^{\mathcal{T}}, \quad m \text{ even} \\ \left[\underline{\hat{f}_0}(\mu_{m-1}) \odot \underline{1i^o}\right] \left[\underline{b}(\mu_{m-1} \to \mu_m) \odot \Big(\underline{1} \right. \\ \qquad \left. -\psi \underline{b_p}(\mu_{m-1} \to \mu_m) \odot \underline{b_a}(\mu_{m-1} \to \mu_m)\Big)\right]^{\mathcal{T}}, \quad m \text{ odd.} \end{cases} \tag{4.28}$$

The vector $\underline{\hat{f}_0}(\mu_{m-1}) = [\hat{f}_{0,0}(\mu_{m-1}), ..., \hat{f}_{0,N_t-1}(\mu_{m-1})]$ represents an estimate of the discrete channel f_0 associated with the state μ_{m-1} and the operator $\odot$ is the Hadamard product. The vectors $\underline{1}$, $\underline{1i^e}$ and $\underline{1i^o}$ are N_t element vectors such that $\underline{1} = [1, ..., 1]$, $\underline{1i^e} = [1, j, ..., 1, j, ...]$, $\underline{1i^o} = [j, 1, ..., j, 1, ...]$ (the last element of the vector can be 1 or j, depending on the parity of N_t), respectively. Writing $y(m)$ as above allows considering $\underline{b}_m$ as the channel state instead of $\underline{\rho}_{0,m}$, which reduces the alphabet to binary in place of quaternary ones.

Equation (4.27) shows that the branch metric represents the error between the received sample $y(m)$ and the approximation of its noiseless estimate for all the possible transitions $\mu_{m-1} \to \mu_m$. These errors can then be used to determine the channel $\underline{f_0}$ and track its variations. To do so, we first identify the survivor paths by computing the accumulated metrics $\Gamma(\mu_m)$ as follows

$$\Gamma(\mu_m) = \min_{\mu_{m-1}} \left[\Gamma(\mu_{m-1}) + \lambda(\mu_{m-1} \to \mu_m)\right]. \tag{4.29}$$

Then, the transitions that comply with (4.29) are stored and are used to update the channel estimates via the LMS principle

$$\underline{\hat{f}_0}(\mu_m) = \begin{cases} \underline{\hat{f}_0}(\mu^s_{m-1}) + \beta e(\mu^s_{m-1} \to \mu_m)\Big[\underline{b}(\mu^s_{m-1} \to \mu_m) \odot \Big(\underline{1} \\ \qquad -\psi \underline{b_p}(\mu^s_{m-1} \to \mu_m) \odot \underline{b_a}(\mu^s_{m-1} \to \mu_m)\Big)\Big] \odot (\underline{1 i^e})^*, \quad m \text{ even}, \\ \underline{\hat{f}_0}(\mu^s_{m-1}) + \beta e(\mu^s_{m-1} \to \mu_m)\Big[\underline{b}(\mu^s_{m-1} \to \mu_m) \odot \Big(\underline{1} \\ \qquad -\psi \underline{b_p}(\mu^s_{m-1} \to \mu_m) \odot \underline{b_a}(\mu^s_{m-1} \to \mu_m)\Big)\Big] \odot (\underline{1 i^o})^* \quad m \text{ odd}. \end{cases} \tag{4.30}$$

where $(.)^*$ is the conjugate operator, μ^s_{m-1} is the surviving state, β is the LMS convergence step. The channel estimates can also be done via RLS [28] or Kalman filtering [120]. We give in Figure 4.9 a toy example that shows how updating $\underline{\hat{f}_0}(\mu_m)$ is done where we suppose that $N_t = 3$ and m is even. The power of the PSP compared to the other conventional methods is that it aims to converge the set $(\underline{\hat{f}_0}, \underline{\hat{b}})$ towards the maximum likelihood solution in a decentralized manner, i.e., the search of the best solution in the MLSE sense is not affected by an external and global estimation of the channel that is injected in the Viterbi algorithm. Instead of that, each retained path of the Viterbi algorithm has its own estimation of the channel $\underline{\hat{f}_0}$ (which is referred to as $\underline{\hat{f}_0}(\mu_m)$ in this section).

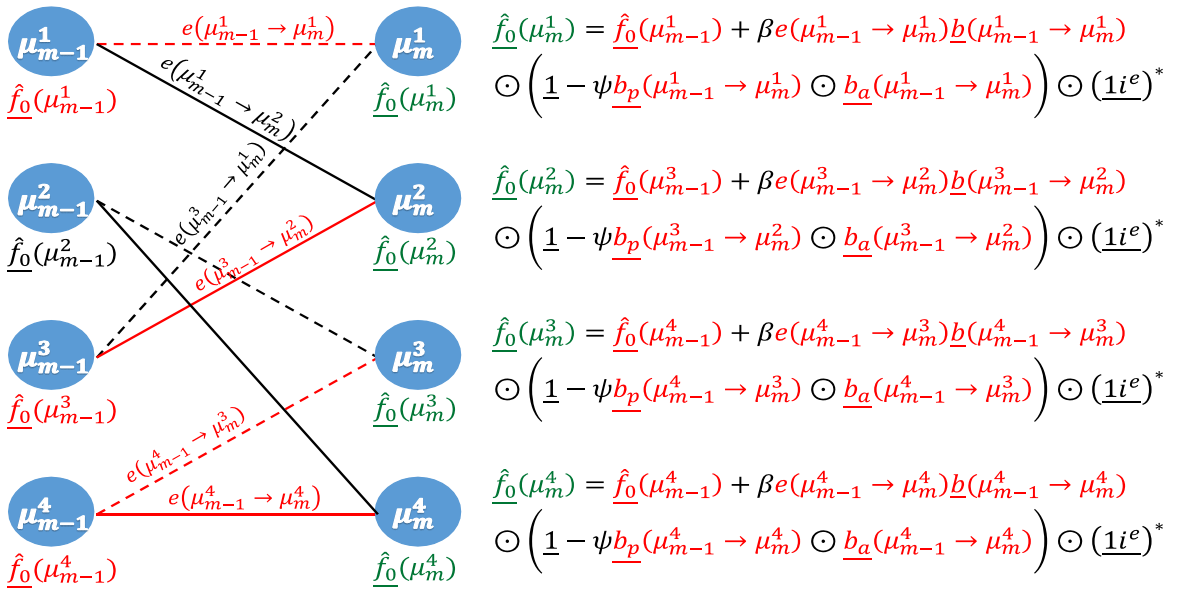

Note: *The dashed line represents a 0 transition and the continuous line is a 1 transition. The survivor paths are highlighted in red. The channel estimates that are being updated are highlighted in green.*

Figure 4.9 – PSP principle for SOQPSK - 4-states trellis

4.4.3 Preliminary Simulation results for PSP

To evaluate the performance of PSP, we use in the system model the integrated network enhanced telemetry (INET) packet structure [20, 121] composed of a preamble of 128 known bits, an asynchronous marker (ASM) of length 64 and a frame that contains 6144 data bits as shown in Figure 4.10. The preamble is used to initialize $\underline{\hat{f}_0}(\mu_m)$ and to determine whether we start with an even bit or an odd one to avoid any phase ambiguity. Then the channel estimates of the PSP are used to track the channel variations when the latter is time-varying.

Preamble	ASM	Data
(128 bits)	(64 bits)	(6144 bits)

Figure 4.10 – INET packet structure

Approx. 1 Vs Approx. 3

We begin evaluating the performance of the proposed PSP by first comparing the MSE values of Approx. 1 (where we suppose that $\psi = 0$) and Approx. 3. To do so, we consider that the signal is corrupted by the three-ray multipath channel given in Table 4.1 and by a noise of 30-dB SNR. Then, after filtering and sampling, we estimate the channel using the LMS algorithm by computing (4.27) and (4.30) at each iteration. However, in this case, the values of x are computed using the data that are used to generate the transmitted signal. The estimated channel is initialized with $(w_0 * \tilde{w}_f)(nT)$, $n \in \{0, ..., N_t - 1\}$. The MSE values of the different approximations are plotted in Figure 4.11, and it can be seen that Approx. 3 offers a 6-dB MSE gain compared to Approx. 1, which confirms the pertinence of the proposed approximation.

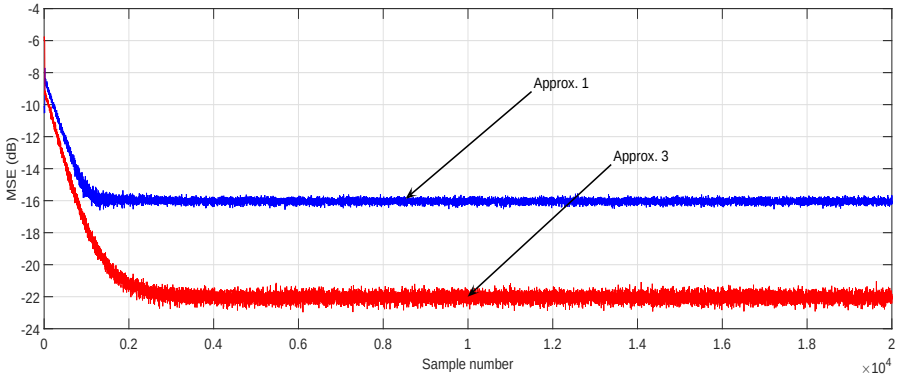

Figure 4.11 – MSE of the channel estimations using Approx. 1 and Approx. 3 - Three-ray channel model - bit rate 10 Mbps

NA-MLSD Vs CA-MLSD Vs PSP

We now highlight the advantage of using the PSP architecture instead of NA-MLSD or CA-MLSD. To do so, we consider the time-varying channel given in Table 4.3 as well as a noise of 30-dB SNR and we compare in Figure 4.12 the BER using the different architectures. The results are averaged over 500 channels, source, and noise realizations. Moreover, Each marker in the figure represents the average BER of 1024 data bits, which means that each 6 consecutive markers of the figure represent one frame of the INET packet. For better visibility, error-free blocks are shown at BER=10^{-7}.

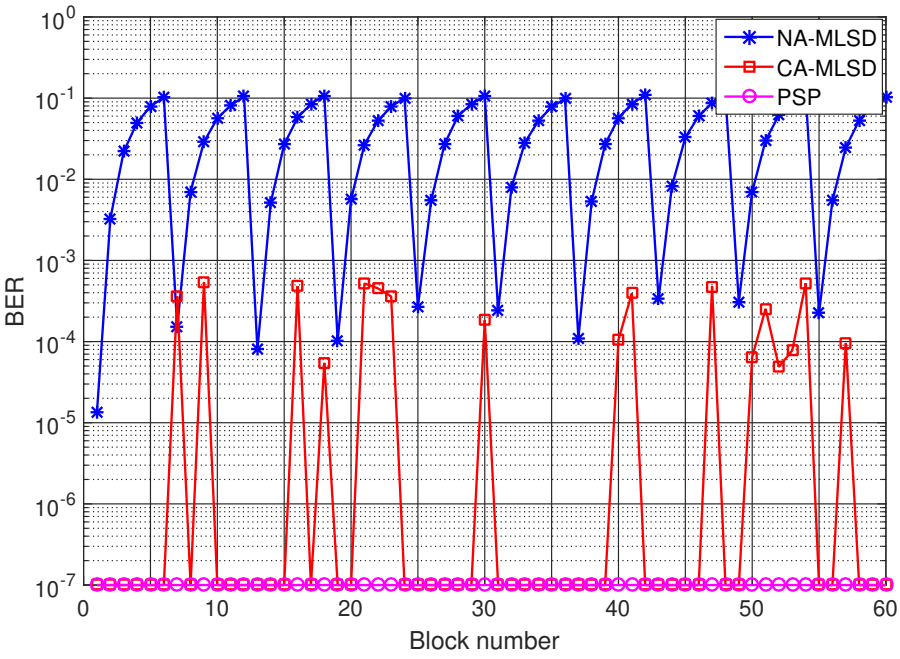

Figure 4.12 – Bit Error rate performance per block - Apron/taxiway TBA - SNR=30 dB

For all the architectures, we use Approx. 3 we suppose that $N_t = 9$, thus the Viterbi algorithm operates with 256 states. It can be seen from Figure 4.12 that the BER is increasing between two pilot sequences when we employ the NA-MLSD architecture. This is due to the extended data frame, and hence, it is essential to introduce tracking mechanism even when the channel is slowly varying. Also, it can be noticed that using the CA-MLSD architecture generates more errors than PSP, which is in accordance with what has been found in [28] for linear modulations.

4.5 Simulation Results

In this section, we present the BER performance of the block CMA, RLS-CMA and the PSP architecture using Approx. 1 and Approx. 3 over the different channels described in Section 4.2. Each architecture is tuned with the best-found parameters (i.e., the block length for the block CMA version, the step size for both block CMA and PSP and the forgetting factor for RLS-CMA) that provide the best BER performance. Note also that once the signal is equalized using the block CMA or RLS-CMA, the data bits are estimated using the reduced complexity Kaleh based detector given in Section 3.2.2. The results are averaged over 500 channel, noise and source realizations.

4.5.1 Time-invariant wide-band channel model: Three ray propagation model

We first give the BER performance in the presence of the time-invariant wide-band channel described in this chapter. It can be seen from Figure 4.13 that the PSP algorithm clearly outperforms both CMA versions while keeping a very low number of states. It can also be noticed that:

- The RLS-CMA performs better than the block CMA, which confirms the observation based on the MSE of the instantaneous frequencies given in Figure 4.3.
- The PSP algorithm provides very acceptable BER performance even at low SNR unlike CMA, and the curves are close to theoretical AWGN curve given in Section 3.2.
- The PSP algorithm provides very acceptable BER performance for different bit rates as shown in Figure 4.14.
- The BER performance improvement due to using Approx. 3 instead of Approx. 1 in the PSP architecture is not significant.

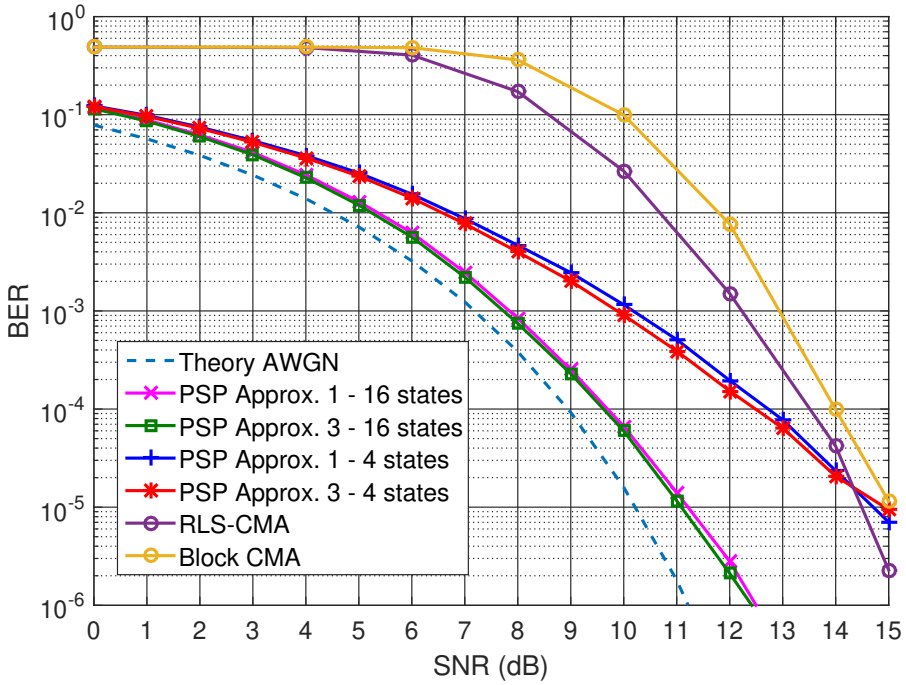

Figure 4.13 – BER performance of PSP and CMA - Three ray channel - bit rate 15 Mbps

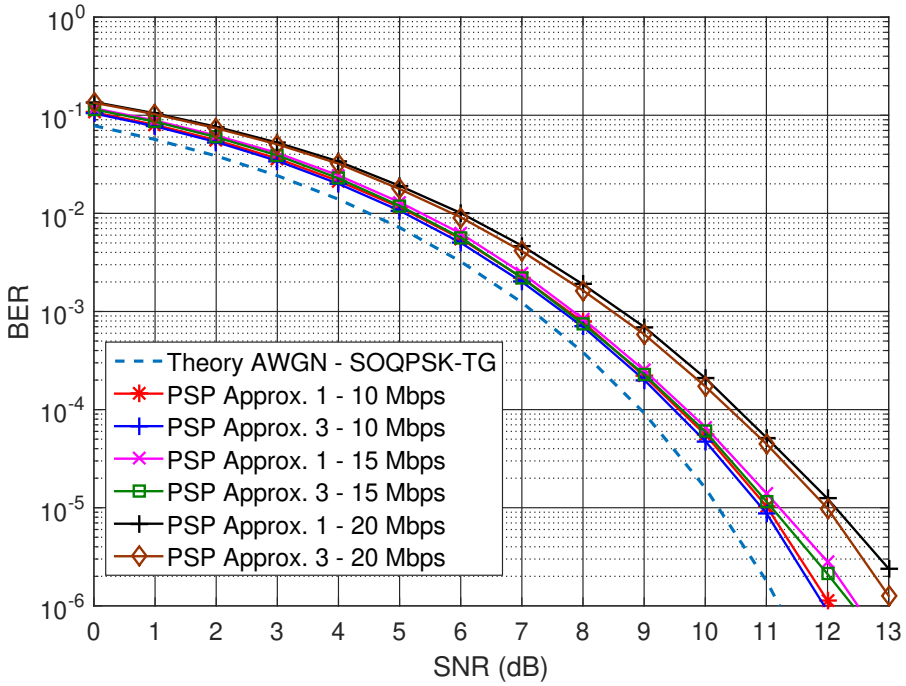

Figure 4.14 – BER performance of PSP for different bit rates - Three ray channel - PSP with 16 states

4.5.2 Time-variant wide-band channel model: Taxiing scenario SMA

We now give the BER performance of the different architectures when we consider the taxiing scenario of Saint Martin airport. It can be seen from Figure 4.15 that we need a high number of states in order to achieve acceptable BER performance due to the relatively important delay spread (compared to the symbol period time, which is 1 μs for this simulation). We can also remark that:

- At least a Viterbi algorithm of 256 states, i.e., taking $N_t = 9$, is necessary to get very acceptable BER performance for PSP. This is not only due to the relatively important delay spread (compared to the symbol period time, which is 1 μs for this simulation), but also due to the lengthy SOQPSK-TG main pulse, which is composed of 3 taps as shown in Section 3.4. Thus, receiving multiple reflections of the signal would greatly increase the number of taps of f_0.
- A significant BER performance improvement at high SNR when we use Approx. 3 instead of Approx 1 in the PSP architecture.
- A significant BER performance improvement of PSP compared to CMA.

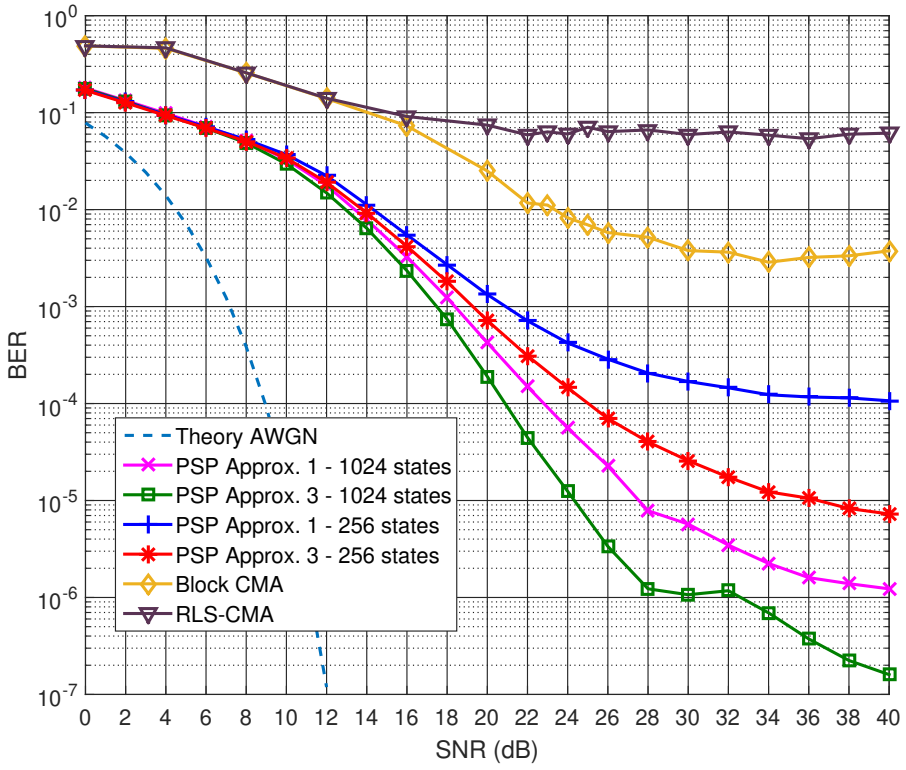

Figure 4.15 – BER performance of PSP and CMA - Taxiing scenario SMA - bit rate 1 Mbps

4.5.3 Narrow-band channel model: Apron/taxiway and runway models

Figure 4.16 and Figure 4.17 show the BER performance of PSP and CMA when a narrow-band channel model is considered. We also plotted the BER curve, namely known data Approx. 3, in the case where all the transmitted data are used to estimate the channel in the PSP architecture. To do so, we estimate at each epoch m the channel f_0 using the known transmitted data and the received SOQPSK-TG sample $y(m)$, then we inject this estimation in (4.26) to calculate the branch metrics of the Viterbi algorithm. The BER is thus the bit error rate between the transmitted symbols and the detected ones via the Viterbi algorithm. This curve represents the case where the estimation is fully aided and can reflect what PSP can optimally reach for a given Rice channel model. We can notice from the curves given in Figure 4.16 and Figure 4.17 that

- A PSP with 256 states, i.e., taking $N_t = 9$, is necessary to get very acceptable BER performance.
- The obtained curves with 256 states are close to the one when data are known.
- Approx. 3 offers an important BER performance improvement compared to Approx. 1.
- PSP performs well in the presence of high Doppler spread, unlike CMA.

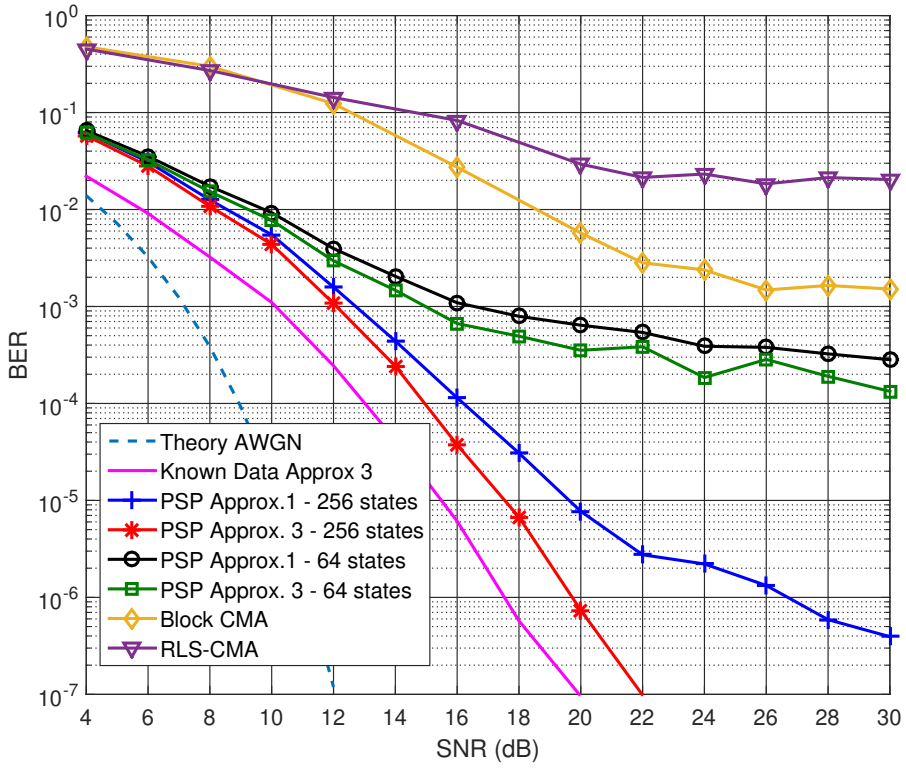

Figure 4.16 – BER performance of PSP and CMA - Apron/taxiway TBA - bit rate 1 Mbps

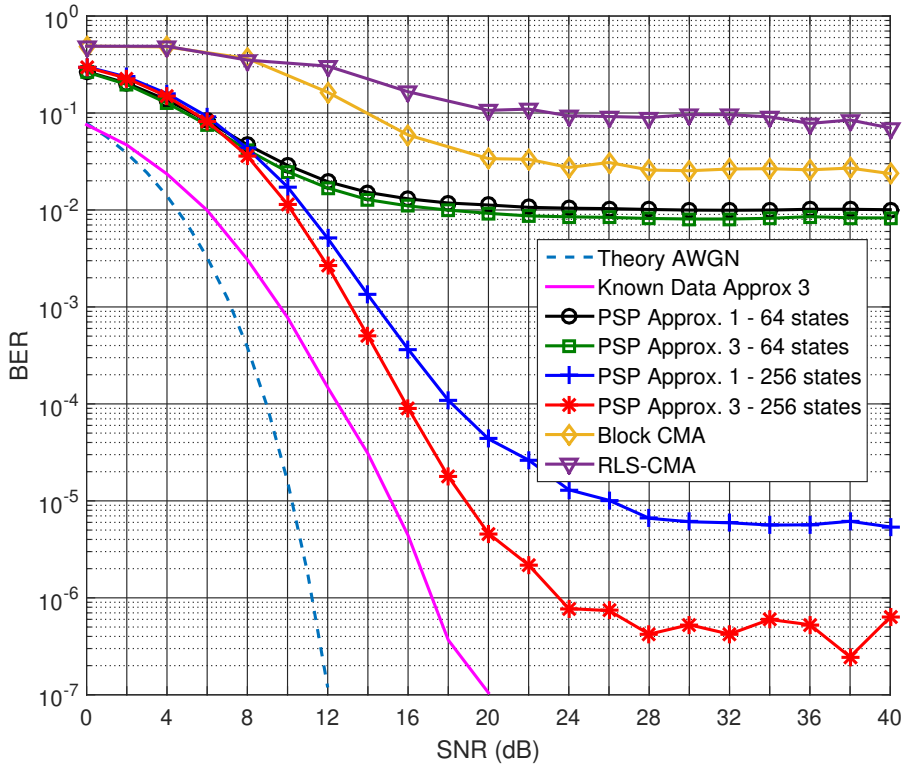

Figure 4.17 – BER performance of PSP and CMA - runway TBA - bit rate 1 Mbps

4.6 Conclusion

In this chapter, we have made a classification of the different aeronautical telemetry channel models that are used in the literature. The models essentially depend on how the sounding experiments are done and what measures can be extracted. In some cases, it is possible to characterize the attenuations and delays of the echoes fully, and in others, these echoes are not fully resolvable, and thus it is necessary to use probabilistic models. Also, in some models, the channel is assumed to be time-invariant over a short time interval and in others, the channel variations are taken into account, and the Doppler analysis is given.

We then studied the time-domain equalizers that can be used for SOQPSK-TG to mitigate the channel fadings. We first focused on the CMA and its variants, and we showed that the block CMA version is the most suitable solution among the other studied variants. We then proposed to use the PSP algorithm based on the revamped PAM decomposition of SOQPSK-TG to estimate the channel and the data symbols jointly. The PSP principle has already been studied in the literature for MSK-type signals such as GMSK (see for example [120, 122, 123]). However, to the best of our knowledge, all these works consider that these MSK-type signals can be approximated by using only 1 PAM pulse. In this chapter, we showed that using a new approximation, namely Approx. 3 that takes into account the contribution of the

pseudo-symbols that modulate the pulse $w_1(t)$ in the PSP architecture offers a significant BER performance improvement in the presence of time-varying channels compared to the classical PSP architectures. All the results are obtained for SOQPSK-TG, but they can also be extended to other SOQPSK versions as well as low-BT GMSK. The number of the necessary states to get very acceptable BER performance depends on the channel model and the used bit rate. The time-invariant models described in this chapter (which are the most common ones in aeronautical telemetry) require very low number of states whereas the time-variant ones make the use of PSP with 256 states necessary.

Due to the absence of a cyclic prefix in the IRIG recommendations and the INET packet structure, we have not considered any frequency domain equalization. However, thanks to the proposed PAM decomposition and if it is foreseeable to insert a cyclic prefix or a unique word in the packet structure, the works that are described in [91, 92, 94] can fully be applied to SOQPSK-TG.

Chapter 5

IRIG Space Time Coding for Aeronautical Telemetry: Proposed Receivers

Contents

5.1 Introduction

In the previous chapters, the different algorithms are built regardless of the number of the transmit antennas on the aircraft. However, the latter parameter has a significant impact on the aeronautical telemetry link. In fact, for certain types of air vehicles that do not make extreme maneuvers in clear areas, placing one transmit antenna can be sufficient since the line of sight component is always visible to the ground station. Nevertheless, for some air vehicles such as fighter jets and missiles, performing extreme maneuvers or rotations pushes the use of two transmitting antennas instead of one to guarantee an omnidirectional transmission. This solution can be efficient if the signals are sent using different carrier frequencies or when the receiver only captures one LOS component as shown in Figure 5.1a. However, If the same signal is simultaneously transmitted through both transmit antennas with the same carrier frequency and the two antennas are visible to the ground station as depicted in Figure 5.1b, the received signal could suffer from severe destructive interference due to the large change of the phase angle difference between the two transmit signals. This problem has been illustrated during some flight experiments in [22, 124], and it has appeared because the two-antenna system behaves like a single antenna array with an undesirable gain pattern [13], which degrades the telemetry link. This phenomenon is known as the "two-antenna problem" in aeronautical telemetry.

A straightforward solution for the two-antenna problem is to send the signals using two different carrier frequencies. However, due to the limited available bandwidth and the high data rate requirements, this solution is impractical. A more efficient one is proposed by Jensen et al. in [13] where it has been shown that Alamouti encoding [23] overcomes this problem without expanding the required bandwidth. Moreover, the data can be recovered whether only one or two transmit antennas are visible to the ground station. This encoding technique was initially developed for M-ary PSK-type modulations to improve the received signal quality while keeping simple processing operations at the receiver side. However, migrating this idea to practical aeronautical telemetry systems is not as obvious as it might seem. This is mainly due to the following factors:

- The particular nature of the aeronautical telemetry modulation (SOQPSK-TG): unlike linear modulations, SOQPSK-TG is a memory dependent modulation if we use the CPM definition. This property is also reflected in the PAM decomposition by the presence of non-Nyquist PAM waveforms as well as memory dependent pseudo-symbols.

- Applying Alamouti encoding on the binary data symbols does not necessarily result in Alamouti encoded pseudo-symbols. This obstacle might prevent from rigorously satisfying the angle-independent condition given in [13] and the orthogonality condition given in [125]. The dissatisfaction of both conditions shows that the design cannot provide the maximum possible transmission rate (i.e., the SOQPSK-TG signals can mutually interfere) and that the maximum likelihood detection rule can be computationally complex.

- The signals which are received from each antenna arrive with different delays. The difference between the delays appears since both the distance between the transmit antennas and the bit rate are relatively high. If we take the example where the antennas are placed on the tail, and the nose of an aircraft, the distance between them can approximately be 30 meters for midsize airplanes, and therefore the signals can arrive with a differential delay of the order of tens of nanoseconds. This differential delay can be a significant fraction of the bit interval T in the case where a data rate starting from 10 Mbps is used. This unusual feature makes this system different from the usual Alamouti systems used for cellular networks.

In this chapter, we first present the IRIG standardized encoder that is used to solve the two-antenna problem for aeronautical telemetry. We then briefly describe the state of the art decoders for SOQPSK-TG. These decoders rely on the XTCQM representation given in chapter 1. We then propose to reformulate the problem using the PAM decomposition, and we design two decoders:

- The first one relies on the first PAM approximation (Approx. 1) of SOQPSK-TG and uses a matrix-based approach to decode the data symbols. It also takes into account the presence of the differential delay, which makes it different from all the architectures of the literature designed for linear modulations [23, 125] or offset modulations [126] or MSK-type ones [127, 128, 129].

- The second one relies on the second PAM approximation (Approx. 2) of SOQPSK-TG and uses the least squares approach. We show that taking this approximation instead of the XTCQM one reduces the complexity of the decoder compared to the one introduced in [16, 130].

All the aforementioned decoders operate while supposing that the ground station captures only the line of sight components. However, as shown in Section 4.2, some reflections are also present due to the nature of the aeronautical telemetry environment and can be added to the LOS paths. To mitigate multipath in the space-time coding (STC) scenario, we propose a novel multipath interference estimator that can be paired with the proposed PAM based least squares decoder.

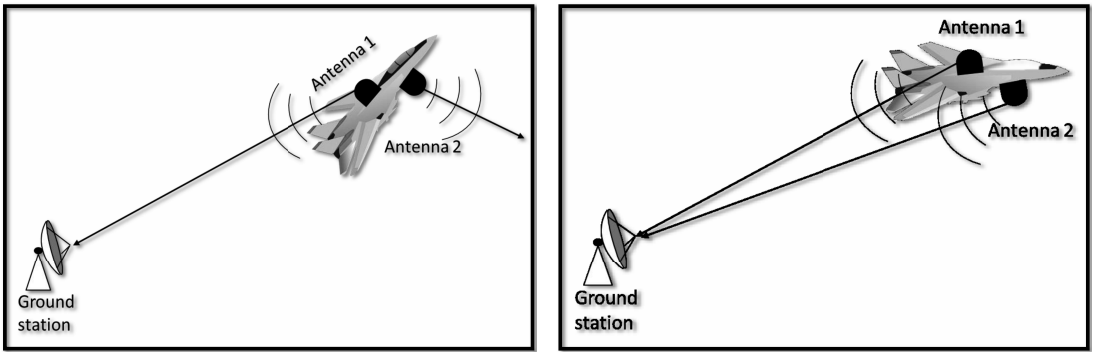

(a) Scenario 1 **(b)** Scenario 2

Figure 5.1 – The two-antenna problem

5.2 System model

5.2.1 Space-time block coding (STBC): IRIG encoding

The standardized IRIG STBC encoding is described in [5] and consists of encoding the bit stream $\underline{b} = [b_i]_{i\in\mathbb{N}}$ into two parallel bit streams ($\underline{b}^0 = [b_i^0]_{i\in\mathbb{N}}$, $\underline{b}^1 = [b_i^1]_{i\in\mathbb{N}}$) as follows

$$\underline{b}^0 = [... \quad b_{4n},\ b_{4n+1},\ -b_{4n+2},\ b_{4n+3}, \quad ...] \tag{5.1}$$

$$\underline{b}^1 = [... \quad b_{4n+2},\ b_{4n+3},\ b_{4n},\ -b_{4n+1}, \quad ...]. \tag{5.2}$$

This encoding is nothing else than the Alamouti encoding of a QPSK constellation, and it is used for SOQPSK-TG due to the following reason: the described encoding fulfills the desired properties for the OQPSK modulation since it guarantees a maximum possible transmission rate (thus resolves the two-antenna problem) while keeping simple processing operations at the receiver side. Since SOQPSK-TG can be interpreted as an OQPSK-type modulation thanks to the XTCQM interpretation given in Chapter 1, the encoding process is also extended to this telemetry modulation.

In each bit stream, a pilot sequence of 128 bits is inserted periodically, then each stream is passed through a SOQPSK-TG modulator and transmitted over an antenna with the same carrier frequency as shown in Figure 5.2. The pilot sequences are used to estimate the frequency offset, the channel gains and the differential delay between the two received signals as described in [131].

5.2.2 Received Signal Model

In this work, we consider the MISO case, i.e., the receiver only contains one antenna. Thus, the received signal model is the following

$$r(t) = \left[h_0 s_0(t) + h_1 s_1(t - \Delta\epsilon)\right] e^{j2\pi f_0 t} + n(t), \tag{5.3}$$

where $s_0(t)$ and $s_1(t)$ are two SOQPSK-TG signals containing the bit streams $\underline{b}^0$ and $\underline{b}^1$ and are affected by complex-valued attenuations h_0 and h_1, respectively. The parameter $\Delta\epsilon$ is a differential delay that is generally present in aeronautical telemetry as explained in the introduction of this chapter, f_0 is the frequency offset and $n(t)$ is an AWGN. The received signal is filtered using a detection filter f (for example one of the detection filters given in Section 3.4.2) and sampled at the bit rate at $t = kT$ and $t = kT + \Delta\epsilon$. We first suppose that f_0 is null, therefore the sampled signal y can be written as

$$\begin{cases} y(k) = y(t = kT) = h_0 \tilde{s}_0(kT) + h_1 \tilde{s}_1((k - \Delta\tau)T) + \tilde{n}(kT), \\ y_{\Delta\tau}(k) = y(t = kT + \Delta\epsilon) = h_0 \tilde{s}_0((k + \Delta\tau)T) + h_1 \tilde{s}_1(kT) + \tilde{n}((k + \Delta\tau)T), \end{cases} \tag{5.4}$$

where y, $\tilde{s}_0$, $\tilde{s}_1$ and $\tilde{n}$ are the filtered versions of r, s_0, s_1 and n, respectively, i.e.,

$$y(t) = \int r(\tilde{t}) f(\tilde{t} - t) d\tilde{t}, \tag{5.5}$$

$$\tilde{s}_i(t) = \int s(\tilde{t}) f(\tilde{t} - t) d\tilde{t}, \qquad i \in \{0, 1\}, \tag{5.6}$$

$$\tilde{n}(t) = \int n(\tilde{t}) f(\tilde{t} - t) d\tilde{t}. \tag{5.7}$$

The parameter $\Delta\tau = \frac{\Delta\epsilon}{T}$ is the differential delay relative to the sample time and it is supposed that $|\Delta\tau| < 1$.

The aim of the decoder is to recover the bit stream $\underline{b}$ that is used to generate $(\underline{b}^0, \underline{b}^1)$ from $y(t)$. To do so, it is necessary to estimate the channel parameters before decoding. In this chapter, we firstly suppose that these parameters are perfectly estimated using the estimators described in [131]. Then, we evaluate the performance of the overall architecture (i.e., with the estimators) when multipaths are present.

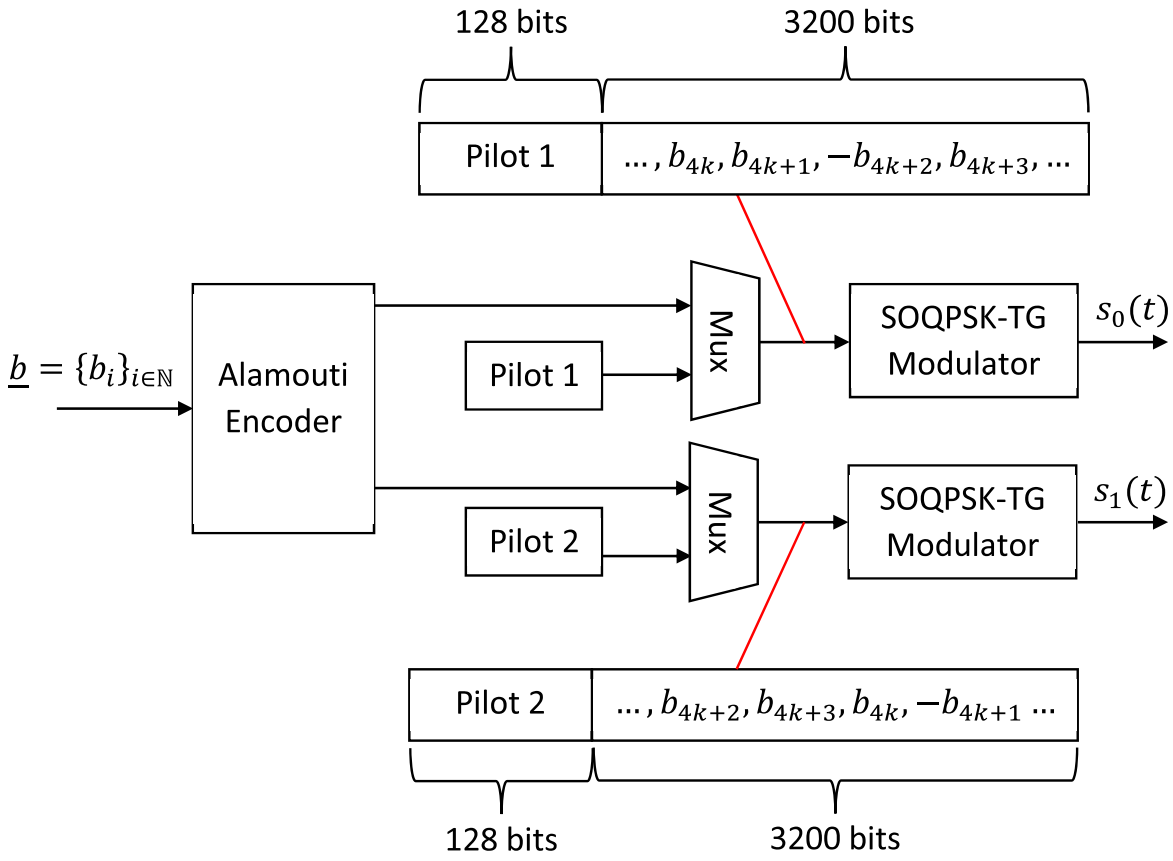

Figure 5.2 – IRIG - STBC transmitter

5.3 State of the art decoders: XTCQM based decoders

5.3.1 Using Cavers/ Ungerboeck approach: ML-ASM decoder

Nelson first proposed in [16] a matrix-based decoder inspired from the one used for OQPSK and SOQPSK-MIL signals. In this solution, the differential delay is supposed to be zero and the maximum likelihood (ML) problem formulation is done using the XTCQM approximation of SOQPSK-TG since it creates a link between the data bits and the traces of the signal eye-diagram. The solution is thus called maximum likelihood - approximate signal model (ML-ASM) and approximates the output of the detection filter as

$$\underline{y} \approx \mathbf{RH}\underline{s} + \underline{n}, \tag{5.8}$$

where $\underline{y} = [y(0), y(1), ..., y(nT), ...]^{\mathcal{T}}$ is a vector of N elements if we suppose that N data symbols $\{b_i\}_{\{i\in[0,N-1]\}}$ are transmitted. The used detection filter is the non-zero 2-XTCQM waveform given in Chapter 1. The vector $\underline{s}$ is a function of the data symbols b_i, and $\mathbf{R}$ is the

deterministic auto-correlation matrix of the detection filter f, i.e.,

$$\mathbf{R} = \begin{bmatrix} R(0) & R(T) & 0 & \dots & \dots & 0 \\ R(-T) & R(0) & R(T) & 0 & \ddots & \vdots \\ 0 & R(-T) & R(0) & R(T) & \ddots & \vdots \\ \vdots & \ddots & \ddots & \ddots & \ddots & 0 \\ \vdots & \ddots & \ddots & \ddots & \ddots & R(T) \\ 0 & \dots & \dots & 0 & R(-T) & R(0) \end{bmatrix}, \qquad \underline{s} = \begin{bmatrix} b_0 \\ jb_1 \\ b_2 \\ jb_3 \\ \vdots \\ b_n \\ jb_{n+1} \\ b_{n+2} \\ jb_{n+3} \\ \vdots \end{bmatrix}, \tag{5.9}$$

and

$$R(kT) = \int f(t) f(t - kT) dt. \tag{5.10}$$

The matrix $\mathbf{H}$ is composed of the channel gain values as follows

$$\mathbf{H} = \begin{bmatrix} \mathbf{H}_4 & \mathbf{0}_4 & \dots & \dots \\ \mathbf{0}_4 & \mathbf{H}_4 & \ddots & \vdots \\ \vdots & \ddots & \mathbf{H}_4 & \ddots \\ \vdots & \dots & \ddots & \ddots \end{bmatrix}, \qquad \mathbf{H}_4 = \begin{bmatrix} h_0 & 0 & h_1 & 0 \\ 0 & h_0 & 0 & h_1 \\ h_1 & 0 & -h_0 & 0 \\ 0 & -h_1 & 0 & h_0 \end{bmatrix}, \tag{5.11}$$

where $\mathbf{0}_4$ is a zero matrix with 4 rows and 4 columns. The vector $\underline{n}$ is the vector of the filtered noise samples $\tilde{n}$. These samples are zero-mean, Gaussian random variables with auto-correlation matrix $\mathbf{M} = N_0 \mathbf{R}^{\mathcal{T}}$. The ML metric for a signal expressed as (5.8) is [127]

$$\Lambda\left(\underline{y}, \underline{s}\right) = \left(\underline{y} - \mathbf{R}\mathbf{H}\underline{s}\right)^{\mathcal{H}} \mathbf{M}^{-1} \left(\underline{y} - \mathbf{R}\mathbf{H}\underline{s}\right), \tag{5.12}$$

where $(.)^{\mathcal{H}}$ is the conjugate transpose operator. Based on Cavers development given in [127], Nelson showed that the metric to be maximized can be expressed as

$$\Lambda\left(\underline{y}, \underline{s}\right) = 2Re\left\{\underline{s}^{\mathcal{H}} \mathbf{H}^{\mathcal{H}} \underline{y}\right\} - \underline{s}^{\mathcal{H}} \mathbf{H}^{\mathcal{H}} \mathbf{R} \mathbf{H} \underline{s}. \tag{5.13}$$

The computation of (5.13) is not practical for any value of N. Thus, Nelson used Ungerboeck's formulation of the metric by exploiting the Hermitian property of $\mathbf{R}$, which can be expressed as

$$\mathbf{R} = \mathbf{R}_D + \mathbf{R}_U + \mathbf{R}_L, \tag{5.14}$$

where $\mathbf{R}_D$, $\mathbf{R}_U$, $\mathbf{R}_L$ are diagonal, strictly upper triangular and strictly lower triangular matrices, respectively. Moreover, we have $\mathbf{R}_L = \mathbf{R}_U^{\mathcal{H}}$, therefore (5.13) becomes

$$\Lambda\left(\underline{y}, \underline{s}\right) = 2Re\left\{\underline{s}^{\mathcal{H}}\mathbf{H}^{\mathcal{H}}\underline{y}\right\} - 2\underline{s}^{\mathcal{H}}\mathbf{H}^{\mathcal{H}}R_U\mathbf{H}\underline{s}. \tag{5.15}$$

Formulating the ML metric as above makes using a Viterbi algorithm possible to estimate $\underline{s}$. The shape of the trellis of the Viterbi algorithm is not given in [16, 132] but its performance is depicted in Figure 5.3. It can clearly be seen that the different approximations that have been used to get the ML-ASM decoder are not suitable for SOQPSK-TG.

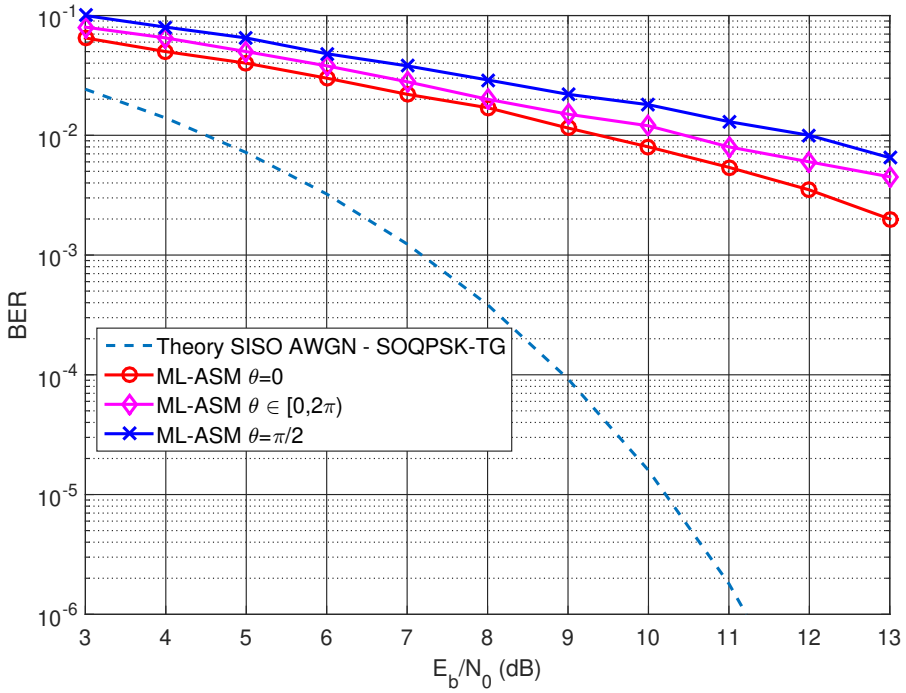

Figure 5.3 – BER performance of ML-ASM decoder for SOQPSK-TG - θ is the phase angle difference between $s_1(t)$ and $s_0(t)$, $|h_0| = |h_1| = \dfrac{\sqrt{2}}{2}$

5.3.2 Offset-Decode (OD) detector using the least squares (LS) approach: OD-LS

Another decoder has been evaluated to get a better BER performance for SOQPSK-TG. It is also inspired from a solution initially developed for OQPSK and then extended to SOQPK-MIL, namely offset-decode (OD) detector [132]. The main idea of this detector consists of exploiting the fact that the information is alternatively carried by the In-phase (or the real part) and the Quadrature-phase (or the imaginary part) components while compensating the cross-correlation between them. To do so, Nelson first proposed to equalize the filtered samples y with the

channel gains matrix $\mathbf{H}_2$

$$\mathbf{H}_2 = \begin{bmatrix} h_0 & h_1 \\ h_1^* & -h_0^* \end{bmatrix}. \tag{5.16}$$

The equalization is done as described in the two following equations [16]

$$\underline{z}_{4k} = Re\left\{\mathbf{H}_2^{\mathcal{H}} \begin{bmatrix} y(4k) \\ y(4k+2)^* \end{bmatrix}\right\} = \underline{v}_{4k} + \underline{u}_{4k}, \tag{5.17}$$

$$\underline{z}_{4k+1} = Im\left\{\mathbf{H}_2^{\mathcal{H}} \begin{bmatrix} y(4k+1) \\ y(4k+3)^* \end{bmatrix}\right\} = \underline{v}_{4k+1} + \underline{u}_{4k+1}, \tag{5.18}$$

where $\underline{v}_{4k}$, $\underline{v}_{4k+1}$ are data dependent 2×1 vectors. Both vectors are expressed in [16] as functions of the XTCQM representation of the filtered signal y. The vector $\underline{v}_{4k}$ is a function of the bits $\{b_{4k-4}, ..., b_{4k+4}, b_{4k+6}\}$ and $\underline{v}_{4k+1}$ is a function of the bits $\{b_{4k-3}, b_{4k-1}, b_{4k}, ..., b_{4k+7}\}$. Both $\underline{u}_{4k+1}$, $\underline{u}_{4k}$ are noise vectors. After storing $\underline{z}_{4k}$ and $\underline{z}_{4k+1}$ in a vector $\underline{Z}$, $\underline{v}_{4k}$ and $\underline{v}_{4k+1}$ in a vector $\underline{V}(\underline{s})$, and $\underline{u}_{4k}$ and $\underline{u}_{4k+1}$ in a vector $\underline{U}$, we get

$$\underline{Z} = \underline{V}(\underline{s}) + \underline{U}. \tag{5.19}$$

Due to the use of the XTCQM representation, the contribution of each bit that composes the vector $\underline{s}$ cannot be extracted. This results in a data dependent vector $\underline{V}(\underline{s})$, and therefore, Cavers/Ungerboeck approach described in Section 5.3.1 cannot be applied in this case. Moreover, the noise samples $\underline{U}$ are correlated. To cope with these issues, the author of [16] has proposed to use the following LS detector in order to estimate $\underline{s}$

$$\hat{\underline{s}} = \underset{\underline{s} \in \{\pm 1, \pm j\}^{2N}}{\operatorname{argmin}} \left\{ |\underline{Z} - \underline{V}(\underline{s})|^2 \right\}. \tag{5.20}$$

The BER performance of this detector is depicted in Figure 5.4 for different values of θ, where $\theta = arg(h_1) - arg(h_0)$. It can be seen that this decoder performs better than the ML-ASM one. However, the BER performance degradation is still high especially when we consider the case where the BER is averaged over different values of θ. The worst case scenario is when $\theta = \dfrac{\pi}{2}$ for this decoder.

Despite the attractive performance of the above decoders for SOQPSK-MIL [16], it can obviously be seen that it is no longer the case for SOQPSK-TG because of its long memory. Moreover, the decoders mentioned above do not consider the case where a differential delay is present, which is a particular impairment of the aeronautical telemetry channel. Furthermore, formulating the problem via the XTCQM representation makes building the matrices hardly tractable and pushes the use of certain simplifications that amplify the mismatch between the

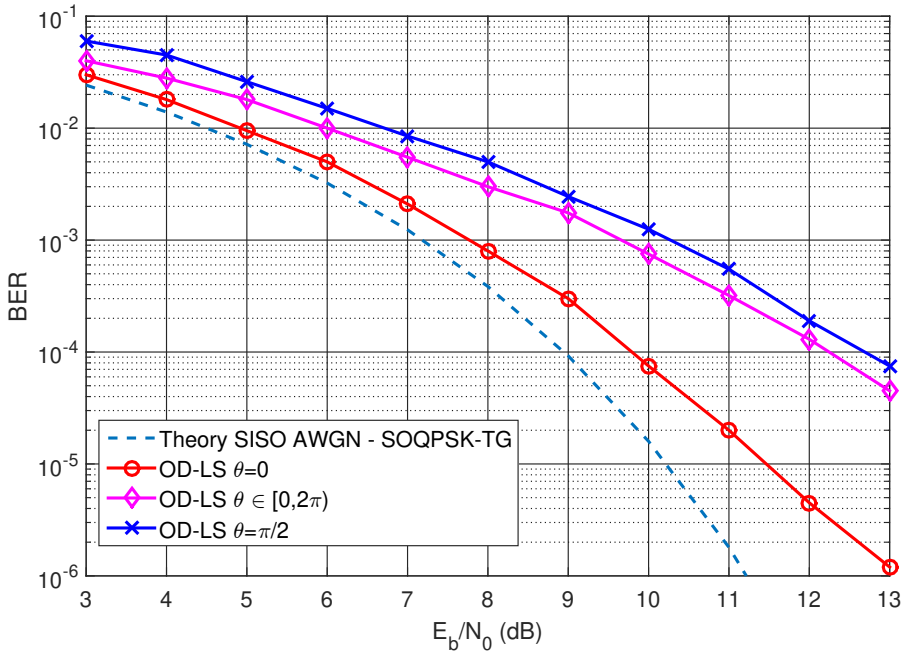

Figure 5.4 – BER performance of OD-LS decoder for SOQPSK-TG - $|h_0| = |h_1| = \frac{\sqrt{2}}{2}$

transmitting system model and the receiver. We show in the following sections that formulating the problem with the revamped PAM decomposition (i.e., DBD) allows getting an explicit construction of the different vectors and matrices. We then propose in Section 5.4 a solution similar to the OD one that takes into account the presence of the differential delay.

5.3.3 XTCQM based decoder using the LS approach: STBD-XTCQM-LS

Nelson et al. have proposed in [16, 130] a LS decoder without resorting to a matrix-based approach and without equalizing the signal with the channel gains like the classical approach for Alamouti decoding. This decoder is referred to as STBD-XTCQM-LS in this manuscript. To do so, a LS estimate has been defined for this system as

$$\hat{b}_{4k}, \hat{b}_{4k+1}, \hat{b}_{4k+2}, \hat{b}_{4k+3} = \underset{b_{4k}, b_{4k+1}, .., b_{4k+3} \in \{-1,+1\}^4}{\operatorname{argmin}} \left\{ \sum_{i=0}^{3} \left(\left| \Upsilon_{4k+i}^{(0)} \right|^2 + \left| \Upsilon_{4k+i}^{(\Delta\tau)} \right|^2 \right) \right\}, \tag{5.21}$$

where $\Upsilon_{4k+i}^{(0)}$ and $\Upsilon_{4k+i}^{(\Delta\tau)}$ are function of the filtered signal y and its corresponding XTCQM representation. When $\Delta\tau \geq 0$, the metrics $\Upsilon_{4k+i}^{(0)}$ and $\Upsilon_{4k+i}^{(\Delta\tau)}$ are defined as [130]

$$\begin{aligned} \Upsilon_{4k+i}^{(0)} = y(4k+1+i) - h_0 \tilde{x}_8 \left(0; b_{4k+1+i}^0, b_{4k+2+i}^0, b_{4k+3+i}^0\right) \\ - h_1 \tilde{x}_{16} \left(-\Delta\tau T; b_{4k+1+i}^1, b_{4k+2+i}^1, b_{4k+3+i}^1, b_{4k+4+i}^1\right), \end{aligned} \tag{5.22}$$

$$\Upsilon_{4k+i}^{(\Delta\tau)} = y_{\Delta\tau}(4k+i) - h_0\tilde{x}_{16}\left(\Delta\tau T; b_{4k+i}^0, b_{4k+1+i}^0, b_{4k+2+i}^0, b_{4k+3+i}^0\right) - h_1\tilde{x}_8\left(0; b_{4k+i}^1, b_{4k+1+i}^1, b_{4k+2+i}^1\right). \quad (5.23)$$

When $\Delta\tau < 0$, the metrics $\Upsilon_{4k+i}^{(0)}$ and $\Upsilon_{4k+i}^{(\Delta\tau)}$ are defined as

$$\Upsilon_{4k+i}^{(0)} = y(4k+i) - h_0\tilde{x}_8\left(0; b_{4k+i}^0, b_{4k+1+i}^0, b_{4k+2+i}^0\right) - h_1\tilde{x}_{16}\left(-\Delta\tau T; b_{4k+i}^1, b_{4k+1+i}^1, b_{4k+2+i}^1, b_{4k+3+i}^1\right), \quad (5.24)$$

$$\Upsilon_{4k+i}^{(\Delta\tau)} = y_{\Delta\tau}(4k+i) - h_0\tilde{x}_{16}\left(\Delta\tau T; b_{4k+i}^0, b_{4k+1+i}^0, b_{4k+2+i}^0, b_{4k+3+i}^0\right) - h_1\tilde{x}_8\left(0; b_{4k+i}^1, b_{4k+1+i}^1, b_{4k+2+i}^1\right), \quad (5.25)$$

where y and $y_{\Delta\tau}$ are defined in (5.4), and we remind that b_i^0 and b_i^1 are functions of the data symbols b_i. The used detection filter is given in [130] and it is of length $2T$. The sample $\tilde{x}_8(.;.)$ is a function of the 8-XTCQM representation of the filtered signal. If we take for instance the signal $\{s_k(t)\}_{k\in\{0,1\}}$, it has been shown in Section 1.5.4 that it can be written as follows

$$s_i(t) \approx \sum_n X_8(t-2nT; b_{2n-1}^k, b_{2n}^k, b_{2n+1}^k), \qquad k \in \{0,1\}. \quad (5.26)$$

The filtered signal can thus be written as

$$s_k(t) * f(t) \approx \sum_n \left(X_8(t-2nT; b_{2n-1}^k, b_{2n}^k, b_{2n+1}^k) * f(t)\right), \quad (5.27)$$

$$\approx \sum_n \tilde{x}_8(t-2nT; b_{2n-1}^k, b_{2n}^k, b_{2n+1}^k), \qquad k \in \{0,1\}. \quad (5.28)$$

The same illustration is valid for $\tilde{x}_{16}(.;.)$, which is a function of the 16-XTCQM representation of the filtered signal. We now explain why both representations are used when computing (5.22)—(5.25): when the signal is sampled at its optimum sampling time, i.e., at $t = 2nT$ for $s_0(t)$, the three-bit representation is sufficient to get a very good approximation of $s_0(2nT)$. Therefore we can use $\tilde{x}_8(.,.)$. However, if this signal is sampled at $t = 2nT + \Delta\tau T$, this three-bit representation is no longer accurate, and therefore the signal representation should be extended to a four bit one. This can be done using for example the 32-XTCQM representation of the

filtered signal $\tilde{x}_{32}(.;.)$ as follows

$$\tilde{x}_{16}(t; b_{2n-2}^k, b_{2n-1}^k, b_{2n}^k, b_{2n+1}^k) = \frac{1}{2}\Big(\tilde{x}_{32}(t; b_{2n-2}^k, b_{2n-1}^k, b_{2n}^k, b_{2n+1}^k, -1) + \tilde{x}_{32}(t; b_{2n-2}^k, b_{2n-1}^k, b_{2n}^k, b_{2n+1}^k, +1)\Big), \qquad -T < t < T,\ k \in \{0,1\}. \quad (5.29)$$

We give in Figure 5.5 an illustration of this representation without using a detection filter. The pulse shapes that have the same color share the same last three consecutive bits $b_{2n-1}^0, b_{2n}^0, b_{2n+1}^0$. It can clearly be seen that when $t = 0$, we have

$$\tilde{x}_{16}(0; -1, b_{2n-1}^k, b_{2n}^k, b_{2n+1}^k) = \tilde{x}_{16}(0; +1, b_{2n-1}^k, b_{2n}^k, b_{2n+1}^k) = \tilde{x}_8(0; b_{2n-1}^k, b_{2n}^k, b_{2n+1}^k). \quad (5.30)$$

However, when $t = \Delta\tau T$, we have

$$\tilde{x}_{16}(\Delta\tau; -1, b_{2n-1}^k, b_{2n}^k, b_{2n+1}^k) \neq \tilde{x}_{16}(\Delta\tau; +1, b_{2n-1}^k, b_{2n}^k, b_{2n+1}^k). \quad (5.31)$$

Due to the fact that the expressions of the metrics given in (5.21) depend on the sign of $\Delta\tau$, two different trellises are proposed in [16]. Each one of them is composed of 16, 16, 32, 64, 128, 128, 64 and 32 states. Moreover, it is necessary to perform 960 multiplications and 1920 additions to detect a block of 4 bits.

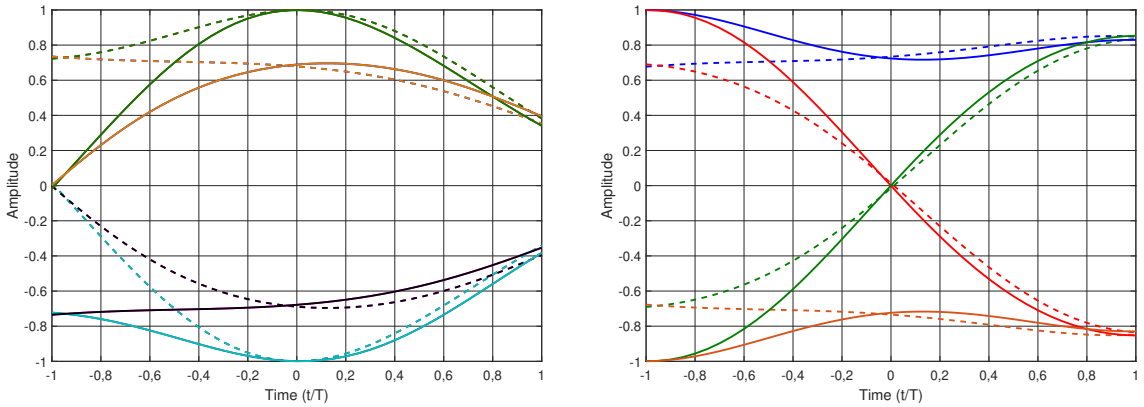

(a) I Channel (a) Q Channel

legend: dashed line: $\tilde{x}_{16}(t; -1, b_{2n-1}^0, b_{2n}^0, b_{2n+1}^0)$, continuous line: $\tilde{x}_{16}(t; +1, b_{2n-1}^0, b_{2n}^0, b_{2n+1}^0)$

Figure 5.5 – Illustration of (5.29)

The performance of this decoder is given in Figure 5.6 for different channel configurations. It can be seen that this decoder has similar performance for different values of θ unlike the OD-LS decoder described in Section 5.3.2. If a differential delay is present, it can be noticed that a BER performance degradation of 1 dB is present compared to the best case scenario ($\Delta\tau = 0$, $\theta = \pi/2$). The case where a negative differential delay is present gives similar performance.

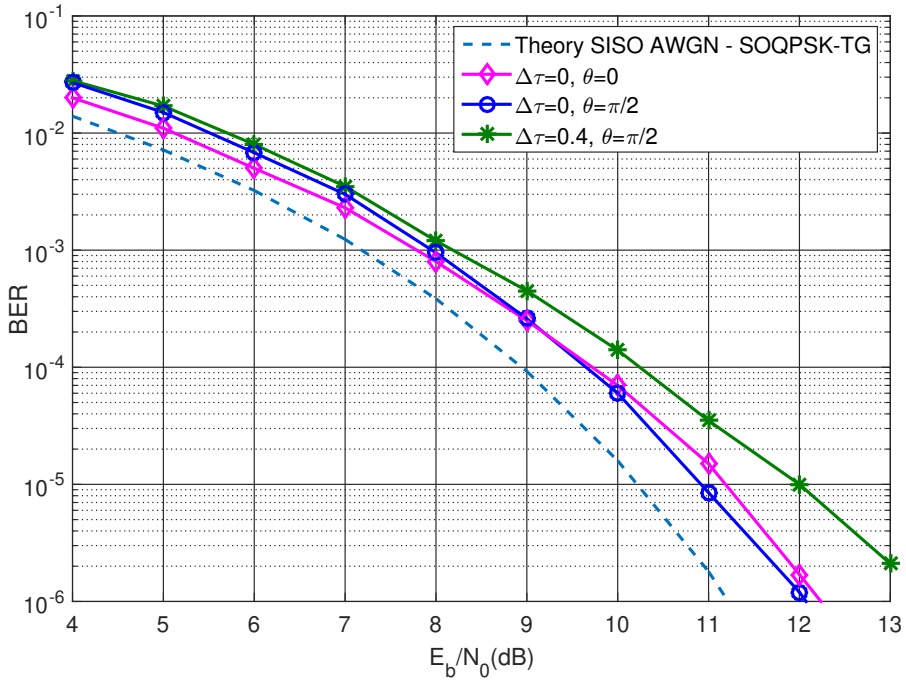

Figure 5.6 – BER performance of LS decoder for SOQPSK-TG - $|h_0| = |h_1| = \frac{\sqrt{2}}{2}$

Discussion

All the aforementioned described algorithms reveal that only the last decoder can give acceptable BER performance despite its relatively high complexity. Several observations can be made regarding this decoder:

- Two techniques are implemented in the decoder to combat the differential delay effect: the first technique is to build the LS estimator using both samples y and $y_{\Delta\tau}$ instead of one of them. As for the second technique, it consists of extending the signal representation from a three-bit level representation to a four-bit one. This extension makes the decoder operate with two different trellises and increases the computational complexity, which is undesirable.

- In aeronautical telemetry, a low parity density check (LDPC) encoder described in [133] is paired with space-time coding. However, the described decoder only delivers hard bits. Therefore, we cannot fully take advantage of the performance improvement offered by the presence of such forward error correction (FEC) systems [84] like the SISO case.

- It has been supposed in the STBC scenario that only the two LOS components have been captured by the ground station. However, as highlighted in Chapter 4, multipath can be present in various telemetry environments. The different estimators described in [131] do not consider the presence of multipath, which can severely impact the performance of the decoder.

All these points will be dealt with in the following sections of this chapter by introducing new PAM based decoders that provide both soft and hard outputs and by developing a multipath channel estimator for this MISO scenario.

5.4 First proposed decoder: PAM based decoder using Cavers/ Ungerboeck approach: STBD-PAM-ML

5.4.1 Received signal model using the first PAM approximation

We first reformulate the problem using the first PAM approximation given in Section 2.3.2. The received signal can thus be approximated as

$$r(t) \approx h_0 \underbrace{\sum_i \rho^0_{0,i} w_0(t - iT)}_{s_0(t)} + h_1 \underbrace{\sum_i \rho^1_{0,i} w_0(t - \Delta\epsilon - iT)}_{s_1(t-\Delta\epsilon)} + n(t), \tag{5.32}$$

where $\rho^0_{0,i}$, $\rho^1_{0,i}$ are the main pulse pseudo-symbols associated with the coded symbols b^0_i and b^1_i, respectively. The expression of the filtered and sampled received signal, however, depends on two factors: the detection filter and the sampling time. We first focus on the impact of the detection filter f on the PAM approximation of $\tilde{s}(t = kT)$ given in (5.6). The classic choice is to take $w_0(t)$ as a detection filter like the works carried for linear modulations [23] or MSK-type signals [127, 128]. However, as shown in Chapter 3, the use of this filter would correlate the noise and would expand the XTCQM-PAM approximation of $\tilde{s}(t = kT)$ from a 3-bit level representation to a 5-bit one, which is undesirable. Therefore, it is necessary to use other alternative detection filters such as the Wiener filter or the Equiripple filter given in Section 3.4.2. The choice between one of these two filters will be justified later when we introduce the proposed decoder structures.

If we take for example the Equiripple filter, we showed that thanks to the performance of the SISO 8-XTCQM-PAM detector, the signal $\tilde{s}_0(4nT)$ given in (5.4) can accurately be approximated as

$$\tilde{s}_0(4nT) = jb^0_{4n-1}\tilde{w}_0(T) + b^0_{4n}\tilde{w}_0(0) + jb^0_{4n+1}\tilde{w}_0(-T) \tag{5.33}$$

where

$$\tilde{w}_0(iT) = \int w_0(t) f(t - iT) dt. \tag{5.34}$$

This approximation can also be observed in Figure 5.7 where we can notice that the contribution of the symbols $b^0_{4n-3}, b^0_{4n-2}, b^0_{4n+2}, b^0_{4n+3}$ that are modulated by $\tilde{w}_0$ is insignificant

when $t = 0$. However, if we now consider the approximation of $\tilde{s}_1(4nT - \Delta\tau T)$ when $\Delta\tau \neq 0$, it can be seen from the same figure that the contribution of either b^1_{4n-2} or b^1_{4n+2} is no longer negligible. In this case, $\tilde{s}_1(4nT - \Delta\tau T)$ can be approximated as

$$\tilde{s}_1(4nT - \Delta\tau T) \approx \begin{cases} jb^1_{4n-1}\tilde{w}_0(T - \Delta\tau T) + b^1_{4n}\tilde{w}_0(-\Delta\tau T) \\ \quad + jb^1_{4n+1}\tilde{w}_0(-T - \Delta\tau T) + b^1_{4n+2}\tilde{w}_0(-2T - \Delta\tau T), & \Delta\tau < 0, \\ jb^1_{4n-1}\tilde{w}_0(T - \Delta\tau T) + b^1_{4n}\tilde{w}_0(-\Delta\tau T) \\ \quad + jb^1_{4n+1}\tilde{w}_0(-T - \Delta\tau T) + b^1_{4n-2}\tilde{w}_0(2T - \Delta\tau T), & \Delta\tau > 0. \end{cases} \tag{5.35}$$

Equation (5.35) shows that the presence of the differential delay extends the approximation of $\tilde{s}_1(4nT - \Delta\tau T)$ to a 4-bit level one. This observation is in accordance with what has been presented in Section 5.3.3 using the XTCQM representation. Therefore, the decoder should take the contribution of the fourth symbol into account and/or exploit $y_{\Delta\tau}$ as well since the sampling time $t = 4nT + \Delta\tau T$ is the optimal one for $\tilde{s}_1(4nT - \Delta\tau T)$. In the state of the art solution described in Section 5.3.3, both options have been implemented together in the LS decoding algorithm. In this work, we choose to only use the second option, i.e., to use both samples of y and $y_{\Delta\tau}$ in the decoding algorithm while keeping a 3-bit level approximation even in the presence of a differential delay, i.e.,

$$\begin{array}{ll} \tilde{s}_1(4nT - \Delta\tau T) \approx \sum_{i=-1}^{+1} \rho^1_{0,4n-i}\tilde{w}_0(iT - \Delta\tau T), & |\Delta\tau| < 1, \\ \tilde{s}_0(4nT + \Delta\tau T) \approx \sum_{i=-1}^{+1} \rho^0_{0,4n-i}\tilde{w}_0(iT + \Delta\tau T), & |\Delta\tau| < 1. \end{array} \tag{5.36}$$

We show in the following sections that this choice leads to many attractive simplifications.

5.4.2 Description of the algorithm

We first incorporate the approximation of (5.36) in (5.4) to get

$$\begin{cases} y(4k) = h_0 \sum_{i=-1}^{+1} \rho^0_{0,4k-i}\tilde{w}_0(iT) + h_1 \sum_{i=-1}^{+1} \rho^1_{0,4k-i}\tilde{w}_0(iT - \Delta\tau T) + \tilde{n}(4kT), & (5.37) \\ y_{\Delta\tau}(4k) = h_0 \sum_{i=-1}^{+1} \rho^0_{0,4k-i}\tilde{w}_0(iT + \Delta\tau T) + h_1 \sum_{i=-1}^{+1} \rho^1_{0,4k-i}\tilde{w}_0(iT) + \tilde{n}(4kT + \Delta\tau T) & (5.38) \end{cases}$$

We then define the following metric

$$B^k_m = \frac{1}{2}\left(y(4k + m) + y_{\Delta\tau}(4k + m)\right), \quad m \in \{0, ..., 3\}. \tag{5.39}$$

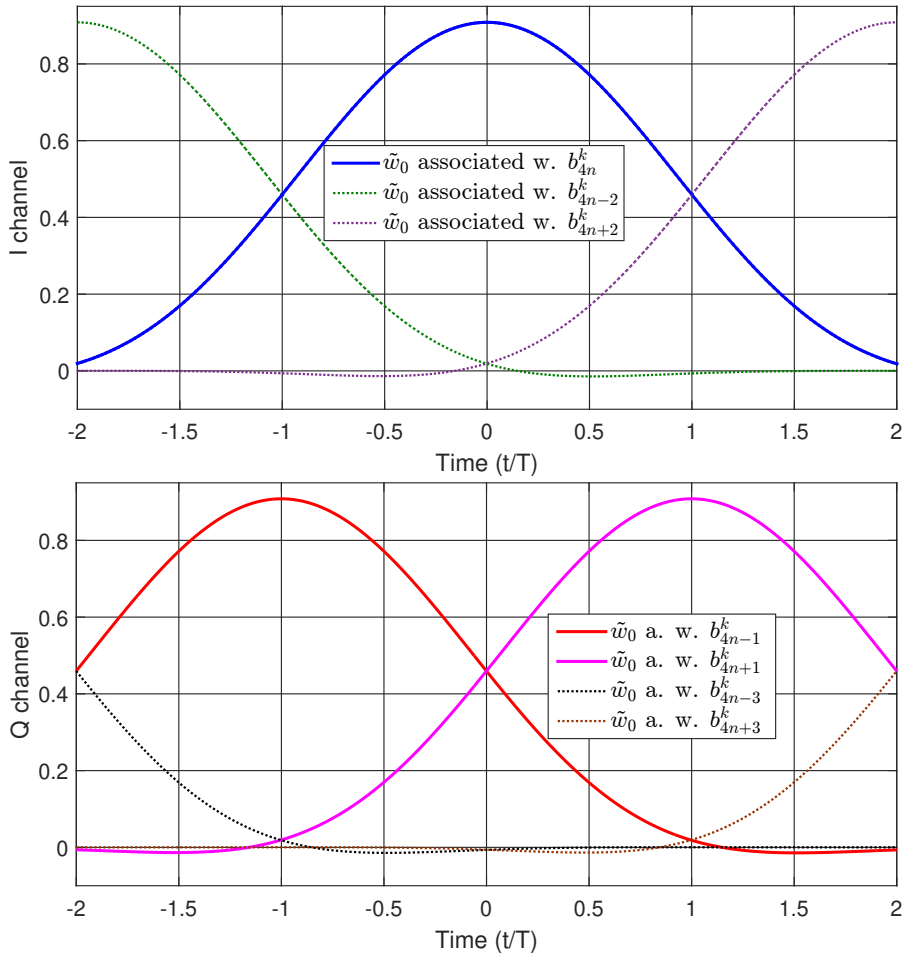

Figure 5.7 – Illustration of the differential delay effect on the PAM approximation of the filtered signal

By developing (5.39), we get

$$B_0^k = h_0\left(Ab_{4k} + jCb_{4(k-1)+3} + jDb_{4k+1}\right) + h_1\left(Ab_{4k+2} - jDb_{4(k-1)+1} + jCb_{4k+3}\right) + \tilde{n}_\Delta(4kT), \quad (5.40)$$

$$B_1^k = h_0\left(jAb_{4k+1} + Cb_{4k} - Db_{4k+2}\right) + h_1\left(jAb_{4k+3} + Db_{4k+2} + Cb_{4k}\right) + \tilde{n}_\Delta((4k+1)T), \quad (5.41)$$

$$B_2^k = h_0\left(-Ab_{4k+2} + jCb_{4k+1} + jDb_{4k+3}\right) + h_1\left(Ab_{4k} + jDb_{4k+3} - jCb_{4k+1}\right) + \tilde{n}_\Delta((4k+2)T), \quad (5.42)$$

$$B_3^k = h_0\left(jAb_{4k+3} - Cb_{4k+2} + Db_{4(k+1)}\right) + h_1\left(-jAb_{4k+1} + Db_{4k} + Cb_{4(k+1)+2}\right) + \tilde{n}_\Delta((4k+3)T), \quad (5.43)$$

where

$$\begin{cases} A = \dfrac{1}{2}\left(\tilde{w}_0(0) + \tilde{w}_0(\Delta\tau T)\right) = \dfrac{1}{2}\left(\tilde{w}_0(0) + \tilde{w}_0(-\Delta\tau T)\right), & (5.44) \\ C = \dfrac{1}{2}\left(\tilde{w}_0(-T) + \tilde{w}_0(-T + \Delta\tau T)\right) = \dfrac{1}{2}\left(\tilde{w}_0(T) + \tilde{w}_0(T - \Delta\tau T)\right), & (5.45) \\ D = \dfrac{1}{2}\left(\tilde{w}_0(T) + \tilde{w}_0(T + \Delta\tau T)\right) = \dfrac{1}{2}\left(\tilde{w}_0(-T) + \tilde{w}_0(-T - \Delta\tau T)\right), & (5.46) \\ \tilde{n}_\Delta(kT) = \dfrac{1}{2}(\tilde{n}(kT) + \tilde{n}(kT + \Delta\tau T)). & (5.47) \end{cases}$$

When $\Delta\tau \neq 0$, we have $C \neq D$. We group B_0^k with $(B_2^k)^*$ and B_1^k with $(B_3^k)^*$, we get,

$$\begin{bmatrix} B_0^k \\ (B_2^k)^* \end{bmatrix} = A\begin{bmatrix} h_0 & h_1 \\ h_1^* & -h_0^* \end{bmatrix}\begin{bmatrix} b_{4k} \\ b_{4k+2} \end{bmatrix} + jC\begin{bmatrix} h_0 & 0 \\ 0 & -h_0^* \end{bmatrix}\begin{bmatrix} b_{4(k-1)+3} \\ b_{4k+1} \end{bmatrix} + jD\begin{bmatrix} h_0 & 0 \\ 0 & -h_0^* \end{bmatrix}\begin{bmatrix} b_{4k+1} \\ b_{4k+3} \end{bmatrix} + jD\begin{bmatrix} -h_1 & 0 \\ 0 & -h_1^* \end{bmatrix}\begin{bmatrix} b_{4(k-1)+1} \\ b_{4k+3} \end{bmatrix} + jC\begin{bmatrix} h_1 & 0 \\ 0 & h_1^* \end{bmatrix}\begin{bmatrix} b_{4k+3} \\ b_{4k+1} \end{bmatrix} + \begin{bmatrix} \tilde{n}_\Delta(4kT) \\ \tilde{n}_\Delta^*((4k+2)T) \end{bmatrix}, \quad (5.48)$$

$$\begin{bmatrix} B_1^k \\ (B_3^k)^* \end{bmatrix} = jA\begin{bmatrix} h_0 & h_1 \\ h_1^* & -h_0^* \end{bmatrix}\begin{bmatrix} b_{4k+1} \\ b_{4k+3} \end{bmatrix} + C\begin{bmatrix} h_0 & 0 \\ 0 & -h_0^* \end{bmatrix}\begin{bmatrix} b_{4k} \\ b_{4k+2} \end{bmatrix} + D\begin{bmatrix} -h_0 & 0 \\ 0 & h_0^* \end{bmatrix}\begin{bmatrix} b_{4k+2} \\ b_{4(k+1)} \end{bmatrix} + D\begin{bmatrix} h_1 & 0 \\ 0 & h_1^* \end{bmatrix}\begin{bmatrix} b_{4+2} \\ b_{4k} \end{bmatrix} + C\begin{bmatrix} h_1 & 0 \\ 0 & h_1^* \end{bmatrix}\begin{bmatrix} b_{4k} \\ b_{4(k+1)+2} \end{bmatrix} + \begin{bmatrix} \tilde{n}_\Delta((4k+1)T) \\ \tilde{n}_\Delta^*((4k+3)T) \end{bmatrix}. \quad (5.49)$$

We define the matrix $\mathbf{H}_2$, which is composed of the channel gains

$$\mathbf{H}_2 = \begin{bmatrix} h_0 & h_1 \\ h_1^* & -h_0^* \end{bmatrix}, \quad (5.50)$$

and we multiply (5.48) on the left by $\mathbf{H}_2^{\mathcal{H}}$. We then take the real part of the obtained 2×1 vector, we get

$$Re\left\{\mathbf{H}_2^{\mathcal{H}}\begin{bmatrix}B_0^k\\(B_2^k)^*\end{bmatrix}\right\}=\begin{bmatrix}l_0^k\\l_1^k\end{bmatrix}=\begin{bmatrix}A\chi b_{4k}+D\zeta b_{4(k-1)+1}+C\zeta b_{4k+1}+(D-C)\zeta b_{4k+3}\\A\chi b_{4k+2}+C\zeta b_{4(k-1)+3}+D\zeta b_{4(k+1)+3}+(D-C)\zeta b_{4k+1}\end{bmatrix}+Re\left\{\begin{bmatrix}h_0^*\tilde{n}_\Delta(4kT)+h_1\tilde{n}_\Delta^*((4k+2)T)\\h_1^*\tilde{n}_\Delta(4kT)-h_0\tilde{n}_\Delta^*((4k+2)T)\end{bmatrix}\right\},\tag{5.51}$$

where $\chi=|h_0|^2+|h_1|^2$ and $\zeta=Im(h_0^*h_1)$. We also multiply (5.49) on the left by $\mathbf{H}_2^{\mathcal{H}}$ and take this time the imaginary part of the obtained vector as follows

$$Im\left\{\mathbf{H}_2^{\mathcal{H}}\begin{bmatrix}B_1^k\\(B_3^k)^*\end{bmatrix}\right\}=\begin{bmatrix}l_2^k\\l_3^k\end{bmatrix}=\begin{bmatrix}A\chi b_{4k+1}+C\zeta b_{4k}+D\zeta b_{4(k+1)}+(D-C)\zeta b_{4k+2}\\A\chi b_{4k+3}+D\zeta b_{4k+2}+C\zeta b_{4(k+1)+2}+(D-C)\zeta b_{4k}\end{bmatrix}+Im\left\{\begin{bmatrix}h_0^*\tilde{n}_\Delta((4k+1)T)+h_1\tilde{n}_\Delta^*((4k+3)T)\\h_1^*\tilde{n}_\Delta((4k+1)T)-h_0\tilde{n}_\Delta^*((4k+3)T)\end{bmatrix}\right\}.\tag{5.52}$$

When $\Delta\tau=0$, we have $C=D$. In this case, the symbols that appear in l_0^k and l_2^k do not appear in l_1^k and l_3^k. Thus l_0^k and l_2^k can be processed separately from l_1^k and l_3^k. This particular case matches what has been found in [126] for OQPSK. However when $\Delta\tau\neq 0$, it is necessary to jointly process the four elements $\{l_m^k\}_{m\in\{0,\dots,3\}}$ together. Using (5.51) and (5.52), we define the following vectors

$$\underline{x}=\left(\dots,l_0^k,l_2^k,l_1^k,l_3^k,l_0^{k+1},l_2^{k+1},l_1^{k+1},l_3^{k+1},\dots\right)^{\mathcal{T}}\tag{5.53}$$

$$\underline{b}=\left(\dots,b_{4k},b_{4k+1},b_{4k+2},b_{4k+3},b_{4k+4},b_{4k+5},b_{4k+6},b_{4k+7},\dots\right)^{\mathcal{T}},\tag{5.54}$$

and we show that we can link them as follows

$$\underline{x}=\mathbf{G}\underline{b}+\underline{u},\tag{5.55}$$

where

$$\mathbf{G}=\begin{bmatrix}\mathbf{G}_1&\mathbf{G}_2^{\mathcal{T}}&\mathbf{0}_4&\dots&\dots&\mathbf{0}_4\\\mathbf{G}_2&\mathbf{G}_1&\mathbf{G}_2^{\mathcal{T}}&\mathbf{0}_4&\ddots&\vdots\\\mathbf{0}_4&\mathbf{G}_2&\mathbf{G}_1&\mathbf{G}_2^{\mathcal{T}}&\ddots&\vdots\\\vdots&\ddots&\ddots&\ddots&\ddots&\mathbf{0}_4\\\vdots&\ddots&\ddots&\ddots&\ddots&\mathbf{G}_2^{\mathcal{T}}\\\mathbf{0}_4&\dots&\dots&\mathbf{0}_4&\mathbf{G}_2&\mathbf{G}_1\end{bmatrix},\tag{5.56}$$

and

$$\mathbf{G}_1 = \begin{bmatrix} A\chi & C\zeta & 0 & 0 \\ C\zeta & A\chi & (D-C)\zeta & 0 \\ 0 & (D-C)\zeta & A\chi & D\zeta \\ 0 & 0 & D\zeta & A\chi \end{bmatrix}, \quad \mathbf{G}_2 = \begin{bmatrix} 0 & D\zeta & 0 & 0 \\ 0 & 0 & 0 & 0 \\ 0 & 0 & 0 & C\zeta \\ 0 & 0 & 0 & 0 \end{bmatrix}. \tag{5.57}$$

The vector $\underline{u}$ is composed of the noise terms in (5.51)−(5.52) and is built in the same way as $\underline{x}$. The auto-correlation matrix of the noise $\underline{u}$ is then $\mathbf{M}_u = N_0\tilde{\mathbf{G}}$, where $\tilde{\mathbf{G}}$ has the same shape as $\mathbf{G}$. However, the coefficients A, C and D are a function of the auto-correlation of the detection filter and not of the convolution of w_0 and the detection filter f.

As highlighted in [127], the maximum likelihood metric for a signal expressed as (5.55) is

$$\Lambda\left(\underline{x}, \underline{b}\right) = \left(\underline{x} - \mathbf{G}\underline{b}\right)^{\mathcal{H}} \mathbf{M}_u^{-1} \left(\underline{x} - \mathbf{G}\underline{b}\right). \tag{5.58}$$

To simplify the above expression, it is necessary to assume that $\tilde{\mathbf{G}} \approx \mathbf{G}$. The accuracy of this assumption depends on the used detection filter. Ideally, the best candidate would be the main pulse w_0. However, this choice makes the 3-bit representation of the signal unaccurate. Fortunately, since the combined filter given in Chapter 3 is derived from the expression of the main pulse w_0 while keeping a 3-bit approximation reliable, this filter could be a good candidate. Based on Cavers development given in [127] and since $\underline{x}$, $\underline{b}$ and $\mathbf{G}$ are composed of real values, the metric to be maximized can be expressed as

$$\Lambda\left(\underline{x}, \underline{b}\right) = 2\underline{b}^{\mathcal{T}}\underline{x} - \underline{b}^{\mathcal{T}}\mathbf{G}\underline{b}. \tag{5.59}$$

If we look at the expression of $\mathbf{G}$, we can notice that this matrix can be decomposed as follows

$$\mathbf{G} = \mathbf{G}_D + \mathbf{G}_U + \mathbf{G}_U^{\mathcal{T}}, \tag{5.60}$$

where $\mathbf{G}_D$ is a diagonal matrix and $\mathbf{G}_U$ is a strictly upper triangular one. Then, (5.59) becomes

$$\Lambda\left(\underline{x}, \underline{b}\right) = 2\underline{b}^{\mathcal{T}}\underline{x} - 2\underline{b}^{\mathcal{T}}\mathbf{G}_U\underline{b} - \underline{b}^{\mathcal{T}}\mathbf{G}_D\underline{b}. \tag{5.61}$$

The computation of (5.61) provides the following result

$$\begin{aligned}\Lambda\left(\underline{x},\underline{b}\right) = &\sum_k b_{4k}\left(2x_{4k} - (D-C)\zeta b_{4k+3} - C\zeta b_{4k+1} - D\zeta b_{4(k-1)+1}\right) - A\chi|b_{4k}|^2 \\ &+ \sum_k b_{4k+1}\left(2x_{4k+1} - (D-C)\zeta b_{4k+2} - C\zeta b_{4k} - D\zeta b_{4(k+1)}\right) - A\chi|b_{4k+1}|^2 \\ &+ \sum_k b_{4k+2}\left(2x_{4k+2} - (D-C)\zeta b_{4k+1} - D\zeta b_{4k+3} - C\zeta b_{4(k-1)+3}\right) - A\chi|b_{4k+2}|^2 \\ &+ \sum_k b_{4k+3}\left(2x_{4k+3} - D\zeta b_{4k+2} - C\zeta b_{4(k+1)+2}\right) - A\chi|b_{4k+3}|^2, \end{aligned} \tag{5.62}$$

where x_k is the k^{th} element of the vector $\underline{x}$. The above result shows that estimating $\underline{b}$ requires a Viterbi algorithm whose branch metric $\lambda(n)$ depends on the output of n modulo 4, i.e.,

$$\lambda(n) = \begin{cases} b_n\left(2x_n - (D-C)\zeta b_{n+3} - C\zeta b_{n+1} - D\zeta b_{n-3}\right) - A\chi|b_n|^2, & \text{if } n = 4k, \\ b_n\left(2x_n - (D-C)\zeta b_{n+1} - C\zeta b_{n-1} - D\zeta b_{n+3}\right) - A\chi|b_n|^2, & \text{if } n = 4k+1, \\ b_n\left(2x_n - (D-C)\zeta b_{n-1} - D\zeta b_{n+1} - C\zeta b_{n-3}\right) - A\chi|b_n|^2, & \text{if } n = 4k+2, \\ b_n\left(2x_n - D\zeta b_{n-1} - C\zeta b_{4n+3}\right) - A\chi|b_n|^2, & \text{if } n = 4k+3. \end{cases} \tag{5.63}$$

The branch metric is then defined by the 7-tuple

$$\sigma_n = \left(b_{n-3}, b_{n-2}, b_{n-1}, b_n, b_{n+1}, b_{n+2}, b_{n+3}\right), \tag{5.64}$$

and the Viterbi algorithm operates with 64 states with 2 branches coming out from each state.

Discussion:

- We can notice from (5.63) that the branch metric only depends on 4 symbols out of 7 when $n = 4k + m,\ m \in \{0, 1, 2\}$ and 3 symbols out of 7 when $n = 4k + 3$. Therefore, decoding a block of 4 symbols only requires the computation of 56 branches, which is much less significant than what is required using STBD-XTCQM-LS given in Section 5.3.3 (480 branches are needed for the STBD-XTCQM-LS solution). The complexity is thus approximately reduced by a factor of 8.

- We focused on the 3-bit level representation to approximate the samples $\{\tilde{s}_i\}_{i\in\{0,1\}}$ because the above development is only valid for this case. If we take the 4-bit level representation or the 5-bit level one, for instance, we cannot get the desired simplifications described above.

- The proposed algorithm, namely STBD-PAM-ML, initially provides hard outputs, but since it operates using a Viterbi algorithm with 2 branches coming out from each state, a

soft output Viterbi algorithm (SOVA) [134] can be applied to get log-likelihood ratios (LLRs).

5.4.3 Preliminary simulation results

In this section, the transmitted signal is the first PAM approximation of SOQPSK-TG, i.e.,

$$s_k(t) = \sum_i \rho_{0,i}^k w_0(t - iT), \qquad k \in \{0, 1\}. \tag{5.65}$$

The modulus of the channel gains are $|h_0| = |h_1| = \frac{\sqrt{2}}{2}$. We start by plotting the BER performance of the proposed decoder as a function of the detection filter. We take the 3 filters given in Section 3.4.2: the main pulse w_0, the optimal combined (Wiener) filter $\tilde{w}_0$ and the Equiripple FIR. We also take $\Delta\tau = 0$ and $\theta = 0$. We remind that $\theta = arg(h_1) - arg(h_0)$. It can be seen from Figure 5.8 that using the main pulse as a detection filter does not give acceptable BER performance for this channel configuration. However, if we use the combined filter, the BER curve is close to the optimal curve of OQPSK. This observation confirms our earlier analysis regarding the importance of the detection filter's choice. Hence, we choose the combined filter $\tilde{w}_0$ for this decoder.

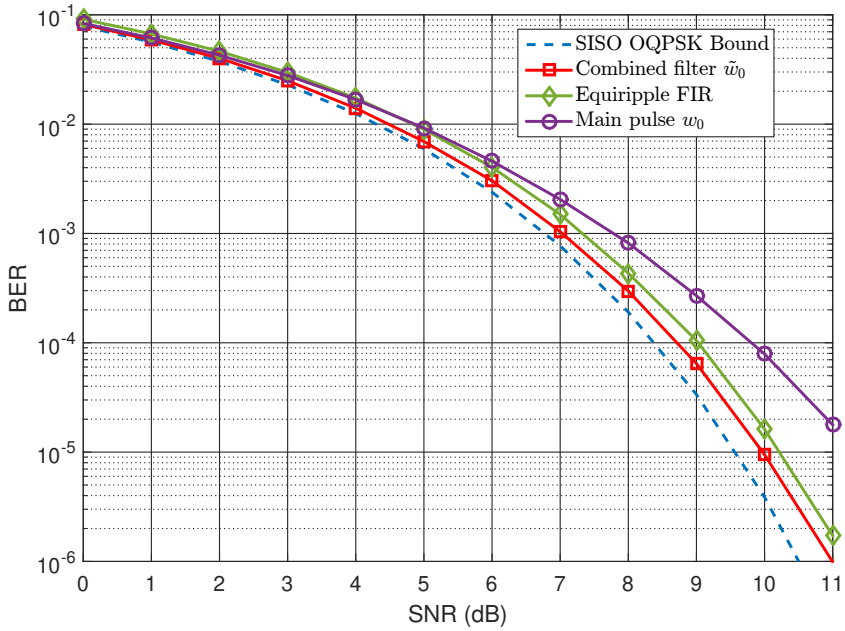

Note: The transmitted signal is the first PAM approximation of SOQPSK-TG

Figure 5.8 – BER performance of the proposed decoder using different detection filters

We also plot in Figure 5.9 the BER curves for different values of θ and the average BER curve when the angle θ varies over the interval $[0, 2\pi)$ in steps of 0.1π. We notice that the

proposed decoder offers almost identical performance whatever the angle between h_0 and h_1. We now introduce a non-zero differential delay and we depict in Figure 5.10 the BER performance of the proposed decoder. We also highlight the effect of not mitigating this differential delay by decoding the symbols while considering that $\Delta\tau = 0$ at the receiver side (dashed lines). The different curves show that it is important to take into account this differential delay when decoding and this can successfully be done using the proposed decoder.

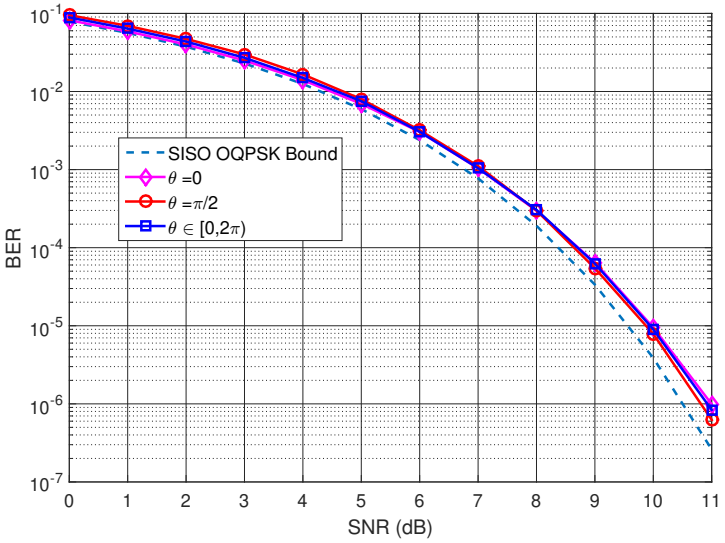

Note: The transmitted signal is the first PAM approximation of SOQPSK-TG

Figure 5.9 – BER performance of the proposed decoder for different θ values

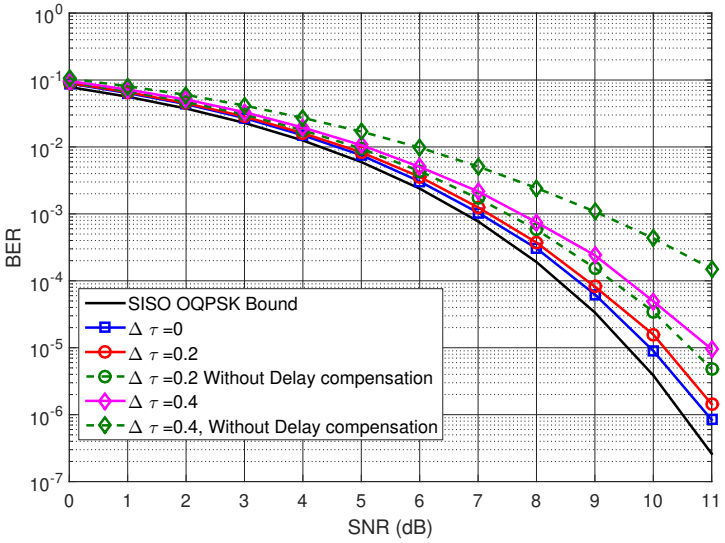

Note: The transmitted signal is the first PAM approximation of SOQPSK-TG

Figure 5.10 – BER performance of the proposed decoder for different $\Delta\tau$ values, $\theta \in [0, 2\pi)$

5.4.4 Final simulation Results

In this section, we consider that the exact SOQPSK-TG signal is transmitted and we plot the BER performance of the proposed decoder for different values of θ and $\Delta\tau$. The BER performance curves are depicted in Figure 5.11 and Figure 5.12 and are compared to the best state of the art solution, which is described in Section 5.3.3. Several remarks can be made from these figures:

- When $\theta = \frac{\pi}{2}$, the proposed decoder slightly outperforms the state of the art solution.
- The proposed decoder successfully reduces the differential delay effect as shown in Figure 5.12 and gives very acceptable BER performance for the different θ angle values.
- The performance gap between the case where $\theta = \frac{\pi}{2}$ and the case where $\theta = 0$ is higher than the one reached by STBD-XTCQM-LS. However, it is much less important than the one obtained using the OD-LS decoder of Section 5.3.2.
- The BER performance gap between the case where $\theta = \frac{\pi}{2}$ and the case where $\theta = 0$ is not present if the PAM approximation is transmitted instead of the exact signal as shown in Figure 5.9. This suggests that the remaining PAM components of each signal $\{s_k\}_{k\in\{0,1\}}$ mutually interfere and thus the signals s_k are not rigorously orthogonal. This observation can also be verified by giving the expression the pseudo-symbols $\rho_{1,n}^k$ as a function of the data symbols b:

$$\begin{aligned}\underline{\rho_1}^0 &= [..., -b_{4(n-1)+3}b_{4n}b_{4n+1},\ jb_{4n}b_{4n+1}b_{4n+2},\ b_{4n+1}b_{4n+2}b_{4n+3},\ jb_{4n+2}b_{4n+3}b_{4(n+1)}, ...]\\ \underline{\rho_1}^1 &= [..., b_{4(n-1)+1}b_{4n+2}b_{4n+3},\ -jb_{4n+2}b_{4n+3}b_{4n},\ b_{4n+3}b_{4n}b_{4n+1},\ jb_{4n}b_{4n+1}b_{4(n+1)+2}, ...]\end{aligned} \tag{5.66}$$

We can see that these pseudo-symbols are not Alamouti encoded and have no particular link that connect them together. Due to the memory effect of the modulation, it is unlikely to build a STBC that begets full diversity for SOQPSK-TG. However, it is possible to mitigate the interference of the pseudo-symbols $\rho_{1,n}^k$ by including their contributions in the decoding algorithm (this has been done implicitly in STBD-XTCQM-LS via the XTCQM representation and will also be performed in the following section) or by introducing a new encoder that reduces the interference of $\rho_{1,n}^k$ and further improves the quality of the received signal (Chapter 6 of the manuscript).

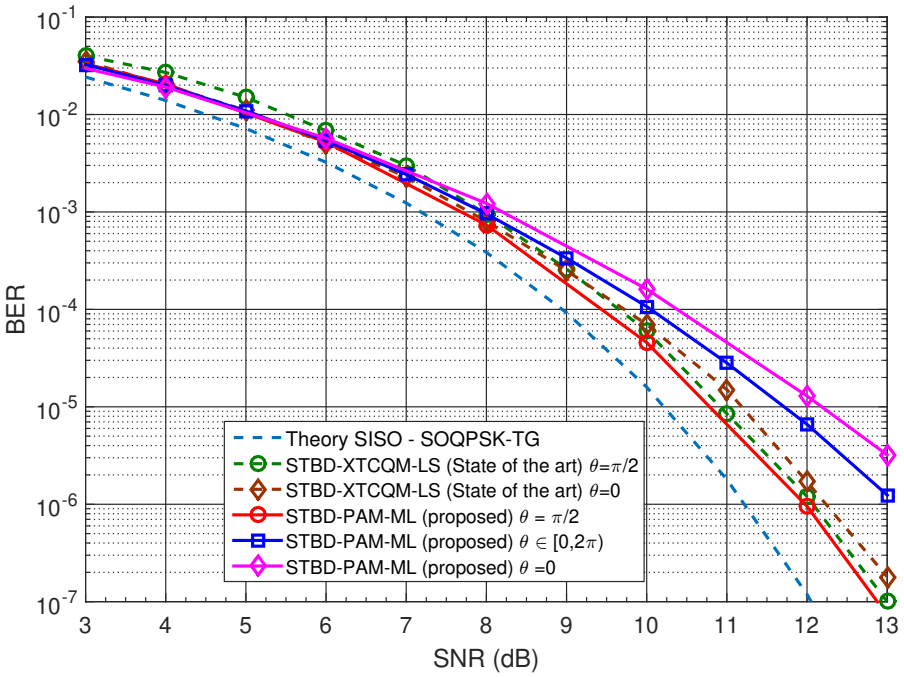

Figure 5.11 – BER performance of the proposed decoder - $\Delta\tau = 0$

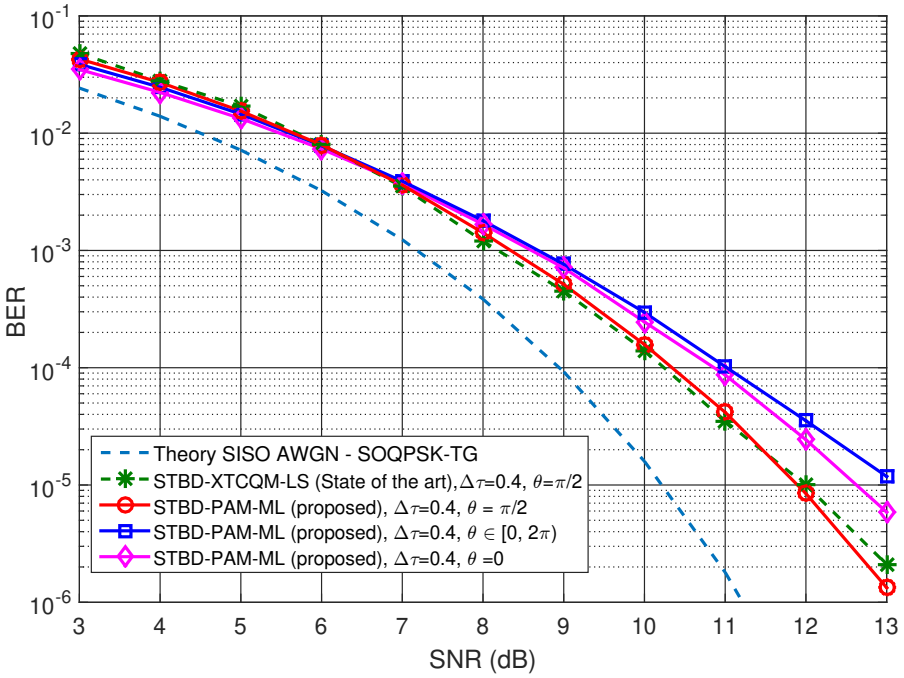

Figure 5.12 – BER performance of the proposed decoder - $\Delta\tau = 0.4$

5.5 Second proposed decoder: PAM based decoder using the LS approach: STBD-PAM-LS

5.5.1 Received signal model using the second PAM approximation

In this section, we include the contribution of the pseudo-symbols $\{\rho_{1,i}^m\}_{m\in\{0,1\}}$ in the decoding algorithm. To do so, we use the second approximation of the revamped PAM decomposition. The received signal is thus approximated as

$$r(t) \approx h_0 \left(\sum_i \rho_{0,i}^0 w_0(t-iT) + \sum_i \rho_{1,i}^0 w_1'(t-iT) \right) + h_1 \left(\sum_i \rho_{0,i}^1 w_0(t-\Delta\epsilon-iT) + \sum_i \rho_{1,i}^1 w_1'(t-\Delta\epsilon-iT) \right) + n(t). \quad (5.67)$$

We now focus on the filtered samples $\{\tilde{s}_k\}_{k\in\{0,1\}}$ and we use the same approach of Section 5.4.1. We keep a 3-bit level approximation and we express the samples as

$$\begin{array}{l} \tilde{s}_1(4nT-\Delta\tau T) \approx \sum_{i=-1}^{+1} \rho_{0,4n-i}^1 \tilde{w}_0(iT-\Delta\tau T), +\rho_{1,4n}^1 \tilde{w}_1(-\Delta\tau T), \quad |\Delta\tau|<1 \\ \tilde{s}_0(4nT+\Delta\tau T) \approx \sum_{i=-1}^{+1} \rho_{0,4n-i}^0 \tilde{w}_0(iT+\Delta\tau T) + \rho_{1,4n}^0 \tilde{w}_1(+\Delta\tau T), \quad |\Delta\tau|<1, \end{array} \quad (5.68)$$

where

$$\tilde{w}_1(kT) = \int w_1'(t) f(t-kT) dt. \quad (5.69)$$

Thus, y and $y_{\Delta\tau}$ become

$$\begin{cases} y(4k) = h_0 \sum_{i=-1}^{+1} \rho_{0,4k-i}^0 \tilde{w}_0(iT) + h_0 \rho_{1,4k}^0 \tilde{w}_1(0) + h_1 \sum_{i=-1}^{+1} \rho_{0,4k-i}^1 \tilde{w}_0(iT-\Delta\tau T) \\ \quad + h_1 \rho_{1,4k}^1 \tilde{w}_1(-\Delta\tau T) + \tilde{n}(4kT), \quad (5.70) \\ y_{\Delta\tau}(4k) = h_0 \sum_{i=-1}^{+1} \rho_{0,4k-i}^0 \tilde{w}_0(iT+\Delta\tau T) + h_0 \rho_{1,4k}^0 \tilde{w}_1(\Delta\tau T) + h_1 \sum_{i=-1}^{+1} \rho_{0,4k-i}^1 \tilde{w}_0(iT) \\ \quad + h_1 \rho_{1,4k}^1 \tilde{w}_1(0) + \tilde{n}(4kT+\Delta\tau T), \quad (5.71) \end{cases}$$

5.5.2 Description of the algorithm

Due to the mapping between $\{\rho_{1,n}^m\}_{m\in\{0,1\}}$ and the data symbols $\underline{b}$, which exhibits the memory effect of the SOQPSK modulation, we were unable to formulate the problem similarly to (5.55). Therefore, we use the least squares approach to develop the decoding algorithm. This approach is inspired from both the STBD-XTCQM-LS decoder and the LS detector developed in Section 3.4. We first consider that the received signal is filtered using the Equiripple FIR filter given

in Section (3.4.2). This filter keeps the noise samples $\tilde{n}(nT)$ almost white after filtering. If we also suppose that the noise samples $\tilde{n}(nT + \Delta\tau T)$ are also white and that N symbols are transmitted, then the LS estimate is

$$\hat{\underline{b}} = \underset{b}{\operatorname{argmin}}\{\Lambda(\underline{b})\}, \tag{5.72}$$

where

$$\Lambda(\underline{b}) = \sum_{n=0}^{N-1} |y(k) - (h_0\tilde{s}_0(nT) + h_1\tilde{s}_1(kT - \Delta\tau T))|^2 + |y_{\Delta\tau}(k) - (h_0\tilde{s}_0(nT + \Delta\tau T) + h_1\tilde{s}_1(nT))|^2 . \tag{5.73}$$

The log-likelihood function $\Lambda(\underline{b})$ represents the error between the received samples and a reconstructed version of the noiseless signal. The complexity of the decoder depends on the used model to generate $\{\tilde{s}_i(nT)\}_{i\in\{0,1\}}$. For this solution, we use the PAM approximation of $\{\tilde{s}_i(nT)_{i\in\{0,1\}}\}$ given in (5.68).

To resolve (5.72), we define an equivalent symbol S_n as the concatenation of the 4 consecutive bits involved in the Alamouti encoding process, i.e., $S_n = [\tilde{b}_{4n},\ \tilde{b}_{4n+1},\ \tilde{b}_{4n+2},\ \tilde{b}_{4n+3}]$, such that $\tilde{b}_{4n} = \frac{1}{2}(b_{4n} + 1)$. The LS estimate of (5.72) is equivalent to the following one

$$\hat{\underline{S}} = \underset{S}{\operatorname{argmin}}\{\Lambda(\underline{S})\}, \tag{5.74}$$

where

$$\Lambda(\underline{S}) = \sum_{n=0}^{(N-1)/4} \left(\sum_{m=-1}^{2} \left|B_{n,m}^{(0)}\right|^2 + \left|B_{n,m}^{(\Delta\tau)}\right|^2 \right), \tag{5.75}$$

and

$$\begin{aligned} B_{n,m}^{(0)} &= y(4n+m) - (h_0\tilde{s}_0(4nT + mT) + h_1\tilde{s}_1(4nT + mT - \Delta\tau T)), \\ B_{n,m}^{(\Delta\tau)} &= y_{\Delta\tau}(4n+m) - (h_0\tilde{s}_0(4nT + mT + \Delta\tau T) + h_1\tilde{s}_1(4nT + m)). \end{aligned} \tag{5.76}$$

We then replace $s_i(nT)_{i\in\{0,1\}}$ by their approximations given in (5.68) and we obtain the following expressions of $B_{n,m}^{(0)}$ and $B_{n,m}^{(\Delta\tau)}$

$$B_{n,m}^{(0)} = y(4n+m) - h_0\left(\sum_{i=-1}^{+1} \rho_{0,4n+m-i}^{0}\tilde{w}_0(iT) + \rho_{1,4n+m}^{0}\tilde{w}_1(0)\right) - h_1\left(\sum_{i=-1}^{+1} \rho_{0,4n+m-i}^{1}\tilde{w}_0(iT - \Delta\tau T) + \rho_{1,4n+m}^{1}\tilde{w}_1(-\Delta\tau T)\right), \tag{5.77}$$

$$B_{n,m}^{(\Delta\tau)} = y_{\Delta\tau}(4n+m) - h_0\left(\sum_{i=-1}^{+1}\rho_{0,4n+m-i}^{0}\tilde{w}_0(iT+\Delta\tau T) + \rho_{1,4n+m}^{0}\tilde{w}_1(\Delta\tau T)\right) - h_1\left(\sum_{i=-1}^{+1}\rho_{0,4n+m-i}^{1}\tilde{w}_0(iT) + \rho_{1,4n+m}^{1}\tilde{w}_1(0)\right). \quad (5.78)$$

Thanks to the proposed 3-bit level approximation of SOQPSK, the expressions of $B_{n,m}^{(0)}$ and $B_{n,m}^{(\Delta\tau)}$ remain unchanged whatever the sign of $\Delta\tau$. Formulating the problem as in (5.74) allows us a Viterbi algorithm to estimate the equivalent symbol sequence $\underline{S}$. The trellis of the Viterbi algorithm is given in Figure 5.13 and is composed of 16 states and 256 branches. Let the state of the node i at the epoch n be denoted $S_n(i)$. Using (5.75), (5.77) and (5.78), the branch metric associated with the transition $S_{n-1}(i) \to S_n(j)$ is defined as

$$\lambda(S_{n-1}(i), S_n(j)) = \sum_{m=-1}^{2}\left|B_{n,m}^{(0)}\right|^2 + \left|B_{n,m}^{(\Delta\tau)}\right|^2. \quad (5.79)$$

We develop below the expressions of $B_{n,m}^{(0)}$ and $B_{n,m}^{(\Delta\tau)}$ as a function of the branch bits:

$$B_{n,-1}^{(0)} = y(4n-1) - h_0\left[-b_{4n-2}\tilde{w}_0(T) + jb_{4n-1}\tilde{w}_0(0) + b_{4n}\tilde{w}_0(-T) + jb_{4n-2}b_{4n-1}b_{4n}\tilde{w}_1(0)\right] - h_1\left[b_{4n-4}\tilde{w}_0(T-\Delta\tau T) - jb_{4n-3}\tilde{w}_0(-\Delta\tau T) + b_{4n+2}\tilde{w}_0(-T-\Delta\tau T) + jb_{4n-4}b_{4n-3}b_{4n+2}\tilde{w}_1(-\Delta\tau T)\right], \quad (5.80)$$

$$B_{n,-1}^{(\Delta\tau)} = y_{\Delta\tau}(4n-1) - h_0\left[-b_{4n-2}\tilde{w}_0(T+\Delta\tau T) + jb_{4n-1}\tilde{w}_0(\Delta\tau T) + b_{4n}\tilde{w}_0(-T+\Delta\tau T) + jb_{4n-2}b_{4n-1}b_{4n}\tilde{w}_1(+\Delta\tau T)\right] - h_1\left[b_{4n-4}\tilde{w}_0(T) - jb_{4n-3}\tilde{w}_0(0) + b_{4n+2}\tilde{w}_0(-T) + jb_{4n-4}b_{4n-3}b_{4n+2}\tilde{w}_1(0)\right], \quad (5.81)$$

$$B_{n,0}^{(0)} = y(4n) - h_0\left[jb_{4n-1}\tilde{w}_0(T) + b_{4n}\tilde{w}_0(0) + jb_{4n+1}\tilde{w}_0(-T) - b_{4n-1}b_{4n}b_{4n+1}\tilde{w}_1(0)\right] - h_1\left[-jb_{4n-3}\tilde{w}_0(T-\Delta\tau T) + b_{4n+2}\tilde{w}_0(-\Delta\tau T) + jb_{4n+3}\tilde{w}_0(-T-\Delta\tau T) + b_{4n-3}b_{4n+2}b_{4n+3}\tilde{w}_1(-\Delta\tau T)\right], \quad (5.82)$$

$$B_{n,0}^{(\Delta\tau)} = y_{\Delta\tau}(4n) - h_0\left[jb_{4n-1}\tilde{w}_0(T+\Delta\tau T) + b_{4n}\tilde{w}_0(\Delta\tau T) + jb_{4n+1}\tilde{w}_0(-T+\Delta\tau T) - b_{4n-1}b_{4n}b_{4n+1}\tilde{w}_1(\Delta\tau T)\right] - h_1\left[-jb_{4n-3}\tilde{w}_0(T) + b_{4n+2}\tilde{w}_0(0) + jb_{4n+3}\tilde{w}_0(-T) + b_{4n-3}b_{4n+2}b_{4n+3}\tilde{w}_1(0)\right], \quad (5.83)$$

$$B_{n,1}^{(0)} = y(4n+1) - h_0\left[b_{4n}\tilde{w}_0(T) + jb_{4n+1}\tilde{w}_0(0) - b_{4n+2}\tilde{w}_0(-T) + jb_{4n}b_{4n+1}b_{4n+2}\tilde{w}_1(0)\right] - h_1\left[b_{4n+2}\tilde{w}_0(T-\Delta\tau T) - jb_{4n+3}\tilde{w}_0(-\Delta\tau T) + b_{4n}\tilde{w}_0(-T-\Delta\tau T) - jb_{4n+2}b_{4n+3}b_{4n}\tilde{w}_1(-\Delta\tau T)\right], \quad (5.84)$$

$$B_{n,1}^{(\Delta\tau)} = y_{\Delta\tau}(4n+1) - h_0\left[b_{4n}\tilde{w}_0(T+\Delta\tau T) + jb_{4n+1}\tilde{w}_0(\Delta\tau T) - b_{4n+2}\tilde{w}_0(-T+\Delta\tau T) + jb_{4n}b_{4n+1}b_{4n+2}\tilde{w}_1(\Delta\tau T)\right] - h_1\left[b_{4n+2}\tilde{w}_0(T) - jb_{4n+3}\tilde{w}_0(0) + b_{4n}\tilde{w}_0(-T) - jb_{4n+2}b_{4n+3}b_{4n}\tilde{w}_1(0)\right], \quad (5.85)$$

$$B_{n,2}^{(0)} = y(4n+2) - h_0\left[jb_{4n+1}\tilde{w}_0(T) - b_{4n+2}\tilde{w}_0(0) + jb_{4n+3}\tilde{w}_0(-T) + b_{4n+1}b_{4n+2}b_{4n+3}\tilde{w}_1(0)\right] - h_1\left[jb_{4n+3}\tilde{w}_0(T-\Delta\tau T) + b_{4n}\tilde{w}_0(-\Delta\tau T) - jb_{4n+1}\tilde{w}_0(-T-\Delta\tau T) + b_{4n+3}b_{4n}b_{4n+1}\tilde{w}_1(-\Delta\tau T)\right], \quad (5.86)$$

$$B_{n,2}^{(\Delta\tau)} = y_{\Delta\tau}(4n+2) - h_0\left[jb_{4n+1}\tilde{w}_0(T+\Delta\tau T) - b_{4n+2}\tilde{w}_0(\Delta\tau T) + jb_{4n+3}\tilde{w}_0(-T+\Delta\tau T) + b_{4n+1}b_{4n+2}b_{4n+3}\tilde{w}_1(\Delta\tau T)\right] - h_1\left[jb_{4n+3}\tilde{w}_0(T) + b_{4n}\tilde{w}_0(0) - jb_{4n+1}\tilde{w}_0(-T) + b_{4n+3}b_{4n}b_{4n+1}\tilde{w}_1(0)\right], \quad (5.87)$$

Equations (5.80) —(5.87) are valid whatever the sign of $\Delta\tau$ unlike the sub-metrics described in (5.22)—(5.25). Equation (5.79) shows that the proposed branch metric is a sum of 8 sub-metrics $B_{n,m}^{(0)}$ and $B_{n,m}^{(\Delta\tau)}$, and therefore, one can assume that it is necessary to compute 2048 different sub-metric values to get (5.79). Fortunately, each sub-metric does not involve all the underlying bits that compose the trellis of Figure 5.13. If we look for instance at (5.80), we can notice that it only involves 6 different bits out of 8. Thus, only 64 different values of this sub-metric are computed instead of 256. Following the same line of reasoning, it is necessary to only compute 16 different values of (5.84) and (5.85) since each one of them is a function of 4 different bits.

As a consequence, the total number of the computed sub-metric values goes from 2048 to 320. The obtained result is less important than 480, which is the number of branch metrics required by the state of the art solution [131] to decode a block of 4 bits. This optimization process does not affect the final output of (5.79) since the calculated values of the sub-metrics are simply duplicated and rearranged with respect to the proposed trellis.

Once the branch metrics $\lambda(S_{n-1}(i), S_n(j))$ are calculated, the cumulative metrics $\Gamma_n(S_n(j))$ can be updated as follows

$$\Gamma_n(S_n(j)) = \min_i\left[\xi_n(S_{n-1}(i), S_n(j))\right], \ (i,j) \in \{1,...,16\}^2, \quad (5.88)$$

where

$$\xi_n(S_{n-1}(i), S_n(j)) = \Gamma_{n-1}(S_{n-1}(i)) + \lambda(S_{n-1}(i), S_n(j)). \tag{5.89}$$

Once the cumulative metrics are calculated and the survivor paths are stored for a given depth δ, we perform a trace-back loop to get $\underline{\hat{S}}$ and therefore the estimated underlying bit sequence $\underline{\hat{b}}$. The described algorithm provides hard outputs. We show in the following how to get soft decisions, which is very advantageous when the STC scheme is paired with FEC systems.

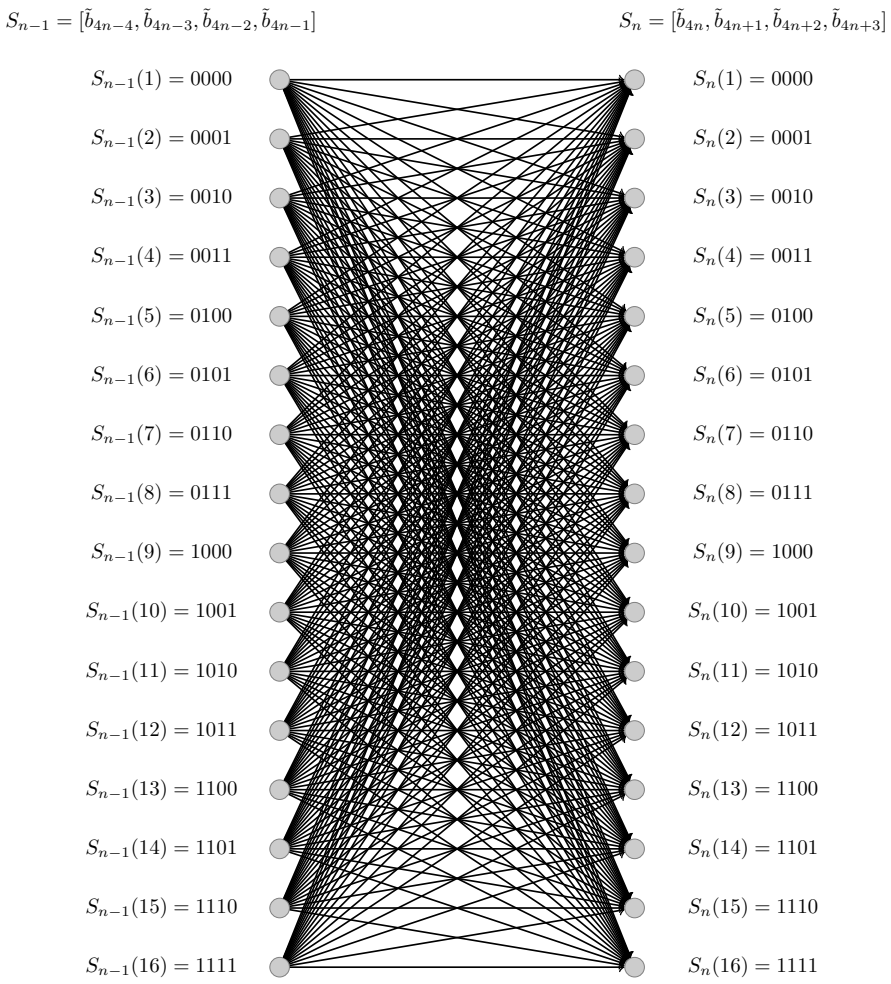

Figure 5.13 – Proposed trellis of the STBD-PAM-LS solution

Soft Decision Alamouti Decoder

In order to extract soft decisions instead of hard ones, we apply the MAX-Log-MAP equivalent SOVA for non-binary codes that has been introduced in [135]. This solution suits our case since the proposed trellis is built on the equivalent non-binary symbol S_n and since the branch

metrics introduced in (5.79) represent the forward recursion of the SOVA thanks to the elegant interpretation of the MAX-LOG-MAP algorithm given in [136]. Based on [134] and instead of storing the survivor paths, we instead store the reliability difference at epoch n whose definition is

$$R_n(S_{n-1}(i), S_n(j)) = \Gamma_n(S_n(j)) - \xi_n(S_{n-1}(i), S_n(j)), \quad (i,j) \in (\{1, ..., 16\})^2. \tag{5.90}$$

The reliability difference of the survivor path then equals zero in our case. Once (5.90) is computed for a given depth, the backward recursion is yielded and the Max-Log joint probability is obtained as follows

$$P(S_{n-1}(i), S_n(j), r) = \beta_n(S_n(i)) + R_n(S_{n-1}(i), S_n(j)), \tag{5.91}$$

where

$$\beta_{n-1}(S_{n-1}(j)) = \min_i \left[R_n(S_{n-1}(i), S_n(j)) + \beta_n(S_n(i)) \right]. \tag{5.92}$$

Finally the soft output of the symbol S_n is

$$P(\hat{S}_n = S_n(j) \setminus r) = \min_i \left[P(S_{n-1}(i), S_n(j), r) \right], \tag{5.93}$$

Since S_n is composed of the 4 bits $[\tilde{b}_{4n}, \tilde{b}_{4n+1}, \tilde{b}_{4n+2}, \tilde{b}_{4n+3}]$, the conversion of the soft output (LLR) to the bit level is straightforward.

Besides optimizing the number of calculated sub-metrics as shown above, further complexity reduction techniques can be applied to the soft-output version of this decoder and the hard-output one. We propose in the following a sub-optimal method that allows reducing the complexity of the trellis search.

5.5.3 Optimizing the computational complexity

The classical approach to estimate the underlying bit sequence and its soft information consists of making a full trellis search up to a certain depth δ and then performing a trace-back loop. This means in our case that it is necessary to calculate 256 branch metrics at each epoch and to store 16δ values for hard decoding and 256δ reliability values for soft decoding. In this work, we propose to reduce the number of operations via the M-algorithm whose concept is introduced in [137] for hard decoding and in [138, 139] for soft decoding. This technique is a sub-optimal tree search since it only crosses a part of the trellis. It consists of extending the M best states instead of all the states from one epoch to the next. This partial extension reduces in our case the number of calculated branch metrics since it goes down from 256 to $16M$. As for soft decoding, we propose to combine the M-algorithm with the MAX-Log-MAP SOVA presented in the previous section, and we call it M-SOVA. This approach is different from the soft output

M-algorithm (SOMA) introduced in [139] since the latter is based on the conventional SOVA for binary codes [134]. The proposed algorithm is described in Algorithm 1.

Result: Bit level LLRs
Initialization Let $\{i_1, ..., i_M\}$ be the best M states;
$i_1 = 1, ..., i_M = M$;
for $n = 1$ **to** δ **do**
  Compute sub-metrics: (5.80) —(5.87);
  Compute competing paths cumulative metrics $\xi_n(S_{n-1}(i), S_n(j))$ using (5.79) and (5.89) for $i \in \{i_1, ..., i_M\}$ and $j \in \{1, ..., 16\}$;
  Update $\Gamma_n(S_n(j))$ using (5.88);
  Compute the reliability difference values $R_n(S_{n-1}(i), S_n(j))$ using and (5.90) for $i \in \{i_1, ..., i_M\}$ and $j \in \{1, ..., 16\}$;
  Sort $\Gamma_n(S_n(j))$ and update $(i_1, ..., i_M)$;
  Store $(i_1, ..., i_M)$ and $R_n(S_{n-1}(i), S_n(j))$;
end
Backward recursion;
for $n = \delta$ **down to** 1 **do**
  Compute $\beta_n(S_n(j))$ using (5.92) for $j \in \{i_1, ..., i_M\}$ and $i \in \{1, ..., 16\}$;
end
LLR;
for $n = 1$ **to** δ **do**
  Compute LLRs using (5.91) and (5.93) for $i \in \{i_1, ..., i_M\}$ and $j \in \{1, ..., 16\}$;
  Convert symbol LLRs to bit LLRs
end

Algorithm 1: Proposed M-SOVA algorithm for space time block decoding

5.5.4 Simulation Results

In this section we consider that the exact SOQPSK-TG signal is transmitted and that $|h_0| = |h_1| = \frac{\sqrt{2}}{2}$.

BER performance without FEC systems

We begin by evaluating the different algorithms without applying channel coding. We plot in Figure 5.14 the BER performance of the STBD-PAM-LS solution for different θ values. This figure shows that the proposed decoder outperforms the STBD-XTCQM-LS solution whatever the value of the angle θ. Even though the 3 bit level approximation of the PAM representation and 3 bit level approximation of the XTCQM representation are equivalent as highlighted in Section 2.4, the performance improvement can be due to several factors such as the detection filter type, the use of a Viterbi algorithm and the choice of sub-metrics that are employed to calculate the branch metric.

We can also notice that STBD-PAM-LS varies with respect to the angle between h_0 and h_1. However, the gap between the best case scenario ($\theta = \frac{\pi}{2}$) and the worst case scenario ($\theta = 0$) is less critical than the one using the STBD-PAM-ML solution of Section 5.4. This gap reduction is due to taking into account the presence of the pulse w_1 when calculating the branch metrics. Another way to verify the impact of the presence of w_1 is to take the same structure of STBD-PAM-LS algorithm and to compute the branch metrics given in (5.80)-(5.87) while setting $w_1 = 0$. The BER performance of this case is plotted in the same figure with a triangular marker, and it highlights a more significant gap between the $\theta = 0$ curve and the $\theta = \frac{\pi}{2}$ one.

We now evaluate the impact of $\Delta\tau$ on the performance of STBD-PAM-LS solution. It can be seen from Figure 5.15 that the proposed solution is more robust to this channel impairment than the STBD-XTCQM-LS algorithm despite keeping a 3-bit level approximation at the receiver side. The performance loss when $\Delta\tau = 0.4$ is 1 dB for the state of the art solution whereas the loss is less than 0.2 dB when we consider the proposed solution. The robustness of the proposed algorithm is also highlighted in Figure 5.16 where different differential delay values are considered. Each curve of this figure represents the average BER curve when the angle θ varies over the interval $[0, 2\pi)$ in steps of 0.1π. Note also that the BER curves when the differential delay is negative are identical.

In Figure 5.17, we plot the BER curves of the STBD-PAM-LS M-algorithm for different values of M. It can be seen that taking the 2 best states instead of 16 at each epoch is sufficient to get very near optimal performance. Thus, incorporating the M-algorithm for hard decoding can offer an important complexity reduction while maintaining very satisfying BER performance.

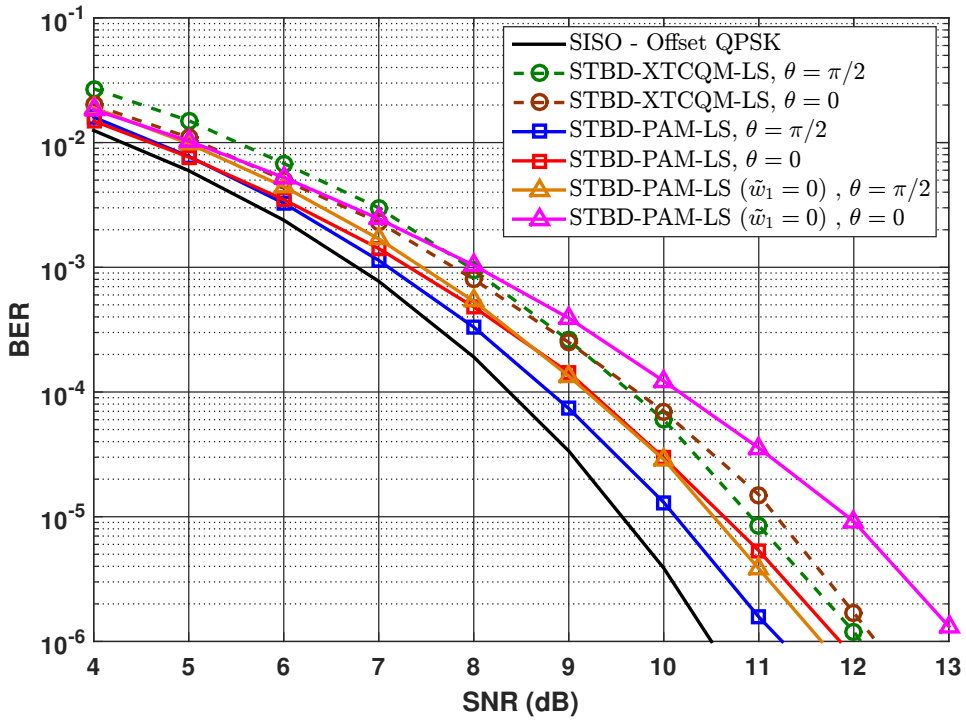

Figure 5.14 – BER performance of the STBD-PAM-LS solution - $\Delta\tau = 0$

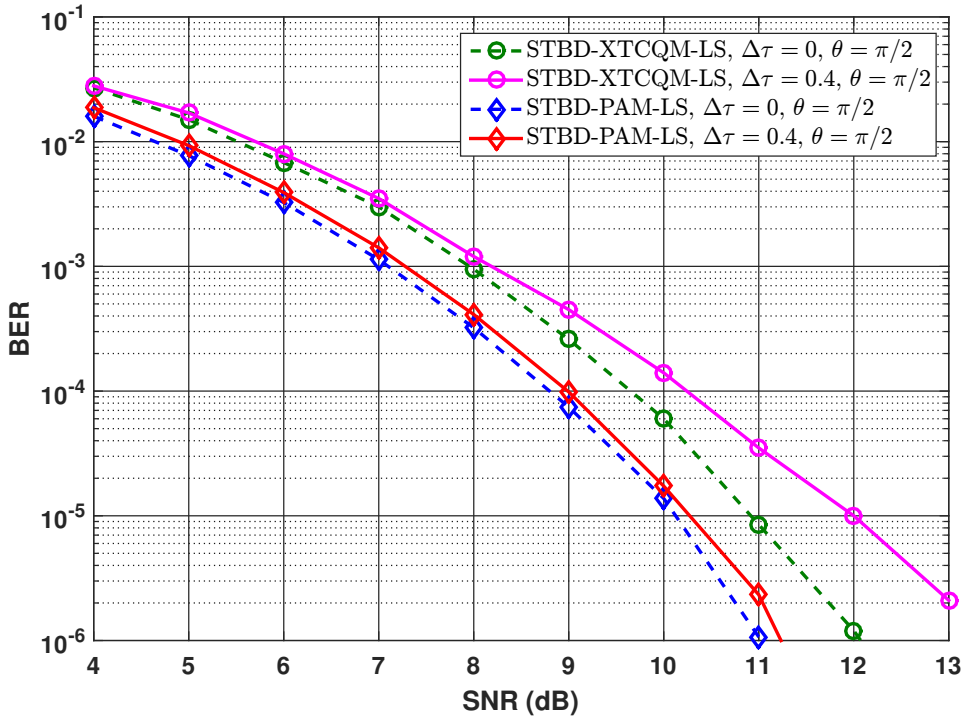

Figure 5.15 – BER performance of the STBD-PAM-LS solution - $\Delta\tau = 0.4$

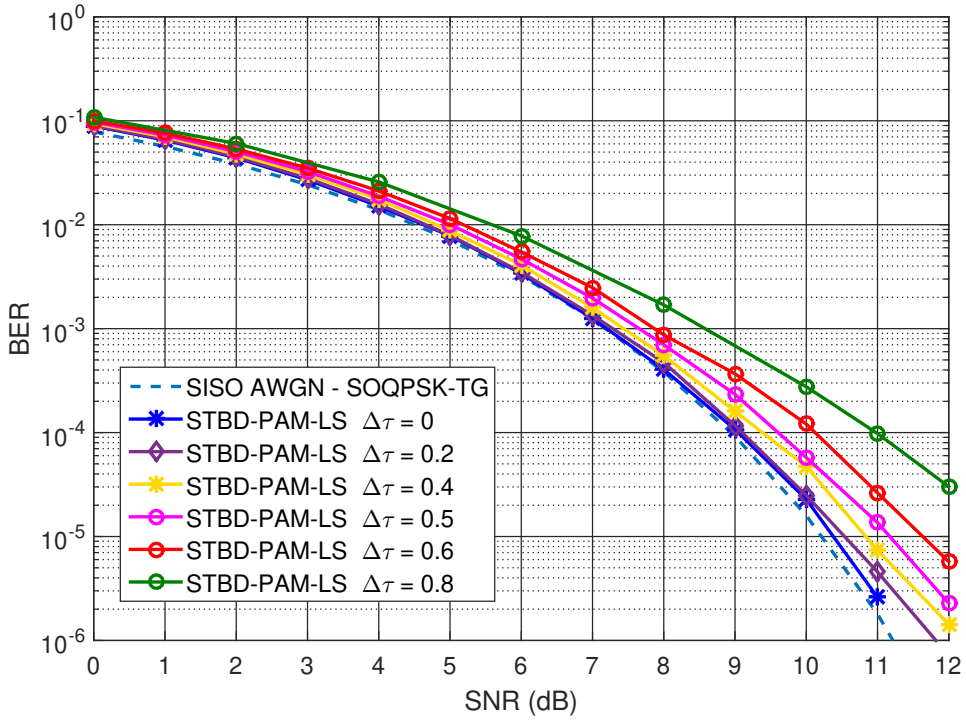

Figure 5.16 – BER performance of the STBD-PAM-LS solution for different $\Delta\tau$ values - $\theta \in [0, 2\pi)$

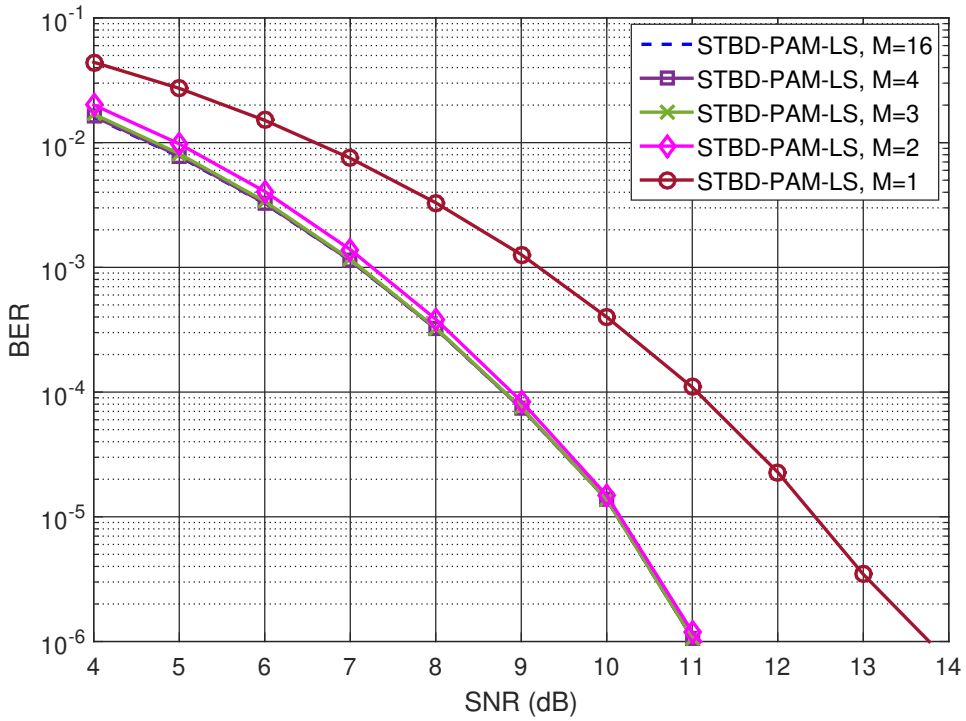

Figure 5.17 – BER performance for different M values, $\Delta\tau = 0$, $\theta = \frac{\pi}{2}$

BER performance with FEC systems

In this section, we evaluate the BER performance of the M-SOVA. To do so, the bit stream $\underline{b}$ is encoded using a low density parity check (LDPC) encoder of rate $R = \frac{2}{3}$ and whose number of bits contained in the information word K is equal to 4096. This encoder is developed at NASA's JPL and fully described in [133]. It is also standardized in IRIG [5] as of this writing. The LDPC-encoded bits are then Alamouti encoded as described in Section 5.2 to generate the two signals s_0 and s_1. The received signal is demodulated using the M-SOVA and the estimated LLRs are fed to the LDPC-decoder, which performs a maximum of $N_{it} = 200$ iterations. The BER performance curves are plotted in Figure 5.18 for different values of M. We also show in this figure the BER performance of the SOVA detector for the SISO case [84] to use it as a reference. We can see that the 5-SOVA performs within 0.3 dB of 16-SOVA case. Moreover, we can notice that the BER performance is more sensitive to M when we apply soft decoding since the LRRs get more and more over-estimated as long as we decrease M. Despite that, the proposed M-SOVA gives close BER performance when $M \geq 5$.

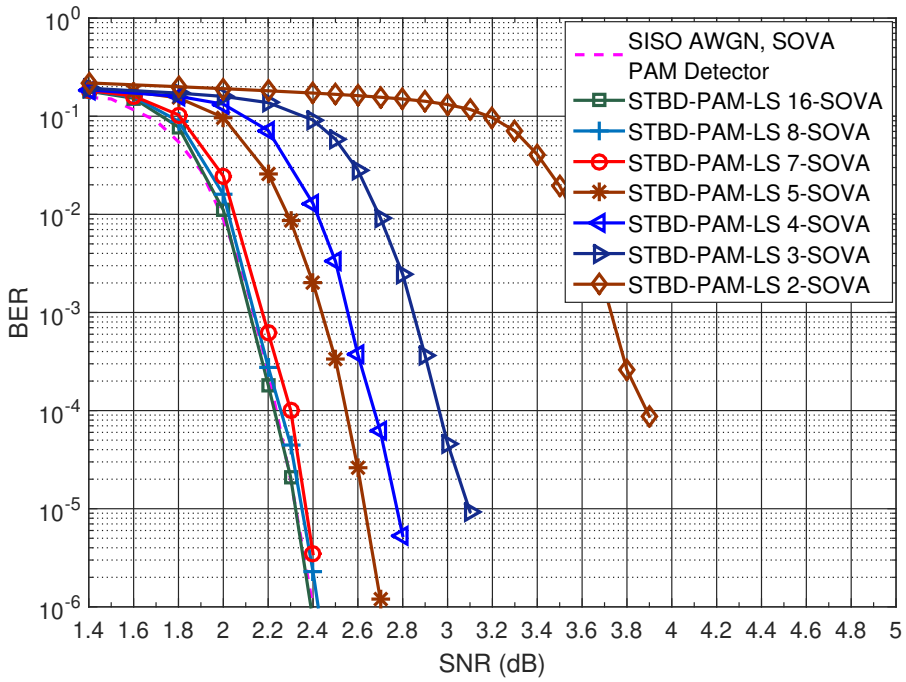

Figure 5.18 – BER performance for LDPC when paired with M-SOVA, $\Delta\tau = 0$, $\Delta\phi = 0$

As highlighted at the end of Section 5.4.2, it is also possible to get soft outputs if we pair the STBD-PAM-ML solution with the SOVA given in [134]. This solution has been implemented and compared to STBD-PAM-LS 16-SOVA. The obtained results are depicted in Figure 5.19 and show that the performance gap between the two solutions is low (≤ 0.4 dB) when $\Delta\tau = 0$.

This result is expected since both solutions have close BER performance when the SNR is low. However, the performance gap increases when $\Delta\tau \neq 0$.

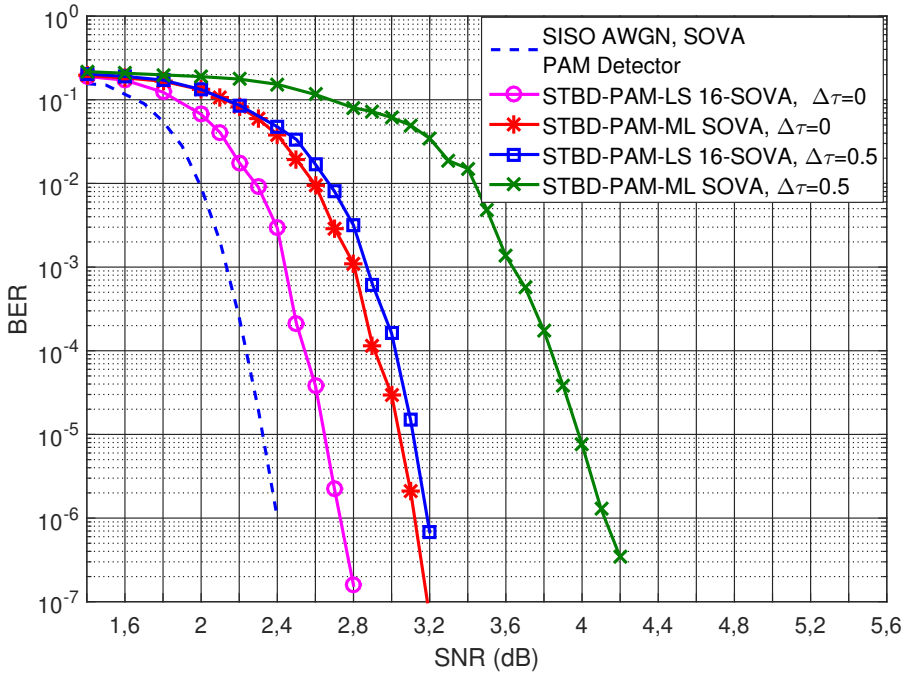

Figure 5.19 – STBD-PAM-LS M-SOVA Vs STBD-PAM-ML SOVA - $\theta \in [0, 2\pi)$

5.6 Complexity comparison of the different Alamouti decoders

We compare in Table 5.1 the necessary number operations to estimate one block of 4 bits via the state of the art solution (SBTD-XTCQM-LS) and the proposed algorithms (i.e., by taking a depth $\delta = 1$). It can be seen that the STBD-PAM-ML solution offers very low complexity compared to the other solutions. However, this comes at the expense of some BER performance loss for certain angles θ between h_0 and h_1. It can also be noticed that the number of additions and multiplications is relatively important for LS solutions. This is mainly due to the sub-metrics computation since they require 960 multiplications and 1920 additions if we take the state of the art solution [16]. On the other hand, the computation of the 8 sub-metrics involves 640 multiplications and 640 additions in our case. The use of the M-algorithm can further reduce the number of operations and the required storage memory without adding a significant complexity due to the use of sorting algorithms since these algorithms have an average complexity order of $O(16\log(16))$ [139].

Table 5.1 – Complexity comparison of the different Alamouti decoders

	State of the art STBD-XTCQM-LS	Proposed solution STBD-PAM-LS with M-algorithm	Proposed solution STBD-PAM with M-SOVA	Proposed solution STBD-PAM-ML
Addition	3968	$640 + 128M$	$644 + 176M$	576
Multiplication	960	640	640	64
$\|.\|^2$	480	320	320	–
Comparison	240	$15M$	$46M + 40$	256
Sorting operation of 16 elements	0	1	1	0
Number of stored values	16	16	$17M$	64 for hard decoding 128 for soft decoding

In all the simulations above, we considered that the receiver only captures the line of sight components. However, this scenario is particular as highlighted in Chapter 4 since the ground station can also capture multiple reflections of the transmitted signals. In the following section, we formulate the problem in the presence of multipath, and we propose a new multipath channel estimator for this scenario.

5.7 Multipath Channel Estimation in The STBC Scenario

Implementing space-time block decoders in practical systems requires estimating the channel parameters such as the differential delay and the channel gains along with the frequency offset before decoding. The different estimators are described in [131] and they are composed of:

- a frame synchronization block that allows finding the start of the pilot sequences in the received signal,
- a carrier frequency offset (CFO) estimator,
- a differential delay estimator,
- a channel gains estimator.

The overall system is illustrated in Figure 5.20 and offers satisfying performance when the ground station only captures the line of sight components. However, multipaths are present in aeronautical telemetry channels as highlighted in Chapter 4 and they can cause severe performance loss if not mitigated at the receiver side. In this section, we propose a solution that allows estimating multipath interference in the STC scenario. This solution is placed after the differential delay estimator and replaces the channel gains estimator block since channel gains will be implicitly estimated in the proposed block. The new architecture is given in Figure 5.21.

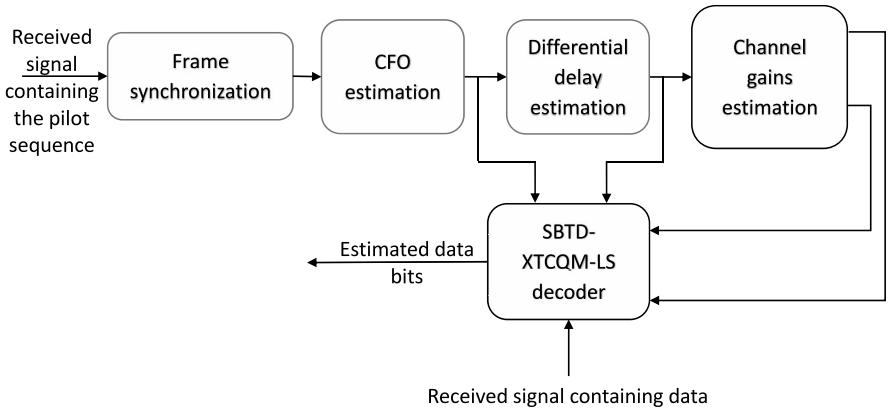

Figure 5.20 – Illustration of the state of the art architecture for the STC scenario

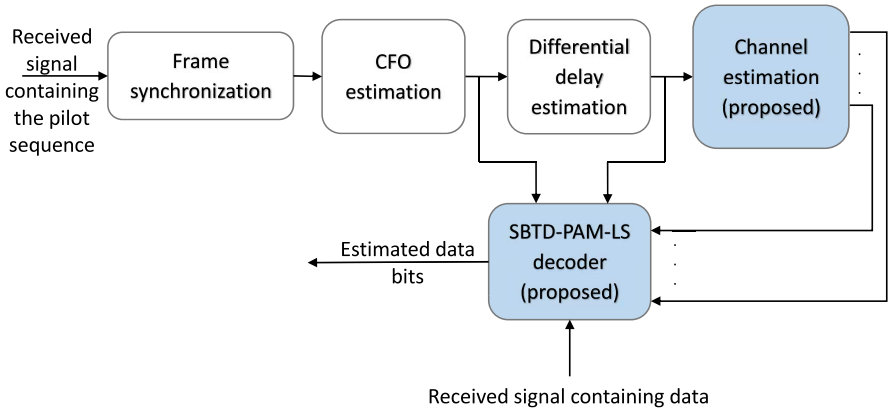

Figure 5.21 – Illustration of the proposed architecture with the channel estimator for STBC Scenario

5.7.1 Received signal model in the presence of multipath

In this section, we only consider the time-invariant wide-band channel model and we suppose that L_0 copies of $s_0(t)$ and L_1 copies of $s_1(t)$ are captured by the ground station. The received signal is then expressed as

$$r(t) = \left[\sum_{i=0}^{L_0-1} h_{2i} s_0(t-\epsilon_{2i}) + \sum_{i=0}^{L_1-1} h_{2i+1} s_1(t-\epsilon_{2i+1}) \right] e^{j2\pi f_0 t} + n(t) \tag{5.94}$$

where $\{h_i\}_{i\in\{0,2,\ldots,2L_0,1,3,\ldots,2L_1+1\}}$ are complex valued attenuations, $\{\epsilon_i\}_{i\in\{0,2,\ldots,2L_0,1,3,\ldots,2L_1+1\}}$ are time delays, and f_0 is the frequency offset. The channel gains $\{h_0, h_1\}$ and the delays $\{\epsilon_0, \epsilon_1\}$ are associated with the line of sight components. The frequency offset is supposed to be null. Using the second approximation of the revamped PAM decomposition, the received

signal at $t+\epsilon_0$ and at $t=t+\epsilon_1$ can be expressed as

$$r(t+\epsilon_0) \approx \sum_{m=0}^{1}\sum_{i}\rho_{m,i}^{0} f_m^0(t-iT) + \sum_{m=0}^{1}\sum_{i}\rho_{m,i}^{1} f_m^1(t-iT-\Delta\epsilon) + n(t+\epsilon_0) \tag{5.95}$$

$$r(t+\epsilon_1) \approx \sum_{m=0}^{1}\sum_{i}\rho_{m,i}^{0} f_m^0(t-iT+\Delta\epsilon) + \sum_{k=0}^{1}\sum_{i}\rho_{m,i}^{1} f_m^1(t-iT) + n(t+\epsilon_1) \tag{5.96}$$

where $\Delta\epsilon = \epsilon_1 - \epsilon_0$ and

$$f_m^0(t) = w_k(t) * \left(h_0\delta(t) + \sum_{i=1}^{L_0-1} h_{2i}\delta(t-(\epsilon_{2i}-\epsilon_0)) \right), \quad m \in \{0,1\}, \tag{5.97}$$

$$f_m^1(t) = w_k(t) * \left(h_1\delta(t) + \sum_{i=1}^{L_1-1} h_{2i+1}\delta(t-(\epsilon_{2i+1}-\epsilon_1)) \right), \quad m \in \{0,1\}. \tag{5.98}$$

The channels $f_m^0(t)$ and $f_m^1(t)$ are defined this way to make the differential delay between the two LOS components visible. The received signal is filtered using the Equiripple detection filter f and sampled at $t=nT+\epsilon_0$ and $t=nT+\epsilon_1$ the same way as in (5.4), we then get

$$y(k) = y(t=kT+\epsilon_0) \approx \sum_{m=0}^{1}\left(\sum_{i=-\frac{N_t^m-1}{2}}^{\frac{N_t^m-1}{2}} \rho_{m,k-i}^{0}\tilde{f}_m^0(i) \right) + \sum_{m=0}^{1}\left(\sum_{i=-\frac{N_t^m-1}{2}}^{\frac{N_t^m-1}{2}} \rho_{m,k-i}^{1}\tilde{f}_m^{1,\Delta\tau}(i) \right) + \tilde{n}(kT+\epsilon_0), \tag{5.99}$$

$$y_{\Delta\tau}(k) = y(t=kT+\epsilon_1) \approx \sum_{m=0}^{1}\left(\sum_{i=-\frac{N_t^m-1}{2}}^{\frac{N_t^m-1}{2}} \rho_{m,k-i}^{0}\tilde{f}_m^{0,\Delta\tau}(i) \right) + \sum_{m=0}^{1}\left(\sum_{i=-\frac{N_t^m-1}{2}}^{\frac{N_t^m-1}{2}} \rho_{m,k-i}^{1}\tilde{f}_m^{1}(i) \right) + \tilde{n}(kT+\epsilon_1), \tag{5.100}$$

where $\Delta\tau = \dfrac{\Delta\epsilon}{T}$, $\tilde{f}_m^0$, $\tilde{f}_m^{0,\Delta\tau}$, $\tilde{f}_m^1$, $\tilde{f}_m^{1,\Delta\tau}$ are composed of N_t^m taps and they are functions of the filtered version of $\left\{f_m^k\right\}_{(k,m)\in(\{0,1\})^2}$ as follows

$$\begin{cases} \tilde{f}_m^k(i) = \tilde{f}_m^k(t = iT), & (k,m) \in (\{0,1\})^2,\ i \in \{-\frac{N_t^m-1}{2}, ..., \frac{N_t^m-1}{2}\}\ , \\ \tilde{f}_m^{0,\Delta\tau}(i) = \tilde{f}_m^0(t = iT + \Delta\tau T), & m \in \{0,1\},\ i \in \{-\frac{N_t^m-1}{2}, ..., \frac{N_t^m-1}{2}\}\ , \\ \tilde{f}_m^{1,\Delta\tau}(i) = \tilde{f}_m^1(t = iT - \Delta\tau T), & m \in \{0,1\},\ i \in \{-\frac{N_t^m-1}{2}, ..., \frac{N_t^m-1}{2}\}\ , \end{cases} \tag{5.101}$$

where

$$\tilde{f}_m^k(t) = \int f_m^k(\tilde{t}) f(\tilde{t} - t) d\tilde{t}, \quad (k,m) \in (\{0,1\})^2. \tag{5.102}$$

Example

We take the case where $L_0 = L_1 = 1$, i.e., no reflected paths are captured and $N_t^0 = 3$, $N_t^1 = 1$. We obtain

$$\begin{cases} \tilde{f}_0^k(i) = h_k \tilde{w}_0(iT), & k \in \{0,1\},\ i \in \{-1, ..., 1\}\ , \\ \tilde{f}_1^k(0) = h_k \tilde{w}_1(0), & k \in \{0,1\}, \\ \tilde{f}_0^{0,\Delta\tau}(i) = h_0 \tilde{w}_0(iT + \Delta\tau T), & i \in \{-1, ..., 1\}\ , \\ \tilde{f}_1^{0,\Delta\tau}(0) = h_0 \tilde{w}_1(\Delta\tau T), & \\ \tilde{f}_0^{1,\Delta\tau}(i) = h_1 \tilde{w}_0(iT - \Delta\tau T), & i \in \{-1, ..., 1\} \\ \tilde{f}_1^{1,\Delta\tau}(0) = h_1 \tilde{w}_1(-\Delta\tau T), & \end{cases} \tag{5.103}$$

and therefore we go back to the expressions given in (5.70), (5.71). We can see that the filters contain both the channel gains and the taps of the PAM waveforms. This reveals that estimating the 8 filters $\left(\tilde{f}_m^k, \tilde{f}_m^{k,\Delta\tau}\right)_{(k,m)\in(\{0,1\})^2}$ is equivalent to estimating the impulse response of channels associated with the signals $s_0(t)$ and $s_1(t)$ at $t = iT + \epsilon_0$ and $t = iT + \epsilon_1$.

5.7.2 Description of the algorithm: Least Mean Square (LMS) Based Channel Estimator

In order to estimate the channels given in (5.99), (5.100), we take advantage of the presence of the pilot sequences that are periodically inserted as described in Figure 5.2. The pilot bit sequence associated with the signal $\{s_k(t)\}_{k\in\{0,1\}}$ is denoted $\underline{b}^{k,p} = \left\{b_0^{k,p}, b_1^{k,p}, ..., b_{L_p-1}^{k,p}\right\}$, where $L_p = 128$ and p is an abbreviation for "pilot". The pseudo-symbols associated with these pilot bits are expressed as:

$$\begin{array}{ll} \rho_{0,i}^{k,p} = b_i^{k,p}, & \rho_{1,i}^{k,p} = -b_{i-1}^{k,p} b_i^{k,p} b_{i+1}^{k,p}, \quad i \text{ even}, \\ \rho_{0,i}^{k,p} = j b_i^{k,p}, & \rho_{1,i}^{k,p} = -j b_{i-1}^{k,p} b_i^{k,p} b_{i+1}^{k,p}, \quad i \text{ odd}. \end{array} \tag{5.104}$$

For the sake of simplicity, we consider that the first samples $y(0), ..., y(L_p-1)$, $y_{\Delta\tau}(0), ..., y_{\Delta\tau}(L_p-1)$ are modulated by the pilot sequences. Let $\hat{f}^k_{m,n}$ be the estimation of $\tilde{f}^k_m$, and $\hat{f}^{k,\Delta\tau}_{m,n}$ be the estimation of $\tilde{f}^{k,\Delta\tau}_m$ at the n^{th} iteration. Since we have no prior knowledge regarding the channel, these filters are initialized using (5.103) while supposing that $h_0 = h_1 = \frac{\sqrt{2}}{2}$.
The estimation algorithm is inspired from the least mean square principle. It consists of calculating the following error functions

$$e_n = y(n) - \sum_{m=0}^{1} \left(\sum_{i=-\frac{N_t^m-1}{2}}^{\frac{N_t^m-1}{2}} \rho^{0,p}_{m,n-i} \hat{f}^0_{m,n}(i) \right) - \sum_{m=0}^{1} \left(\sum_{i=-\frac{N_t^m-1}{2}}^{\frac{N_t^m-1}{2}} \rho^{1,p}_{m,n-i} \hat{f}^{1,\Delta\tau}_{m,n}(i) \right), \tag{5.105}$$

$$e^{\Delta\tau}_n = y_{\Delta\tau}(n) - \sum_{m=0}^{1} \left(\sum_{i=-\frac{N_t^m-1}{2}}^{\frac{N_t^m-1}{2}} \rho^{0,p}_{m,n-i} \hat{f}^{0,\Delta\tau}_{m,n}(i) \right) - \sum_{m=0}^{1} \left(\sum_{i=-\frac{N_t^m-1}{2}}^{\frac{N_t^m-1}{2}} \rho^{1,p}_{m,n-i} \hat{f}^{1}_{m,n}(i) \right), \tag{5.106}$$

and then using them to update the 8 filters as follows:

$$\begin{cases} \hat{f}^0_{m,n+1}(i) = \hat{f}^0_{m,n}(i) + \beta e_n \left(\rho^{0,p}_{m,n-i}\right)^*, & (5.107) \\ \hat{f}^{1,\Delta\tau}_{m,n+1}(i) = \hat{f}^{1,\Delta\tau}_{m,n}(i) + \beta e_n \left(\rho^{1,p}_{m,n-i}\right)^*, & (5.108) \\ \hat{f}^{0,\Delta\tau}_{m,n+1}(i) = \hat{f}^{0,\Delta\tau}_{m,n}(i) + \beta e^{\Delta\tau}_n \left(\rho^{0,p}_{m,n-i}\right)^*, & (5.109) \\ \hat{f}^{1}_{m,n+1}(i) = \hat{f}^{1}_{m,n}(i) + \beta e^{\Delta\tau}_n \left(\rho^{1,p}_{m,n-i}\right)^*, & (5.110) \end{cases}$$

where β is the step size, $i \in \left\{-\frac{N_t^m-1}{2}, ..., \frac{N_t^m-1}{2}\right\}$ and $m \in \{0, 1\}$. We keep repeating the same process until we reach $n_p = L_p - 1 - max(\frac{N_t^0-1}{2}, \frac{N_t^1-1}{2} + 1)$. Since multiple frames are sent during data transmission, the estimated filters in the k^{th} frame can be used to initialize the filters of $k^{\text{th}} + 1$ frame.

5.7.3 New STBD-PAM-LS decoder structure

The new decoder relies on the same principle described in Section 5.5. It uses a Viterbi algorithm whose branch metric is given in (5.79). However, the expressions of $B^{(0)}_{n,m}$ and $B^{(\Delta\tau)}_{n,m}$ are changed as follows

$$B_{n,m}^{(0)} = y(4n+m) - \sum_{i=-\frac{N_t^0-1}{2}}^{\frac{N_t^0-1}{2}} \rho_{0,4n+m-i}^{0} \hat{f}_{0,n_p}^{0}(i) - \sum_{i=-\frac{N_t^1-1}{2}}^{\frac{N_t^1-1}{2}} \rho_{1,4n+m-i}^{0} \hat{f}_{1,n_p}^{0}(i) - \sum_{i=-\frac{N_t^0-1}{2}}^{\frac{N_t^0-1}{2}} \rho_{0,4n+m-i}^{1} \hat{f}_{0,n_p}^{1,\Delta\tau}(i) - \sum_{i=-\frac{N_t^1-1}{2}}^{\frac{N_t^1-1}{2}} \rho_{1,4n+m-i}^{1} \hat{f}_{1,n_p}^{1,\Delta\tau}(i), \quad (5.111)$$

$$B_{n,m}^{(\Delta\tau)} = y_{\Delta\tau}(4n+m) - \sum_{i=-\frac{N_t^0-1}{2}}^{\frac{N_t^0-1}{2}} \rho_{0,4n+m-i}^{0} \hat{f}_{0,n_p}^{0,\Delta\tau}(i) - \sum_{i=-\frac{N_t^1-1}{2}}^{\frac{N_t^1-1}{2}} \rho_{1,4n+m-i}^{0} \hat{f}_{1,n_p}^{0,\Delta\tau}(i) - \sum_{i=-\frac{N_t^0-1}{2}}^{\frac{N_t^0-1}{2}} \rho_{0,4n+m-i}^{1} \hat{f}_{0,n_p}^{1}(i) - \sum_{i=-\frac{N_t^1-1}{2}}^{\frac{N_t^1-1}{2}} \rho_{1,4n+m-i}^{1} \hat{f}_{1,n_p}^{1}(i). \quad (5.112)$$

The size of the trellis depends on the length of the different filters. Since the memory of the pseudo-symbols $\rho_{1,i}$ is of size 2, we assume that $N_t^1 = N_t^0 - 2$. Moreover, we choose to use the same trellis given in Figure 5.13 to keep an acceptable complexity. Therefore, N_t^0 can take values from 3 to 5. If $N_t^0 = 3$, then the STBD-PAM-LS decoder has the same complexity as the original decoder of Section 5.5 because it also needs computing 320 different values of the sub-metrics $B_{n,m}^{(0)}$, $B_{n,m}^{(\Delta\tau)}$ to get (5.79). However, if we take $N_t^0 = 5$, equation (5.79) requires computing 592 different values of the aforementioned sub-metrics.

5.7.4 Simulation results in the presence of multipath

We evaluate the BER performance of the proposed architecture in the presence of multipath, and we compare it to the state of the art architecture given in Figure 5.20, which does not introduce a multipath mitigation algorithm. To do so, we use the different estimators to estimate channel parameters, and then we decode the signal. We remind that difference between the state of the art solution and our proposed one is that the first one only estimates the channel gains of the two LOS components, and decodes the signal via the STBD-XTCQM-LS decoder whereas the proposed architecture estimates the impulse response of the different channels, and then feeds them to the STBD-PAM-LS decoder.

We give in Table 5.2 and Table 5.2 the channel configurations used to evaluate the two architectures. In these tables, even and odd path numbers are associated with the echoes of $s_0(t)$ and $s_1(t)$, respectively. We consider two scenarios: the first one assumes that the reflections

ith path	0	1	2	3
Channel gain $\|h_i\|$ (dB)	-2	-2	-5	-5
delay ϵ_i (t/T)	0	0.25	0.5	0.75

Table 5.2 – STBC multipath channel configuration - Scenario 1

ith path i	0	1	2	3
Channel gain $\|h_i\|$ (dB)	-2	-2	-5	-5
delay ϵ_i (t/T)	0	0.5	1	1.5

Table 5.3 – STBC multipath channel configuration - Scenario 2

arrive within the symbol time interval whereas the second one considers the case where the time delay of the reflections can exceed the symbol time T. In both scenarios, the channel gains are complex valued constants. Their attenuations are given in the above tables, and their angles are randomly chosen at every realization. The different BER curves are depicted in Figure 5.22 and Figure 5.23. Several remarks can be given regarding the obtained results

- The proposed architecture clearly outperforms the state of the art one for both scenarios.
- The choice of the value of N_t^0 depends on the delay spread of the channel. The BER curves are very similar for $N_t^0 = 3$ and $N_t^0 = 5$ when the delay spread is very low (Figure 5.22). However, there is a noticeable BER performance improvement in the second scenario if we take $N_t^0 = 5$ (Figure 5.23).
- The presence of multipath has a negative impact not only on the decoding algorithm but also on the estimators; in fact, we noticed that the presence of the reflections deteriorates the quality of the differential delay estimation $\Delta\tau$. This deterioration can cause severe BER performance loss for the state of the art architecture because the XTCQM coefficients are extracted from a lookup table as a function of the estimated delay, and therefore, these coefficients can greatly mismatch the correct coefficients of the XTCQM representation at the erroneous delay $\Delta\tau$. However, since our proposed solution instead estimates the channel impulse response at $t = \Delta\tau T$, the erroneous estimation of the differential delay $\Delta\tau$ does not cause an important BER performance loss.

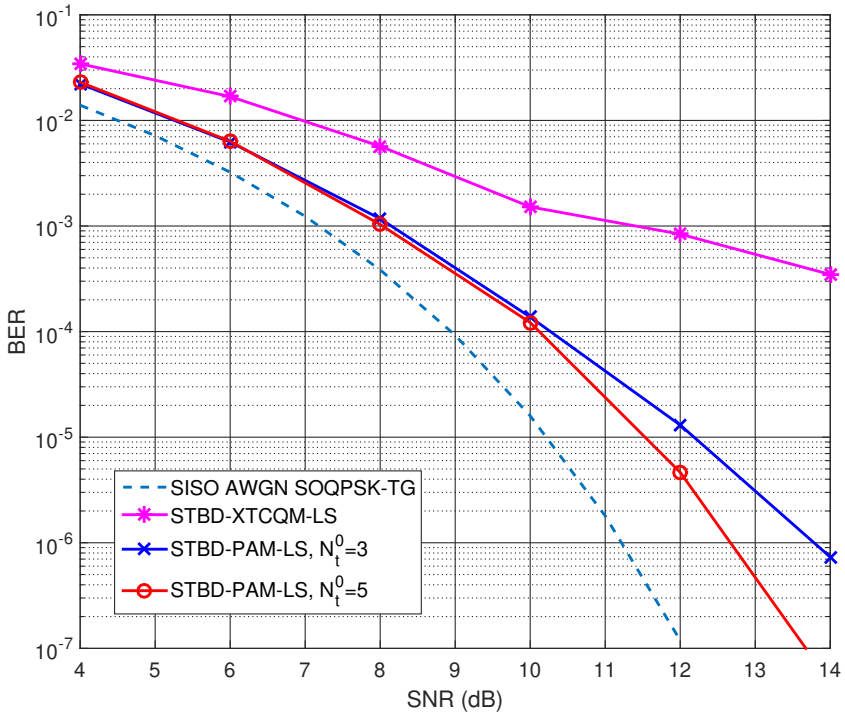

Figure 5.22 – BER performance of the proposed solution in the presence of multipath - Scenario 1

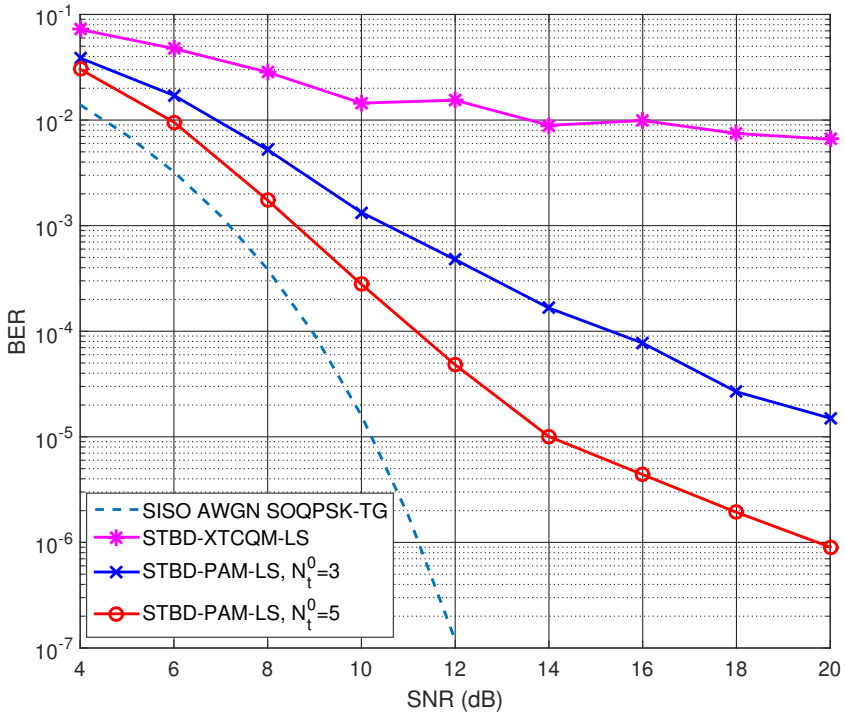

Figure 5.23 – BER performance of the proposed solution in the presence of multipath - Scenario 2

5.8 Conclusion

In this chapter, we studied decoding solutions of Alamouti encoded SOQPSK-TG signals. The encoding technique is used to resolve the two antenna problem, and its use for aeronautical telemetry is challenging due to the used modulation (SOQPSK-TG) and to the presence of an unusual channel impairment, which is the differential delay between the transmitted signals.

After introducing the state of the art decoders, we reformulated the problem using the PAM decomposition, and we proposed several decoding solutions: the first one relies on the first PAM approximation and is in accordance with the attractive properties of Alamouti schemes since the proposed solution incurs very low complexity. Moreover, the novelty of this solution is that it takes into account the presence of the differential delay $\Delta\tau$, which makes it suitable for aeronautical telemetry applications. The first solution gives attractive decoding efficiency overall but suffers from an angle-dependent BER performance. The change of the BER performance is due to the mutual interference of the secondary PAM waveforms and in particular the pseudo-symbols $\rho_{1,i}$ that are modulated by w_1. To cope with this situation, we proposed a least squares based decoder (STBD-PAM-LS) that includes the contribution of the pseudo-symbols $\rho_{1,i}$ while keeping a complexity lower than the state of the art solution (STBD-XTCQM-LS) thanks to the deployment of a unique trellis that can be used whatever the sign of the differential delay. The STBD-PAM-LS solution and its different variants successfully reduce the differential delay effect and offer very attractive BER performance.

We then focused on the scenario where multipath is present, and we showed that it is possible to mitigate their interference in the space-time coding context by introducing a new estimator and adapting the STBD-PAM-LS structure. Simulation results show that the state of the art architecture (the estimators + STBD-XTCQM-LS) is highly multipath-sensitive whereas the proposed architecture is more robust against the presence of reflections. However, improvements need to be done on the unchanged estimators (frame synchronization block - differential delay estimator) since they exhibit some inaccuracies in the presence of multipath.

Chapter 6

Other Solutions for Mitigating the Two-Antenna Problem

Contents

6.1 Introduction

In this chapter, we explore alternative solutions to overcome the two-antenna problem introduced in Chapter 5. We first focus on the improvement of the STBC scheme since we highlighted in the previous chapter that the IRIG standardized encoding does not rigorously produce two orthogonal SOQPSK-TG signals due to the memory effect of this modulation. We show that the transmission rate can further be improved by proposing another encoding scheme. This new scheme reduces the mutual interference between the pseudo-symbols $\rho_{1,i}^{k}$ associated with the k^{th} transmitted SOQPSK-TG signal. We then propose a decoding algorithm for this encoder similar to the one proposed in Section 5.4, and we prove via simulation results that the BER performance of this scheme is less angle-dependent than the one of Chapter 5.

In the second part of this chapter, we show that the two-antenna problem can also be solved by only creating time diversity. This diversity can be achieved by artificially introducing a time delay between the two transmitted signals. We first determine the desired delay by simulation. Then, we show that the received signal can be demodulated using the solutions given in Chapter 4.

6.2 New space time block coding for SOQPSK-TG

6.2.1 New encoder structure

The IRIG standardized encoder involves 4 bits $b_{4n}, b_{4n+1}, b_{4n+2}, b_{4n+3}$ and has been adopted for SOQPSK-TG because it ensures a good transmission rate for offset modulations in general and an optimal one for OQPSK modulation in particular. However, there are two major differences between SOQPSK-TG and OQPSK.

- The first one is the pulse shape $w_0(t)$ of SOQPSK-TG whose auto-correlation is non-zero for $t \geq 2T$ unlike the rectangular pulse shape of OQPSK. This problem has been tackled in chapter 5 by filtering the signal with the combined filter introduced in chapter 3 instead of the matched filter.

- The second one is the presence of the PAM waveforms $\{w_k\}_{k\in[1,255]}$ which ensure the constant envelope nature of SOQPSK-TG. The existence of these waveforms affects the transmission rate when the standardized scheme is employed due to mutual interference.

In this work, we focus on reducing the mutual interference of the pseudo-symbols $\{\rho_{1,i}^{k}\}_{k\in\{0,1\}}$ that modulate the pulse w_1. To do so, we propose to change the encoding scheme to get a better transmission rate and to reduce the angle-dependency of the BER performance as follows: we first attempt to apply Alamouti encoding on $\rho_{1,i}$. This operation requires involving 6 bits since each pseudo-symbol $\rho_{1,i}$ is a function of 3 consecutive bits b_{i-1}, b_i, b_{i+1}. We then get the

following code matrix

$$\mathbf{M} = \begin{bmatrix} -jb_{6n}b_{6n+1}b_{6n+2} & -(-b_{6n+3}b_{6n+4}b_{6n+5})^* \\ -b_{6n+3}b_{6n+4}b_{6n+5} & (-jb_{6n}b_{6n+1}b_{6n+2})^* \end{bmatrix} = \begin{bmatrix} -jb_{6n}b_{6n+1}b_{6n+2} & b_{6n+3}b_{6n+4}b_{6n+5} \\ -b_{6n+3}b_{6n+4}b_{6n+5} & jb_{6n}b_{6n+1}b_{6n+2} \end{bmatrix} \tag{6.1}$$

$$= \begin{bmatrix} \rho_{1,6n+1} & -\rho^*_{1,6n+4} \\ \rho_{1,6n+4} & \rho^*_{1,6n+1} \end{bmatrix}. \tag{6.2}$$

The ith row of the matrix $\mathbf{M}$ depicts the pseudo-symbols of the ith signal $s_i(t)$. We can see from the above matrix that this encoding involves the pseudo-symbols $\rho_{1,6n+1}$ and $\rho_{1,6n+4}$. Moreover, the transmission of $\rho_{1,6n+4}$ occurs at $t = (6n+1)T$ and the transmission $\rho_{1,6n+1}$ occurs at $t = (6n+4)T$ for the second signal $s_1(t)$. Therefore, the second row of the matrix $\mathbf{M}$ should be multiplied by j to respect the definition of the $\rho_{1,i}$. We then rearrange the elements b_i in each sequence $\{\underline{b}^m\}_{m\in\{0,1\}}$ to get Alamouti encoded pseudo-symobols $\rho^m_{0,i}$ of the main w_0 while ensuring enough time diversity. This operation gives the following two parallel bit streams ($\underline{b}^0 = [b^0_i]_{i\in\mathbb{N}}$, $\underline{b}^1 = [b^1_i]_{i\in\mathbb{N}}$)

$$\underline{b}^0 = [\ldots \quad b_{6n},\ b_{6n+1},\ b_{6n+2},\ b_{6n+3},\ -b_{6n+4},\ b_{6n+5} \quad \ldots] \tag{6.3}$$

$$\underline{b}^1 = [\ldots \quad -b_{6n+3},\ b_{6n+4}, -b_{6n+5},\ b_{6n}, b_{6n+1},\ b_{6n+2} \quad \ldots]. \tag{6.4}$$

To verify the aforementioned properties, we write the sequence $\underline{\rho}^m_k = \{\rho^m_{k,i}\}$ as a function of $\underline{\rho}_k$:

$$\begin{aligned} \underline{\rho}^0_0 &= [\ldots, \rho_{0,6n},\ \rho_{0,6n+1},\ \rho_{0,6n+2}, -\rho^*_{0,6n+3}, -\rho^*_{0,6n+4}, -\rho^*_{0,6n+5}, \ldots] \\ \frac{\underline{\rho}^1_0}{j} &= [\ldots, \rho_{0,6n+3},\ \rho_{0,6n+4}, \rho_{0,6n+5},\ \rho^*_{0,6n}, \rho^*_{0,6n+1},\ \rho^*_{0,6n+3}, \ldots]. \end{aligned} \tag{6.5}$$

$$\begin{aligned} \underline{\rho}^0_1 &= [\ldots, \rho_{1,6n},\ \rho_{1,6n+1},\ \rho_{1,6n+2}, -\rho_{1,6n+3}, -\rho^*_{1,6n+4}, -\rho_{0,6n+5}, \ldots] \\ \frac{\underline{\rho}^1_1}{j} &= [\ldots, -jb_{6n-4}b_{6n+3}b_{6n+4},\ \rho_{1,6n+4}, -jb_{6n+4}b_{6n+5}b_{6n},\ b_{6n+5}b_{6n}b_{6n+1}, \rho^*_{1,6n+1}, \\ &\qquad b_{6n+1}b_{6n+2}b_{6n+9}, \ldots]. \end{aligned} \tag{6.6}$$

We can notice from (6.5) that each set $\{\rho_{0,6n+k}, \rho_{0,6n+k+3}\}_{k\in\{0,1,2\}}$ is Alamouti encoded. Therefore, all the pseudo-symbols $\rho_{0,i}$ of the main pulse are Alamouti encoded in the streams $\underline{\rho}^0_0$ and $\underline{\rho}^1_0$. However, only a portion of the pseudo-symbols $\rho_{1,i}$ are Alamouti encoded due to the memory effect. The obtained result is nevertheless better than the IRIG encoding of chapter 5 and to illustrate this improvement, we plot in Figure 6.1 the power of the received signal $r(t) = h_0 s_0(t) + h_1 s_1(t)$ for random complex values of h_0 and h_1 such that $|h_0|^2 + |h_1|^2 = 1$. We consider the case where the exact SOQPSK-TG signal is sent as well as the case where

$s_i(t) = \sum_k \rho^i_{m,k} w_m(t - kT),\ (m,i) \in (\{0,1\})^2$. We can notice from this figure that the power of the received signal is more clustered around 1 when the proposed encoder is used. The reason of this improvement is due to reducing the interference of the pseudo-symbols $\rho_{1,i}$ for any value of h_0 and h_1.

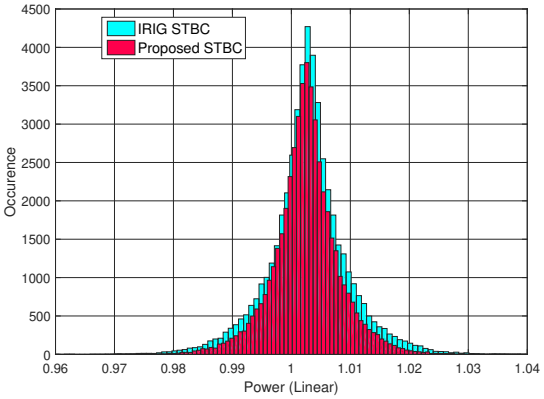

(a) Transmitted signal: only the normalized PAM associated with $\rho_{0,i}$

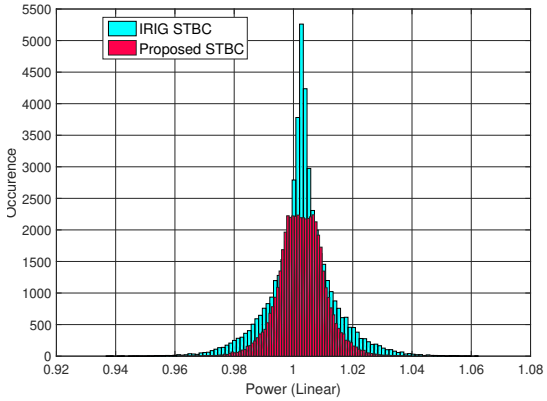

(b) Transmitted signal: only the normalized PAM associated with $\rho_{1,i}$

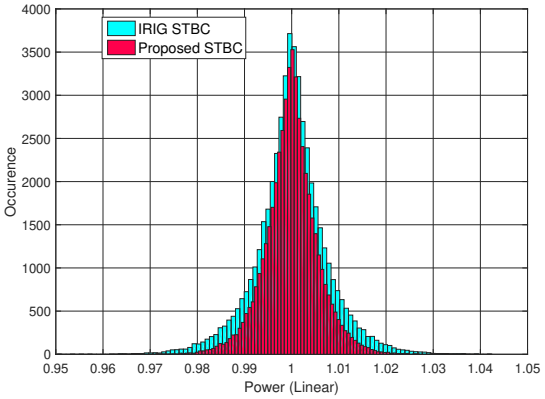

(c) Transmitted signal: Exact SOQPSK-TG

Figure 6.1 – Power of the received signal for different channel gain values

After presenting the new encoding scheme, we focus on the decoding architecture in the following sections.

6.2.2 Received signal model

We consider in this chapter the MISO case as well, i.e., the receiver only contains one antenna. Thus, the received signal model is the following

$$r(t) = h_0 s_0(t) + h_1 s_1(t - \Delta\epsilon) + n(t), \tag{6.7}$$

where $s_0(t)$ and $s_1(t)$ are two SOQPSK-TG signals containing the bit streams $\underline{b}^0$ and $\underline{b}^1$ and are affected by complex-valued attenuations h_0 and h_1, respectively. We also remind that $\Delta\epsilon$ is the differential delay. The received signal is filtered and sampled like in the previous chapter at $t = kT$ and $t = kT + \Delta\epsilon$. We then get

$$\begin{cases} y(k) = y(t = kT) = h_0\tilde{s}_0(kT) + h_1\tilde{s}_1((k - \Delta\tau)T) + \tilde{n}(kT), \\ y_{\Delta\tau}(k) = y(t = kT + \Delta\epsilon) = h_0\tilde{s}_0((k + \Delta\tau)T) + h_1\tilde{s}_1(kT) + \tilde{n}((k + \Delta\tau)T), \end{cases} \tag{6.8}$$

where y, $\tilde{s}_0$, $\tilde{s}_1$ and $\tilde{n}$ are the filtered versions of r, s_0, s_1 and n, respectively. We choose to use the 3-bit level approximation of $\tilde{s}_i$ given (5.36), and hence we obtain the following approximations of y and $y_{\Delta\tau}$

$$\begin{cases} y(6k) = h_0 \sum_{i=-1}^{+1} \rho^0_{0,6k-i}\tilde{w}_0(iT) + h_1 \sum_{i=-1}^{+1} \rho^1_{0,6k-i}\tilde{w}_0(iT - \Delta\tau T) + \tilde{n}(6kT), & (6.9) \\ y_{\Delta\tau}(6k) = h_0 \sum_{i=-1}^{+1} \rho^0_{0,6k-i}\tilde{w}_0(iT + \Delta\tau T) + h_1 \sum_{i=-1}^{+1} \rho^1_{0,6k-i}\tilde{w}_0(iT) + \tilde{n}(6kT + \Delta\tau T), & (6.10) \end{cases}$$

6.2.3 Decoder architecture using Cavers/Ungerboeck approach

The goal of the decoder is to recover the bit stream $\underline{b} = \{b_i\}_{i\in\mathbb{N}}$ using the samples y and $y_{\Delta\tau}$. To do so, we define the following metric

$$B^k_m = \frac{1}{2}\left(y(6k + m) + y_{\Delta\tau}(6k + m)\right), \quad m \in \{0, ..., 5\}. \tag{6.11}$$

We group B^k_0 with B^k_3, B^k_1 with B^k_4, and B^k_2 with B^k_5 as follows

$$\begin{aligned} \begin{bmatrix} B^k_0 \\ j(B^k_3)^* \end{bmatrix} = A \begin{bmatrix} h_0 & -h_1 \\ h_1^* & h_0^* \end{bmatrix} \begin{bmatrix} b_{6k} \\ b_{6k+3} \end{bmatrix} + jC \begin{bmatrix} h_0 & 0 \\ 0 & h_0^* \end{bmatrix} \begin{bmatrix} b_{6(k-1)+5} \\ b_{6k+2} \end{bmatrix} \\ + jC \begin{bmatrix} h_1 & 0 \\ 0 & h_1^* \end{bmatrix} \begin{bmatrix} b_{6k+4} \\ b_{6k+1} \end{bmatrix} + jD \begin{bmatrix} h_0 & 0 \\ 0 & -h_0^* \end{bmatrix} \begin{bmatrix} b_{6k+1} \\ b_{6k+4} \end{bmatrix} + jD \begin{bmatrix} h_1 & 0 \\ 0 & -h_1^* \end{bmatrix} \begin{bmatrix} b_{6(k-1)+2} \\ b_{6k+5} \end{bmatrix} \\ + \begin{bmatrix} \tilde{n}_\Delta(6kT) \\ j\tilde{n}^*_\Delta((6k + 3)T) \end{bmatrix}, \end{aligned} \tag{6.12}$$

$$\begin{bmatrix} -jB_1^k \\ (B_4^k)^* \end{bmatrix} = A \begin{bmatrix} h_0 & h_1 \\ h_1^* & -h_0^* \end{bmatrix} \begin{bmatrix} b_{6k+1} \\ b_{6k+4} \end{bmatrix} - jC \begin{bmatrix} h_0 & 0 \\ 0 & h_0^* \end{bmatrix} \begin{bmatrix} b_{6k} \\ b_{6k+3} \end{bmatrix} + jC \begin{bmatrix} h_1 & 0 \\ 0 & -h_1^* \end{bmatrix} \begin{bmatrix} b_{6k+5} \\ b_{6k+2} \end{bmatrix} - jD \begin{bmatrix} h_0 & 0 \\ 0 & h_0^* \end{bmatrix} \begin{bmatrix} b_{6k+2} \\ b_{6k+5} \end{bmatrix} + jD \begin{bmatrix} h_1 & 0 \\ 0 & -h_1^* \end{bmatrix} \begin{bmatrix} b_{6k+3} \\ b_{6k} \end{bmatrix} + \begin{bmatrix} -j\tilde{n}_\Delta((6k+1)T) \\ \tilde{n}_\Delta^*((6k+4)T) \end{bmatrix}, \quad (6.13)$$

$$\begin{bmatrix} B_2^k \\ j(B_5^k)^* \end{bmatrix} = A \begin{bmatrix} h_0 & -h_1 \\ h_1^* & h_0^* \end{bmatrix} \begin{bmatrix} b_{6k+2} \\ b_{6k+5} \end{bmatrix} + jC \begin{bmatrix} h_0 & 0 \\ 0 & -h_0^* \end{bmatrix} \begin{bmatrix} b_{6k+1} \\ b_{6k+4} \end{bmatrix} + jC \begin{bmatrix} h_1 & 0 \\ 0 & -h_1^* \end{bmatrix} \begin{bmatrix} b_{6k} \\ b_{6(k+1)+3} \end{bmatrix} + jD \begin{bmatrix} h_0 & 0 \\ 0 & h_0^* \end{bmatrix} \begin{bmatrix} b_{6k+3} \\ b_{6(k+1)} \end{bmatrix} + jD \begin{bmatrix} h_1 & 0 \\ 0 & h_1^* \end{bmatrix} \begin{bmatrix} b_{6k+4} \\ b_{6k+1} \end{bmatrix} + \begin{bmatrix} \tilde{n}_\Delta((6k+2)T) \\ j\tilde{n}_\Delta^*((6k+5)T) \end{bmatrix}, \quad (6.14)$$

where the parameters A, C, D and $\tilde{n}_\Delta$ are defined in (5.22)−(5.25). We now define the following matrices

$$\mathbf{H}_2^0 = \begin{bmatrix} h_0 & -h_1 \\ h_1^* & h_0^* \end{bmatrix}, \qquad \mathbf{H}_2^1 = \begin{bmatrix} h_0 & h_1 \\ h_1^* & -h_0^* \end{bmatrix}, \quad (6.15)$$

and we multiply (6.12), (6.14) on the left by $\left(\mathbf{H}_2^0\right)^{\mathcal{H}}$ and (6.13) on the left by $\left(\mathbf{H}_2^1\right)^{\mathcal{H}}$. By taking the real part of the obtained vectors we get,

$$Re\left\{\left(\mathbf{H}_2^0\right)^{\mathcal{H}} \begin{bmatrix} B_0^k \\ j(B_3^k)^* \end{bmatrix}\right\} = \begin{bmatrix} l_0^k \\ l_1^k \end{bmatrix} \quad (6.16)$$

$$= \begin{bmatrix} A\chi b_{6k} - D\zeta b_{6(k-1)+2} - C\zeta b_{6k+2} + (D-C)\zeta b_{6k+4} \\ A\chi b_{6k+3} - C\zeta b_{6(k-1)+5} + D\zeta b_{6(k+1)+3} - (D-C)\zeta b_{6k+1} - D\zeta b_{6k+5} \end{bmatrix} + Re\left\{\begin{bmatrix} h_0^*\tilde{n}_\Delta(6kT) + jh_1\tilde{n}_\Delta^*((6k+3)T) \\ -h_1^*\tilde{n}_\Delta(6kT) + jh_0\tilde{n}_\Delta^*((6k+3)T) \end{bmatrix}\right\}, \quad (6.17)$$

$$Re\left\{\left(\mathbf{H}_2^1\right)^{\mathcal{H}} \begin{bmatrix} -jB_1^k \\ (B_4^k)^* \end{bmatrix}\right\} = \begin{bmatrix} l_2^k \\ l_3^k \end{bmatrix} = \begin{bmatrix} A\chi b_{6k+1} - (D-C)\zeta b_{6k+3} + (D-C)\zeta b_{6k+5} \\ A\chi b_{6k+4} + (D-C)\zeta b_{6k} - (D-C)\zeta b_{6k+2} \end{bmatrix} + Re\left\{\begin{bmatrix} -jh_0^*\tilde{n}_\Delta((6k+1)T) + h_1\tilde{n}_\Delta^*((6k+4)T) \\ -jh_1^*\tilde{n}_\Delta((6k+1)T) - h_0\tilde{n}_\Delta^*((6k+4)T) \end{bmatrix}\right\}, \quad (6.18)$$

$$Re\left\{\left(\mathbf{H}_2^0\right)^{\mathcal{H}}\begin{bmatrix}B_2^k\\ j(B_5^k)^*\end{bmatrix}\right\}=\begin{bmatrix}l_4^k\\ l_5^k\end{bmatrix} \tag{6.19}$$

$$=\begin{bmatrix}A\chi b_{6k+2}-C\zeta b_{6k}-(D-C)\zeta b_{6k+4}-D\zeta b_{6(k+1)}\\ A\chi b_{6k+5}+(D-C)\zeta b_{6k+1}-D\zeta b_{6k+3}-(D-C)\zeta b_{6(k+1)+3}\end{bmatrix}$$
$$+Re\left\{\begin{bmatrix}h_0^*\tilde{n}_\Delta((6k+2)T)+jh_1\tilde{n}_\Delta^*((6k+5)T)\\ -h_1^*\tilde{n}_\Delta((6k+2)T)+jh_0\tilde{n}_\Delta^*((6k+5)T)\end{bmatrix}\right\}, \tag{6.20}$$

where $\zeta = Im(h_0^*h_1)$ and $\zeta = |h_0|^2+|h_1|^2$. We can notice from (6.17)−(6.20) that the even symbols b_{6k+2p} only appear in l_0^k, l_3^k, l_4^k whereas the scalars l_1^k, l_2^k, l_5^k are only functions of the odd symbols $b_{6k+2p-1}$. Therefore, even symbols can be processed separately from odd ones in the presence of a non-zero differential delay unlike the scheme presented in chapter 5. We now define the following vectors $\underline{x}_e=\{x_i^e\}_{i\in\mathbb{N}}$, $\underline{x}_o=\{x_i^o\}_{i\in\mathbb{N}}$, $\underline{b}_e=\{b_i^e\}_{i\in\mathbb{N}}$, $\underline{b}_o=\{b_i^o\}_{i\in\mathbb{N}}$

$$\underline{x}_e=\left(...,l_0^k,l_4^k,l_3^k,l_0^{k+1},l_4^{k+1},l_3^{k+1},...\right)^{\mathcal{T}}, \tag{6.21}$$

$$\underline{x}_o=\left(...,l_2^k,l_1^k,l_5^k,l_2^{k+1},l_1^{k+1},l_5^{k+1},...\right)^{\mathcal{T}}, \tag{6.22}$$

$$\underline{b}_e=\left(...,b_{6k},b_{6k+2},b_{6k+4},b_{6(k+1)},b_{6(k+1)+2},b_{6(k+1)+4},...\right)^{\mathcal{T}}. \tag{6.23}$$

$$\underline{b}_o=\left(...,b_{6k+1},b_{6k+3},b_{6k+5},b_{6(k+1)+1},b_{6(k+1)+3},b_{6(k+1)+5},...\right)^{\mathcal{T}}, \tag{6.24}$$

and we formulate the problem as

$$\underline{x}_e=\mathbf{G}_e\underline{b}_e+\underline{u}_e, \tag{6.25}$$

$$\underline{x}_o=\mathbf{G}_o\underline{b}_o+\underline{u}_o, \tag{6.26}$$

where

$$\mathbf{G}_e=\begin{bmatrix}\mathbf{G}_{e,1} & \mathbf{G}_{e,2}^{\mathcal{T}} & \mathbf{0}_3 & \dots & \dots & \mathbf{0}_3\\ \mathbf{G}_{e,2} & \mathbf{G}_{e,1} & \mathbf{G}_{e,2}^{\mathcal{T}} & \mathbf{0}_3 & \ddots & \vdots\\ \mathbf{0}_3 & \mathbf{G}_{e,2} & \mathbf{G}_{e,1} & \mathbf{G}_{e,2}^{\mathcal{T}} & \ddots & \vdots\\ \vdots & \ddots & \ddots & \ddots & \ddots & \mathbf{0}_3\\ \vdots & \ddots & \ddots & \ddots & \ddots & \mathbf{G}_{e,2}^{\mathcal{T}}\\ \mathbf{0}_3 & \dots & \dots & \mathbf{0}_3 & \mathbf{G}_{e,2} & \mathbf{G}_{e,1}\end{bmatrix}, \tag{6.27}$$

$$\mathbf{G}_o = \begin{bmatrix} \mathbf{G}_{o,1} & \mathbf{G}_{o,2}^{\mathcal{T}} & \mathbf{0}_3 & \dots & \dots & \mathbf{0}_3 \\ \mathbf{G}_{o,2} & \mathbf{G}_{o,1} & \mathbf{G}_{o,2}^{\mathcal{T}} & \mathbf{0}_3 & \ddots & \vdots \\ \mathbf{0}_3 & \mathbf{G}_{o,2} & \mathbf{G}_{o,1} & \mathbf{G}_{o,2}^{\mathcal{T}} & \ddots & \vdots \\ \vdots & \ddots & \ddots & \ddots & \ddots & \mathbf{0}_3 \\ \vdots & \ddots & \ddots & \ddots & \ddots & \mathbf{G}_{o,2}^{\mathcal{T}} \\ \mathbf{0}_3 & \dots & \dots & \mathbf{0}_3 & \mathbf{G}_{o,2} & \mathbf{G}_{o,1} \end{bmatrix}, \tag{6.28}$$

and

$$\mathbf{G}_{e,1} = \begin{bmatrix} A\chi & -C\zeta & (D-C)\zeta \\ -C\zeta & A\chi & -(D-C)\zeta \\ (D-C)\zeta & -(D-C)\zeta & A\chi \end{bmatrix}, \quad \mathbf{G}_{e,2} = \begin{bmatrix} 0 & -D\zeta & 0 \\ 0 & 0 & 0 \\ 0 & 0 & 0 \end{bmatrix}, \tag{6.29}$$

$$\mathbf{G}_{o,1} = \begin{bmatrix} A\chi & -(D-C)\zeta & (D-C)\zeta \\ -(D-C)\zeta & A\chi & -D\zeta \\ (D-C)\zeta & -D\zeta & A\chi \end{bmatrix}, \quad \mathbf{G}_{o,2} = \begin{bmatrix} 0 & 0 & 0 \\ 0 & 0 & -C\zeta \\ 0 & 0 & 0 \end{bmatrix}. \tag{6.30}$$

The matrix $\mathbf{0}_3$ is a zero matrix composed of 3 rows and 3 columns. The vectors $\underline{u}_e$ and $\underline{u}_o$ are composed of noise terms and they are built in the same way as $\underline{x}_e$ and $\underline{x}_o$, respectively. We keep the same line of reasoning as done in Section 5.4.2, and we suppose that the auto-correlation matrix of the noise $\underline{u}_e$ is $\mathbf{M}_{u_e} = N_0\mathbf{G}_e$ and the auto-correlation matrix of the noise $\underline{u}_o$ is $\mathbf{M}_{u_o} = N_0\mathbf{G}_o$. Both matrices $\mathbf{G}_e$ and $\mathbf{G}_o$ can be decomposed as sums of a diagonal matrix, a strictly upper triangular matrix and a strictly lower triangular one. After writing $\mathbf{G}_e$ as $\mathbf{G}_e = \mathbf{G}_D^e + \mathbf{G}_U^e + (\mathbf{G}_U^e)^{\mathcal{T}}$ and $\mathbf{G}_o$ as $\mathbf{G}_o = \mathbf{G}_D^o + \mathbf{G}_U^o + (\mathbf{G}_U^o)^{\mathcal{T}}$, the ML metric for the even case can be written as

$$\Lambda\left(\underline{x}_e, \underline{b}_e\right) = 2\underline{b}_e^{\mathcal{T}}\underline{x}_e - 2\underline{b}_e^{\mathcal{T}}\mathbf{G}_U^e\underline{b}_e - \underline{b}_e^{\mathcal{T}}\mathbf{G}_D^e\underline{b}_e, \tag{6.31}$$

$$= \sum_n \lambda_e(n), \tag{6.32}$$

where

$$\lambda_e(n) = \begin{cases} b_n^e\left(2x_n^e + C\zeta b_{n+1}^e + D\zeta b_{n-2}^e - (D-C)\zeta b_{n+2}^e\right) - A\xi|b_n^e|^2, & \text{if } n = 3k, \\ b_n^e\left(2x_n^e + C\zeta b_{n-1}^e + D\zeta b_{n+2}^e + (D-C)\zeta b_{n+1}^e\right) - A\xi|b_n^e|^2, & \text{if } n = 3k+1, \\ b_n^e\left(2x_n^e - (D-C)\zeta b_{n-2}^e + (D-C)\zeta b_{n-1}^e\right) - A\xi|b_n^e|^2, & \text{if } n = 3k+2, \end{cases} \tag{6.33}$$

and the ML metric for the odd case can be expressed as

$$\Lambda\left(\underline{x}_o, \underline{b}_o\right) = 2\underline{b}_o^{\mathcal{T}}\underline{x}_o - 2\underline{b}_o^{\mathcal{T}}\mathbf{G}_U^o\underline{b}_o - \underline{b}_o^{\mathcal{T}}\mathbf{G}_D^o\underline{b}_o, \tag{6.34}$$

$$= \sum_n \lambda_o(n), \tag{6.35}$$

where

$$\lambda_o(n) = \begin{cases} b_n^o\left(2x_n^o + (D-C)\zeta b_{n+1}^o - (D-C)\zeta b_{n+2}^o\right) - A\xi|b_n^o|^2, & \text{if } n = 3k, \\ b_n^o\left(2x_n^o + (D-C)\zeta b_{n-1}^o + D\zeta b_{n+1}^o + C\zeta b_{n-2}^o\right) - A\xi|b_n^o|^2, & \text{if } n = 3k+1, \\ b_n^o\left(2x_n^o - (D-C)\zeta b_{n-2}^o + D\zeta b_{n-1}^o + C\zeta b_{n+2}^o\right) - A\xi|b_n^o|^2, & \text{if } n = 3k+2. \end{cases} \tag{6.36}$$

Both even and odd branch metrics are defined by a 5-tuple, and therefore the Viterbi algorithm operates with 16 states with 2 branches coming out from each state. The decoder structure is given in Figure 6.2.

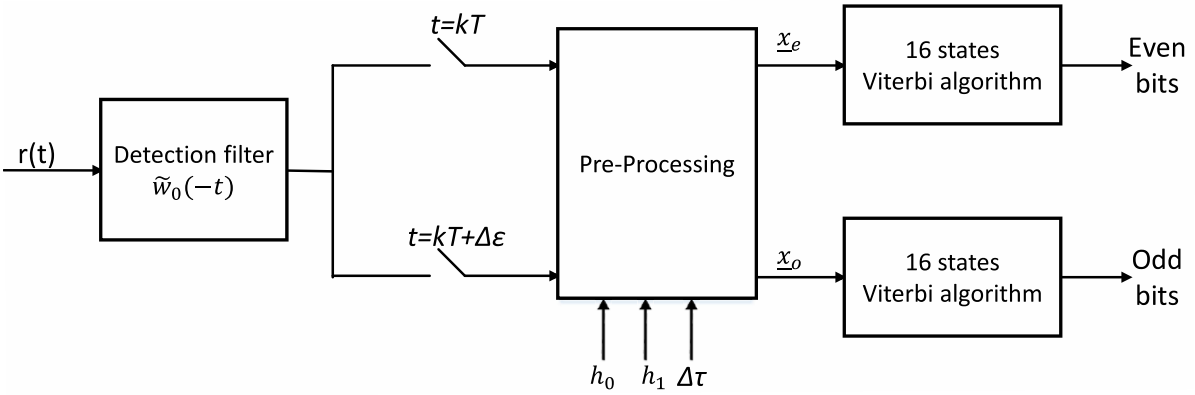

Figure 6.2 – Decoder structure for proposed encoding scheme

Several remarks can be made regarding the obtained architecture:

- Only 80 branches are needed instead of 192 to decode a block of 6 symbols,. If we take for instance the branch metric $\lambda_o(n)$, we can see that it is a function of 3 symbols out of 5 when $n = 3k$ and a function of 4 symbols out of 5 when $n = 3k + m,\ m \in \{1, 2\}$.
- Decoding a block of 6 symbols requires 272 additions and 80 multiplications. If we focus on the complexity per symbol (and not per block), we conclude that the obtained decoder is slightly less complex than STBD-PAM-ML decoder given in Section 5.4.
- Even though the proposed encoding rule further expands the diversity in time, the obtained decoder is less complex than the one used for IRIG STBC. This result may seem counter-intuitive at first since more time diversity generally leads to more complexity. However, the proposed encoding allows decoding the even bits separately from the odd

ones when a differential delay is present. This interesting property greatly reduces the number of operations in the decoding scheme.

- The initial goal behind the proposed encoding rule is to reduce the interference associated with the pseudo-symbols $\rho_{1,i}$ at the transmitter side. Nevertheless, we showed that this encoding is more advantageous than expected since the resulting decoder is an OQPSK-type STB decoder even in the presence of a non-zero differential delay (i.e., the information carried by the I channel (even bits) can be decoded separately from the information carried by the Q channel (odd bits)). Therefore, this architecture (encoder + decoder) can be generalized to any OQPSK-type modulation (such as OQPSK itself, FQPSK [44], SOQPSK-MIL or precoded GMSK [67], etc.) in the presence of a differential delay.

- A LS decoder similar to the STBD-PAM-LS of Section 5.5 can also be proposed for this scheme. However, it would be highly complex since it requires a Viterbi algorithm operating with 64 states and 4096 branches.

6.2.4 Simulation results

We now evaluate the BER performance of the proposed architecture when SOQPSK-TG signals are transmitted. The magnitudes of the channel gains are $|h_0| = |h_1| = \frac{\sqrt{2}}{2}$. We first consider in Figure 6.3 the case where $\Delta\tau = 0$, and we plot the BER curves for different angles $\theta = arg(h_1) - arg(h_0)$. We can seen from this figure that the BER performance loss between the best case scenario ($\theta = \frac{\pi}{2}$) and the worst case one ($\theta = 0$) is very low compared to what has been obtained in Figure 5.11. We also depict the average BER curve when θ varies over the interval $[0, 2\pi)$ in steps of 0.1π. It can be seen that the proposed architecture offers a performance gain of 0.65 dB. We now focus on the influence of $\Delta\tau$, and we plot in Figure 6.4 the BER curves for different values of $\Delta\tau$. This figure shows an improvement of the BER performance due to the employment of the proposed architecture when $|\Delta\tau| \leq 0.5$. However, when $0.5 < |\Delta\tau| < 1$, taking advantage of the proposed encoder or the IRIG encoder results in similar decoding efficiencies. In this case, the main advantage of using the proposed architecture is the complexity reduction.

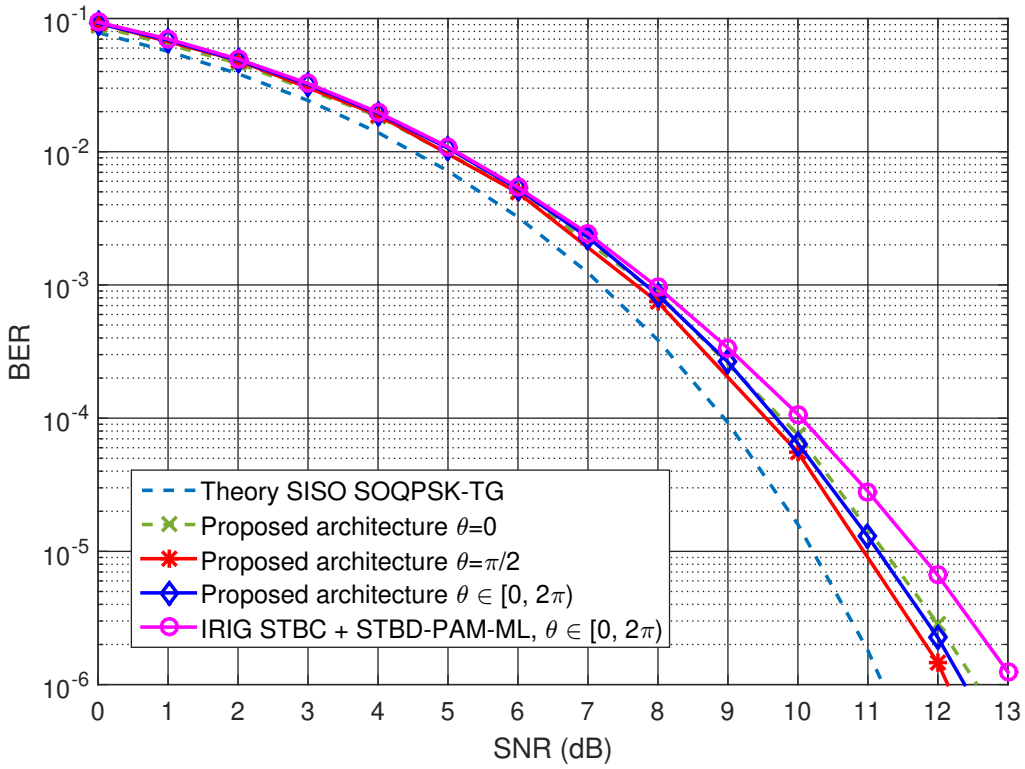

Figure 6.3 – BER performance of the proposed architecture for different θ values

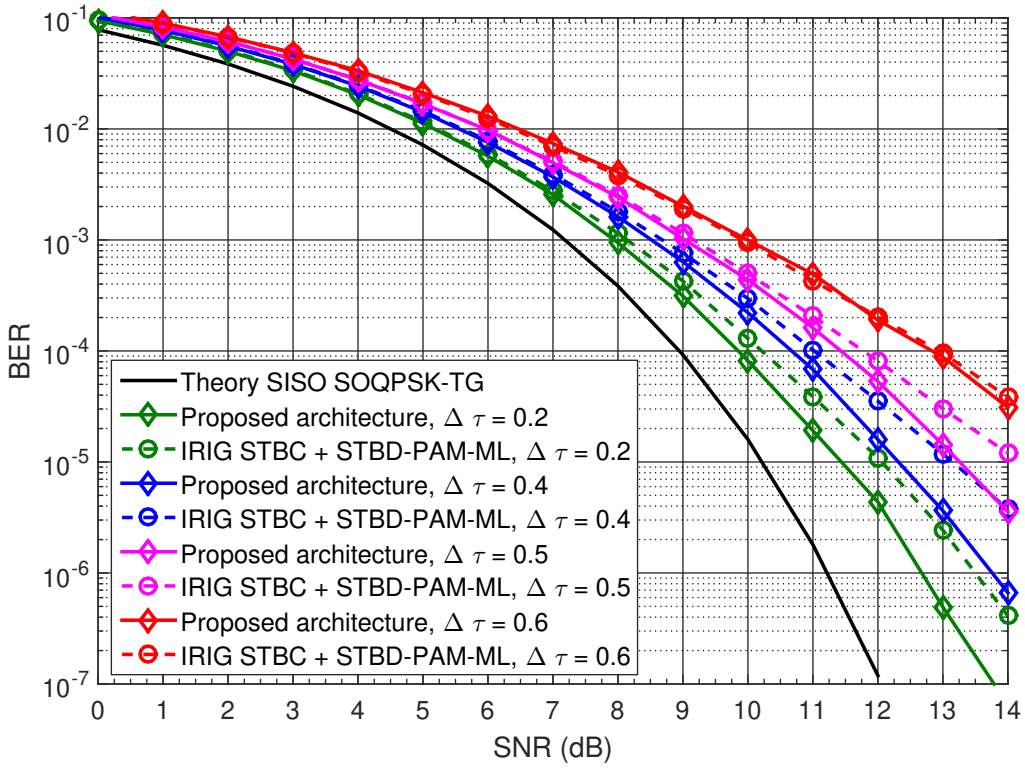

Figure 6.4 – BER performance of the proposed architecture for different $\Delta\tau$ values - $\theta \in [0, 2\pi)$

6.3 The time diversity approach

The two-antenna problem appears when the same signal is simultaneously transmitted through both transmit antennas with the same carrier frequency. In this scenario, the SOQPSK-TG signals can mutually interfere in a destructive way, which results in an important loss of the BER performance. To overcome this problem, we presented in Chapter 5 and Section 6.2 of Chapter 6 two solutions based on space-time coding. These solutions consist of transmitting two "different" SOQPSK-TG signals to avoid mutual interference, then to exploit the space diversity and the encoding rule to decode the signal. Despite the attractive benefits of these solutions, they require, however, training sequences and special signal processing tools at the receiver side. In this section, we rather propose a solution to mitigate the two-antenna problem while keeping the same architecture of the SISO case.

6.3.1 Artificial multipath channel generation

The proposed solution consists of artificially creating a multipath channel by transmitting the same signal on both transmitting antennas. To avoid the mutual interference of these signals, we artificially apply a differential delay ΔN_x multiple of the bit period. Therefore, the first antenna transmits the signal $s_0(t) = s(t)$ and the second antenna transmits the delayed version $s_1(t) = s(t - \Delta N_x T)$. The received signal is now expressed as

$$r(t) = h_0 s_0(t) + h_1 s_1(t - \Delta\tau T) + n(t), \tag{6.37}$$

$$= h_0 s(t) + h_1 s(t - \Delta N_x T - \Delta\tau T) + n(t), \tag{6.38}$$

where h_0, h_1 are the channel gains and $\Delta\tau$ is the differential delay that can also be present in this scenario. This differential delay $\Delta\tau$ is not artificially created, but it appears due the distance between the antennas and the used bit rate as explained in Chapter 5. The received signal can also be expressed as

$$r(t) = s(t) * l(t) + n(t), \tag{6.39}$$

where

$$l(t) = h_0\delta(t) + h_1\delta(t - \Delta N_x T - \Delta\tau T). \tag{6.40}$$

Equation (6.39) shows that the received signal is then a convolution of the transmitted signal $s(t)$ and a multipath channel $l(t)$ in addition to AWGN. Therefore, we go back to the scenario described in Chapter 4. As a consequence, multipath mitigation techniques such as PSP can be used to equalize the channel and estimate the transmitted bit sequence.

Due to using the same signal $s(t)$, it is necessary to determine what delay ΔN_x should be applied to reduce the mutual interference of $s(t)$ and therefore to avoid the two-antenna problem on the one hand. On the other hand, it is important to take the lowest possible value of ΔN_x to keep the complexity of the equalizers low. To do so, we run a Monte Carlo simulations, and we plot in Figure 6.5 the histogram of the power of the received signal as a function of ΔN_x for different complex values of h_0 and h_1. In each Monte Carlo simulation run, the complex gains are normalized such that $|h_0|^2 + |h_1|^2 = 1$. It can be seen from this figure that the power of the received signal becomes satisfyingly clustered around 1 when $\Delta N_x \geq 3$. The higher the delay $\Delta N_x T$, the better the quality of the received signal. If we consider the same assumption taken in Chapter 5 regarding the range of the differential delay $\Delta\tau$, which is $|\Delta\tau| < 1$, then choosing $\Delta N_x = 4$ is sufficient to create enough diversity.

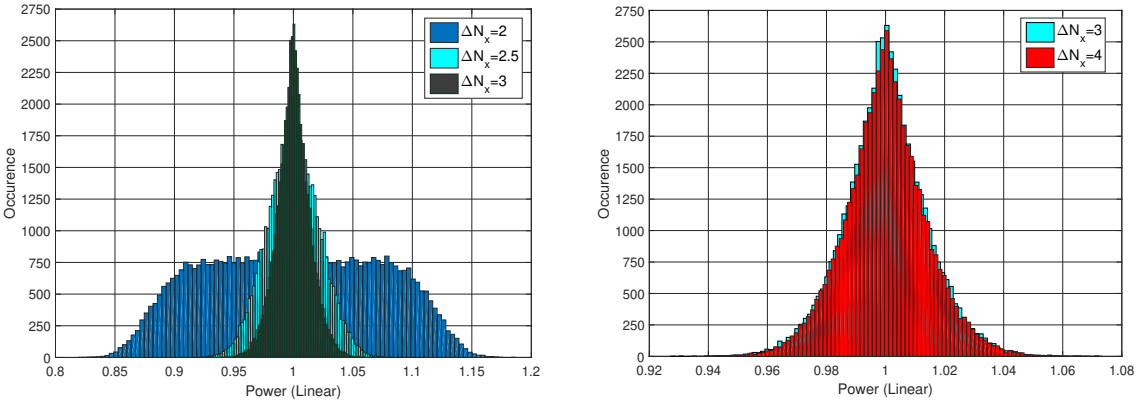

(a) (b)

Figure 6.5 – Power of the received signal for different ΔN_x values

We now compare in Figure 6.6 the histogram of $\Delta N_x = 4$ with the one obtained in Figure 6.1 using space-time coding. We notice that space-time coding offers narrower power distribution than the technique proposed in this section, which was expected since space-time coding solutions take advantage of the diversity in both time and space. Nevertheless, the obtained result using the time diversity approach can also be satisfying since the destructive interference is greatly reduced despite transmitting the same data sequence through both antennas.

6.3.2 Simulation results using PSP

We evaluate in this section the BER performance of the proposed system composed of two antennas transmitting the same signal with an artificial delay of $4T$ and one receiving antenna. The received signal is fed to PSP to estimate the channel f_0 and the data sequence. We remind that $f_0 = w_0 * l * f$, and we choose Approx. 3 in the PSP algorithm. We also assume that the receiver has no prior knowledge of the differential delays (i.e., the artificial one ΔN_x and the residual one $\Delta\tau$). To determine the number of states of PSP, we plot in Figure 6.7 the taps of

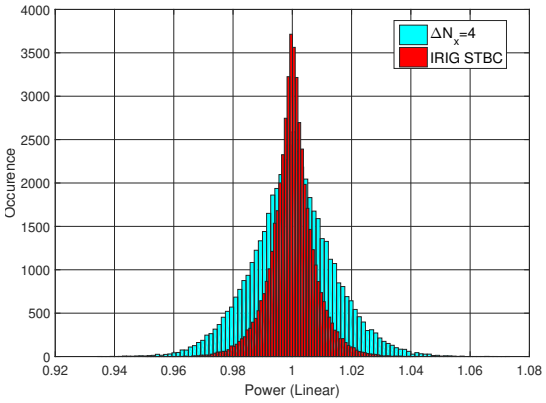

Figure 6.6 – Power of the received signal using different diversity techniques

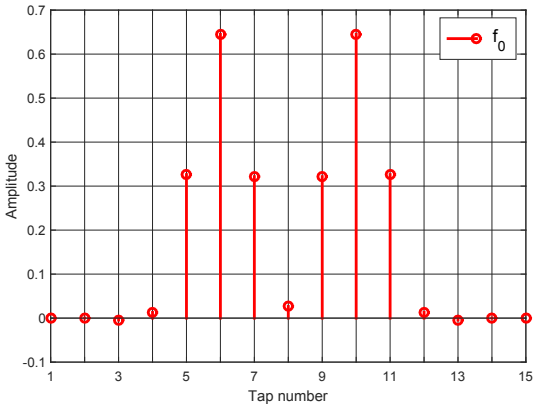

Figure 6.7 – Illustration of the taps of f_0 when $\Delta N_x = 4$.

f_0 in the case where $h_0 = h_1 = \frac{\sqrt{2}}{2}$. It can be seen from this figure that we can merely consider the taps located between 5 and 11 instead of 15. Therefore, we can take $N_t = 7$, which makes PSP operating with $2^{N_t-1} = 64$ states.

We plot in Figure 6.8 the BER performance of the proposed system for different differential delays $\Delta\tau$. We take $|h_0| = |h_1| = \frac{\sqrt{2}}{2}$, and we illustrate the average BER curves over different θ values. Several remarks can be formulated from this figure:

- When $\Delta\tau = 0$, the proposed solution offers very attractive BER performance since the obtained curve is close to theoretical curve of the SISO case (within 1 dB at BER= 10^{-5}).
- When $-1 \leq \Delta\tau \leq 0.5$, the proposed solution has similar performance, which is desirable in our scenario.
- When $\Delta\tau = 1$, we notice a performance loss of 2.5 dB at BER= 10^{-5} compared to the case where $\Delta\tau = 0$. This result was expected since the presence of a differential delay $\Delta\tau = 1$ with $\Delta N_x = 4$ is equivalent of taking an artificial delay $\Delta N_x = 5$. Therefore, the BER performance can be improved by extending the trellis of the PSP as shown in Figure 6.9.

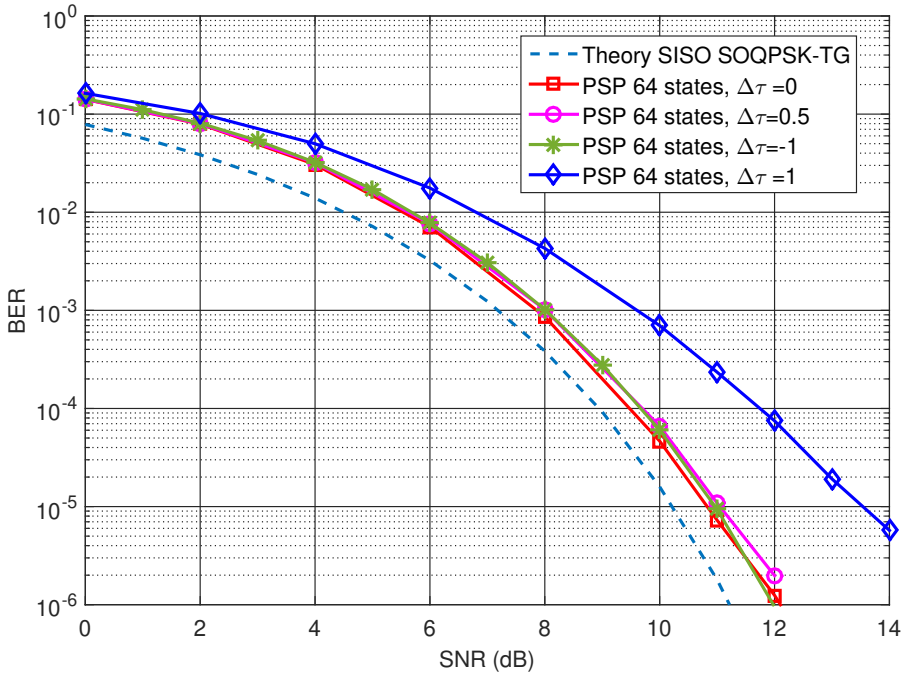

Figure 6.8 – BER performance of the proposed system for different differential delays - $\Delta N_x = 4$, $N_t = 7$

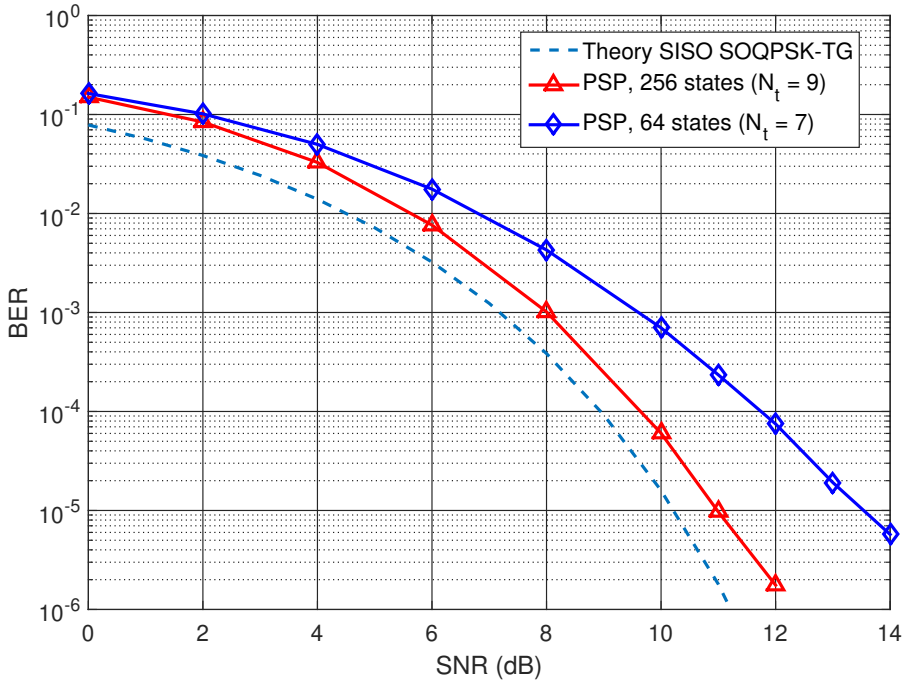

Figure 6.9 – BER performance of the proposed system for different N_t values, $\Delta N_x = 4$, $\Delta\tau = 1$.

6.4 Conclusion

In this chapter, we have proposed two original solutions to overcome the two antenna problem. The first one relies on space-time coding like the solution given in Chapter 5. However, it provides better transmission rate, better BER performance as well as lower complexity than the state of the art scheme. This improvement has been achieved thanks to the modification of the encoder structure, which involves 6 bits instead of 4. The second solution consists of transmitting the signal through one antenna and its delayed copy through the second antenna. The advantage of this approach is that the received signal model is composed of the transmitted signal followed by a multipath channel. Therefore, the receiver architecture given in Chapter 4 (PSP) can also be used in this scenario. Simulation results show that a delay of $4T$ ensures an excellent received signal quality and allows getting attractive BER performance if the PSP operates with 64 states.

General Conclusion and Perspectives

In this PhD thesis, we focused on studying reception algorithms for SOQPSK-TG under different scenarios. This study first requires a deep understanding of the signal features, which are different from the conventional linear modulations. In fact, SOQPSK-TG is an aeronautical telemetry modulation that has been considered for a long time as a particular CPM due to its ternary alphabet generated using a specific precoder and its long frequency pulse. Moreover, the fact that this modulation is not a linear function of its transmitted symbols makes handling this modulation a hard task. These features have pushed the use of particular decompositions of the signal such as ternary PAM decomposition (PRD) and the XTCQM representation to make the signal more versatile. Each representation has its pros and cons.

On the one hand, the PRD allows approximating the signal as a sum of two linear modulations. However, the resulting pseudo-symbols still inherit the memory effect of the modulation. On the other hand, the XTCQM representation provides an accurate approximation of the signal using a bank of XTCQM waveforms with a small memory. Nevertheless, these waveforms are data dependent and thus we cannot separate contribution of the data independently from the pulse shape. The contrasting features of these representations, which are presented in details in **Chapter 1**, imply a limited use to specific scenarios.

In this work, we first focused on the SOQPSK precoder structure before tackling the signal representation aspect. We showed that this precoder could be decomposed into a recursive encoder that eliminates the infinite memory of the modulation and a duobinary encoder that converts the binary symbols to ternary ones to increase the spectral efficiency. Thanks to this new vision of the precoder, we showed that SOQPSK-TG could be seen as a duobinary CPM whose PAM decomposition, namely DBD, retains the key features of the Laurent decomposition of binary CPM. As a consequence, SOQPSK-TG can accurately be approximated as a single PAM or as a sum of two PAMs. Moreover, the presence of the recursive encoder has been exploited to reduce the memory effect in the expressions of the pseudo-symbols and to get a direct mapping between the pseudo-symbols and the binary data. Therefore, we proposed a new

representation of SOQPSK that gathers better features than the state of the art representations as fully described in **Chapter 2**.

As a direct consequence of this new PAM decomposition, we proposed in **Chapter 3** a wide range of reduced complexity detectors via several approaches (Kaleh approach, Ungerboeck approach, and Forney approach). The very near-optimal performance of these detectors confirms the accuracy of the proposed DBD approximations. However, they also show that the main pulse of DBD generates significant inter-symbol interference that should be mitigated at the receiver side.

In **Chapter 4**, we took advantage of the PAM decomposition (with DBD) to propose a new joint channel estimation and detection algorithm for SOQPSK-TG. This algorithm is inspired by the PSP principle to mitigate the multipath effects, which are present in the aeronautical telemetry environment. This solution operates using two different approximations of the signal and significantly outperforms the constant modulus algorithm.

In **Chapter 5**, we focused on the scenario where two antennas are mounted on the aircraft to get an omnidirectional transmission to resolve the two-antenna problem. This use case requires creating diversity by using Alamouti encoding. However, it makes the decoding process different from what has been proposed for linear modulations because of the used modulation (SOQPSK-TG) and because of the presence of a differential delay. After presenting the state of the art solutions, we proposed in this chapter two main decoding structures. The first one relies on the first PAM approximation of SOQPSK-TG, i.e., by considering that SOQPSK-TG is a linear modulation (or more precisely, an offset modulation) and provides acceptable BER performance while benefiting from an important complexity reduction compared to the state of the art solution. The second decoding structure considers that SOQPSK-TG can be approximated as a sum of two linear modulations and greatly outperforms the state of the art solution. Both structures take into account the presence of the differential delay and provide soft outputs. In **Chapter 5**, we also considered the presence of multipath in the STC scenario. After formulating the problem using multipath, we proposed a new channel estimator and showed that this solution could be used along with the second decoding structure.

In the final chapter of this dissertation, we explored other solutions to resolve the two-antenna problem. The first proposed solution takes into account the observations made in Chapter 5 where it has been shown that the standardized encoding scheme does not eliminate the mutual interference of SOQPSK-TG signals. For this reason, we proposed a new encoding scheme that is more suitable for SOQPSK-TG. This scheme allows gathering all the attractive features of a STC system since it provides better transmission rate than the state of the art encoding and results in a reduced complexity decoding structure with attractive BER performance (within 1.1 dB of the SISO bound). In the second part of **Chapter 6**, we considered the time diversity approach, and we proposed sending one signal over one antenna and its time delayed version

over the other. This delay is created artificially to reduce the mutual interference of the signals. The advantage of this approach is that the receiver considers that the transmitted signal is corrupted by a multipath channel whose interference can successfully be mitigated using the techniques introduced in Chapter 4.

Perspectives

We present in the following the possible areas of future studies

Equalization in the SISO scenario:

- In this dissertation, the PSP algorithm operates using the duobinary PAM decomposition (DBD) of SOQPSK-TG. However, thanks to the mapping found between the pseudo-symbols and the data bits using PRD (Chapter 2), it may be possible to apply the PSP principle to the PRD PAM approximation. Since both PRD and DBD have different characteristics, the resulting algorithms may have different behaviors.
- To the best of our knowledge, the INET packet structure does not contain any cyclic prefix. However, a new packet structure can be imagined for SOQPSK-TG so that the frequency equalization algorithms introduced in [91, 92, 93, 94] can be used, tested in the presence of aeronautical telemetry channels, and compared with the proposed algorithms of this work.

Decoding and Multipath mitigation in the STC scenario:

- In this work, we proposed two decoding structures for the STC scenario. The first one relies on Ungerboeck/Cavers approach, and the second one uses the least squares approach (which is equivalent to Forney approach in the SISO case). These decoders take advantage of the "linearized" version of SOQPSK-TG but they do not take into account its CPM nature. Thus, it may be relevant to extend Kaleh approach (which exploits the constant envelope nature of CPM when calculating the log-likelihood function) from the SISO case to the MISO one to get a third decoding structure.
- The multipath mitigation technique developed in this dissertation for the STC scenario only works using the second proposed decoding structure. Further works regarding frequency domain or time domain equalizers need to be done for the STC scenario. Ideally, the equalizer should work regardless of the used decoding structure.

STC estimators:

- The complexity of the developed estimators in [130] is relatively high. More work needs to be done to reduce the complexity, and it may be accomplished using the new PAM decomposition.
- The simulation results given in Section 5.7 show that the estimators are highly multipath-sensitive. More work needs to be done to improve their performance for this scenario.

New aeronautical telemetry systems:

Conceiving power and spectrally efficient systems is a constant challenge for aeronautical telemetry. However, achieving this goal requires evolving the IRIG standard as well as the actual infrastructure. We can imagine for instance

- Pairing MIMO systems with SOQPSK to increase the spectral efficiency while taking advantage of the constant envelope nature of the modulation. The MISO case has already been standardized in IRIG to resolve the two-antenna problem without increasing the spectral efficiency. Therefore, we can imagine an extension of this concept to reach the latter goal. A feasibility study should also be carried to determine how many antennas can be mounted on board the aircraft and how many receiving antennas can be used.
- Defining different modes for different CPM modulations as done in the tactical communications standards [32]. Each modulation fulfills a certain spectral efficiency and power trade-off. Switching between one mode to the other can be done manually or autonomously (the latter case may require an ulplink mode).
- Adopting non-constant envelope signals, which beget better spectral efficiency than CPM such as COFDM [88] or APSK [140].

Appendix A

Appendix for Chapter 2: Inter-Correlation of the Pseudosymbols for Duobinary CPM

In all the following sections, we assume that the symbols γ_k are i.i.d.

A.1 Pseudo-symbols of PRD

In this section, we calculate the inter-correlation of the pseudo-symbols associated with PRD for duobinary CPM. We only consider the pseudo-symbols of the main pulses. We first define the inter-correlation as

$$P_{i,j}(q) = E\{\nu_{i,k}\nu^*_{i,k+q}\}, \quad (i,j) \in (\{0,1\})^2, \tag{A.1}$$

where $q \in \mathbb{Z}$. The inter-correlation function satisfies the following properties as the binary case

$$P_{i,j}(q) = P^*_{j,i}(q) = P_{j,i}(-q), \tag{A.2}$$

We detail in the following the computation of $P_{i,j}(q)$.

A.1.1 Computation of $P_{0,0}(q)$

We use (2.3) to compute $P_{0,0}(q)$ and we suppose without loss of generality that $q \geq 1$, we first get

$$P_{0,0}(q) = E\left\{\exp\left(-jh\pi\sum_{n=0}^{q-1}\gamma_{k+n}\right)\exp\left(j\frac{h\pi}{2}(\gamma_k - \gamma_{k+q})\right)\right\}. \tag{A.3}$$

We start by $q = 1$. Since the symbols γ_k are i.i.d, we obtain

$$P_{0,0}(1) = E\left\{\prod_{n=0}^{1} exp\left(-j\frac{h\pi}{2}\gamma_{k+n}\right)\right\}, \tag{A.4}$$

$$= \prod_{n=0}^{1} E\left\{exp\left(-j\frac{h\pi}{2}\gamma_{k+n}\right)\right\}, \tag{A.5}$$

$$= \frac{1}{2}\left(1 + \cos(h\pi)\right). \tag{A.6}$$

We can notice from (A.6) that $P_{0,0}(1) \neq 0$ because $0 < h < 1$. Therefore, the pseudo-symbols $\nu_{0,k}$ and $\nu_{0,k+1}$ are correlated. We then focus on the case where $q \geq 2$:

$$P_{0,0}(q) = E\left\{\prod_{n=1}^{q-1} exp\left(-jh\pi\gamma_{k+n}\right)\exp\left(-j\frac{h\pi}{2}(\gamma_k + \gamma_{k+q})\right)\right\}, \tag{A.7}$$

$$= \frac{1}{2}\cos(h\pi)^{|q|-1}\left(1 + \cos(h\pi)\right). \tag{A.8}$$

Equation (A.8) shows that $\nu_{0,k}$ and $\nu_{0,k+q}$ are uncorrelated when $h = 1/2$ and $|q| \geq 2$. Moreover, this equation is valid for $|q| = 1$ as well. Therefore, the values of $P_{0,0}(q)$ can be summarized as follows

$$P_{0,0}(q) = \begin{cases} 1, & q = 0, \\ \frac{1}{2}\cos(h\pi)^{|q|-1}\left(1 + \cos(h\pi)\right), & \text{otherwise.} \end{cases} \tag{A.9}$$

A.1.2 Computation of $P_{1,1}(q)$

We use (2.4) to compute $P_{1,1}(q)$. We first consider the case where $q = 1$, we get

$$P_{1,1}(1) = \frac{1}{4}E\left\{\exp\left(-j\frac{h\pi}{2}(\gamma_k + \gamma_{k+1})\right) + \exp\left(-j\frac{h\pi}{2}(\gamma_k + \gamma_{k-1})\right)\right.$$
$$\left.\exp\left(j\frac{h\pi}{2}(\gamma_k + \gamma_{k+1})\right) + \exp\left(-jh\pi\gamma_k\right)\right\}. \tag{A.10}$$

This yields to following result

$$P_{1,1}(1) = \frac{1}{8}\left(5\cos(h\pi) + 3\right). \tag{A.11}$$

We then consider the case where $q \geq 2$ and we obtain the following result

$$P_{1,1}(q) = \frac{1}{16}\cos(h\pi)^{|q|-2}\left(1 + 6\cos(h\pi) + 9\cos(h\pi)^2\right) \tag{A.12}$$

$$= \frac{1}{16}\cos(h\pi)^{|q|-2}\left(3\cos(h\pi) + 1\right)^2. \tag{A.13}$$

We summarize below the obtained expressions:

$$P_{1,1}(q) = \begin{cases} \frac{1}{4}\left(\cos(h\pi) + 3\right), & q = 0, \\ \frac{1}{8}\left(5\cos(h\pi) + 3\right), & q = 1, \\ \frac{1}{16}\cos(h\pi)^{|q|-2}\left(3\cos(h\pi) + 1\right)^2, & \text{otherwise.} \end{cases} \tag{A.14}$$

A.1.3 Computation of $P_{1,0}(q)$ and $P_{0,1}(q)$

We use (2.3) (2.4) to compute $P_{1,0}(q)$ and we get the following result

$$P_{1,0}(q) = \begin{cases} \frac{1}{2}\left(\cos(\frac{h\pi}{2})^2 + \cos(\frac{h\pi}{2})\cos(h\pi)^2\right), & q = 0, \\ \frac{1}{2}\cos(h\pi)^{|q|-1}\cos(\frac{h\pi}{2})\left(\cos(\frac{h\pi}{2})^2 + \cos(h\pi)^3\right), & \text{otherwise.} \end{cases} \tag{A.15}$$

The inter-correlation $P_{0,1}(q)$ can be obtained using (A.2). The different results of this section show that the pseudo-symbols of PRD are generally correlated when $|q| \leq 2$. However, when $q > 2$ and $h = 1/2$, the inter-correlation functions $P_{i,j}(q)$ become null.

A.2 Pseudo-symbols of DBD when h is non-integer

Since the expressions of the pseudo-symbols of DBD are similar to the ones found for the binary case, their correlations $\{C_{i,j}\}_{\{i,j\}\in(0,\ldots,M_d-1)^2}$ can be computed the same as in [15] as follows

$$C_{i,j}(p) = E\{\rho_{i,k}\rho^*_{j,k+p}\}, \tag{A.16}$$

$$= C_{i,j}(-p) = [\cos(h\pi)]^{\Delta(i,j,p)}, \tag{A.17}$$

where

$$\Delta(i,j,p) = |p| + \sum_{k=0}^{L_d-1} (\eta_{i,k}^d + \eta_{j,k}^d) - 2 \left[\sum_{\substack{k\le -p-1 \\ k\le L_d-1}}^{} \sum_{k\ge 0} \eta_{i,k}^d + \sum_{\substack{k\le p-1 \\ k\le L_d-1}}^{} \sum_{k\ge 0} \eta_{j,k}^d + \sum_{\substack{k\le L_d-p-1 \\ k\le L_d-1}}^{} \sum_{\substack{k\ge 0 \\ k\ge 1-p}} \eta_{i,k}^d \eta_{j,k+p}^d \right]. \quad \text{(A.18)}$$

When the modulation index h is equal to $1/2$, the pseudo-symbols are uncorrelated ($\Delta(i,j,p)$ can only be zero when $i = j$ and $p = 0$).

A.3 Pseudo-symbols of DBD when h is integer

When the modulation index is integer, it has been shown in [54] that

$$E\left\{a_{i,k} a_{j,k+q}^*\right\} = \begin{cases} 1, & i = j,\ q = 0, \\ 0, & \text{otherwise.} \end{cases} \quad \text{(A.19)}$$

Therefore, the pseudo-symbols of this decomposition are uncorrelated.

Appendix B

Appendix for Chapter 2: Pseudosymbols of PRD for SOQPSK

In this appendix we detail how (2.27) and (2.28) have been obtained starting from (2.3).

B.1 Computing $\nu_{0,i}$ for SOQPSK

By introducing γ_n using (2.1), we obtain

$$\nu_{0,i} = \exp\left\{ j\frac{\pi}{4}\left(\sum_{n=0}^{i} \gamma_n + \sum_{n=0}^{i} \gamma_{n-1} \right) \right\}. \tag{B.1}$$

After making an index change, gathering the common terms of the two sums and transforming the sum to a product, we obtain

$$\nu_{0,i} = \left(\prod_{n=0}^{i-1} e^{j\frac{\pi}{2}\gamma_n} \right) e^{j\frac{\pi}{4}\gamma_i} e^{j\frac{\pi}{4}\gamma_{-1}}. \tag{B.2}$$

Since $\gamma_n \in \{-1, +1\}$, we can write (B.2) as

$$\begin{aligned} \nu_{0,i} &= \frac{1}{2}\left(\prod_{n=0}^{i-1} j\gamma_n \right)(1 + j\gamma_i)(1 + j\gamma_{-1}), \\ &= \frac{1}{2} j^i \left(\prod_{n=0}^{i-1} \gamma_n \right)\left(1 - \gamma_{-1}\gamma_i + j(\gamma_{-1} + \gamma_i)\right). \end{aligned} \tag{B.3}$$

To simplify (B.3), we use the following property of the recursive precoder of (2.2)

$$\begin{aligned}\gamma_n \times \gamma_{n-1} &= (-1)^{n+1} b_n b_{n-1} \times (-1)^n b_{n-1} b_{n-2}, \\ &= -b_n b_{n-2}. \end{aligned} \tag{B.4}$$

Without loss of generality, we consider that $\gamma_{-1} = -1$ and $b_{-1} = b_{-2} = 1$. Then we distinguish two cases:

- i is even, i.e. $i = 2p$:

$$\begin{aligned}\prod_{n=0}^{2p-1} \gamma_n &= \prod_{n=1}^{p} \gamma_{2n-1}\gamma_{2n-2}, \\ &= (-1)^p b_{-1} b_1 \times b_3 b_1 ... \times b_{2p-1} b_{2p-3}, \\ &= (-1)^p b_{i-1}. \end{aligned} \tag{B.5}$$

  Therefore,

$$\begin{aligned}\nu_{0,i} &= \frac{1}{2} j^{2p} (-1)^p b_{i-1} (1 - (-1)^{i+1} b_i b_{i-1}, \\ &\quad + j(1 + (-1)^{i+1} b_i b_{i-1})), \\ &= \frac{1}{2}(b_{i-1} + b_i + j(b_{i-1} - b_i)). \end{aligned} \tag{B.6}$$

- i is odd, i.e. $i = 2p + 1$:

$$\begin{aligned}\prod_{n=0}^{2p} \gamma_n &= \gamma_0 \prod_{n=1}^{p} \gamma_{2n}\gamma_{2n-1}, \\ &= -b_0 b_{-1} (-1)^p b_0 b_2 \times b_4 b_2 ... \times b_{2p} b_{2p-2}, \\ &= (-1)^{p+1} b_{i-1}. \end{aligned} \tag{B.7}$$

  Thus,

$$\begin{aligned}\nu_{0,i} &= \frac{1}{2} j^{2p+1} (-1)^{p+1} b_{i-1} (1 - (-1)^{i+1} b_i b_{i-1}, \\ &\quad + j(1 + (-1)^{i+1} b_i b_{i-1})), \\ &= \frac{1}{2}(b_{i-1} + b_i - j(b_{i-1} - b_i)). \end{aligned} \tag{B.8}$$

By combining (B.6) and (B.8), we obtain (2.27) for all i.

B.2 Computing $\nu_{1,i}$ for SOQPSK

In order to simplify the expression of $\nu_{1,i}$, we follow the same steps as described in Appendix B.1 by introducing γ_n in (2.3) and by making an index change. We then get

$$\nu_{1,i} = \frac{1}{2}\left(\prod_{n=0}^{i-2} e^{j\frac{\pi}{2}\gamma_n}\right)\left(e^{j\frac{\pi}{4}\gamma_{i-1}} \times e^{j\frac{\pi}{4}\gamma_i} + e^{j\frac{\pi}{2}\gamma_{i-1}}\right) e^{j\frac{\pi}{4}\gamma_{-1}}. \tag{B.9}$$

We use the same transformation made in (B.3), thus

$$\nu_{1,i} = \frac{\sqrt{2}}{8}\left(j^{i-1}\prod_{n=0}^{i-2}\gamma_n\right)((1+j\gamma_{i-1})(1+j\gamma_i)+2j\gamma_{i-1})) \times (1+j\gamma_{-1}). \tag{B.10}$$

Using the property of γ_n (see (B.4)), and by distinguishing whether i is even or odd, we simplify the expression of the product found in (B.10) and we obtain (2.28).

Appendix C

Appendix for Chapter 2: Pseudosymbols of DBD for SOQPSK

In this appendix, we prove how we get the final expressions of the pseudo-symbols $\rho_{0,i}$ and $\rho_{1,i}$ for SOQPSK as described in (2.31). First of all, we suppose that for $n \leq 0$, $\alpha_n = 0$, i.e. $\sum_{n=-\infty}^{0} \gamma_n = 0$. This hypothesis is fundamental to define the initial phase of the signal.

C.0.1 Computing $\rho_{0,i}$ for SOQPSK

Starting from (2.20) we obtain

$$\rho_{0,i} = \exp\left\{ j\frac{\pi}{2} \sum_{n=1}^{i} \gamma_n \right\}. \tag{C.1}$$

Like in Appendix B, we transform the sum inside the exponential into a product of i exponentials and we use the fact that $e^{j\frac{\pi}{2}\gamma_n} = j\gamma_n$. Therefore,

$$\rho_{0,i} = \prod_{n=1}^{i} j\gamma_n = j^i \prod_{n=1}^{i} \gamma_n. \tag{C.2}$$

Then we use the property of γ_n introduced in (B.4) and we distinguish two cases:

- i is even, i.e. $i = 2p$:

$$\begin{aligned}\rho_{0,i} &= j^{2p} \prod_{n=1}^{p} \gamma_{2n}\gamma_{2n-1}, \\ &= (-1)^p \times (-1)^p \times b_2 b_0 \times b_4 b_2 ... \times b_{2p} b_{2p-2}, \\ &= b_0 b_i. \end{aligned} \tag{C.3}$$

- i is odd, i.e. $i = 2p + 1$:

$$\begin{aligned}\rho_{0,i} &= j^{2p+1} \left(\prod_{n=1}^{p} \gamma_{2n}\gamma_{2n-1} \right) \gamma_{2p+1}, \\ &= j(-1)^p \times (-1)^p b_0 b_{i-1} \times b_i b_{i-1}, \\ &= j b_0 b_i. \end{aligned} \tag{C.4}$$

Without loss of generality, we assume that $b_0 = 1$ and therefore the final expression of $\rho_{0,i}$ found in (2.31) is achieved.

C.0.2 Computing $\rho_{1,i}$ for SOQPSK

Once the simplification of $\rho_{0,i}$ is made, the final expression of $\rho_{1,i}$ can easily be found since

$$\rho_{1,i} = \rho_{0,i} \times e^{-j\frac{\pi}{2}\gamma_{i-1}}. \tag{C.5}$$

Using the fact that $e^{-j\frac{\pi}{2}\gamma_{i-1}} = -j\gamma_{i-1}$, we obtain (2.31).

Appendix D

Appendix for Chapter 3: Reduced complexity detector based on PRD

In this appendix we detail the reduced complexity detector algorithm given in [14, 18]. This detector relies on Kaleh approach and uses the PAM approximation of PRD.

We remind that SOQPSK is corrupted by AWGN $n(t)$. The received signal is thus expressed as

$$r(t) = s(t;\underline{\alpha}) + n(t). \tag{D.1}$$

If we suppose that N ternary symbols are transmitted, then the log-likelihood function $\lambda(\underline{b})$ is described in (3.2). We follow the same line of reasoning of Section 3.2 to get (3.4). Then, we replace $s(t;\underline{\alpha})$ with its PRD described in Section 1.5.3 of Chapter 1 to obtain the following expression of $\lambda(\underline{b})$

$$\Lambda(\underline{b}) = \frac{2}{N_0}\sum_{n=0}^{N-1} Re\left\{\int_0^{NT} r(t)\left(\sum_{k=0}^{R-1}\nu_{k,i}^{*}p_k(t-nT)\right)dt\right\}. \tag{D.2}$$

By permuting the integral and the second sum and by discarding the constant term $\frac{2}{N_0}$ in (3.5), the optimal detector maximizes the following branch metric

$$\Lambda(\underline{b}) = \sum_{n=0}^{N-1}\lambda(n), \tag{D.3}$$

where

$$\begin{cases} \lambda(n) = Re\left(\sum_{k=0}^{R-1} y_k(n)\nu_{k,n}^*\right), & \text{(D.4)} \\ y_k(n) = \int_{nT}^{(n+D_k^{\mathrm{p}})T} r(t)p_k(t-nT)dt. & \text{(D.5)} \end{cases}$$

The parameter D_k^{p} is the length of the pulse $p_k(t)$. The complexity of the detector depends on the value of R and the memory of $\nu_{k,n}$. We remind that SOQPSK-MIL can be exactly decomposed into a sum of 2 PAM waveforms using PRD. The same number of pulses is also needed to accurately approximate SOQPSK-TG. Therefore, equation (D.4) becomes

$$\lambda(n) = Re\left(\sum_{k=0}^{1} y_k(n)\nu_{k,n}^*\right). \tag{D.6}$$

We now focus on the expressions of $\nu_{0,n}$ and $\nu_{1,n}$ given in (1.25). These pseudo symbols are a function of $(\gamma_{1,n}, \gamma_{2,n}) \in (\{-1,+1\})^2$ such that $\alpha_n = \frac{1}{2}(\gamma_{1,n} + \gamma_{2,n})$. Simultaneously, we have $\alpha_n = (-1)^{n+1}\frac{b_{n-1}}{2}(b_n - b_{n-2})$ (Eq. (1.9)), i.e.,

$$\begin{aligned} \alpha_n &= (-1)^{n+1}\frac{b_{n-1}}{2}(b_n - b_{n-2}), & \text{(D.7)} \\ &= \frac{1}{2}(\gamma_{1,n} + \gamma_{2,n}). & \text{(D.8)} \end{aligned}$$

Therefore, it is necessary to find a link between $(\gamma_{1,n}, \gamma_{2,n})$ and b_n. To do so, Perrins proposed the following steps:

- The first step is to describe the SOQPSK-precoder using a trellis. The mapping given in (D.7) results in a time-varying trellis. The states and the transitions of the trellis depend on the parity of the epoch. Without loss of generality, we suppose that n is even and we depict in Figure D.1 the trellis at epoch n and epoch $n+1$. The label above each branch shows the input bits/output symbol pair at each epoch, i.e., at epoch n the displayed pair is b_n/α_n and at epoch $n+1$, the displayed pair is b_{n+1}/α_{n+1}.

- The second step links the expression of the pseudo-symbols $\{\nu_{k,n}\}_{k\in\{0,1\}}$ given in (1.25) with the trellis. To do so, Perrins showed that the pseudo-symbols can be rewritten as follows

$$\nu_{k,n} = e^{j\theta_{n-1}}\upsilon_k, \tag{D.9}$$

where

$$\theta_{n-1} = \frac{\pi}{2}\sum_{i=0}^{n-1}\alpha_i, \tag{D.10}$$

and

$$\begin{cases} \upsilon_0 = \alpha_n = \dfrac{1}{2}(\gamma_{1,n} + \gamma_{2,n}) & \text{(D.11)} \\ \upsilon_1 = \dfrac{1}{2}\left(e^{j\frac{\pi}{4}\gamma_{1,n}} + e^{j\frac{\pi}{4}\gamma_{2,n}}\right). & \text{(D.12)} \end{cases}$$

Since the value of α_n is known in the trellis because it is a function of the triplet (b_{n-2}, b_{n-1}, b_n), it is thus possible to infer the values of $\upsilon_k(\alpha_n)$ using (D.8) as shown in Table D.1. The second parameter that must be linked with the trellis is the phase θ_{n-1}, which can take values in the set $\{-\frac{\pi}{2}, 0, \frac{\pi}{2}, \pi\}$. It has been shown in [18] that there is one-to-one mapping between the different states of the trellis and the possible values of θ_{n-1}. This mapping is given in Table D.2.

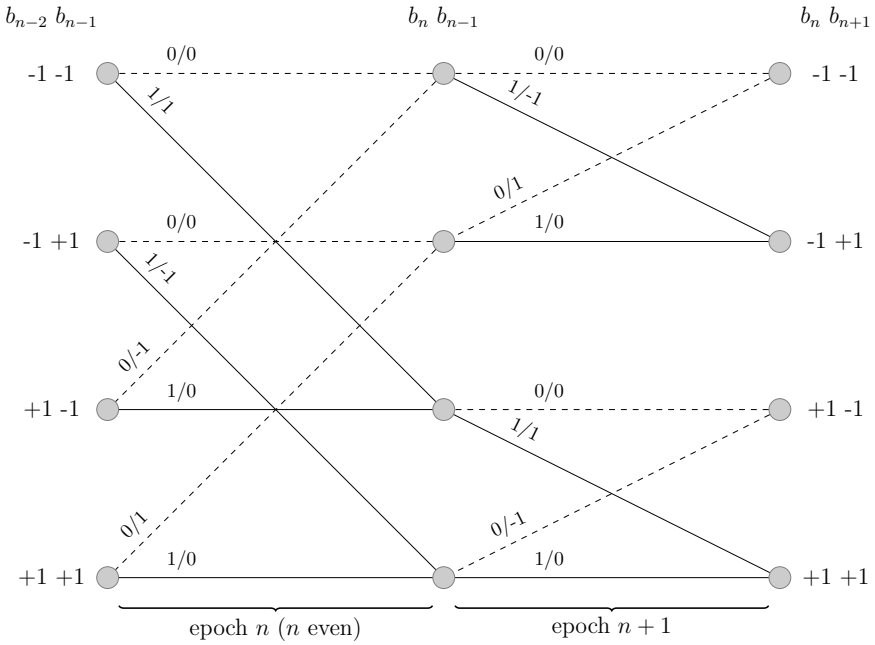

Figure D.1 – Time-varying trellis using PRD. The label above each the branch shows the input bits/output symbol pair at each epoch..

Table D.1 – Link between α_n and $\upsilon_k(\alpha_n)$

α_n	$\gamma_{1,n}$ $\gamma_{2,n}$	υ_0	υ_1
-1	-1 -1	$\exp(-j\pi/2) = -j$	$\exp(-j\pi/4) = \frac{1}{\sqrt{2}}(1-j)$
0	-1 -1, or 1 -1	1	$\cos(\pi/4) = \frac{1}{\sqrt{2}}$
1	1 1	$\exp(j\pi/2) = j$	$\exp(j\pi/4) = \frac{1}{\sqrt{2}}(1+j)$

Table D.2 – Link between θ_{n-1} and the trellis states of Figure D.1

State of the trellis	θ_{n-1}
-1 -1	$-\frac{\pi}{2}$
-1 1	π
1 -1	0
1 1	$\frac{\pi}{2}$

As a consequence, a Viterbi algorithm operating with a time-varying trellis composed of 4 states is necessary to detect the data bits. This algorithm is optimal for SOQPSK-MIL (Figure 3.7) and very near-optimal for SOQPSK-TG (Figure 3.8).

Remark: Thanks to the proposed new vision of the SOQPSK precoder given in Figure 2.1, we were able to find a direct mapping between the pseudo-symbols $\{\nu_{k,n}\}_{k\in\{0,1\}}$ and the binary symbol b_n. This mapping is described in (2.27) and (2.28) (Chapter 2) and shows that is not necessary to employ a time-varying trellis for the Viterbi algorithm even if we rely on PRD. Only the expression of the branch metric depends on the parity of n.

List of Publications

International Journals

[IJ-2] **Othman, R.**, Skrzypczack, A., Louët, Y. " Reduced Complexity Detectors Based on SOQPSK Linearzations,", in *IEEE Transactions on Aerospace and Electronic Systems*, 2018 (Major Revision)

[IJ-1] **Othman, R.**, Skrzypczack, A., Louët, Y., " PAM Decomposition of Ternary CPM With Duobinary Encoding,", in *IEEE Transactions on Communications*, vol. 65, no. 10, pp. 4274-4284, doi: 10.1109/TCOMM.2017.2723567, Oct 2017

International Conferences

[IC-5] **Othman, R.**, Louët, Y., Skrzypczack, A. "Linear Decision Feedback Detector for SOQPSK,", in *URSI AP-RASC*, 2019 (Submitted)

[IC-4] **Othman, R.**, Louët, Y., Skrzypczack, A. "A Reduced Complexity OQPSK-Type Detector For SOQPSK,", in *IEEE 88th Vehicular Technology Conference (VTC-Fall)*,Chicago,Sep 2018 (to be published)

[IC-3] **Othman, R.**, Louët, Y., Skrzypczack, A. "Joint Channel Estimation and Detection of SOQPSK Using the PAM Decomposition,", in *IEEE 25th International Conference on Telecommunications (ICT)*, St. Malo, pp. 154-158. doi: 10.1109/ICT.2018.8464828, Jun 2018

[IC-2] **Othman, R.**, Louët, Y., Skrzypczack, A. "Analysis of Duobinary Encoding for CPM Signals,", in *URSI General Assembly and Symposium*, Montreal, Aug 2017

[IC-1] **Othman, R.**, Skrzypczack, A., Louët, Y. " Phase offset estimation of SOQPSK waveform by the analysis of the angle distribution,", in *IEEE 13th International Symposium on Wireless Communication Systems*, Poznan, pp. 16-21. doi: 10.1109/ISWCS.2016.7600847, Sep 2016

National Conferences

[NC-1] **Othman, R.**, Louët, Y., Skrzypczack, A. "Décomposition PAM d'un signal CPM avec encodage duo-binaire - Application à la modulation SOQPSK,", in *GRETSI*, Juan-Les-Pins, France, Sep 2017

Other National Communications

[ONC-3] **Othman, R.**, Louët, Y., Skrzypczack, A. "A New PAM Decomposition for SOQPSK in Aernautical Telemetry Context,", in *Journée Des Doctorants de l'IETR*, Rennes, France, Jul 2017

[ONC-2] **Othman, R.**, Louët, Y., Skrzypczack, A. "Etude de techniques d'égalisation aveugles et aidées pour les modulations de fréquence,", in *SCEE Seminar*, Rennes, France, Jun 2017

[ONC-1] **Othman, R.**, Louët, Y., Skrzypczack, A. "Etude de techniques d'égalisation aveugles et aidées pour les modulations de fréquence,", in *Journée Des Doctorants de l'IETR*, Rennes, France, Jun 2016

Patents

[PT-1] **Othman, R.**, Louët, Y., Skrzypczack, A. " Nouvelle architecture de décodage spatio-temporel basée sur la décomposition PAM pour la modulation SOQPSK-TG," (pending)

List of Figures

List of Tables

List of Algorithms

Bibliography

[1] The Editors of Encyclopaedia Britannica, "Telemetry." Encyclopædia Britannica, inc., Apr 2013.

[2] D. Stacey, *Aeronautical Radio Communication Systems and Networks*. Wiley InterScience online books, Wiley, 2008.

[3] R. J. Punnoose, "Re-Engineering PCM/FM as a Phase Modulation Scheme," *International Telemetering Conference Proceedings*, Oct 2008.

[4] J. B. Anderson, T. Aulin, and C.-E. Sundberg, *Digital Phase Modulation*. New York: Plenum Press, 1986.

[5] IRIG, "Telemetry Standards, IRIG Standard 106-17 (Part 1), Chapter 2," Aug 2017.

[6] International Telecommunications Union, "ICT Facts and Figures 2017," Oct 2018.

[7] P. Goldstein, "It's Over: FCC's AWS-3 Spectrum Auction Ends at Record $44.9B in Bids." Fiercewireless, Jan Jan, 2015.

[8] T. Chalfant, "Ninja Telemetry AMT Survival in a Congested Spectral Environment," *European Test and Telemetry Conference*, June 2018.

[9] D. E. Ernst, C. A. Kahn, and D. L. Portigal, "The Economic Importance of Adequate Aeronautical Telemetry Spectrum." MITRE Technical Report, Jan 2007.

[10] C. A. Kahn, "Economic Impact of Telemetry and Its Essential Role in the Aerospace Industry," *International Telemetering Conference Proceedings*, Oct 2003.

[11] M. Rice, A. Davis, and C. Bettweiser, "Wideband Channel Model for Aeronautical Telemetry," *IEEE Transactions on Aerospace and Electronic Systems*, vol. 40, pp. 57–69, Jan 2004.

[12] T. A. Chalfant and C. E. Irving, "Range Telemetry Improvement and Modernization," *International Telemetering Conference Proceedings*, Oct 1997.

[13] M. A. Jensen, M. D. Rice, and A. L. Anderson, "Aeronautical Telemetry using Multiple-Antenna Transmitters," *IEEE Transactions on Aerospace and Electronic Systems*, vol. 43, pp. 262–272, Jan 2007.

[14] S. E. Perrins, *Reduced Complexity Detection Methods for Continuous Phase Modulation*. PhD thesis, Brigham Young University - Provo, July 2005.

[15] P. Laurent, "Exact and Approximate Construction of Digital Phase Modulations by Superposition of Amplitude Modulated Pulses (AMP)," *IEEE Transactions on Communications*, vol. 34, pp. 150–160, Feb 1986.

[16] N. T. Nelson, *Space-Time Coding with Offset Modulations*. PhD thesis, Brigham Young University - Provo, 2007.

[17] M. Geoghegan, "Optimal Linear Detection of SOQPSK," *International Telemetering Conference Proceedings*, Oct 2002.

[18] E. Perrins and M. Rice, "Reduced-Complexity Approach to Iterative Detection of Coded SOQPSK," *IEEE Transactions on Communications*, vol. 55, pp. 1354–1362, July 2007.

[19] M. Rice, M. Saquib, A. Cole-Rhodes, F. Moazzami, and E. Perrins, *Phase 1 Final Report: Preamble Assisted Equalization for Aeronautical Telemetry (PAQ)*. Brigham Young University, 2014.

[20] A. Cole-Rhodes and M. Rice, "A Block Processing Approach to CMA Equalization of SOQPSK for Aeronautical Telemetry," *IEEE Military Communications Conference*, pp. 440–444, Oct 2014.

[21] S. KoneDossongui, O. Opasina, H. Umuolo, H. Betelle, S. Thang, and R. Shrestha, "Evaluation of CMA+AMA Equalization for SOQPSK Modulation in Aeronautical Telemetry," Oct 2013.

[22] M. Pedroza, "Antenna Pattern Evaluation for Link Analysis," *International Telemetering Conference Proceedings*, Oct 1996.

[23] S. M. Alamouti, "A Simple Transmit Diversity Technique for Wireless Communications," *IEEE Journal on Selected Areas in Communications*, vol. 16, pp. 1451–1458, Oct 1998.

[24] M. Rice, T. Nelson, J. Palmer, C. Lavin, and K. Temple, "Space-Time Coding for Aeronautical Telemetry: Part II –; Decoder and System Performance," *IEEE Transactions on Aerospace and Electronic Systems*, vol. 53, pp. 1732–1754, Aug 2017.

[25] G. K. Kaleh, "Simple Coherent Receivers for Partial Response Continuous Phase Modulation," *IEEE Journal on Selected Areas in Communications*, vol. 7, pp. 1427–1436, Dec 1989.

[26] G. Ungerboeck, "Adaptive Maximum-Likelihood Receiver for Carrier-Modulated Data-Transmission Systems," *IEEE Transactions on Communications*, vol. 22, pp. 624–636, May 1974.

[27] G. Forney, "Maximum-Likelihood Sequence Estimation of Digital Sequences in The Presence of Intersymbol Interference," *IEEE Transactions on Information Theory*, vol. 18, pp. 363–378, May 1972.

[28] R. Raheli, A. Polydoros, and C.-K. Tzou, "Per-Survivor Processing: a General Approach to MLSE in Uncertain Environments," *IEEE Transactions on Communications*, vol. 43, pp. 354–364, Feb 1995.

[29] M. Mouly and M.-B. Pautet, *The GSM System for Mobile Communications*. Telecom Publishing, 1992.

[30] L. Lampe, R. Schober, and M. Jain, "Noncoherent Sequence Detection Receiver for Bluetooth Systems," *IEEE Journal on Selected Areas in Communications*, vol. 23, pp. 1718–1727, Sept 2005.

[31] E. Casini, D. Fertonani, and G. Colavolpe, "Advanced CPM Receiver for the NATO Tactical Narrowband Waveform," *MILITARY COMMUNICATIONS CONFERENCE (MILCOM)*, pp. 1725–1730, Oct 2010.

[32] AHWG/2 - SC/6, *Standardisation Agreement STANAG: Technical Standards for Narrowband Physical Layer of the NATO Networking Enabled Communications Waveform and VHF Propagation Models*. NATO, Mar 2009.

[33] DVB BlueBook A155-2 (03/11), *DVB-RCS2 Lower Layer Satellite Specification*. DVB, Jul 2018.

[34] R. Baroni, F. Lombardo, R. Suffritti, E. A. Candreva, A. Vanelli-Coralli, G. E. Corazza, G. Colavolpe, G. Gallinaro, and N. Alagha, "Performance Analysis of a Mesh Satellite System based on Linear and Continuous Phase Modulations," *IEEE International Conference on Communications (ICC)*, pp. 3255–3259, June 2012.

[35] M. K. Simon, *Bandwidth-Efficient Digital Modulation with Application to Deep-Space Communications*. John Wiley & Sons, 2005.

[36] M. J. Dapper and T. J. Hill, "SBPSK: A Robust Bandwidth-Efficient Modulation for Hard-Limited Channels," in *MILCOM 1984 - IEEE Military Communications Conference*, vol. 3, pp. 458–463, Oct 1984.

[37] D. I. S. Agency, "Department of Defense Interface Standard, Interoperability Standard for Single-Access 5-kHz and 25-kHz UHF Satellite Communications Channels," 1999.

[38] H. Farès, C. Glattli, Y. Louët, C. Moy, J. Palicot, and P. Roulleau, "New Binary Single Side Band CPM," in *2017 24th International Conference on Telecommunications (ICT)*, pp. 1–5, May 2017.

[39] A. N. Premji and D. Taylor, "A Practical Receiver Structure for Multi-h CPM Signals," *IEEE Transactions on Communications*, vol. 35, pp. 901–908, Sep 1987.

[40] C. Fewer and S. Wilmot, "Enhancing the PCM/FM Link - Without The Math," *International Telemetering Conference Proceedings*, Oct 2007.

[41] J. B. Anderson and A. Svensson, *Coded Modulation Systems*. Norwell, MA, USA: Kluwer Academic Publishers, 2002.

[42] E. Perrins and M. Rice, "Reduced-Complexity Detectors for Multi-h Cpm in Aeronautical Telemetry," *IEEE Transactions on Aerospace and Electronic Systems*, vol. 43, pp. 286–300, Jan 2007.

[43] T. J. Hill, "An Enhanced, Constant Envelope, Interoperable Shaped Offset QPSK (SOQPSK) Waveform For Improved Spectral Efficiency," *International Telemetering Conference Proceedings*, Oct 2000.

[44] P. S. K. Leung and K. Feher, "F-QPSK-a Superior Mmodulation Technique For Mobile and Personal Communications," *IEEE Transactions on Broadcasting*, vol. 39, pp. 288–294, Jun 1993.

[45] E. Perrins and M. Rice, "PAM Representation of Ternary CPM," *IEEE Transactions on Communications*, vol. 56, pp. 2020–2024, Dec 2008.

[46] M. Geoghegan, "Description and Performance Results for a Multi-h CPM Telemetry Waveform," in *MILCOM 2000 Proceedings. 21st Century Military Communications. Architectures and Technologies for Information Superiority (Cat. No.00CH37155)*, vol. 1, pp. 353–357, Oct 2000.

[47] R. J. Punnoose, "Re-engineering PCM/FM as a Phase Modulation Scheme," in *International Telemetering Conference Proceedings*, International Foundation for Telemetering, Oct 2008.

[48] E. Perrins and M. Rice, "A New Performance Bound for PAM-based CPM Detectors," *IEEE Transactions on Communications*, vol. 53, pp. 1688–1696, Oct 2005.

[49] I. Sasase and S. Mori, "Multi-h Phase-Coded Modulation," *IEEE Communications Magazine*, vol. 29, pp. 46–56, Dec 1991.

[50] M. Geoghegan, "Implementation and Performance Results for Trellis Detection of SOQPSK," *International Telemetering Conference Proceedings*, Oct 2001.

[51] B. E. Rimoldi, "A Decomposition Approach to CPM," *IEEE Transactions on Information Theory*, vol. 34, pp. 260–270, Mar 1988.

[52] P. Moqvist and T. M. Aulin, "Orthogonalization by Principal Components Applied to CPM," *IEEE Transactions on Communications*, vol. 51, pp. 1838–1845, Nov 2003.

[53] Q. Zhao and G. L. Stuber, "Robust Time and Phase Synchronization for Continuous Phase Modulation," *IEEE Transactions on Communications*, vol. 54, pp. 1857–1869, Oct 2006.

[54] X. Huang and Y. Li, "The PAM Decomposition of CPM Signals with Integer Modulation Index," *IEEE Transactions on Communications*, vol. 51, pp. 543–546, Apr 2003.

[55] U. Mengali and M. Morelli, "Decomposition of M-ary CPM Signals into PAM Waveforms," *IEEE Transactions on Information Theory*, vol. 41, pp. 1265–1275, Sep 1995.

[56] E. Perrins and M. Rice, "PAM Decomposition of M-ary Multi-h CPM," *IEEE Transactions on Communications*, vol. 53, pp. 2065–2075, Dec 2005.

[57] M. P. Wylie-Green, "A New PAM Decomposition for Continuous Phase Modulation," *2006 40th Annual Conference on Information Sciences and Systems*, pp. 705–710, Mar 2006.

[58] U. Mengali and A. N. D'Andrea, *Synchronization Techniques for Digital Receivers*. Applications of communications theory, New York, London: Plenum Press, 1997.

[59] B. Kumaraswamy and E. Perrins, "Simplified 2-State Detectors for SOQPSK," *MILCOM 2007 - IEEE Military Communications Conference*, pp. 1–7, Oct 2007.

[60] M. Simon and L. Li, "A Cross-Correlated Trellis-Coded Quadrature Modulation Representation of MIL-STD Shaped Offset Quadrature Phase-Shift Keying," *Interplanetary Network Progress Report, Jet Propulsion Laboratory*, pp. 42–154, 2003.

[61] L. Li and M. K. Simon, "Performance of Coded OQPSK and MIL-STD SOQPSK with Iterative Decoding," *IEEE Transactions on Communications*, vol. 52, pp. 1890–1900, Nov 2004.

[62] T. Nelson and M. Rice, "A Unified Perspective on ARTM Tier I Waveforms - Part I: Common Representations," in *MILCOM 2005 - 2005 IEEE Military Communications Conference*, pp. 897–903 Vol. 2, Oct 2005.

[63] T. Nelson, E. Perrins, and M. Rice, "Near Optimal Common Detection Techniques for Shaped Offset QPSK and Feher's QPSK," *IEEE Transactions on Communications*, vol. 56, pp. 724–735, May 2008.

[64] J. G. Proakis, *Digital Communications*. McGraw-Hill New York, 1983.

[65] A. Lender, "The Duobinary Technique for High-Speed Data Transmission," *Transactions of the American Institute of Electrical Engineers, Part I: Communication and Electronics*, vol. 82, pp. 214–218, May 1963.

[66] R. Othman, A. Skrzypczak, and Y. Louët, "PAM Decomposition of Ternary CPM With Duobinary Encoding," *IEEE Transactions on Communications*, vol. 65, pp. 4274–4284, Oct 2017.

[67] CCSDS, *Bandwidth-Efficient Modulations: Summary of Definition, Implementation, and Performance*. Green Book. Issue 2, Oct 2009.

[68] N. Al-Dhahir and G. Saulnier, "A High-Performance Reduced-Complexity GMSK Demodulator," in *Asilomar Conference on Signals, Systems and Computers*, pp. 612–616 vol 1, Nov 1996.

[69] G. M. A. Sessler, R. Abello, N. James, R. Madde, and E. Vassallo, "GMSK Demodulator Implementation for ESA Deep-Space Missions," *Proceedings of the IEEE*, vol. 95, pp. 2132–2141, Nov 2007.

[70] K. H. Hwang and M. A. Wickert, "A Soft Output GMSK Demodulator using a 4-filter MLSE for Small BT Product," in *2002 IEEE International Conference on Communications. Conference Proceedings. ICC 2002 (Cat. No.02CH37333)*, vol. 5, pp. 2957–2961 vol.5, May 2002.

[71] H. Mathis, "Differential Detection of GMSK Signals with Low BtT using the SOVA," *IEEE Transactions on Communications*, vol. 46, pp. 428–430, Apr 1998.

[72] M. Rice, B. McIntire, and O. Haddadin, "Data-Aided Carrier Phase Estimation for GMSK," in *Communications, 2003. ICC '03. IEEE International Conference on*, vol. 5, pp. 3560–3564 vol.5, May 2003.

[73] L. Jiang, *Propagation Properties of Duobinary Transmission in Optical Fibers*. Massachusetts Institute of Technology, Department of Electrical Engineering and Computer Science; and, Thesis (B.S.), 1998.

[74] M. Messai, A. Piemontese, G. Colavolpe, K. Amis, and F. Guilloud, "Binary CPMs With Improved Spectral Efficiency," *IEEE Communications Letters*, vol. 20, pp. 85–88, Jan 2016.

[75] A. Barbieri, D. Fertonani, and G. Colavolpe, "Spectrally-Efficient Continuous Phase modulations," *IEEE Transactions on Wireless Communications*, vol. 8, pp. 1564–1572, Mar 2009.

[76] D. M. Arnold, H. A. Loeliger, P. O. Vontobel, A. Kavcic, and W. Zeng, "Simulation-Based Computation of Information Rates for Channels With Memory," *IEEE Transactions on Information Theory*, vol. 52, pp. 3498–3508, Aug 2006.

[77] A. Barbieri and G. Colavolpe, "Simplified Soft-Output Detection of CPM Signals Over Coherent and Phase Noise Channels," *IEEE Transactions on Wireless Communications*, vol. 6, pp. 2486–2496, July 2007.

[78] M. Messai, G. Colavolpe, K. Amis, and F. Guilloud, "Binary Continuous Phase Modulations Robust to a Modulation Index Mismatch," *IEEE Transactions on Communications*, vol. 63, pp. 4267–4275, Nov 2015.

[79] G. Colavolpe, G. Montorsi, and A. Piemontese, "Spectral Efficiency of Linear and Continuous Phase Modulations Over Nonlinear Satellite Channels," *IEEE International Conference on Communications (ICC)*, pp. 3175–3179, June 2012.

[80] B. Younes, J. Brase, C. Patel, and J. Wesdock, "An Assessment of Shaped Offset QPSK for Use in NASA Space Network and Ground Network Systems," *Meetings of Consultative Committee for Space Data Systems*, Oct 2000.

[81] I. Lakkis, J. Su, and S. Kato, "A Simple Coherent GMSK Demodulator," *12th IEEE International Symposium on Personal, Indoor and Mobile Radio Communications*, vol. 1, pp. A–112–A–114 vol.1, Sep 2001.

[82] T. Benaddi, *SparseGraph-Based Coding Schemes for Continuous Phase Modulations*. PhD thesis, Institut National Polytechnique de Toulouse (INP Toulouse), Dec 2015.

[83] T. Benaddi, C. Poulliat, M.-L. Boucheret, B. Gadat, and G. Lesthievent, "Récepteur Exact pour la Décomposition de Laurent pour les CPM," in *25eme Edition du Colloque Groupe de Recherche et d'Etudes du Traitement du Signal et des Images (GRETSI)*, (Lyon, France), pp. pp. 1–4, Sep 2015.

[84] E. Perrins, "FEC Systems for Aeronautical Telemetry," *IEEE Transactions on Aerospace and Electronic Systems*, vol. 49, pp. 2340–2352, Oct 2013.

[85] D. Raphaeli, "A Reduced Complexity Equalizer for OQPSK," *IEEE Transactions on Communications*, vol. 58, pp. 46–51, Jan 2010.

[86] M. V. Eyuboglu and S. U. H. Qureshi, "Reduced-State Sequence Sstimation with Set Partitioning and Decision Feedback," *IEEE Transactions on Communications*, vol. 36, pp. 13–20, Jan 1988.

[87] A. Svensson, "Reduced State Sequence Detection of Partial Response Continuous Phase Modulation," *IEE Proceedings I - Communications, Speech and Vision*, vol. 138, pp. 256–268, Aug 1991.

[88] A. Skrzypczak, A. Thomas, and G. Duponchel, "Paradigms Optimization for a C-Band COFDM Telemetry with High Bit Efficiency," *International Telemetering Conference Proceedings*, Oct 2013.

[89] C. Bluemm, C. Heller, B. Fourestie, and R. Weigel, "Wideband aeronautical channel sounding and modeling for c-band telemetry," *2013 IEEE 24th Annual International Symposium on Personal, Indoor, and Mobile Radio Communications (PIMRC)*, pp. 264–269, Sep 2013.

[90] D. Godard, "Self-Recovering Equalization and Carrier Tracking in Two-Dimensional Data Communication Systems," *IEEE Transactions on Communications*, vol. 28, pp. 1867–1875, Nov 1980.

[91] J. Tan and G. L. Stuber, "Frequency-Domain Equalization for Continuous Phase Modulation," *2004 IEEE 15th International Symposium on Personal, Indoor and Mobile Radio Communications (IEEE Cat. No.04TH8754)*, vol. 3, pp. 2267–2272 Vol.3, Sep 2004.

[92] F. Pancaldi and G. M. Vitetta, "Equalization Algorithms in the Frequency Domain for Continuous Phase Modulations," *IEEE Transactions on Communications*, vol. 54, pp. 648–658, Apr 2006.

[93] W. V. Thillo, F. Horlin, J. Nsenga, V. Ramon, A. Bourdoux, and R. Lauwereins, "Low-Complexity Linear Frequency Domain Equalization for Continuous Phase Modulation," *IEEE Transactions on Wireless Communications*, vol. 8, pp. 1435–1445, Mar 2009.

[94] R. Chayot, N. Thomas, C. Poulliat, M. L. Boucheret, N. V. Wambeke, and G. Lesthievent, "Channel Estimation and Equalization for CPM with Application for Aeronautical Communications via a Satellite Link," *IEEE Military Communications Conference (MILCOM)*, pp. 888–893, Oct 2017.

[95] Q. Lei and M. Rice, "Multipath Channel Model for Over-Water Aeronautical Telemetry," *IEEE Transactions on Aerospace and Electronic Systems*, vol. 45, pp. 735–742, Apr 2009.

[96] C. J. Hogstrom, "A Survey of Sparse Channel Estimation in Aeronautical Telemetry," Master's thesis, Brigham Young University, 2017.

[97] S. Saleem, *Frequency-Domain Equalization for Multi-h Continuous Phase Modulation*. PhD thesis, Georgia Institute of Technology, Dec 2013.

[98] P. Bello, "Characterization of Randomly Time-Variant Linear Channels," *IEEE Transactions on Communications Systems*, vol. 11, pp. 360–393, Dec 1963.

[99] M. Rice, R. Dye, and K. Welling, "Narrowband Channel Model for Aeronautical Telemetry," *IEEE Transactions on Aerospace and Electronic Systems*, vol. 36, pp. 1371–1376, Oct 2000.

[100] P. Matthias, *Mobile Fading Channels*. John Wiley & Sons,Ltd, 2003.

[101] W. C. Lee, *Mobile Communications Engineering*. McGraw-Hill Professional, 1982.

[102] R. S. O., "Statistical Properties of a Sine Wave Plus Random Noise," *Bell System Technical Journal*, vol. 27, no. 1, pp. 109–157, 1948.

[103] E. Lutz, D. Cygan, M. Dippold, F. Dolainsky, and W. Papke, "The Land Mobile Satellite Communication Channel-Recording, Statistics, and Channel Model," *IEEE Transactions on Vehicular Technology*, vol. 40, pp. 375–386, May 1991.

[104] S. Zhu, T. S. Ghazaany, S. M. R. Jones, R. A. Abd-Alhameed, J. M. Noras, T. V. Buren, J. Wilson, T. Suggett, and S. Marker, "Probability Distribution of Rician K-Factor in Urban, Suburban and Rural Areas Using Real-World Captured Data," *IEEE Transactions on Antennas and Propagation*, vol. 62, pp. 3835–3839, July 2014.

[105] H. D. Tu and S. Shimamoto, "A Proposal of Wide-Band Air-to-Ground Communication at Airports Employing 5-GHz Band," *2009 IEEE Wireless Communications and Networking Conference*, pp. 1–6, April 2009.

[106] R. Johnson, P. Schniter, T. J. Endres, J. D. Behm, D. R. Brown, and R. A. Casas, "Blind Equalization Using the Constant Modulus Criterion: a Review," *Proceedings of the IEEE*, vol. 86, pp. 1927–1950, Oct 1998.

[107] O. Shalvi and E. Weinstein, "New Criteria for Blind Deconvolution of Nonminimum Phase Systems (Channels)," *IEEE Transactions on Information Theory*, vol. 36, pp. 312–321, Mar 1990.

[108] S. Vembu, S. Verdu, R. A. Kennedy, and W. Sethares, "Convex cost functions in blind equalization," *IEEE Transactions on Signal Processing*, vol. 42, pp. 1952–1960, Aug 1994.

[109] P. Bianchi, *Demodulation Aveugle de Modulations Non Lineaires a Phase Continue*. PhD thesis, Universite de Marne la Vallee, France, 2003.

[110] P. Bianchi and P. Loubaton, "On the Blind Equalization of Continuous Phase Modulated Signals Using the Constant Modulus Criterion," *IEEE Transactions on Signal Processing*, vol. 55, pp. 1047–1061, Mar 2007.

[111] B. Agee, "The Least-Squares CMA: A New Technique for Rapid Correction of Constant Modulus Signals," *ICASSP '86. IEEE International Conference on Acoustics, Speech, and Signal Processing*, vol. 11, pp. 953–956, Apr 1986.

[112] P. A. Regalia, "A Finite-Interval Constant Modulus Algorithm," *2002 IEEE International Conference on Acoustics, Speech, and Signal Processing*, vol. 3, pp. III–2285–III–2288, May 2002.

[113] R. Pickholtz and K. Elbarbary, "The Recursive Constant Modulus Algorithm; A New Approach for Real-Time Array Processing," *Proceedings of 27th Asilomar Conference on Signals, Systems and Computers*, pp. 627–632 vol.1, Nov 1993.

[114] Y. Chen, T. Le-Ngoc, B. Champagne, and C. Xu, "Recursive Least Squares Constant Modulus Algorithm for Blind Adaptive Array," *IEEE Transactions on Signal Processing*, vol. 52, pp. 1452–1456, May 2004.

[115] V. Zarzoso and P. Comon, "Optimal Step-Size Constant Modulus Algorithm," *IEEE Transactions on Communications*, vol. 56, pp. 10–13, Jan 2008.

[116] C. B. Papadias and D. T. M. Slock, "Normalized Sliding Window Constant Modulus and Decision-Directed Algorithms: a Link Between Blind Equalization and Classical Adaptive Filtering," *IEEE Transactions on Signal Processing*, vol. 45, pp. 231–235, Jan 1997.

[117] F. Magee and J. Proakis, "Adaptive Maximum-Likelihood Sequence Estimation for Digital Signaling in the Presence of Intersymbol Interference (Corresp.)," *IEEE Transactions on Information Theory*, vol. 19, pp. 120–124, Jan 1973.

[118] W. Lee and F. Hill, "A maximum-likelihood sequence estimator with decision-feedback equalization," *IEEE Transactions on Communications*, vol. 25, pp. 971–979, Sep 1977.

[119] A. Polydoros and K. M. Chugg, *Per-Survivor Processing (PSP)*, pp. 41–72. Boston, MA: Springer US, 1997.

[120] M. E. Rollins and S. J. Simmons, "Simplified Per-Survivor Kalman Processing in Fast Frequency-Selective Fading Channels," *IEEE Transactions on Communications*, vol. 45, pp. 544–553, May 1997.

[121] D. S. Skelley, "Integrated Network-Enhanced Telemetry," *International Telemetering Conference Proceedings*, Oct 2003.

[122] G. Castellini, F. Conti, E. D. Re, and L. Pierucci, "A Continuously Adaptive MLSE Receiver for Mobile Communications: Algorithm and Performance," *IEEE Transactions on Communications*, vol. 45, pp. 80–89, Jan 1997.

[123] A. E. S. El-Mahdy, "Adaptive Channel Estimation and Equalization for Rapidly Mobile Communication Channels," *IEEE Transactions on Communications*, vol. 52, pp. 1126–1135, Jul 2004.

[124] M. Rice and E. Law, "Aeronautical Telemetry Fading Sources At Test Ranges," *International Telemetering Conference Proceedings*, Oct 1997.

[125] V. Tarokh, H. Jafarkhani, and A. R. Calderbank, "Space-Time Block Codes from Orthogonal Designs," *IEEE Transactions on Information Theory*, vol. 45, pp. 1456–1467, Jul 1999.

[126] T. Nelson and M. Rice, "Detection of Alamouti Space-Time Encoded Offset QPSK," *IEEE GLOBECOM 2007 - IEEE Global Telecommunications Conference*, pp. 3538–3542, Nov 2007.

[127] J. K. Cavers, "Space-Time Coding using MSK," *IEEE Transactions on Wireless Communications*, vol. 4, pp. 185–191, Jan 2005.

[128] R. H. H. Yang, S.-J. Chern, G.-C. Shiu, and M.-T. Lee, "Space-Time Coded GMSK for Wireless Communication," in *2005 International Symposium on Intelligent Signal Processing and Communication Systems*, pp. 413–416, Dec 2005.

[129] L. Xian, R. Punnoose, and H. Liu, "Space-Time Block Coded GMSK With Low-Complexity Linear Receiver," *2006 IEEE International Conference on Communications*, vol. 11, pp. 4876–4881, June 2006.

[130] M. Rice, T. Nelson, J. Palmer, C. Lavin, and K. Temple, "Space-Time Coding for Aeronautical Telemetry: Part I — Estimators," *IEEE Transactions on Aerospace and Electronic Systems*, vol. 53, pp. 1709–1731, Aug 2017.

[131] M. Rice, T. Nelson, J. Palmer, C. Lavin, and K. Temple, "Space-Time Coding for Aeronautical Telemetry: Part II — Decoder and System Performance," *IEEE Transactions on Aerospace and Electronic Systems*, vol. PP, pp. 1–1, Aug 2017.

[132] T. Nelson and M. Rice, "Detection of Alamouti Encoded Shaped Offset QPSK," in *MILCOM 2007 - IEEE Military Communications Conference*, pp. 1–7, Oct 2007.

[133] CCSDS, *Low Density Parity Check Codes for Use in Near-Earth and Deep Space Applications*. Consultative Committee for Space Data Systems, 131.1-O-2 Orange Book, Sep 2007.

[134] J. Hagenauer and P. Hoeher, "A Viterbi Algorithm with Soft-Decision Outputs and Its Applications," *Global Telecommunications Conference and Exhibition 'Communications Technology for the 1990s and Beyond' (GLOBECOM), 1989. IEEE*, pp. 1680–1686 vol.3, Nov 1989.

[135] J. Tan and G. L. Stuber, "A MAP Equivalent SOVA for Non-Binary Turbo Codes," *2000 IEEE International Conference on Communications. ICC 2000. Global Convergence Through Communications. Conference Record*, vol. 2, pp. 602–606 vol.2, June 2000.

[136] A. J. Viterbi, "An Intuitive Justification and a Simplified Implementation of The MAP Decoder for Convolutional Codes," *IEEE Journal on Selected Areas in Communications*, vol. 16, pp. 260–264, Feb 1998.

[137] J. B. Anderson, *Instrumentable Tree Encoding of Information Sources*. School of Electrical Engineering, Cornell University, Ithaca, N.Y., 1969.

[138] V. Franz and J. B. Anderson, "Concatenated Decoding with a Reduced-Search BCJR Algorithm," *IEEE Journal on Selected Areas in Communications*, vol. 16, pp. 186–195, Feb 1998.

[139] K. K. Y. Wong, *The Soft-Output M-Algorithm and Its Applications*. Queen's University, 2006.

[140] C. Shaw and M. Rice, "Turbo-Coded APSK for Telemetry," *International Telemetering Conference Proceedings*, Oct 2007.

UNIVERSITE BRETAGNE LOIRE / MATHSTIC

CentraleSupélec

Titre : Étude de techniques de réception des modulations de fréquence pour la télémesure aéronautique

Mots clés :

Résumé :

.

Title :

Keywords:

Abstract: